

Second IEEE/LEOS Benelux Chapter, November 26th, 1997, Eindhoven University of Technology, The Netherlands

Citation for published version (APA):

Karouta, F., Haverkort, J. E. M., Kennis, F. J. J., & Peeters, A. P. (Eds.) (1997). *Second IEEE/LEOS Benelux Chapter, November 26th, 1997, Eindhoven University of Technology, The Netherlands*. STW Technology Foundation.

Document status and date:

Published: 01/01/1997

Document Version:

Publisher's PDF, also known as Version of Record (includes final page, issue and volume numbers)

Please check the document version of this publication:

- A submitted manuscript is the version of the article upon submission and before peer-review. There can be important differences between the submitted version and the official published version of record. People interested in the research are advised to contact the author for the final version of the publication, or visit the DOI to the publisher's website.
- The final author version and the galley proof are versions of the publication after peer review.
- The final published version features the final layout of the paper including the volume, issue and page numbers.

[Link to publication](#)

General rights

Copyright and moral rights for the publications made accessible in the public portal are retained by the authors and/or other copyright owners and it is a condition of accessing publications that users recognise and abide by the legal requirements associated with these rights.

- Users may download and print one copy of any publication from the public portal for the purpose of private study or research.
- You may not further distribute the material or use it for any profit-making activity or commercial gain
- You may freely distribute the URL identifying the publication in the public portal.

If the publication is distributed under the terms of Article 25fa of the Dutch Copyright Act, indicated by the "Taverne" license above, please follow below link for the End User Agreement:

www.tue.nl/taverne

Take down policy

If you believe that this document breaches copyright please contact us at:

openaccess@tue.nl

providing details and we will investigate your claim.

Proceedings

1997 IEEE/LEOS Symposium Benelux Chapter



COBRA



Technology
Foundation



Electro-Optics



RIXTRON



Editors:

F.Karouta, J.E.M. Haverkort, F.J.J. Kennis and A.P. Peeters

November 26, 1997

Eindhoven University of Technology, The Netherlands

proceedings 1997
second
ieee/leos symposium
benelux chapter



November 26th, 1997
Eindhoven University of Technology
The Netherlands

editors

F. Karouta
J.E.M. Haverkort
F.J.J. Kennis
A.P. Peeters

supported by

Technology Foundation STW
COBRA Research Institute
Eindhoven University of Technology
Senter - IOP Electro-Optics
Philips Optoelectronics
Aixtron GmbH (Germany)

published by

Technology Foundation STW
p.o. box 3021
3502 GA Utrecht

Raadstede 15 - 19
3413 HA Nieuwegein

phone +31 (0) 30 600 12 11

fax +31 (0) 30 601 44 08

e-mail leos@stw.nl

www <http://www.stw.nl/commtech>

editors

F. Karouta
J.E.M. Haverkort
F.J.J. Kennis
A.P. Peeters

proceedings 1997 symposium of the ieee/leos benelux chapter ISBN 90-73461-13-8

keywords

integrated optics, photonics, lasers, lightwave
technology, nonlinear optics, optical communication,
optical materials, optical sensors, quantum
electronics

copyright©

copyright 1997
Technology Foundation STW
Nieuwegein, the Netherlands

Abstracting is permitted with credit to the source. Individual readers and libraries acting for them are permitted to make fair use of the material in these proceedings, such as to copy an article for use in teaching or research, provided that such copies are not sold. Authors are permitted to copy or reprint their own papers. For other copying or republication permission, write to the publisher.

The papers in this book comprise the digest of the meeting mentioned on the cover and title page. They reflect the authors' opinions and are published as presented and without change, in the interest of timely dissemination. Their inclusion in this publication does not necessarily constitute endorsement by the publisher.

Printed in the Netherlands

STW-1997 11 10-01

preface

It is with a great pleasure and a great honour to welcome the Second Annual Symposium of the IEEE/LEOS Benelux Chapter at the Eindhoven University of Technology.

The Benelux Chapter of the Institute of Electrical and Electronics Engineers, Lasers and Electro-Optics Society, was founded in 1996. LEOS fields of interest are: lasers and integrated optics, optical communication systems and devices, optical sensors, physics of novel materials, polymers and inorganic materials, nonlinear optics, quantum electronics and quantum optics. One of the main objectives of the annual symposium is to bring together scientists and engineers working in universities, industries and other research institutes and to stimulate scientific discussion, knowledge transfer and possible future collaboration. Another objective is the promotion of the IEEE/LEOS Benelux Chapter. In this respect the Chapter has been successful as it received in 1997 the award of best membership increase.

The first symposium held at the University of Twente, welcomed 180 participants representing most Dutch and Belgian universities and companies. While I wrote this preface the number of early registrants exceeded already 140 persons. This is very encouraging and promising for the future, illustrating the need for this symposium within the scientific and engineering community of the Benelux dealing with LEOS fields. Moreover, this will guarantee the continuity of this event.

The Second Symposium is a one-day event like the first one. In total 67 contributions will be presented covering most of the LEOS fields of interest. Most of these contributions are posters (45). The Proceedings book includes the papers of both the oral and poster presentations.

I am very happy with the increasing interest among the physicists at this symposium. Such a trend can only be encouraged as I believe that their contribution to the understanding of fundamental physical aspects and phenomena is absolutely indispensable for all LEOS topics including the communication systems.

I would like to thank all participants, speakers, especially invited speakers, members of the organising and Program committees. I would like to thank all sponsors who made it possible to organise this symposium: the Eindhoven University of Technology, The Technology Foundation STW, COBRA InterUniversity Research Institute, Senter IOP Electro-Optics, Philips Optoelectronics and Aixtron GmbH - Aachen. Finally, I would like to thank Mrs. Annemiek Peeters from STW for her outstanding help in the organisation of this symposium.

Fouad Karouta
Eindhoven University of Technology

7 November 1997



program committee

J.H. Haverkort
R.G.F. Baets
A. Driessen
F. Karouta
D. Lenstra
J.C. v.d. Plaats
B.H. Verbeek

Eindhoven University of Technology
University of Ghent IMEC
University of Twente (Enschede)
Eindhoven University of Technology
The Vrije Universiteit (Amsterdam)
Lucent Technologies (Huizen)
Philips Research Laboratories (Eindhoven)

organizing committee

F. Karouta
A. Driessen
J.H. Haverkort
F.J.J. Kennis
J.P. Veen
A.P. Peeters

Eindhoven University of Technology
University of Twente (Enschede)
Eindhoven University of Technology
Eindhoven University of Technology
Technology Foundation STW (Nieuwegein)
Technology Foundation STW (Nieuwegein)

Contents

Title page	i
General information	ii
Preface by F. Karouta	iii
Composition committees	iv
Contents	v

part one

Invited speakers	1
° Photonic Bandgap Crystals <i>A. Lagendijk</i>	3
° Kilowatt-Class Ytterbium: Yag Lasers <i>P. Muys</i>	5
° The Role of Optics in Future Transport Networks <i>N. Wauters</i>	11
° Characterization of optical amplifiers for multi-wavelength networks <i>F. Willems</i>	13

part two

° WDM Transmission of a 10 Gbit/s Soliton and a 2.5 Gbit/s NRZ Signal over 150 km SSMF using Semiconductor Laser Amplifiers <i>J.G.L. Jennen, R.C.J. Smets, H. de Waardt</i>	1
° First EDFA for Single Fibre Tree-and-Branch Broadband Access Networks Carrying uni-directional AM-CATV and bi-directional digital Multi-Wavelength Signals <i>C.A.M. Steenbergen, F.W. Willems, A.W.L. Janssen, J.C. van der Plaats, D. Jacob, M. Prassas</i>	5
° 2.5 Gbit/s, 645 nm GIPOF Transmission Link with Record Receiver Sensitivity using an APD <i>W. Li, H. v.d. Boom, G. Khoe, H. de Waardt, Y. Koike, S. Yamazaki</i>	9

◦ Experimental Demonstration of a Free Space Intrachip Micro-Optical Interconnect <i>G. Verschaffelt, R. Buczynski, P. Tuteleers, P. Vynck, V. Baukens, S. Kufner, M. Kufner, A. Hermanne, J. Genoe, D. Coppée, R. Vounckx, P. Heremans, H. Thienpont, I. Veretennicoff</i>	13
◦ Imaging of the field distribution in integrated optical waveguides <i>M.L.M. Balistreri, X. Borrisé, J.P. Korterik, N.F. van Hulst</i>	17
◦ Technological Aspects of Deep Proton Lithography for the Fabrication of Micro-optical Elements <i>P. Vynck, P. Tuteleers, H. Ottevaere, V. Baukens, G. Verschaffelt, S. Kufner, M. Kufner, A. Hermanne, H. Thienpont, I. Veretennicoff</i>	21
◦ The Spatially Modulated Silicon CMOS detector <i>D. Coppée, W. Pan, J. Stiens, R. Vounckx, M. Kuijk</i>	25
◦ Integrated optical sensor system for detection of chemical concentrations <i>R.G. Heideman, P.V. Lambeck</i>	29
◦ Polymeric integrated optical components for add-drop multiplexing <i>M.B.J. Diemeer, E. Rikkers, D.T. van Veen, G.J.M. Krijnen, M.J. Gilde, J.L. Joppe, A.F. Bakker, M.K. Smit, R.M. de Ridder, A. Driessen, A.M.J. Koonen</i>	33
◦ Tuneable WDM add-drop multiplexer using cascaded Mach-Zehnder wavelength filters <i>B.H. Sikken, R.M. de Ridder, K. Wörhoff, G.J.M. Krijnen, R.G. Heideman, A. Driessen</i>	37
◦ A compact integrated single phasar optical crossconnect on InP <i>C.G.P. Herben, C.G.M. Vreeburg, D.H.P. Maat, S.J.M. Leijters, Y.S. Oei, F.H. Groen, J.J.G.M. van der Tol, P. Demeester, M.K. Smit</i>	41
◦ Monolithic integration using selective area Chemical Beam Epitaxy <i>C.A. Verschuren, P.J. Harmsma, Y.S. Oei, M.R. Leys, H. Vonk, J.H. Wolter</i>	45
◦ Experimental demonstration of 'GIRO-gratings' <i>S. Goeman, B. Dhoedt, K. Caekebeke, S. Verstuyft, R. Baets, P. van Daele, N. Nieuborg, J. Sitens, H. Thienpont, R. Vounckx</i>	49
◦ Polarization-dependent Saturation in Semiconductor Vertical-Cavity Lasers <i>M.P. van Exter, A. Al-Remawi, J.P. Woerdman</i>	53
◦ Self-Pulsation and Mode-Locking in Narrow Stripe Lasers <i>J.L.A. Dubbeldam, D. Lenstra</i>	57
◦ Active mode locking of a p-Ge hot hole laser <i>J.N. Hovenier, T.P. Klaassen, W.Th. Wenckebach</i>	61

° Thermal lateral waveguiding in gain-guided, low confinement laser diodes <i>M. Buda, G.A. Acket, T.G. van de Roer, W.C. van der Vleuten, E. Smalbrugge</i>	65
° Resonator design for a long pulse XeCl excimer laser <i>R.M. Hofstra, M.J. Zwegers, F.A. van Goor, W.J. Witteman</i>	69
<hr/>	
° On the dynamics of solitons in randomly birefringent optical fibres <i>H.J.S. Dorren, J.J.B. van den Heuvel</i>	73
° How does optical cross-talk depend on the network topology? <i>J. Siffels, I. Tafur Monroy, H. de Waardt, H.J.S. Dorren</i>	77
° Theoretical consideration on bandwidth and chirping in injection-locked semiconductor lasers <i>G. Yabre</i>	81
° Pulse Collision in Wavelength Division Multiplexed Optical Communication System <i>H. Wang</i>	85
° Crosstalk analysis of an OXC based on a broadcast and select optical space switch <i>T. Gyselings, G. Morthier, R. Baets</i>	89
° Meshed Wavelength Division Multiplexed Networks partially equipped with wavelength converters <i>W. van Parys, B. van caenegem, B. Vandenberghe, P. Demeester</i>	93
° Impelementation approaches for spare capacity in meshed WDM transport networks <i>B. van caenegem, B. Jacobs, P. Demeester</i>	97
° InP-based LED emitting at $1.55\mu\text{m}$ with 6.8% external QE <i>B. Depreter, J. Blondelle, I. Moerman, R. Baets, P. van Daele, P. Demeester</i>	101
° High Efficiency InGaAsP/InP Phase Modulator at $1.06\mu\text{m}$ <i>G. Flamand, J. Hendrix, K. Jacobs, I. Moerman, B. Dhoedt, R. Baets, P. Demeester, P. van Daele</i>	105
° OLIMPEX: measurement and parameter extraction tools for advanced laser diodes <i>P. Verhoeve, G. Diet, G. Sarlet, G. Morthier, R. Baets, T. Farrell</i>	109

° Termination and Coupling Experiments for a 1 x 12 Small Diameter (125 μm) Plastic Optical Fibre Array and POF Coupling to Micocavity LEDs <i>A. van Hove, R. Bockstaele, T. Coosemans, B. Dhoedt, R. Baets, P. van Daele</i>	113
° Polymeric Waveguide based Optical Interconnect for Datacom Applications <i>J.E. van der Linden, P.P. van Daele, P.M. de Dobbelaere, M.B. Diemeer</i>	117
° Polarization Switching in VCSEL's Due to Thermal Index guiding <i>K. Panajotov, B. Ryvkin, J. Danckaert, M. Peeters, H. Thienpont, I. Veretennicoff</i>	121
° Reconfigurable optical interconnects in free-space optical processing modules using polarization-selective diffractive optical elements <i>N. Nieuborg, A. Goulet, H. Thienpont, A. Kirk, P. Koczyk, P. Heremans, M. Kuijk, C. de Tandt, W. Ranson, R. Vounckx, I. Veretennicoff</i>	125
° Optical performance analysis of free-space and guided-wave optical pathway blocks for intra-MCM interconnects <i>V. Baukens, G. Verschaffelt, P. Tuteleers, P. Vynck, H. Ottevaere, M. Kufner, S. Kufner, H. Thienpont, I. Veretennicoff, B. Dhoedt, R. Baets</i>	129
° The study of the stimulated light scattering accompanied with a two-photon dissociation in liquid ethanol at 308 nm and 248 nm <i>A.A. Pastor, V.V. Bertsev, S.F. Bureiko, A.A. Keller, P.Yu. Serdobintsev</i>	133
° A single channel dropping filter based on a cylindrical micro-resonator <i>F.C. Blom, H. Kelderman, H.J.W.M. Hoekstra, A. Driessen, Th.J.A. Popma</i>	137
° Integrated optical refractometer based on losses in curved waveguides <i>G.J. Veldhuis, P.V. Lambeck</i>	141
° Design method for coplanar waveguides in high-speed integrated electro-optical modulators <i>M. Hoekman, R.M. de Ridder, G.J.M. Krijnen, E. Rikkers, A. Driessen, A. Bakker</i>	145
° Beam pointing stability studies on a long pulse XeCl excimer laser fitted with unstable resonators <i>R.M. Hofstra, M.J. Zweegers, F.A. van Goor, W.J. Witteman</i>	149
° Application of silicon oxynitride in telecommunication devices <i>K. Wörhoff, P.V. Lambeck, R.M. de Ridder, A. Driessen</i>	153
° The spatial structure of a transverse RF excited Ar-He-Xe laser <i>F.J. Blok, I.V. Kochetov, A.P. Napartovich, V.N. Ochkin, P.J.M. Peters, S.A. Starostin, Y.B. Udalov, W.J. Witteman</i>	157
° An x-ray preionised discharge pumped ArF-laser <i>L. Feenstra, O.B. Hoekstra, P.J.M. Peters, W.J. Witteman</i>	161

◦ Coherence multiplexing using differential detection <i>E.J. Kersten, G.H.L.M. Heideman, W. van Etten</i>	165
◦ Estimating Error Probabilities caused by In-band and Out-band Crosstalk in Multi-Wavelength All-Optical Networks <i>A.M.J. Koonen, D.T. van Veen</i>	169
◦ Stability analysis and spectral properties of a diode laser with sluggish phase-conjugate feedback <i>W.A. van der Graaf, L. Pesquera, D. Lenstra</i>	173
◦ Quantum electrodynamical Modeling of Light Emission in Semiconducting Devices <i>C. Hooijer, D. Lenstra</i>	177
◦ Wave propagation in Semiconductor Laser Amplifier <i>T.D. Visser et. al.</i>	<i>withdrawn</i> 181
◦ Chopped InGaAs/InP quantum well for polarization independent interferometric switching at 1.55 μ m <i>B.H.P. Dorren, A. Yu. silov, M.R. Leys, J.E.M. Haverkort, J.H. Wolter</i>	185
◦ Selective Photoluminescence of Self-Assembled Quantum Dots <i>A.W.E. Minnaert, A. Yu. Silov, W. van der Vleuten, J.E.M. Haverkort, J.H. Wolter</i>	189
◦ An improved polarisation independent switch <i>D.H.P. Maat, Y. Zhu, C.G.M. Vreeburg, F.H. Groen, H. van Brug, H.J. Frankena, I. Moerman</i>	193
◦ Optical information processing in Massively Parallel Processing <i>E.E.E. Frietman</i>	197
◦ Integration of Optical Amplifiers and Waveguide Devices on InP <i>P.J. Harmsma, C.G.M. Vreeburg, C.A. Verschuren, M.R. Leys, H. Vonk, Y.S. Oei</i>	201
◦ Photonic IC for Electronic Radar Beam Control <i>J. Stulemeijer, X.J.M. Leijtens, I. Moerman, M.K. Smit</i>	205
◦ High frequency 8 channel WDM-receiver <i>A. Siefke, C.A.M. Steenbergen, Y.C. Zhu, J.W. Pedersen, M. de Kok, I. Moerman, X.J.M. Leijtens, M.K. Smit</i>	209
◦ Integrated Indium Phosphide based Photoreceiver <i>N.G.H. van Melick, F. Karouta, L.M.F. Kaufmann, A. Siefke</i>	213
◦ Microwave-behaviour comparison of bias-probes for on-wafer testing of MMICs and OEICs <i>J.J.M. Kwaspen, H.C. Heyker</i>	217

◦ Monolithical Integration of GaAs-based Laser Photodetector <i>H.A. Langeleer, F. Karouta, J.J.W. van Praagh, W.C. van der Vleuten</i>	221
◦ Intermixing in InGaAs/GaAs Structures for Mirror Protection in High Power Lasers <i>F. Karouta, J.J.W. van Praagh, G.A. Acket, T.J. Eijkemans, C.M. van Es, W.C. van der Vleuten</i>	225
◦ Polarization memory in vertical-cavity semiconductor lasers <i>R.F.M. Hendriks, M.P. van Exter, J.P. Woerdman</i>	229
◦ Polarization Excess Quantum Noise <i>A.M. van der Lee, N.J. van Druten, A.L. Mieremet, M.A. van Eijkelenborg, A.M. Lindberg, M.P. van Exter, J.P. Woerdman</i>	233
◦ Non-linear optical properties of dendrimeric structured chromophores <i>A.W. Gerbrandij, A. Pugžys, C.A.G.O. Varma, S.J.E. Mulders, A.J. Brouwer, R.M.J. Liskamp</i>	237
◦ Germanium Gallium Sulfide glasses as host materials for Pr-doped optical fiber amplifier <i>R.C. Schimmel, A.J. Faber</i>	241
◦ Towards Low PMD Characterisation Techniques for New Generation Optical Fibers <i>F. Ravet, Y. Choquet, B. Heens, X. Wang, J.-C. Froidure, M. Blondel</i>	244
◦ A New Differential Optical Amplifier Based on Nonlinear DFB/F-P Bragg Gratings <i>X. Wang, B. Heens, F. Ravet, J.-C. Froidure, M. Blondel</i>	248
<hr/>	
Index authors	253
<hr/>	



Invited speakers

A. Lagendijk (The Universiteit van Amsterdam)

Photonic Bandgap Crystals

P. Muys (Radius Engineering, Ghent, Belgium)

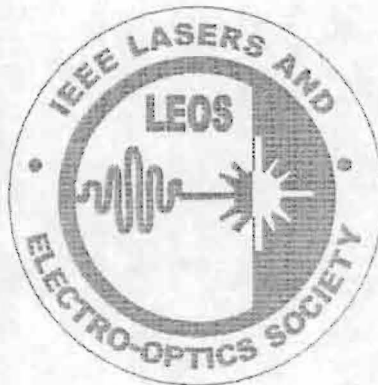
Kilowatt-Class Ytterbium: Yag Lasers

N. Wauters (HERMES Operations and Engineering, Hoeilaart, Belgium)

The Role of Optics in Future Transport Networks

F. Willems (Lucent Technologies, Huizen)

Characterization of optical amplifiers for multi-wavelength networks



A. Lagendijk
(The Universiteit van Amsterdam)

P. Muys
(Radius Engineering/Laser Power Europe, Ghent, Belgium)

1. INTRODUCTION

Due to the recent availability of high power diode lasers (20 W per bar), these devices are being studied now to serve as pump source for solid state lasers.

Since a drastic price drop is expected to occur over the next coming years, these diode lasers will become economical alternatives to Krypton lamps as pump source for solid state lasers. This drive has resulted in a renewed attention to pump laser materials which cannot be efficiently excited by the broad spectral emission of a flashlamp. A particular and important example of this class of materials is the rare earth Ytterbium, doped in the classic YAG-matrix. This material has a number of definite advantages versus the traditional Neodymium. Ytterbium based lasers attract much attention due to their low heat generation, simple electronic structure (absence of unwanted pumping processes such as excited state absorption and concentration quenching) and broad absorption and emission bandwidths. The inherently small quantum defect in Yb^{3+} lasers is a motivating interest for operation at higher power levels. Efficient laser action has been demonstrated in $\text{Yb}:\text{YAG}$ (1,2,3). The major drawback of Ytterbium is that its pumping scheme constitutes a so-called quasi-three level system. Here, the lower laser level stays permanently thermally populated since its energy level is only 612 cm^{-1} above the ground level. This means that it is hard to create a population inversion, just like in the case of a pure three level system such as Ruby. In this paper, we describe the actual state-of-the-art to reach output powers of around 1kW with diode pumped $\text{Yb}:\text{YAG}$ lasers.

2. SPECTROSCOPY OF THE YTTERBIUM-ION.

The relatively high quantum defect of $\text{Nd}:\text{YAG}$ limits its efficiency to about 76%, since the pump wavelength is situated at 808 nm, and the emission wavelength at 1064 nm. Nonradiative decay and upconversion, which are enabled by the large number of energy levels above and between the laser levels, reduce the maximum efficiency to below 68%. In contrast, $\text{Yb}:\text{YAG}$ exhibits an extremely simple energy level scheme, consisting of only two energy levels of the Yb^{3+} ion, which are split into manifolds by the crystal fields of the host due to the Stark effect. The lowest higher energy levels are already located in the UV, above 40.000 cm^{-1} . The pump level is situated at $G_p = 10\,624\text{ cm}^{-1}$, the upper laser level at $G_u = 10\,327\text{ cm}^{-1}$ and the lower laser level at $G_l = 612\text{ cm}^{-1}$. The quantum defect $G_p - G_u$ is very small, resulting in a maximum efficiency of 91% (pump wavelength 940 nm, emission wavelength 1030 nm), which is not reduced by upconversion or nonradiative decay. The fractional heating of $\text{Yb}:\text{YAG}$ is therefore only about 9%, giving at least a threefold improvement over $\text{Nd}:\text{YAG}$. Another advantage, especially for pulsed applications, is the lifetime of the upper laser level of about 1 ms, which is four times longer than for $\text{Nd}:\text{YAG}$, leading to higher pulse energies in cw-pumped pulse applications (Q-switching). The lower laser level, exhibits a thermally induced population of about 4 % of the Yb doping concentration at room temperature, giving rise to a high pump power density threshold of about 1.5 kW/cm^2 . Due to this thermal population, unpumped regions of an $\text{Yb}:\text{YAG}$ crystal reabsorb at the emission wavelength.

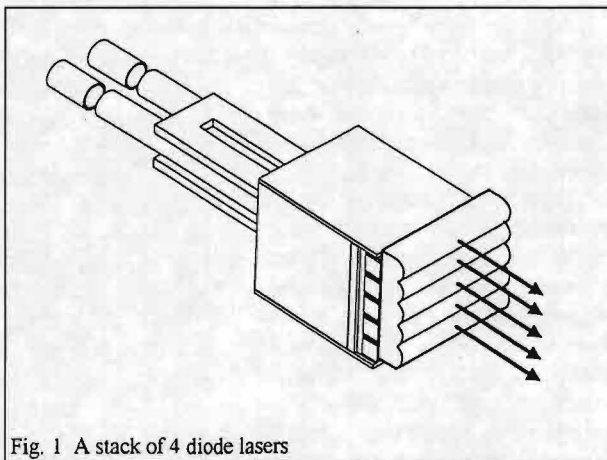


Fig. 1 A stack of 4 diode lasers

The absorption band of Yb:YAG around 940 nm is broad enough (about 10 nm FWHM) to cover the emission linewidth of typical high-power InGaAs laser diode arrays (3-6 nm FWHM), allowing optimal absorption. Together with the possibility of using doping levels in excess of 25 at % without quenching, this leads to absorption lengths as short as 0.5mm.

The pump wavelengths required for Yb-doped crystals allow the use of InGaAs-laser diodes, which are much simpler to fabricate with high yield and reliability than the AlGaAs-diodes used for Nd-doped materials. One bar of such a laser can emit up to 30W of continuous power. These bars can be stacked one on top of the other, calling for proper heat sinking and water flow (see fig. 1).

Stacks up to 2kW of output power have already been realised. Since the bar-to-bar distance is 1.7mm, a 1kW laser is about 80mm high by 15mm wide. Each bar emits a highly astigmatic mode. Combining all these "lines of light" into a narrow high intensity beam, is a major challenge to implement such a laser stack as pump source for a YAG-rod or YAG-slab.

The emission spectrum of Yb:YAG, is dominated by the broad emission line at 1030 nm with a linewidth of 11 nm (FWHM). The peak emission cross-section of Yb:YAG is relatively small ($\approx 1.8 \cdot 10^{-20} \text{ cm}^2$), allowing the storage of high energies without prelasing. On the other hand, the obtainable gain is relatively small compared to Nd:YAG.

3. HEAT GENERATION IN YB-YAG

In Nd:YAG and other Nd^{3+} doped laser gain media, there is nonradiative relaxation from the pump bands to the upper metastable laser level and from the lower laser level to the ground state. These phonons are the primary source of heating, thus laser materials with a smaller difference between the pump wavelength and laser output wavelength may be expected to have lower heating. The output power obtainable from a solid-state laser is ultimately limited by stress fracture due to heating of the gain element by nonradiative relaxation. At average powers below the stress-fracture limit, heating also leads to thermo-optic aberrations, lensing, and birefringence that reduce the efficiency of laser operation, decrease the output beam quality, and change the resonator stability with pump power (6). One way to lessen the impact of gain element heating is to choose gain media that generate less heat. Calorimetric measurements show that the fractional thermal loading in Nd:YAG is more than three times greater than Yb:YAG (4). The fractional thermal load is defined as the fraction of the absorbed pump power that is converted into heat. Thus, Yb:YAG may be the gain medium of choice for high average power laser devices operating near 1 μm .

4. STRATEGIES TO REACH HIGH OUTPUT POWER

How can the diode light be concentrated with high transfer efficiency from the stack of diode lasers to the Yb:YAG crystal? We will review the three most important design-concepts. In this way, a number of power scalable experimental lasers have been set up. All three designs basically attempt to match the YAG-dimensions to the absorption length of Yb in YAG. This is an essential requirement, since unpumped regions of the YAG will absorb the 1030nm radiation and hence this effect will contribute to the generation of heat. Next to the efficient collection of the highly diverging diode light, proper cooling of the YAG-crystal is the second major issue in upscaling the Ytterbium laser to high power.

The three laser types are scheduled to deliver 1kW of output power, by the end of 1997.

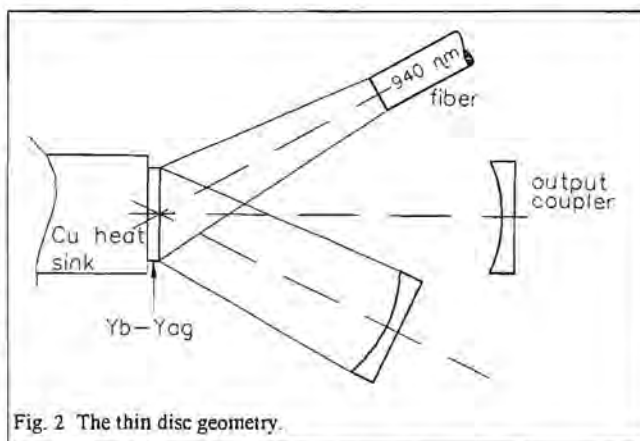


Fig. 2 The thin disc geometry.

4.1. The thin disc geometry or face-pumped resonator (ref. 1)

A YAG-disk, thickness 0.5mm typically, is heavily doped with Yb, up to 25%. This makes the absorption length at 941nm of the order of 1mm. The disk is directly placed in contact with a heat sink (fig.2). The side placed on the heat sink is coated first with a High Reflectivity layer at 1030nm. The other free side is AR coated.

The diode light is transported through a fiber to the laser cavity. There it is imaged with a lens on the free surface of the YAG-disk.

4.2. End-pumped resonators (ref.9)

Fig. 3 is a sketch of an end-pumped Yb:YAG laser. The pump source consisted of a 43 bar stack of 1 cm long InGaAs laser diode bars packaged on microchannel coolers.

The diode light is first conditioned by a microlens directly mounted on each diode package. The microlens allows the diode light to emerge with a far field 1/e divergence of ~10 mrad and ~150 mrad in the fast and slow axis directions respectively. The pump light is then homogenized and concentrated down with a fused silica lens duct to allow for end-pumping of the laser rod. The laser rod is a composite of doped and undoped YAG.

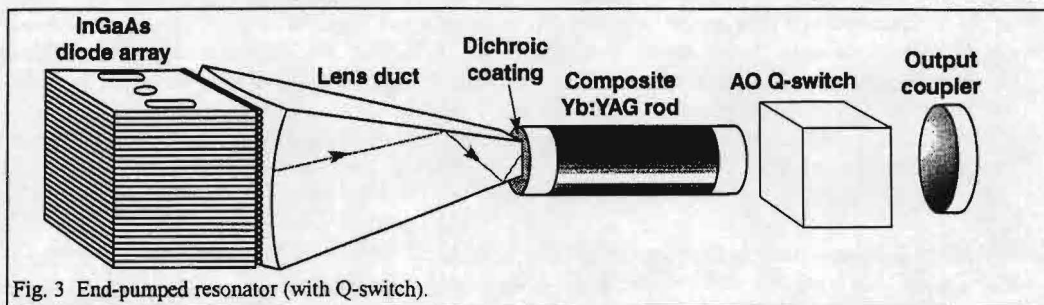


Fig. 3 End-pumped resonator (with Q-switch).

The undoped YAG pieces or endcaps are diffusion bonded to both ends of the doped rod. The endcaps help reduce the thermal loading and stresses on the input and output faces of the rod and therefore help prevent damage. The Yb:YAG composite rod was coated at the pump end of the rod with a multilayered, dichroic coating for high reflectance at 1030 nm and high transmission at 940 nm, thus allowing one end of the rod to perform as a flat high reflector for the laser cavity. A simple broad band anti-reflection coating was placed on the opposite or output end of the rod.

4.3. Side-pumped resonators (ref. 5)

Fig. 4 is a diagram of the prototype head. Only the 2mm-diameter, 20mm-long, 1-at. % Yb³⁺-doped volume is inside the integrating cavity. Both rod ends, outside the cavity, are undoped YAG, diffusion bonded to the center section (total rod length 31mm), facilitating mounting, coolant routing, and optical access. The fine-ground rod circumference is cooled with 15°C methanol impinging upon the rod from laser-drilled holes in the inner sleeve. The outer sleeve is solid glass. Diode bars are inherently bright enough to couple efficiently into this pump cavity, and indeed a cylindrical configuration was deliberately used so that for power scaling, the pump cavity's diameter can be enlarged to accommodate future low-power-density diode packages (with simpler and more economical thermal packaging) while maintaining the integrating cavity's efficiency. Arranged symmetrically as three groups of three 5-bar diode arrays each, 45 bars transversely pump the rod. The diodes were imaged onto the rod through antireflection-coated slots in the pump-cavity barrel, using three lens pairs. Except for these slots, all the pump cavity's outside walls are dielectrically coated for high reflectivity at the 941-nm pump band and low reflectivity, ~50%, at 1.03μm (to hinder parasitic oscillation). The diode-to-slot transport efficiency was only 52% because of slot-size mismatch and lens vignetting.

5. THE RATE EQUATION MODEL (ref. 7, 8)

Due to its quasi three level nature, Yb needs to be pumped hard before it reaches the threshold. Also, regions in the Yb:YAG crystal which remain unpumped, will absorb the generated laser radiation

at 1030 nm, resulting in a inhomogeneous heating of the crystal. This leads to thermal aberations, destroying the beam quality and the extraction efficiency.

In upscaling the diode pumped Yb:YAG laser to high output powers, a realistic potential is present to damage the crystal if the upscaling is not done with the necessary caution. Hence, this situation calls for the simulation of the excitation process by a mathematical model before an actual resonator is built. This model is known in the literature as the rate equation model. Our implementation does not consider space-dependent variations of the intrinsic parameters, only time-dependence is considered. Hence, our model is zero-dimensional (in space). Where it is needed, we will suppose a square cross section of the slab.

Each equation is a differential equation describing the dynamical evolution of resp. the internal energy of the crystal, the pump level population, the upper laser level population, the lower laser level population, the cavity photon density and the energy density of the pump light.

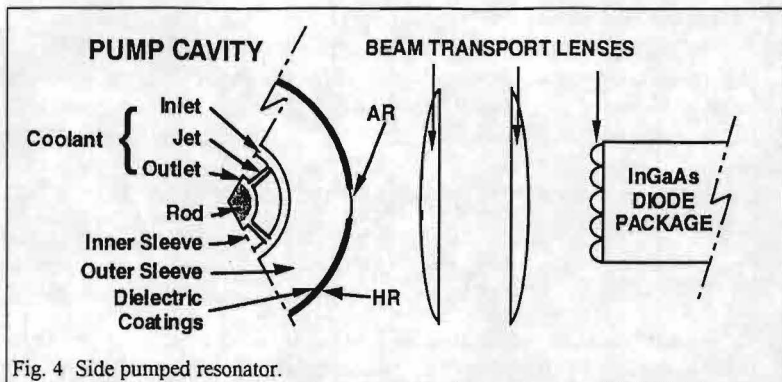


Fig. 4 Side pumped resonator.

E = energy per unit volume deposited in the crystal (i.e. heat)

E_o = ground level energy per unit volume present in the crystal at room temperature

E_p = energy per unit volume in the pump level

E_u = energy per unit volume in the upper laser level

E_l = energy per unit volume in the lower laser level

E_D = energy per unit volume of the pump photons

τ_{pu} = non-radiative decay from the pump to the upper laser level

τ_{lo} = non-radiative decay from the lower laser level to the ground level

ϕ = laser photon density

P_{cool} = power per unit volume flowing to the heat sink

T_o = crystal temperature before excitation

T = steady state temperature of the crystal

N_p = pump level population per unit volume

N_u = upper laser level population per unit volume

N_l = lower laser level population per unit volume

\bar{N}_l = lower laser level population per unit volume at temperature T , without lasing

N_{Yb} = Yb-doping of the crystal

N_o = ground level population per unit volume

N_D = number of pump photons per unit volume

P_{in} = radiant diode power trapped by the YAG-slab

The following relations hold :

$$P_{cool} : (E - E_o) / \tau_{cl} \quad T = E / (\rho c_p) \quad T_o = E_o / (\rho c_p) \quad N_o = N_{Yb} - N_p - N_u - N_l$$

$$\bar{N}_l = N_o \exp \left(- \frac{G_l}{kT} \right) \quad (\text{Maxwell - Boltzmann distribution law})$$

The rate equations are :

$$\frac{dE}{dt} = (G_p - G_u) \frac{N_p}{\tau_{pu}} + G_l \frac{N_l - \bar{N}_l}{\tau_{lo}} - P_{cool} \quad (1)$$

$$\frac{dE_p}{dt} = -\sigma_p c (N_p - N_o) N_D G_p - G_p \frac{N_p}{\tau_{pu}} \quad (2)$$

$$\frac{dE_u}{dt} = G_u \frac{N_p}{\tau_{pu}} - G_u \frac{N_u}{\tau_{sp}} - G_u \sigma c (N_u - N_e) \phi \quad (3)$$

$$\frac{dE_l}{dt} = G_l \frac{N_u}{\tau_{sp}} + G_l \sigma c (N_u - N_l) \phi - G_l \frac{N_l - \bar{N}_l}{\tau_{lo}} \quad (4)$$

$$\frac{d\phi}{dt} = \sigma c (N_u - N_l) \phi - \frac{\phi}{\tau_c} + \varphi \frac{N_u}{\tau_{sp}} \quad (5)$$

$$\frac{dE_D}{dt} = \frac{P_{in}}{\alpha^2 l_r} + G_p \sigma_p c (N_p - N_o) N_D \quad (6)$$

In steady state, the time derivatives become equal to zero. Eq (1) then takes on the form

$$G_l \frac{N_l - \bar{N}_l}{\tau_{lo}} = P_{cool} - (G_p - G_u) \frac{N_p}{\tau_{pu}} \quad (7)$$

By adding eq (3) and (4), we obtain

$$\frac{N_p}{\tau_{pu}} = \frac{N_l - \bar{N}_l}{\tau_{lo}} \quad (8)$$

Substituting (8) in (7) :

$$G_l \frac{N_p}{\tau_{pu}} = P_{cool} - (G_p - G_u) \frac{N_p}{\tau_{pu}} \quad \text{or}$$

$$N_p = P_{cool} \frac{\tau_{pu}}{G_l + G_p - G_u} \quad (9)$$

Adding eq (6) and (2) delivers :

$$\frac{P_{in}}{\alpha^2 l_r} = \frac{G_p N_p}{\tau_{pu}} \quad (10)$$

From (9) and (10) we finally obtain

$$P_{cool} = \frac{G_l + G_p - G_u}{G_p} \frac{P_{in}}{\alpha^2 l_r}$$

$$\text{hence } E - E_o = \frac{G_l + G_p - G_u}{G_p} \frac{P_{in} \tau_{cl}}{\alpha^2 l_r}$$

Using now the theory of heat transfer, one can prove that the characteristic time constant τ_{cl} linked with the cooling capability of the slab, is connected with the thermal diffusivity α through the relation

$$\tau_{cl} = \frac{(a/2)^2}{\alpha} \quad \text{where } \alpha = 0.038 \text{ cm}^2/\text{s} \text{ for YAG}$$

This means :

$$E-E_0 = \frac{G_l + G_p - G_u}{G_p} \frac{P_{in}}{4\alpha l_r}$$

We conclude that the final crystal temperature of the slab is not a function of the width a , only of its length l_r . Also in this approximation, the steady state temperature is not influenced by the laser output power. This is plausible, since the only way to generate heat is by creating photons between the transitions $p \rightarrow u$ and $l \rightarrow o$. We didn't account for any other heat creating path in the model.

6. CONCLUSION

Diode laser pumping of Yb:YAG is a quickly emerging technology to reach high power for industrial materials processing applications. Its favourable excitation scheme induces only a small fraction of the pump power which is rejected as heat. This means that out of a few cubic centimeter of resonator volume, kilowatt class of power extraction can be expected. This evolution is strengthened by a parallel evolution in the further miniaturisation of the diode lasers themselves.

REFERENCES

- (1) A. GIESEN et al Scalable concept for diode-pumped high-power solid state lasers
Appl. Phys.B, 58, 365-372 (1994)
- (2) U. BRAUCH et al Multiwatt diode-pumped Yb:YAG thin disk laser continuously
tunable between 1018 nm and 1053 nm
Optics letters, 20, 713-715 (1995)
- (3) P. LACOVARA et al Room temperature diode-pumped Yb:YAG laser
Optics letters, 16, 1089-1091 (1991)
- (4) T. FAN Heat generation in Nd:YAG and Yb:YAG
IEEE J.Q.E., 29, 1457-1459 (1993)
- (5) H. BRUESSELBACH et al 69-W-average power Yb:YAG laser
Optics letters, 21, 480-482 (1996)
- (6) D. BROWN Ultrahigh-average-power diode pumped Nd:YAG and Yb:YAG
lasers
IEEE J.Q.E., 33, 861-873 (1997)
- (7) T. FAN, R. BYER Modeling and CW operation of a quasi-three level 946 nm Nd:YAG
laser
IEEE J.Q.E., 23, 605-612 (1987)
- (8) T. TAIRA et al Modeling of quasi-three-level lasers and operation of CW Yb:YAG
lasers
Applied Optics, 36, 1867-1874 (1997)
- (9) R. BEACH CW Theory of quasi-three level end-pumped laser oscillators
Optics Comm., 123, 385-392 (1995)

N. Wauters
(HERMES Operations and Engineering, Hoeilaart, Belgium)

1. Introduction

A typical configuration of an Optical Fibre Amplifier (OFA) in a multi-channel application is given in Figure 1. At the transmitting side n signals, coming from n optical transmitters, Tx1, Tx2, . . . , Txn, each with a unique wavelength, $\lambda_1, \lambda_2, \dots, \lambda_n$, respectively, are combined by an optical multiplexer (OM). At the receiving side the n signals at $\lambda_1, \lambda_2, \dots, \lambda_n$, are separated with an optical demultiplexer (OD) and routed to separate optical receivers, Rx1, Rx2, . . . , Rxn, respectively. To characterize the OFA in this multi-channel application an input reference plane and an output reference plane are defined at the OFA input and output ports, respectively, as shown in the Figure.

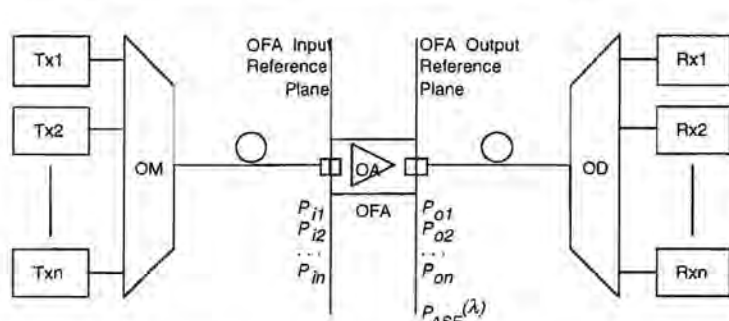


Figure 1 An Optical Fibre Amplifier in a multi-channel application

At the input reference plane, n input signals at the n wavelengths are considered, each with a unique power level, $P_{i1}, P_{i2}, \dots, P_{in}$, respectively. At the output reference plane, n output signals at the n wavelengths, resulting from the optical amplification

of the corresponding n input signals, are considered, each with power level $P_{o1}, P_{o2}, \dots, P_{on}$, respectively. Moreover, the amplified spontaneous emission, ASE, with a noise power spectral density, $P_{ASE}(l)$, is also to be considered at the OFA output port. Several issues apart from definitions and standardisation are to be addressed in measurements of OFAs for WDM applications: among them are spectral hole burning (SHB), channel addition/removal response, measurement efficiency and accuracy. The following sections are ment to introduce these topics and to give an overview of state of the art measurement methods for multi-wavelength optical amplifiers.

2. Important parameters for WDM application of OFAs

Definitions and standardisation of measurement methods for OFAs are currently under study in IEC SC86C-WG3. Recently the study group entered the field of OFAs for multi-wavelength applications. Most of the definitions and test methods available for single wavelength systems can also be applied for multi-channel systems (MCS), such as gain, noise-figure and output power. However, new definition and test methods are required for parameters that are specific to multi-wavelength applications. For networks containing add/drop nodes with amplification, an important parameter is the **Channel addition/removal steady-state gain response** which is defined as "the steady-state change in channel gain of any one of the channels due to the addition/removal of one or more other channels, for a specified multi-channel configuration". Normally, the parameter specified is the maximum channel addition/removal gain response when the final or initial power level of each of the input channels is equal to the minimum allowed. The worst-case channel addition/removal gain response is generally expected to occur when all but one of the channels are added or removed.

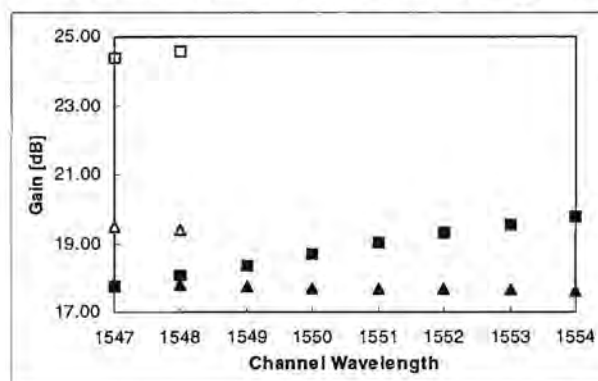


Figure 2: Gain versus wavelength for 8 channel load (closed triangles: overpumped EDFA, closed boxes: standard EDFA) and 2 channel load (open triangles: overpumped EDFA, open boxes: standard EDFA)

Channel addition/removal transient gain response is defined as "for a specified multi-channel configuration, the maximum change in channel gain of any one of the channels due to the addition/removal of one or more other channels, during the transient period after channel addition/removal". Normally, the parameter specified is the maximum channel addition/removal transient gain response when the final or initial power level of each of the input channels is equal to the minimum allowed.

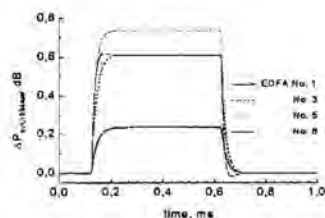


Figure 3: Output power variation at 1554 nm as a function of time along a cascade of overpumped EDFAs when 6 out of 8 channels are square wave modulated

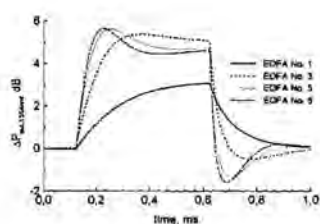


Figure 4: Output power variation at 1554 nm as a function of time along a cascade of standard EDFAs when 6 out of 8 channels are square wave modulated

As an example for the first parameter, we consider two amplifiers that are subjected to 8 channels positioned at wavelengths ranging from 1547 to 1554 nm with 1 nm spacing. The first amplifier is pumped with 200 mW 1480 nm pump, and the second with 74 mW. The length of the Erbium doped fibre is optimized to deliver 18 dB gain at 1547 nm, with an input power of -20 dB/channel. Note the superior channel addition/removal response for the first type: dropping 6 out of 8 channels causes a gain increase in the “surviving” channels, smaller than 2 dB for the 200 mW pumped amplifier, whereas the second amplifier shows more than 6 dB gain increase / channel (see Figure 2). Figure 3 and Figure 4 show an example of the transient response of the output power (or gain) as a function of time for several EDFA positions along a chain of 6 EDFAs each designed to deliver 20 dB gain to compensate for 20 dB of loss between consecutive EDFAs: note the overshoot that develops along the link for the “standard” EDFAs. Currently no measurement technique is standardised.

At least four effects contribute to the line-broadening in doped fibre amplifier: lifetime of the Erbium-ion metastable state, phonon collisions, Stark splitting and inhomogeneity. **Spectral Hole Burning (SHB)** or saturation hole burning is present in systems with inhomogeneity. Random field variations from site to site cause changes in Stark Splitting and center wavelengths of the laser transitions. Saturation at a certain wavelength can leave

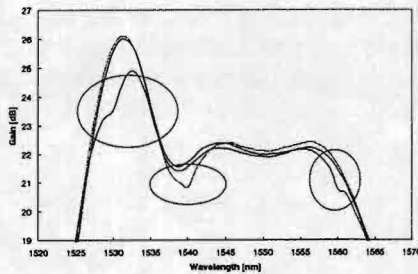


Figure 5 Gain profiles for saturation at three different wavelengths

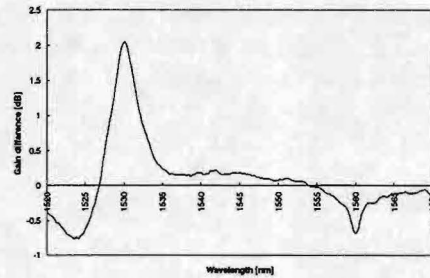


Figure 6: Result of subtracting the curves from figure 5: the Spectral Hole

spectral packets at distant frequencies essentially unchanged, which causes a distinct hole in the spectrum as shown in Figure 5 and Figure 6.

3. Measurement techniques

The “standard” measurement technique to characterize an optical amplifier in a multi-

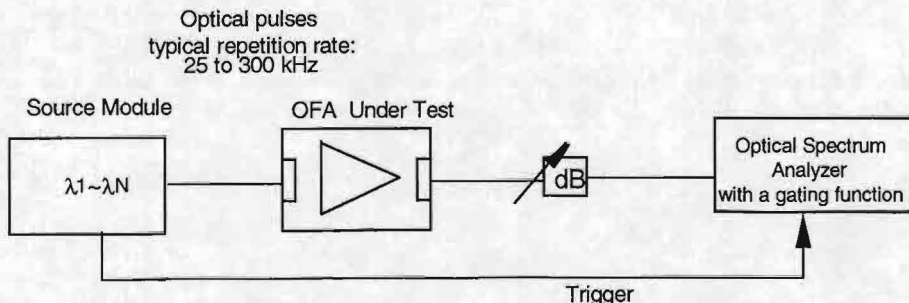


Figure 7 Typical arrangement of the test apparatus for signal-spontaneous noise figure parameter measurement using the gated-OSA technique.

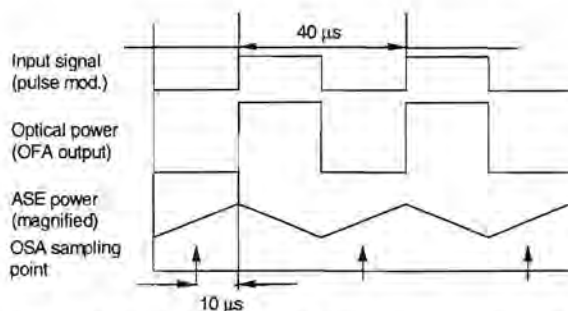


Figure 8 Timing Diagram. Times indicated are for a 25 kHz pulse repetition rate. For higher repetition rates, the timing is adjusted accordingly.

of the ASE at the signal wavelength, which leads to an increased accuracy for gain-slope (required for analog CATV) and spectral hole burning measurements. For cost reasons it would be beneficial to replace the complete set of wavelengths by a single saturating signal that leads to an identical inversion level. Theoretically this is correct if the amplifier exhibits only homogeneous line broadening, i.e. if SHB is virtually absent. In this case, the gain profile can be scanned by a low-power broadband probe, as depicted in Figure 9. The broadband probe is an EELED source. Typical traces resulting from a measurement are shown in Figure 10.

wavelength network is depicted in Figure 7. An optical source provides pulsed light to the OFA under test and a synchronization signal to trigger the OSA gating function. The optical attenuator adjusts the power level to the input of the OSA to a value within the OSA measurement range. The timing diagram shows the sampling points for power and noise. This so called time domain extinction technique enables measurement

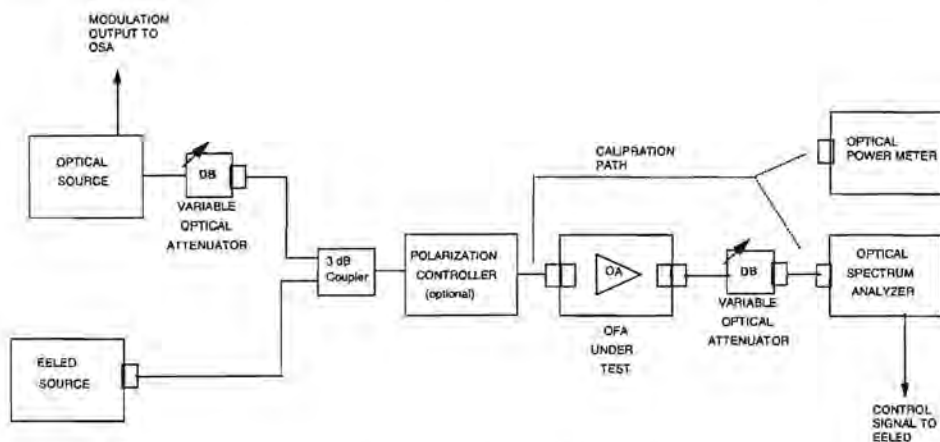


Figure 9 Measurement set-up for measuring multi-wavelength gain-profile with a broadband source

The gain-profile can be calculated by subtracting the ASE-spectrum, trace C, from the spectrum containing the ASE + gain times the spectrum of the EELED and divide this by the EELED spectrum, in other words, by calculating $G=(B-C)/A$. Curve fitting of the gain curve from this calculation, provides an accurate source to determine the gain-slope at the signal wavelength.

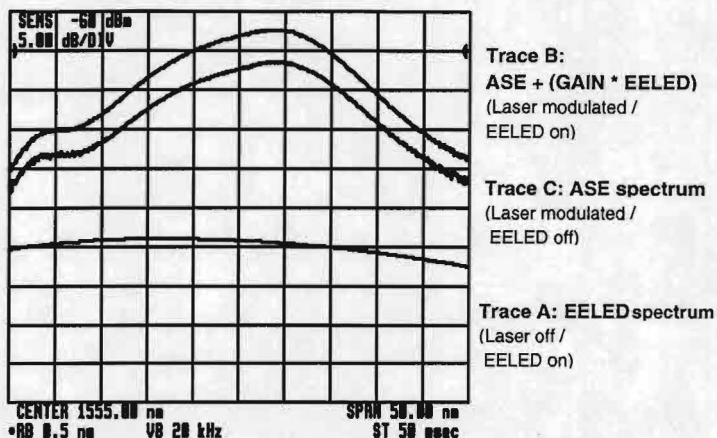


Figure 10 An example of the measurement of the three OSA traces

4. Methods using electrical spectrum analyzer

In general, all parameters discussed can also be measured using “electrical methods”. An electrical spectrum analyzer (ESA) is used to determine the amplifier’s response on a sinusoidally modulated input signal to determine gain. The signal-spontaneous beatnoise can in principle be measured directly by the ESA. No standardisation is currently underway to implement methods using an ESA for multi-wavelength applications, however, since the high-density wavelength division multiplexers (HDWDM) required to separate the contributions from the various wavelengths, still exhibit considerable excess losses.

5. Conclusions

Optical Fibre Amplifiers play an important role in today’s trunk and access networks. The ever increasing number of wavelengths and the introduction of optical amplifiers in “all optical networks” with add/drop nodes leads to a host of new parameters to be measured, like channel addition/removal response and spectral hole burning. Currently the most mature measurement techniques employ an optical spectrum analyzer. Standardisation efforts are under way to ensure the availability of measurement techniques that can be used for matters regarding commerce and trade.



WDM Transmission of a 10 Gbit/s Soliton and a 2.5 Gbit/s NRZ Signal over 150 km SSMF using Semiconductor Laser Amplifiers

J.G.L. Jennen, R.C.J. Smets, H. de Waardt

Eindhoven University of Technology,
P.O. Box 513, 5600 MB Eindhoven, The Netherlands

The feasibility of applying conventional 2.5 Gb/s NRZ traffic over at least a part of an operational 10 Gb/s soliton, long haul transmission link at 1310 nm is questionable. This is based on measurement results obtained from an intermediate haul transmission experiment. During this experiment, we transmitted a 10 Gb/s soliton and a 2.5 Gb/s NRZ signal over 150 km (3 sections of 50 km) using wavelength division multiplexing and semiconductor laser amplifiers.

We observed relatively large penalties (up to 5 dB) and in some cases bit error rate floors for the NRZ channel, when the soliton channel was disabled. Main reason for this effect is that a link optimised for 10 Gb/s soliton transmission is clearly not intended for 2.5 Gb/s NRZ. Transmission of only the soliton signal over 150 km showed a slight improvement in receiver sensitivity of 0.5 dB. However, when both signals were transmitted simultaneously over the soliton optimised link, bit error rate floors in the soliton transmission at about 10^{-11} occurred for channel separations below 4.3 nm. Error free NRZ transmission could not be achieved in any of the studied cases.

Introduction

The principal goal in the ACTS Upgrade project is to show the feasibility of long haul 1310 nm optical transmission at 10 Gb/s and 40 Gb/s using solitons with an RZ data sequence. Intermediate haul 10 Gb/s RZ transmission at 1310 nm was already successfully demonstrated during the Kassel-Hannover field-trail (Cebit'97) [1,2]. It is an challenging option to apply conventional traffic (2.5 Gb/s NRZ) over at least a part of the link using wavelength division multiplexing (WDM) of a 10 Gb/s soliton RZ channel and a 2.5 Gb/s NRZ channel. This should increase the system flexibility considerably.

Therefore, we studied the feasibility of simultaneous transmission of a 10 Gb/s soliton channel and a 2.5 Gb/s NRZ channel over the same fibre. We observed the performance of each channel in an intermediate haul transmission system with and without the presence of the other channel. Among the many possible configurations, we selected a 150 km long link, as an illustrative example, comprising four optical amplifiers in total to study the experimental properties of this type of hybrid transmission.

Experimental set-up

To observe the mutual influences between a 10 Gb/s soliton channel and a 2.5 Gb/s NRZ channel in an intermediate haul transmission system applying semiconductor laser amplifiers, we used the set-up as depicted in Figure 1. We distinguish three parts: a soliton and NRZ transmitter side, a 150 km transmission link and an optically preamplified receiver end.

Soliton and NRZ transmitter side

The optical soliton pulses were generated by an actively mode-locked external cavity laser. This laser was driven by the 10 GHz sine wave from a bit error rate (BER) test-set signal generator. The pulse width was 3 ps FWHM and the 3 dB spectral bandwidth was 0.8 nm. The bias current of the laser was set to 90 mA and the electrical power used for mode-locking was about +27 dBm. Operating at 20 °C the wavelength of the soliton source was set to 1312.5 nm.

Finally, the optical pulse train was modulated by an external LiNbO₃ intensity modulator with a 10 Gb/s, 2³¹-1 PRBS data signal from the first pulse pattern generator.

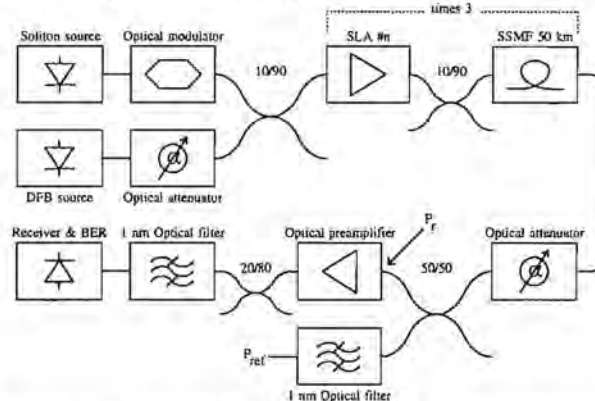


Figure 1: Set-up used for the hybrid transmission experiment.

For the generation of the 2.5 Gb/s NRZ channel we used two DFB lasers. These laser diodes were directly modulated by a 2.5 Gb/s, 2²³-1 PRBS data signal from another pulse pattern generator. Extinction ratios of 6:1 could be obtained. Different operating conditions, summarised in Table 1, were used for the generation of the NRZ signal.

Table 1: Operating conditions for the NRZ channel.

Laser no.	Bias current	Temp.	Wavelength
2184	47.3 mA	21.5 °C	1306.6 nm
2184	47.3 mA	40 °C	1308.2 nm
2284	42.2 mA	25 °C	1308.9 nm
2284	50.5 mA	40 °C	1310.2 nm

Applying a 10/90 coupler we combined 90% of the soliton signal with 10% of the NRZ signal. Additionally, an optical attenuator after the DFB laser diode was used to change the intensity of the NRZ channel with respect to the intensity of the soliton channel. Initially, we operated both channels with equal intensity. The intensity of the soliton signal at the input of SLA #1 remained -16 dBm during the measurements.

150 km Transmission link

The transmission link comprised three sections each containing a semiconductor laser amplifier, a 10/90 coupler and 50 km of standard single mode fibre exhibiting 18-19 dB loss and a zero dispersion wavelength of 1312 nm. All amplifiers were operated at 25 °C. The drive currents of SLA #1, SLA #2 and SLA #3 were 65 mA, 160 mA and 365 mA respectively with corresponding signal gains of about 10 dB, 20 dB and 25 dB. We optimised these settings for the 10 Gb/s soliton channel, being the main data stream.

Preamplified receiver end

The input stage at the receiver end consisted of an optical attenuator, necessary to generate the BER curves, and a 50/50 coupler for simultaneously measuring the BER and the received optical power P_r . To obtain a value for the optical power of the desired channel only, we inserted a 1 nm optical filter at the reference output of the coupler. A similar filter was also placed in front of the optical front-end. At the other coupler output a semiconductor laser amplifier was implemented as preamplifier. This amplifier was operated at 25 °C and 400 mA (~25 dB gain). The 20/80 coupler was inserted for monitoring purposes.

For the reception of the soliton and NRZ channels we used two separate and independent receiver configurations. Figure 2 shows the configuration for the NRZ channel. After a standard O/E-converter we implemented a low pass filter with a 3 dB cut-off frequency of 1.87 GHz followed by a 40 dB broadband amplifier. The amplifier output signal was then directed to a

2.5 Gb/s clock & data recovery circuit. Finally, the recovered clock and data signals were provided to one of two available BER detectors.

The receiver configuration for the soliton channel is illustrated in Figure 3. In front of the soliton receiver an optical attenuator was connected to prevent the receiver from saturating. After detection of the 10 Gb/s optical soliton signal it was amplified, filtered and demultiplexed to a 2.5 Gb/s NRZ data signal. Within the receiver clock and data recovery is provided. The second BER detector was connected to the recovered clock and data outputs.

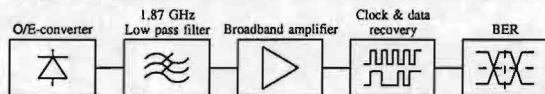


Figure 2: Receiver configuration for the NRZ channel.

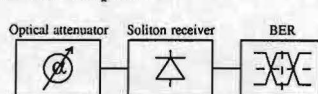


Figure 3: Receiver configuration for the soliton channel.

Results

With the set-up described in the previous section we performed BER measurements for both NRZ and soliton channels. For all operating conditions depicted in Table 1, we determined back-to-back BER curves of each channel individually, and BER curves after 150 km transmission with and without the presence of the other channel.

All obtained BER curves of the NRZ channel at two different wavelengths are provided in Figure 4. The intensity of the NRZ signal at the input of SLA #1 was set to -16 dBm for all curves shown. When considering NRZ transmission only, power penalties varying from 2.5 to 5 dB at 10^{-9} BER were observed. We increased the bias current of SLA#1 to 90 mA when the NRZ channel was operated at 1306.6 nm, otherwise no error free transmission could be achieved. Addition of the soliton channel to the system resulted in BER floors of 10^{-3} , 10^{-9} , 10^{-4} and 10^{-5} at 1306.6 nm, 1308.2 nm, 1308.9 nm and 1310.2 nm respectively.

Figure 5 shows the determined BER curves of the soliton channel with the NRZ channel at two different wavelengths. We observed a 0.5 dB sensitivity improvement at 10^{-9} BER when comparing the back-to-back measurements to the ones after 150 km transmission without the presence of the NRZ channel. When simultaneously transmitting an NRZ channel with equal intensity (-16 dBm), BER floors appeared at 10^{-11} and 10^{-10} for all NRZ wavelengths, except for 1306.6 nm. For this wavelength a 1 dB power penalty at 10^{-9} BER was observed. Reduction of the NRZ intensity by 3 dB revealed no penalty, whereas a 3 dB increment resulted in a BER floor at approximately 10^{-11} .

Discussion & Conclusions

When looking at the back-to-back BER curves for the NRZ channel in Figure 4, we observe quite a difference in receiver sensitivity. The relatively high sensitivity (-35.3 dBm) and BER slope at 1308.2 nm is due to the higher extinction ratio of 12:1 instead of 6:1 for the other NRZ operating conditions. No performance degradation could be detected as a result of the occurring turn-on jitter in this case. The lower gain and more severe saturation effects experienced by the NRZ signal at 1306.6 nm resulted in a poor receiver sensitivity (-29.9 dBm) when compared to the sensitivities observed at 1308.9 nm and 1310.2 nm (-32.5 dBm).

The single channel transmissions showed relatively large penalties (up to 5 dB) for the NRZ signals with respect to the 0.5 dB sensitivity improvement for the soliton signal. The reason for this effect is that the link was optimised for transmission of the soliton signal only. This is shown by the fact that improved results could be achieved when changing the amplifier settings as stated before. At very low (< 100 mA) drive currents, the semiconductor laser amplifiers exhibit a large noise figure. Since the NRZ "1"-level was around 50 times lower than the soliton "1"-level, the NRZ channel exhibited a poor initial signal-to-noise ratio inducing relatively large penalties, whereas the soliton channel did not appear to suffer from the poor noise figure of SLA #1.

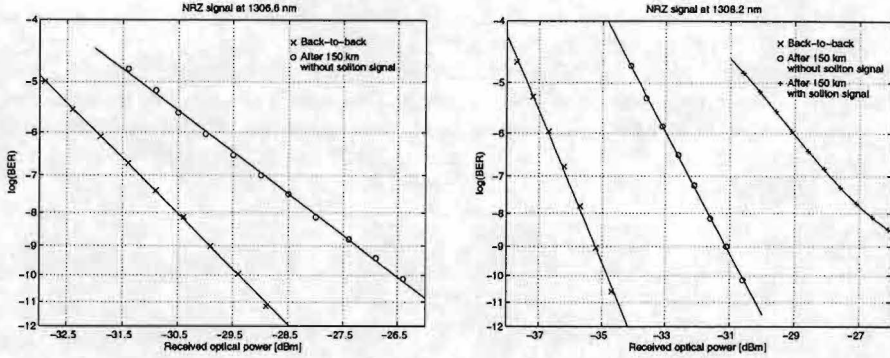


Figure 4: BER curves of the NRZ channel at two different wavelengths, $\lambda_{\text{soliton}} = 1312.5 \text{ nm}$.

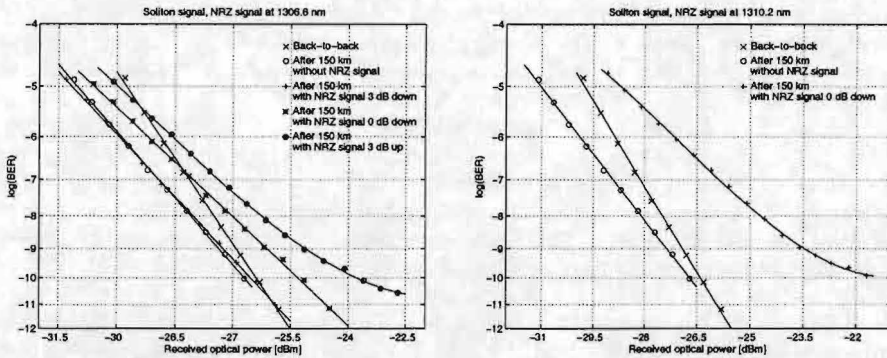


Figure 5: BER curves of the soliton channel at 1312.5 nm with the NRZ channel at two different wavelengths.

When transmitting both channels at the same time, the already poor signal-to-noise ratio of the NRZ channel decreased even further due to extinction ratio degradation as a result of enhanced saturation effects. Therefore, we observed large BER floors in the NRZ transmission. In the soliton transmission, floors also occurred. However, these floors were found at generally lower values, because of the initially higher signal-to-noise ratio at the "1"-level of the soliton signal. Based on our experiment, we conclude that in a semiconductor laser amplifier cascade with a 50 km amplifier spacing it is not feasible to transmit a 2.5 Gb/s NRZ signal simultaneously with a 10 Gb/s soliton signal over three or more in-line amplifiers. In soliton links with a reduced amplifier spacing error free transmission of a parallel NRZ data stream might be possible, since the signal-to-noise ratios at the input of the in-line amplifiers will be improved. However, links developed for single channel, 10 Gb/s soliton transmission are optimised for this purpose only. To find a system design strategy for successful transmission of conventional, 2.5 Gb/s NRZ traffic and 10 Gb/s soliton signals over the same link, future research is indispensable.

Acknowledgement

We express our gratitude to the Dutch Technology Foundation STW for financially supporting this work. We also thank A. Verboven and C. Vroomen for their technical assistance.

References

- [1] J.J.E. Reid, Opt. Amp. and their Appl., paper TuB1, Victoria B.C., Canada, 1997.
- [2] J.J.E. Reid et. al., ECOC'97, paper Mo3A5, pp. 1.79–1.82, Edinburgh, United Kingdom, 1997.

First EDFA for Single Fibre Tree-and-Branch Broadband Access Networks Carrying uni-directional AM-CATV and bi-directional digital Multi-Wavelength Signals

C.A.M. Steenbergen¹, F.W. Willems¹, A.W.L. Janssen¹, J.C. van der Plaats¹
D.Jacob², M. Prassas²

¹Bell labs, Lucent Technologies, Botterstraat 45, 1271 XL Huizen, The Netherlands

²Corning Europe, 7bis Avenue de Valvins, Avon 77210, France

Design and performance characterisation is presented for the prototype bi-directional optical amplifier developed in the ACTS project AC028 "TOBASCO". The amplifier shows excellent noise-figure and gain-slope performance in the CATV-wavelength window. A new time-domain extinction based multi-wavelength gain and noise measurement method is used to characterise the bi-directional behaviour in the interactive services window.

1. Introduction

Optical fibre is penetrating rapidly into subscriber access networks for distribution of CATV services. Today's CATV head-end stations are feeding distributive services to large numbers of subscribers (>10,000) in networks with abundant splitting in the fibre part as well as in the coaxial part. The ACTS project TOBASCO [1] (Towards Broadband Access Systems for CATV Optical networks; see figure 1 for a network overview) is exploring ways to upgrade existing fibre-coax networks to implement such interactive services by developing HDWDM techniques. Bi-directional optical amplifiers are needed to overcome the splitting losses in the optical network. Here, we present the design and performance of a bi-directional multi-wavelength Two Window Optical Branching Amplifier (TWOPA), used to compensate the propagation and splitting losses along the fibre link for bi-directional digital interactive services (IS) signals and downstream analogue CATV signals.

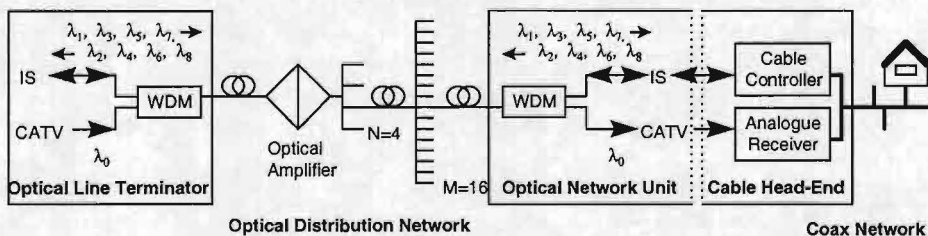


Figure 1: Topology of the TOBASCO network.

2. Amplifier Configuration

Several approaches in bi-directional amplifier design for digital WDM networks are described by [2]. The amplifier configuration used in the TOBASCO network is shown in figure 2. First, the optical spectrum is divided into a blue band for the IS channels (1535-1541 nm) and a red band for the CATV channel (1550-1560 nm). The two amplifier sections, one for the blue band, one for the red band are pumped by two 120 mW laser diodes @ 980 nm. After amplification, IS and CATV are combined by a WDM to improve the noise figure. Finally, a 1:4 splitter is added at the output of the TWOPA.

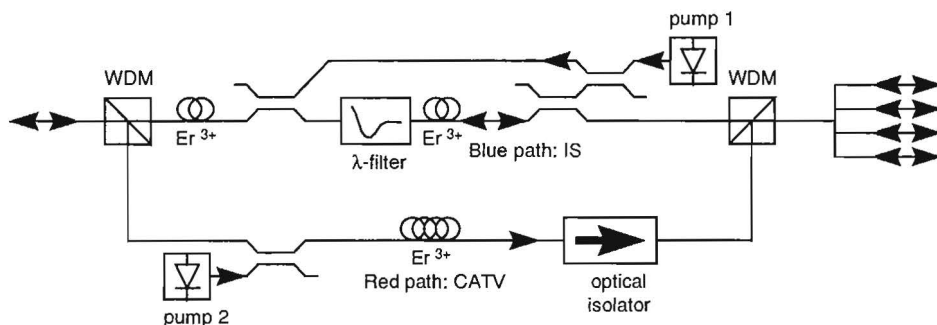


Figure 2: Design of the TWOPA.

The Erbium-doped amplifier section associated with the blue band of the gain spectrum, is allocated for the digital upstream and downstream channels, which are interleaved at a spacing of 100 GHz (0.8 nm). This section consists of two Erbium-doped coils, and a gain-flattening filter inserted between the two coils. The 980/1550 couplers are situated such, that redirection of 980 nm light to the pump laser is not possible. The blue band section can simultaneously amplify the four upstream and four downstream channels since no optical isolator is present.

The Erbium-doped amplifier section associated with the red band of the gain spectrum, is allocated for the analogue CATV downstream channel in order to obtain little second order harmonic distortion induced by the interaction of the local gain slope of the EDFA and the frequency chirp of the directly modulated laser. An optical isolator is added to allow only uni-directional amplification of the analogue CATV signal. Co-pumping is applied to obtain a low noise figure. The combination of the optical isolator and the WDM's for combining and splitting of the IS and CATV channels at the input and output of the TWOPA, ensures that no amplified multiple reflections will disturb the CATV channel.

3. Measurement Set-up

The gain and noise figure of the TWOPA has been measured with the set-up depicted in figure 3, which is based on the time-domain extinction method. First, the CATV channel and the four downstream IS channels are combined by a WDM coupler. A broadband spectrum from the EELED is combined with the CATV and downstream IS channels via a 3 dB coupler and this spectrum is send into the head-end input of the TWOPA. On the subscriber side the four upstream IS channels are send into the TWOPA via one of the

inputs/outputs of the 1:4 coupler. Another output of the 1:4 coupler is used for monitoring of the amplified downstream spectrum. The CATV, downstream IS and upstream IS channels are modulated by a 25 kHz block wave, resulting in on/off switching of the optical power with an extinction ratio better than 40 dB. Attenuators are included to adjust the power level of the various channels. Only the power of the CATV and IS channels set the inversion level of the optical amplifier, when a sufficiently low EELED power is used. By doing so, it is possible to measure the wavelength dependence of the optical amplifier over the entire optical bandwidth of the EELED. We use the 25 kHz block wave as trigger source for the optical spectrum analyser and measure only in the time frame when the CATV and IS channels are switched off. Due to the slow gain dynamics of the Erbium doped amplifier, the inversion level will remain constant during the short period when the CATV and IS channels are switched off. The gain and noise figures can be derived from three measurements:

- measurement 1: $P_1(\lambda)$: power spectrum of the EELED (at TWOPA input)
- measurement 2: $P_2(\lambda)$: amplified spectrum of the EELED + amplified spontaneous emission of the optical amplifier (at TWOPA output, EELED switched on)
- measurement 3: $P_3(\lambda)$: amplified spontaneous emission of the optical amplifier (at the TWOPA output, EELED switched off)

The gain $G(\lambda)$ and noise figure $NF(\lambda)$ then follow from:

$$G(\lambda) = \frac{P_2(\lambda) - P_3(\lambda)}{P_1(\lambda)} \quad NF(\lambda) = \frac{P_3(\lambda)}{h\nu G(\lambda)} = \frac{\lambda^3 ASE(\lambda)}{hc^3 G(\lambda) \Delta\lambda}$$

where h is Plank's constant, c the velocity of light in vacuum, λ the wavelength and $\Delta\lambda$ the resolution bandwidth of the optical spectrum analyser.

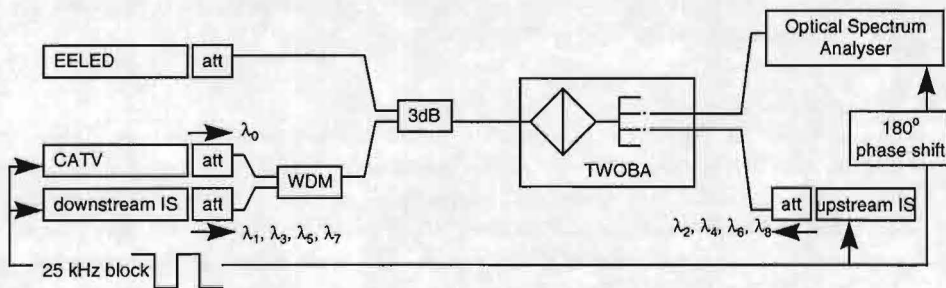


Figure 3: Set-up for gain and noise figure measurements according to the time domain extinction method. For characterisation of the upstream direction, the EELED and optical spectrum analyser should be interchanged.

4. Results

Figure 4 shows the results for the gain and noise figure versus wavelength for a CATV channel power of -5 dBm, total IS downstream power of -15 dBm and total upstream power of -10 dBm, values which are typical for the TOBASCOS network. For this load, the IS upstream channels show a gain of 15-17 dB and a noise figure 12.5-13.5 dB, and the IS downstream channels show a gain of 16-18 dB and a noise figure 8.5-10 dB, within the region of interest: 1535-1541 nm. Note that the noise figure for the upstream channels

include the 6 dB additional penalty arriving from the 1:4 splitter. The presence of the WDM filters are clearly visible in the characteristic of the noise figure, which increases sharply close to the filter edges.

The CATV channel shows a gain of 11.5-12 dB and 5.5-6 dB noise figure in the wavelength range from 1550-1560 nm. In addition to the gain and noise figure measurements, we observed the influence of the TWOPA on the analogue performance by measuring the CNR and CSO. In a back-to-back measurement, without the TWOPA, we measured a CNR of 55 dB and a CSO of -65 dB, at the 48 MHz channel using a BK600 scheme. Including the TWOPA in the set-up, degrades the CNR to 51 dB, and the CSO to -62 dB. In an experiment with 13.4 km fibre before the TWOPA and 11.2 km behind the TWOPA, a CNR of 49.5 dB and CSO of -61 dB were measured.

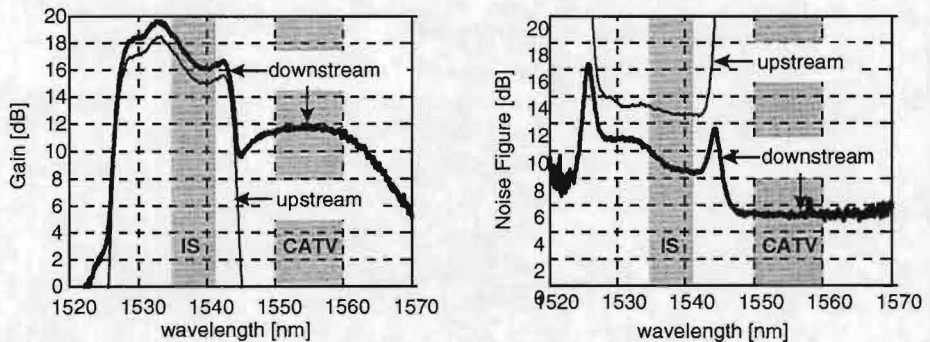


Figure 4: Measured gain and noise figures for downstream and upstream signals. Average input power levels are: -5 dBm for the CATV channel @ 1558 nm, four IS downstream channels @ -13 dBm per wavelength, four IS upstream channels @ -8 dBm per wavelength.

5. Conclusions

In this paper we presented the results of the first prototype two-window bi-directional optical amplifier developed in the ACTS project TOBASCO. Based on the time-domain extinction method, the wavelength dependent gain and noise figure have been characterised in presence of the four upstream IS channels, four downstream IS channels and a CATV channel. Excellent gain-slope and noise figure performance has been measured in the CATV-wavelength window. System experiments including 25 km of fibre show negligible degradation of the quality of the analogue CATV channel.

[1] A.M.J. Koonen et al., "HDWDM Upgrade of CATV Fibre-Coax Networks for Broadband Interactive Services", Proceedings. of the 22nd European Conference on Optical Communications (ECOC'96), September 15-19, 1996, Oslo, Norway, pp. 3.19 - 3.25

[2] M. Yadlowsky, "Bi-directional Optical Amplifiers for high performance WDM systems", Digest of Optical Amplifiers and their applications", Victoria, July 1997, pp. 32-35.

2.5 Gbit/s, 645 nm GIPOF Transmission Link with Record Receiver Sensitivity using an APD

W. Li*, H. v.d. Boom*, G. Khoe*, H. de Waardt*, Y. Koike**, S. Yamazaki***

* COBRA Interuniversity Institute, Eindhoven University of Technology EH-12
PO BOX 513, 5600 MB Eindhoven, Netherlands
email: H.P.A.v.d.Boom@ele.tue.nl

** Keio University, Faculty of Science and Technology
3-14-1, Hiyoshi, Kohoku-ku, Yokohama 223, Japan

*** NEC Corporation, Opto-Electronics Research Laboratories
4-1-1, Miyazaki, Miyamae-ku, Kawasaki 216, Japan

Abstract

We succeeded in realising a 645 nm, 2.5 Gbit/s optical transmission system with Graded Index Polymer Optical Fibre (GIPOF) with a record power budget of 29.5 dB. For the first time a silicon Avalanche Photo Diode has been used. The sensitivity of the front end receiver was -25.5 dBm at a Bit Error Rate of 10^{-9} which is to our knowledge 8.6 dB better than reported so far. The transmitter average output power was 4 dBm.

Introduction

New interactive services requires a broadband communications network, which should extend into the customer's premises up to the terminals. At present twisted pair and coaxial cable are used as the physical medium in customer premises. Twisted pair has a limited bandwidth and is susceptible to ElectroMagnetic Interference (EMI). Coaxial cable offers a large bandwidth, but poses practical problems due to its thickness and the effort required to make a reliable connection. Also, the coaxial cable is not completely immune to EMI. Optical fibre connections offer complete immunity to EMI. Optical silica-glass fibres, however, are not suitable for use within the customer premises because of the requirement of precise handling and thus high cost.

Polymer optical fibres are very attractive for use within the customer premises with their easy and low cost handling because of their relatively thick core. Polymer fibre based systems are commercially available. Examples of suppliers are HP, AMP and Siemens who are offering a variety of components and systems. These systems are based on the use of the multimode Step Index Polymer Optical Fibre (SIPOF), which has a bandwidth times distance product which is limited to 5 MHz*km.

The Graded Index Polymer Optical Fibre (GIPOF) opens the way towards the realisation of optical communication systems which combine attractive features [1-2]. Typical characteristics of the GIPOF are:

- * A large core diameter (typically 750 microns) which allows easy handling, thus the use of low cost devices and interconnection devices (similar to SIPOF).
- * A large bandwidth times distance product (typically 2 GHz*km), which allows for the transmission of information with high bandwidths (this is not offered by SIPOF).

The high bandwidth of the GIPOF (as compared to the SIPOF), is attributable to the graded-index profile in the core. High speed short wavelength light sources (typically 650 nm), and high speed silicon photodiodes are currently available for the realisation of high speed systems employing GIPOF [3-5]. 2.5 Gbit/s, 647 nm transmission over 100 m GIPOF with a receiver sensitivity of -16.9 dBm at a BER of 10^{-9} using a pattern length of $2^{15}-1$ has already been reported [4]. The power budget was 23 dB.

In this publication the use of an Avalanche Photo Diode (APD) instead of a PIN photo diode in a GIPOF transmission system is reported for the first time. The use of an APD increases the sensitivity of the receiver so larger distances can be covered. Moreover, for the BER measurements larger pattern lengths have been used.

Experiment

In figure 1 a block diagram of the set up of the transmission experiment can be seen. In the optical transmitter a 645 nm laser from NEC in combination with a laser driver from Fujitsu has been used.

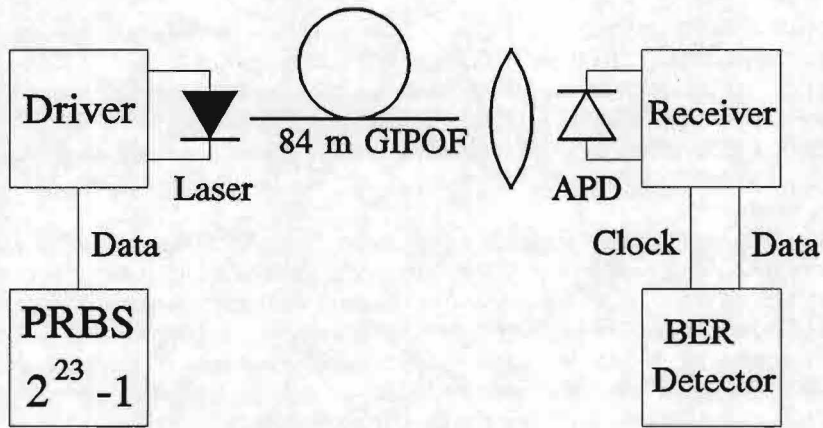


Figure 1: 2.5 Gbit/s, 645 nm GIPOF transmission system.

The laser has been modulated by a 2.5 Gbit/s NRZ Pseudo Random Binary Sequence with a pattern length of $2^{23}-1$. The average output power of the laser was 4 dBm. This power has been stabilised by using the photo diode in the laser package. The laser is mounted in a TO 18 package and has a glass window. The coupling with the GIPOF with a core diameter of $750\text{ }\mu\text{m}$ has been realised by putting a strait cut fibre end to the glass window of the laser package. The attenuation of the GIPOF is 0.21 dB/m at the wavelength used, so the total attenuation of the 84 m GIPOF was 17.6 dB. At the receiving end a lens has been used to couple the optical signal from the GIPOF to a silicon Avalanche Photo Diode with an active area of 0.042 mm^2 . The diameter of the active area was $230\text{ }\mu\text{m}$. To obtain a simple APD receiver the photo diode current was stabilized by controlling the voltage over the APD so no temperature control has been used. The photo diode current was amplified by a HP limiting amplifier. The data clock and the data were recovered by a data and data clock recovery circuit from Lucent. For Bit Error Rate (BER) measure-

ments the data and clock signal are connected to a BER detector.

Measurement results and Discussion

Figure 2 shows the eye diagram after 84 m GIPOF.

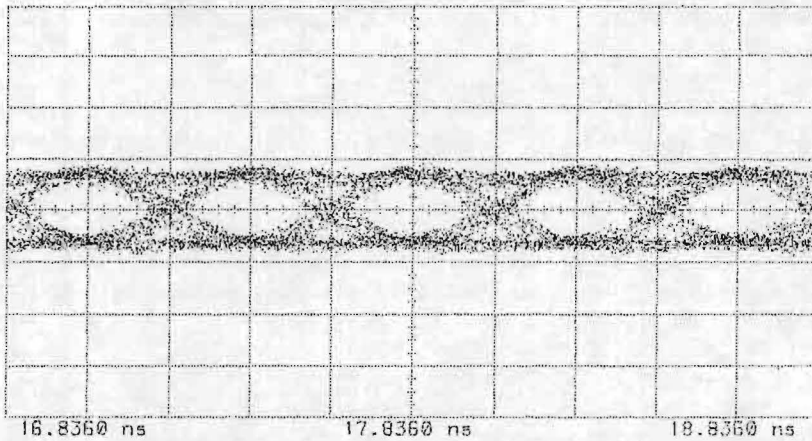


Figure 2: Eye diagram of 2.5 Gbit/s, 645 nm transmitter output signal.

In figure 3 the measured bit error rate against received average power at the input of the APD with and without 84 m GIPOF is shown.

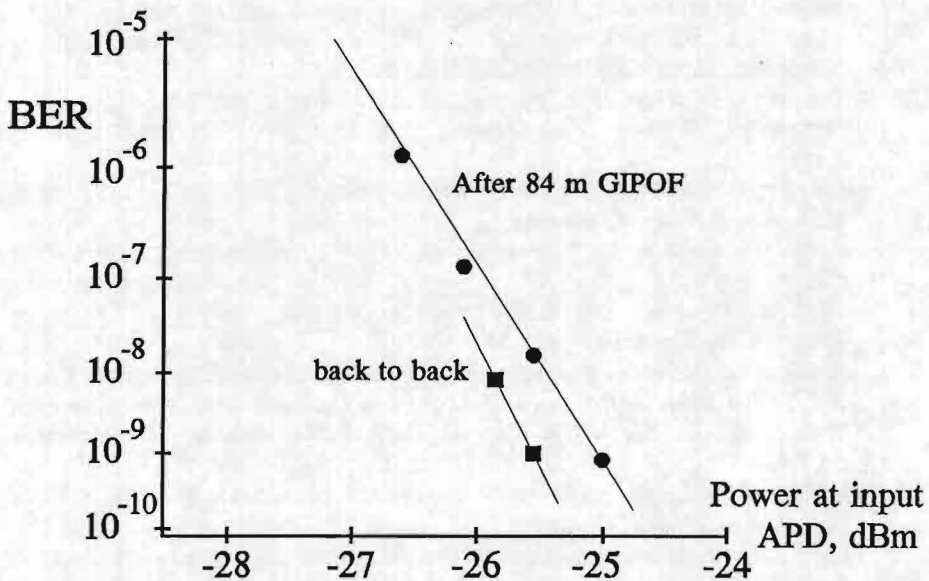


Figure 3: Measured Bit Error Rate of 2.5 Gbit/s transmission system

The received power has been changed by altering the distance between laser and GIPOF. The sensitivity of the receiver was -25.5 dBm at 10^{-9} which is 8.6 dB better than reported so far [4]. The error characteristic with the 84 m GIPOF is almost the same as with back to back transmission. A 0.6 dB receiver sensitivity degradation was observed, due to model dispersion of the fibre. The coupling loss from laser to GIPOF was 3 dB. This can be easily reduced by using a lens to 1 dB. The coupling loss between GIPOF and APD was 1.5 dB.

The experiments were done with 84 m, because currently we had no more GIPOF available. With the same set up a distance of 120 - 130 m should be possible.

Conclusions

By using a silicon APD a 2.5 Gbit/s, 645 nm receiver with a record sensitivity of -25.5 dBm for a BER of 10^{-9} has been realised. This is 8.6 dB better than reported so far [4], so the maximum length of the GIPOF with an attenuation of 0.21 dB/m can be increased with about 40 m.

Acknowledgements

Prof. Y. Koike, Keio University, Provided GIPOF sample

Dr. S. Yamazaki, NEC Corporation, Provided 645 nm laser diodes

This work makes part of the IOP Electro-Optics cluster II framework sponsored by the Dutch ministry of Economic Affairs.

References

1. (Invited) G.D. Khoe and A.N. Sinha,
Polymer Fibre Network for Communication at the Customer Premises,
Third International Conference on Plastic Optical Fibres and Applications,
Yokohama, Japan, October 26-28, 1994, pp. 12-15.
2. (Invited) G.D. Khoe, G.S. Yabre, L. Wei and H.P.A. van den Boom,
Wavelength Division Multiplexing for Graded Index Polymer Optical Fibre Systems,
Polymer Optical Fibre Conference POF'97, Hawaii, Sept. 22-25, 1997, pp.8-9.
3. Y. Koike, E Nihei, T. Ishigure,
Recent Development of Polymer Optical Fibre for High-Speed Data Communication,
Proc. 2nd Optoelectronics & Communications Conference (OECC'97), paper 8D2-1, July 8-11, Seoul, 1997, pp. 64-65.
4. S.Yamazaki, H.Hotta, S.Nakaya, K.Kobayashi, Y.Koike, E.Nihei and T.Ishigure,
A 2.5 Gb/s 100m GRIN Plastic Optical Fibre Data link at 650 nm Wavelength,
Proc. 20th. ECOC, Vol.4, Post Deadline Paper, Sept.25-29, Florence, 1994, pp.1-4.
5. F.Miyasaka, H.Hotta, Y.Ueno, H.Sawano, M.Yamamoto, M.Tsuji, K.Kobayashi, K.Makita, T.Nyu, S.Yamazaki,
High speed light sources and detectors for gigabit-per-second plastic-optical fibre transmission,
Proc. OFC, Febr.26-Mar.3, 1995, San Diego, pp.257-258.

Experimental Demonstration of a Free Space Intrachip Micro-Optical Interconnect

G. Verschaffelt, R. Buczynski, P. Tuteleers, P. Vynck, V. Baukens, S. Kufner, M. Kufner, A. Hermanne*, J. Genoe**, D. Coppée**, R. Vounckx**, P. Heremans***, H. Thienpont and I. Veretennicoff

Laboratory for Photonic Computing and Perception, Faculty of Applied Sciences, Vrije Universiteit Brussel, B-1050, Brussel, Belgium

*Cyclotron Department, Vrije Universiteit Brussel, Laarbeeklaan 103, B-1090 Brussel, Belgium

**Laboratory for Microelectronics, Faculty of Applied Sciences, Vrije Universiteit Brussel, B-1050, Brussel, Belgium

***IMEC, Kapeldreef 75, B-3001 Leuven, Belgium

We demonstrate the proof of principle of optical intra-chip interconnects by establishing a 1Mb/s digital data link between two optoelectronic transceivers positioned on a same chip, making use of a micro-optical bridge. Future performances are discussed in the light of improved lens and emitter characteristics.

Future advances in the application of photonic interconnects will involve the insertion of parallel-channel links into Multi-Chip Modules (MCMs) [1]. These will make use of new device-level components such as arrays of Vertical Cavity Surface Emitting Lasers (VCSEL's) [2] or arrays of Micro Cavity Light-Emitting Diodes (MCLED's) [3] and low power photoreceiver circuits [4]. One of the challenges associated with the development of free-space intra- and inter-MCM optoelectronic interconnects is the fabrication of manufacturable, chip-compatible, and high precision monolithic micro-optical pathway blocks. These three-dimensional modules should integrate micro-optical components to optically interconnect surface-normal transmitters and receivers.

In this paper we first report on the fabrication of such a refractive micro-optical bridge by deep proton lithography [5]. Next we use this component to demonstrate the proof-of-principle of optical intra-chip interconnects by establishing a digital data link between optoelectronic transceivers positioned on the same chip. Finally we project future performances of this approach by extrapolating present-day results in the light of improved lens and emitter characteristics.

Deep proton irradiation of Poly Methyl MethAcrylate (PMMA) is a deep etch lithographic technique that allows the fabrication of monolithic structures integrating refractive microlenses, microprisms, fiber positioning holes, stand-offs and alignment features [5] [6]. The technique works as follows: a proton beam in the energy range between 5 and 10 MeV, passing through a metal mask, impinges on a high molecular weight PMMA substrate. The protons break the polymer chains and decrease the material's molecular weight. Using a specific developer the irradiated zone can then be selectively removed, making it possible to structure the sample to depths of several hundreds of microns with an optical surface quality of better than 20 nm. To demonstrate an intra-chip optical interconnect between two opto-electronic transceiver elements, we have applied this deep proton lithography to fabricate a monolithic

micro-optical bridge consisting of two micromirrors and two cylindrical microlenses (see Fig. 1 and Fig. 2).

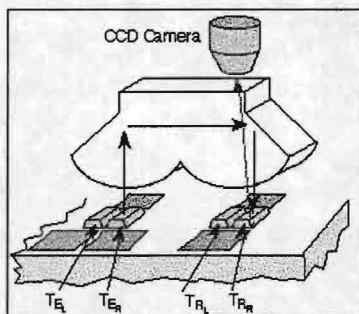


Figure 1 Setup for intra-chip data transcription

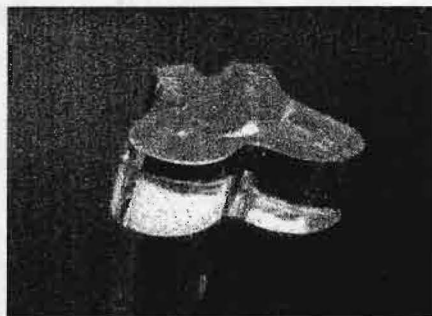


Figure 2 Photograph of the micro-optical bridge used to realize the optical pathway represented in fig. 1

As opto-electronic transceiver elements we have used optical thyristors [7]. These emitter-receiver devices are fabricated as a double heterojunction PnpN structure in the GaAs/AlGaAs material system. They are bistable elements and have an S-shaped quasi-static I-V curve. Thyristors can be operated both in a light emitting (850 nm) and a light detecting mode depending on the control voltage.

For a voltage below the breakover voltage V_{BR} the thyristors are said to be in their 'off' state and they have a high impedance. When a voltage greater than V_{BR} is placed across them, this impedance falls dramatically and they emit light as a LED. External illumination reduces V_{BR} and they are thus optically sensitive. This optical sensitivity can be greatly increased by connecting two devices together with a common resistance in a differential pair configuration. When an optical input is applied to one of the elements photo-induced electron-hole pairs are generated. Placing a voltage across the pair causes a differential competition to take place between the elements. The one which has the lowest break-over voltage (caused by precharging due to the optical input) will begin to switch on first, drawing charge carriers from the other and preventing it from switching on. The energy required to switch such a differential pair is $15 \text{ aJ } \mu\text{m}^{-2}$ optical window area. After emission the devices are reset in less than 5 ns by applying a negative voltage pulse (-8V). The devices used at present have an active window of $16 \mu\text{m} \times 19 \mu\text{m}$. The center separation of each element in the pair is $26 \mu\text{m}$ (see Fig. 3).

In our experiments we used two kinds of thyristor configurations: a thyristor pair where both thyristors are electronically and individually addressable (see Fig. 3a) and a differential pair configuration that is optically addressable (see Fig. 3b). An optical signal sent from the right handside thyristor emitter T_{ER} is routed by the optical bridge to the right handside receiver T_{RR} , and the left handside thyristor emitter T_{EL} signal is routed to the left handside receiver T_{RL} , respectively. Because of the differential nature of the receiving thyristors, it is only the difference in energy received by T_{RR} and T_{RL} that will determine which one of the receiving thyristors will switch on. Therefore data transcription will not be disturbed if some of the light is falling on the wrong receiving thyristor, e.g. if light is going from T_{EL} to T_{RR} .

The distance between the center of the lenses is chosen to match the pitch of the two thyristor pairs ($844 \mu\text{m}$). The lenses have apertures of $844 \mu\text{m}$ and focal lengths of $1044 \mu\text{m}$. Microlens M_1 , positioned above the individually addressable thyristors T_{EL}

and T_{ER} acts as a beam collimator, while microlens M_2 collects incoming light on the optical window of thyristors T_{RL} and T_{RR} respectively, both working in receiver mode. Each micromirror surface makes an angle of 45° with respect to the optical axes of the lenses in order to deflect the collimated beam by 90° . The optical bridge was designed such that the mirrors cover only half of the lens aperture such that a part of the light can escape from the top of the bridge, which allowed us to monitor the optical bitstreams (see Fig. 1).

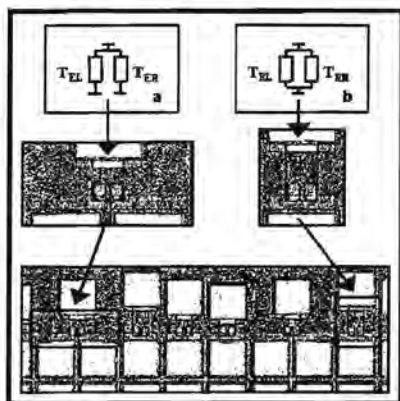


Figure 3 Photograph of the thyristor chip used to realize the optical pathway represented in Fig 1

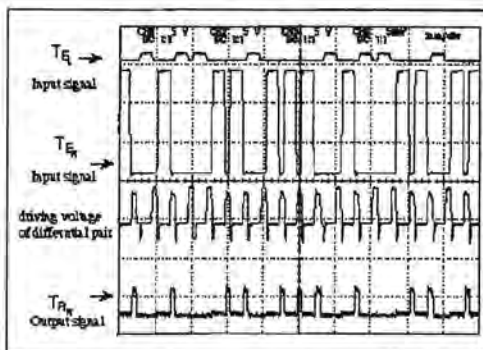


Figure 4 Driving waveforms for emitter (T_E) and receiver (T_R) and the optical output

To perform the experiment the optoelectronic chip was mounted on a probe station. An electrical waveform was applied to the emitting optical thyristor T_{ER} (see trace T_E in Fig. 4) such that a regular optical bitstream was produced and sent to the receiving element T_{RR} (see trace T_R in Fig. 4). In case of a correct data transcription, T_{RR} should switch on and start to emit light only when a logic one (corresponding to a high optical input) was sent by T_{ER} . As can be seen in Fig. 4, the binary input data from T_{ER} are perfectly reproduced by T_{RR} . In order to determine the maximum transmission rate, the duration of the input signals was reduced until reliable transcription was just obtained. The minimum bit length achieved was $1 \mu s$ (consisting of 800 ns for the receiving phase and 200 ns for the reset and emission phase of the differential pair) when an input driving voltage of 14 V was used. This is equivalent to a bit rate of more than 1 Mbs^{-1} .

Using a Monte-Carlo based radiometric simulation we found an optical efficiency η_0 of 0.06% for the photonic data transmission system described above. Together with the switching energy E_s of the differential pair and the power P_e emitted by the individual thyristors, we can determine the minimum duration τ_e^{\min} of the receiving face of the differential pair in order to obtain correct data transcription.

$$\tau_e^{\min} = \frac{E_s}{P_e \eta_0}$$

Using 6 fJ for E_s and 35 μW for P_e , we found a value of 0.3 μs for τ_e^{\min} , which is in good agreement with the experimental value of around 0.8 μs . The difference between the experimental and the expected value can be attributed to misalignment errors.

From the expression for τ_e^{\min} we can see that there are different ways to improve the performance of the interconnection. First it is possible to improve the efficiency of the optical system by replacing the cylindrical lenses with spherical lenses, which can also

be fabricated by deep proton lithography [5]. Next, we can replace the thyristors, which are Lambertian sources, by transceivers with better output characteristics and a higher emission efficiency, such as MCLED's and VCSEL's. Table 1 gives an overview of the calculated optical efficiencies for different configurations. Note that all of these efficiencies can be multiplied with a factor of two by making the micro-mirrors longer, such that the mirrors cover the complete lens aperture. In the case of the MC-LED and the VCSEL based system, the overall system performance will not only increase due to a higher optical efficiency of the optical pathway block, but also because these sources have a higher emission efficiency [3].

Configuration	Optical efficiency (mirrors cover half of the lens aperture)	Optical efficiency (mirrors cover the lens aperture completely)
Cylindrical lenses,LED (div. Angle 180°)	0.06 %	0.12 %
Spherical lenses,LED (div. Angle 180°)	0.9 %	1.8 %
Spherical lenses,MC-LED (div. Angle 100°)	1.5 %	3.0 %
Spherical lenses,VCSEL (div. Angle 12°)	46 %	92 %

Table 1

In this paper we have demonstrated a single channel monolithic free-space micro-optical intra-chip interconnect. The optical bridge was fabricated by deep proton lithography. The concept of this approach can be extended to manufacturable massively parallel optical intra- and inter-chip interconnects. Although we reported on moderate bandwidths only, it can be stated that this technology holds all the potentialities for very large bandwidths and huge aggregate bitrates.

Acknowledgments

This work was funded by the EC-MEL-ARI project OIIC, the FWO, IUAP 13, the GOA research concerted action "Photonics in computing" and the OZR of the Vrije Universiteit Brussel.

References

- [1] R.F.Carson et al., "Low-power approaches for parallel free-space photonic interconnects", SPIE CR 62, Eds. R.T.Chen and P.S.Guilfoyle, pp. 35-63, 1996.
- [2] K.H. Gulden, D. Ruffieux, K. Thelen, M. Moser, D. Leipold, J. Epler, H.P. Schweizer, E. Greger and P. Riel, "16*16 Individually Addressable Top Emitting VCSEL Array with High Uniformity and Low Threshold Voltages", Proc. E.O.S., Conf. On Optics and Information, pp. 6.1, Mulhouse, France, 1995.
- [3] H. De Neve, J. Blondelle, P. van Daele, P.M.A. Demeester, R.G. Baets, G. Borghs, "Planar substrate-emitting microcavity light-emitting diodes with 20% external QE", Proc. of SPIE, vol. 3002, pp. 74-84, SPIE Photonics West, San Jose, California, 1997.
- [4] T.K. Woodward, A.V. Krishnamoorthy, A.L. Lentine, L.M.F. Chirovsky, "Optical receivers for optoelectronic VLSI", IEEE Journal of Selected Topics in Quantum Electronics, vol. 2, pp. 106-116, 1996.
- [5] M. Kufner and S. Kufner, "Micro-optics and Lithography", VUB Press, Brussels, 1997.
- [6] M. Kufner, S. Kufner, "Fabrication of monolithic integrated fiber-lens connector arrays by deep proton irradiation", Microsystem Technologies, pp. 114-118, 1996.
- [7] B. Knupfer, M. Kuijk, R. Vounckx, P. Heremans, G. Borghs, "Cascadable differential PnpN optoelectronic switch operating at 50 Mbit/s with ultrahigh optical input sensitivity", Electr. Letts. 31 pp 485-486, 1995.

Imaging of the field distribution in integrated optical waveguides

M.L.M Balistreri, X.Borrisé, J.P.Kortrik, N.F. van Hulst*

Applied Optics Group, Department of Applied Physics, University of Twente

P.O. Box 217, 7500 AE Enschede, The Netherlands

(e-mail address: M.L.M.Balisteri@Tn.Utwente.Nl)

** Department of Electronical Engineering, University Autònoma of Barcelona
08193 Bellaterra, Spain*

A near-field optical microscope with a shear force height feedback system has been developed to measure the field distribution in integrated optical devices. The microscope has been applied on real devices.

Introduction

The aim of the project is to study the electro-magnetic fields in integrated optical waveguide structures in amplitude, phase, polarization and time, with a spatial resolution of $\lambda/50$. A near-field optical microscope with a shear force height feedback system has been developed to image the amplitude of the optical field distribution. With this microscope it is possible to measure simultaneously the optical field distribution in a waveguide and its topography [1].

Experimental

Piezoelectric bimorph plates have been used for a large area scanner with a range of $250 \times 150 \times 4 \mu\text{m}^3$ for the x, y and z direction, respectively. The whole scanner can be translated in the x and y direction over 6 mm. The sensitivity of the scanner in the z-direction is 0.5 nm. The scanner is built on a tripod system for the coarse approaching of the fiber probe to the waveguide structure. A tuning fork shear-force feedback system has been implemented as distance control mechanism for the microscope which can also be used for the fine approach [2].

The fiber probe scans over the waveguide surface at a distance of a few nm, while the waveguide is fixed. The evanescent wave of the light inside the waveguide is coupled into the fiber probe, due to the frustrated total internal reflection (figure 1a) and is collected with a photo-multiplier tube. The setup for amplitude imaging is shown in figure 1b.

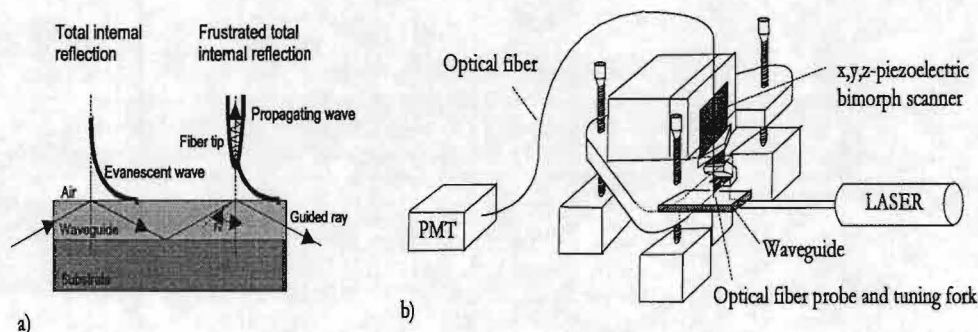


Fig. 1: a) Frustrated total internal reflection, b) Near-field optical microscope for amplitude imaging of the field distribution in integrated optical waveguides.

Results

The topography and the propagation of the light in a Si_3N_4 Mach-Zehnder interferometer is shown in figure 2 and 3. A comparison is made between measurement and simulation in figure 2. The field distribution for different incouple angles is shown in figure 3.

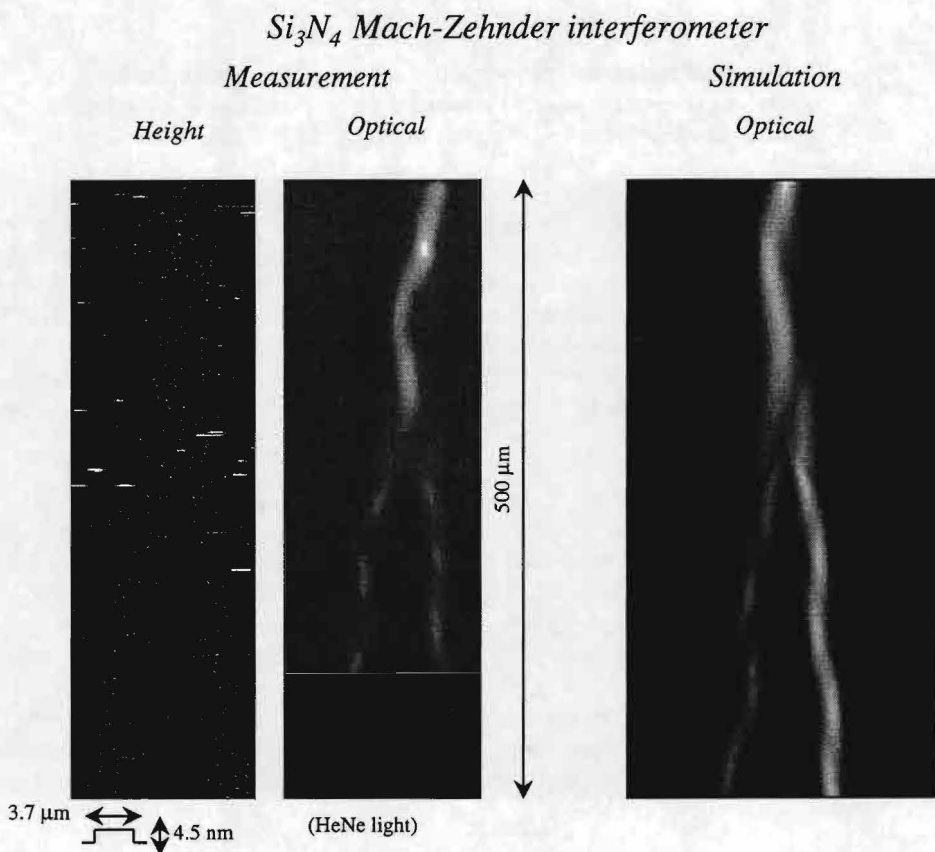


Fig. 2: The measured and the simulated propagation of the light in a Si_3N_4 Mach-Zehnder interferometer. The scan range is $20\ \mu\text{m} \times 500\ \mu\text{m}$. The height of the structure is $4.5\ \text{nm}$. The measured topography is shown in the left image and the measured propagation of the light is shown in the center image. The right image shows the simulated propagation of the light obtained with a "Finite difference beam propagation method" (FDBPM) [3,4].

Si₃N₄ Mach-Zehnder interferometer

Changing the incoupling angle

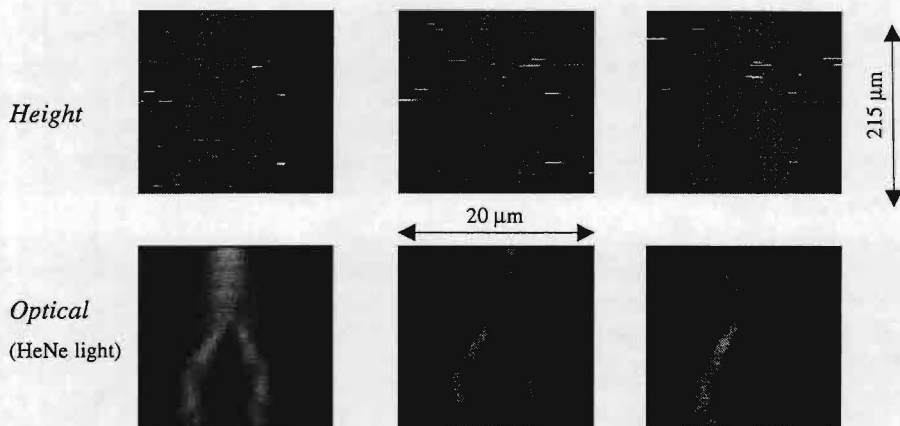


Fig. 3: Light propagation in a Si₃N₄ Mach-Zehnder interferometer for different incoupling angles of the light. The scan range is 20 μm x 215 μm. The height of the structure is 4.5 nm. The topography is shown in the top images and the propagation of the light is shown in the bottom images.

The topography and the propagation of the light in a SiON channel waveguide is shown in figure 4.

SiON channel waveguide

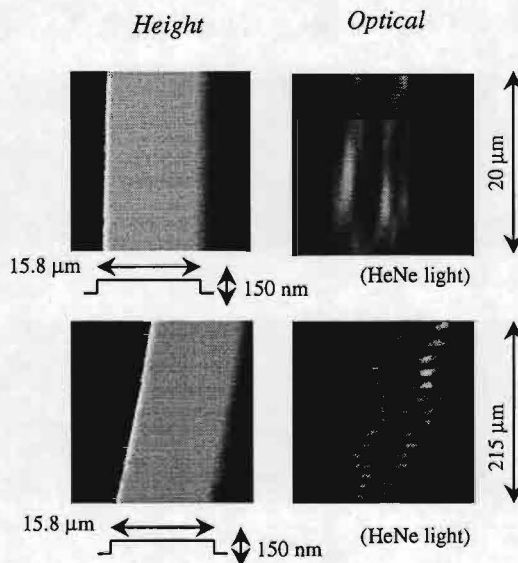


Fig. 4: Light propagation in a SiON channel waveguide. The scan range is 20 μm x 20 μm for the top images and 20 μm x 215 μm for the bottom images. The height of the structure is 150 nm. The topography is shown in the left images and the propagation of the light is shown in the right images.

Conclusions

A near-field optical microscope has been developed to image the amplitude of the optical field distribution in integrated optical waveguide structures. The developed scanner has a scan range of $250 \times 150 \times 4 \mu\text{m}^3$ for the x, y and z direction, respectively. The whole scanner can be translated in the x and y direction over 6 mm. The sensitivity of the scanner in the z-direction is 0.5 nm. The amplitude of the optical field distribution in a SiON channel waveguide and a Si_3N_4 Mach-Zehnder interferometer has been measured simultaneously with the topography. The measured optical field distribution is comparable with the simulated optical field distribution for the Si_3N_4 Mach-Zehnder interferometer.

Future outlook

A position feedback control system will be implemented to compensate for the nonlinearity of the scanner. To obtain phase images the microscope will be integrated in one branch of a Mach-Zehnder interferometer. Phase maps of splitters, converters, (de)multiplexers can be recorded in that way. Furthermore, time maps will show the temporal evolution of ultrafast pulses through the waveguide.

Acknowledgements

This work is supported by the Dutch organization for Fundamental Research on Matter (FOM).

References

- [1] E.G. Borgonjen, M.H.P. Moers, A.G.T. Ruiter, N.F. van Hulst, Probing field distribution on waveguide structures with an atomic force / photon scanning tunneling microscope, "Near-Field Optics" (eds. M.Paesler & P. Moyer), *SPIE 2535*, 125-131, 1995.
- [2] A.G.T. Ruiter, J.A. Veerman, K.O. van der Werf, N.F. van Hulst, Dynamic with a shear force height feedback system of tuning fork shear-force feedback, *Appl. Phys. Lett.*, 71 (1), 28-30, 1997.
- [3] H.J.W.M. Hoekstra, G.J.M. Krijnen, P.V. Lambeck, *IEEE J. Lightw. Techn.*, 10, 1352, 1993.
- [4] T.H. Hoekstra, H.J. van Weerden, P.V. Lambeck, Th. J.A. Popma, *IEEE Photonics Technol. Lett.*, 6, 83, 1994.

Technological Aspects of Deep Proton Lithography for the Fabrication of Micro-optical Elements

P. Vynck, P. Tuteleers, H. Ottevaere, V. Baukens, G. Verschaffelt, S. Kufner, M. Kufner, A. Hermanne, H. Thienpont and I. Veretennicoff*

Vrije Universiteit Brussel, Lab for Photonic Computing and Perception, Applied Physics Department (TW-TONA), Pleinlaan 2, 1050 Brussel, Belgium

tel.: ++ 32 2 629 3613, fax: ++ 32 2 629 3450, e-mail: pvynck@vub.ac.be

**Eenheid Cyclotron, Laarbeeklaan 103, 1090 Brussel, Belgium*

ABSTRACT

Deep proton lithography is a technology for the fabrication and monolithic integration of refractive micro-optical elements in PMMA. We report on our current investigations on the technological aspects of the process and the characteristics of the optical elements.

1. Introduction

The technology of deep proton lithography in PMMA (poly methyl methacrylate) is a fabrication method for monolithic integrated refractive micro-optical elements and micro-mechanical holder structures, which allows structural depths in the order of several hundred microns[1,2]. Different optical functions can be fabricated in one block and form monolithic integrated optical systems. In addition mechanical support structures and alignment features can be integrated with these optical systems. This paper will focus mainly on the technological requirements of the irradiation, development and diffusion setups, which are necessary to achieve predictable and reproducible results.

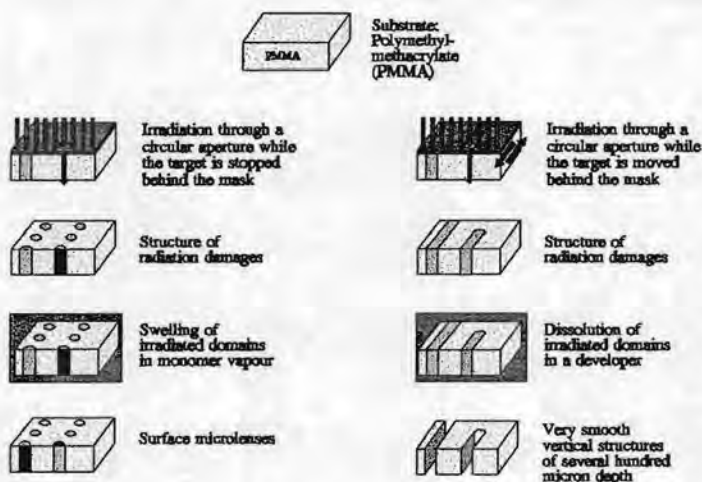


Fig. 1 Basic fabrication processes of deep proton lithography

2. Basic Processes

The fabrication process consists of three basic procedures: an irradiation of a PMMA substrate followed by either a development of the irradiated regions or a swelling of the irradiated regions by organic vapour. (see fig. 1). If required both processes can be applied to different regions within one sample.

The idea of the process is based on the fact that proton irradiation of linear PMMA with high molecular weight splits the polymer chains and thus changes the chemical properties of the material. For the irradiation the PMMA sample is covered by a metal mask which is either fully transparent or fully opaque for the proton beam. The shape of the mask is directly projected onto the PMMA sample where the impinging high energy protons create well defined domains with reduced molecular weight. More complex structures can be created by moving the sample during irradiation behind a mask with only one aperture (eg. a circular hole).

The irradiated domains can be dissolved in a special developer, because they show higher solubility than the non-irradiated domains. This process allows the fabrication of structures with optical quality, which can be used as deflection surfaces. Moreover alignment features and mechanical support structures can be integrated on the same sample during the same irradiation session. For the fabrication of these structures the sample is moved during irradiation behind the mask.

Alternatively to the development a completely different process can be applied to the irradiated PMMA: a swelling of the irradiated domains. This process makes use of the fact that the irradiation of PMMA changes also the swelling behaviour of PMMA when it is exposed to organic vapour, eg. styrene vapour. For the fabrication of microlenses the circular aperture of the mask is directly projected to the PMMA. During diffusion a considerable volume expansion can be observed which forms surface microlenses. Finally these lenses can be stabilized by thermal- or photopolymerization.

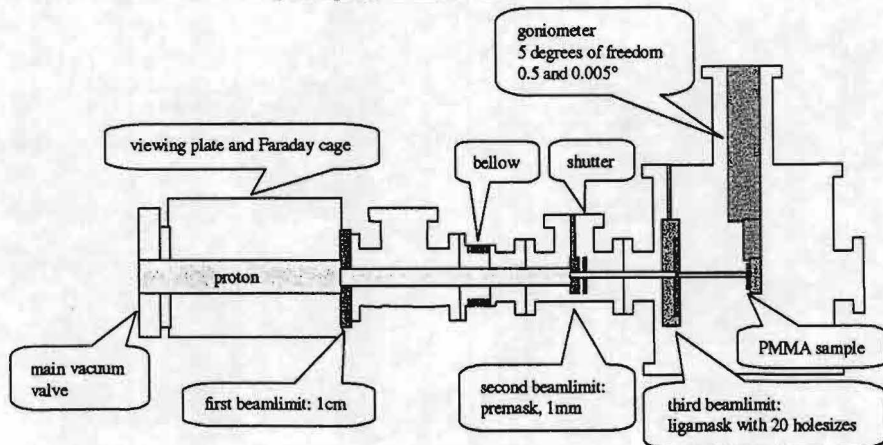


Fig. 2 General overview of the set-up and schematic cross-section

3. Practical Setup

In order to fabricate structures which have at the same time a high aspect ratio, smooth and flat surfaces and a high accuracy in lateral positioning, several requirements to the setup have to be accomplished:

The aspect ratio of the irradiated domains is determined on the one hand by the penetration depth and on the other hand by the size of the mask aperture. The penetration depth of protons in PMMA is determined by the kinetic energy of the incident particles only. To achieve structural depths of several hundred μm until 1 mm, the protons are accelerated in a cyclotron to kinetic energies of some MeV. Fig. 2 shows a schematic cross section of the irradiation setup.

The high energy protons coming from the cyclotron enter the beam line as indicated at the left side of the figure. At this place the beam has a diameter of several centimeters. From here the beam is reduced by three apertures. The first one reduces a large part of the beam and is water-cooled to compensate for the heat-production. The second aperture acts as a premask: by moving it up or down one aperture of the final mask can be selected. The final mask is a 300 μm thick Nickel plate which contains holes in different sizes in a range from 20 μm to 1 mm and has been structured by the so-called LIGA technique [3]. This type of mask has been chosen, because it has to be thick enough to fully absorb the protons. Furthermore the shape of the holes has to be perfectly cylindrical, since any tilt or lateral imperfection in the holes would affect the resulting PMMA structure.

A shutter is installed between the premask and the final mask to enable a fast and easy interrupt of the beam, in case that the sample is moving without the need to irradiate that part of the sample.

The lateral tolerances of the structures are mainly determined by the accuracy of the motor drives which move the sample during irradiation. To achieve high lateral precision the sample, which is typically a disk of 1 inch diameter and 0.5 mm thickness, is mounted on a goniometer. This is an electro-mechanical device for high precision positioning in a vacuum environment. The manipulator has 5 motorized degrees of freedom: 3 translations (x,y,z) and 2 rotations (R1, R2). The translations have a resolution of 0.5 μm and a travel range of ± 50 mm for the z movement and ± 25 mm for x and y. The rotations have an extent of $\pm 180^\circ$ for R1 and $\pm 90^\circ$ for R2 with a resolution of 0.005° . In addition the sample holder is equipped with a heater- and cooling system to control the temperature at the sample and thus to provide a thermally stable environment.

The dose which is locally deposited onto the PMMA is the most critical parameter in the irradiation process, and has therefore to be controlled exactly. This measurement is performed at the sample holder: If the protons have enough energy to pass through the PMMA sample, they reach the backplate of the sample holder, where they induce a current. This current is a measure for the deposited dose and is read out with a pico-amperemeter. For many applications a constant dose deposition over a whole structure is required. This would be straightforward, if a constant current and a constant speed of the motor drive could be assumed. However the intensity of the proton beam is not sufficiently constant. These instabilities can be compensated by a step by step irradiation. This means that the motors will only move to the next position if enough dose is received at that very position. With this

method an exact control of the dose is now possible.

The development of an irradiated PMMA sample is accomplished in a special developer which attacks the irradiated regions by a factor of 1000 faster than the non-irradiated ones [1]. Special care has to be given to the temperature stability of the developer bath and to the stirring of the sample. Typically the temperature is 38° C, and for stirring a ultrasonic stirrer for fast material removal is used.

For the diffusion process the temperature stability is the most critical parameter. In a closed reactor vessel with a volume of 100 cm³ the sample is heated to 90° C. After having reached this temperature 0.5 ml of styrene is injected into the reactor. After a time period of 45 minutes the volume expansion has reached its saturation. For stabilization purposes the temperature in the reactor is reduced to 65° C for 100 minutes.

4. Characteristics of the individual optical components

The profile of the optical deflection surfaces of micromirrors, fabricated with this technology, depends on two different sets of parameters: In the direction of beam incidence the flatness of the mirror is limited by the lateral straggling of the ions in the PMMA. In the direction of the sample movement the flatness is determined by the precision of the movement and the homogeneity of dose deposition during the movement. The surfaces of the micromirrors or -prisms have been measured with a WYKO profilometer. The flatness of these elements can be better than 1 µm, and the roughness is in the range of about 20 nm.

So far microlenses and microlens arrays have been fabricated with diameters from 80 µm to 1800 µm. Numerical apertures between 0.2 and 0.7 have been achieved.

5. Conclusions and Perspectives

The characterisation of the individual optical elements shows that all the necessary elementary optical components for integrated refractive micro-optical components can be provided with the technology of deep proton lithography. Experiments are underway to design and fabrication of micro-optical systems which take advantage of the monolithic integration potential of this technology [4,5].

6. References

- [1] M. Kufner and S. Kufner: "Micro-optics and Lithography", VUB Press, Brussels, 1997.
- [2] M. Kufner, S. Kufner: "Fabrication of monolithic integrated fiber-lens connector arrays by deep proton irradiation", *Microsystems Technology*, Vol. 2, p. 114 - 118, 1996.
- [3] K.-H. Brenner, M. Kufner, S. Kufner, J. Moisel, A. Müller, S. Sinzinger, M. Testorf, J. Göttert, J. Mohr: "Application of three-dimensional micro-optical components formed by lithography, electroforming, and plastic molding", *Appl. Optics* 32 (32), 6464-6469, 1993.
- [4] G. Verschaffelt et al.: "Experimental demonstration of a free-space intrachip micro-optical interconnect", *IEEE LEOS BENELUX annual symposium*, Eindhoven, 1997.
- [5] V. Baukens et al.: "Optical performance analysis of free-space and guided wave optical pathway blocks for intra-MCM interconnects", *IEEE LEOS BENELUX annual symposium*, Eindhoven, 1997.

The Spatially Modulated Silicon CMOS detector

D. Coppée, W. Pan, J. Stiens, R. Vounckx, M. Kuijk

VUB-IMEC

Electronics Division Lab for Microelectronics and Technology

Pleinlaan 2, 1050 Brussels, Belgium

Tel (32).2.629.29.90 fax (32).2.629.28.83

Email dcoppee@vub.ac.be

We present a novel detector for high-speed light detection in standard CMOS. Spatial modulation of incident light and detection zones allow fast detector recovery, yielding bit rates higher than 200 Mbit/s at 0.05 A/W (@ 860 nm) and 0.132 A/W (@ 635 nm) responsivity.

Introduction

Normally, integrated detectors in CMOS-technology exhibit long recovery times, limiting the detector bandwidth to only several MHz. This is due to the long absorption length and slow diffusion speed of photo-generated carriers. Several technologies deviating from standard CMOS-technology have been proposed aiming at higher detector speed [1,2]. But most of these proposals are based on shielding the detector from photo-generated carriers diffusing from deeper levels in the substrate. In our approach, this shielding is no longer required, allowing standard CMOS technology to be used. This implies several substantial advantages: The yield of the CMOS process is maintained (each additional step has a major influence on the yield) and the detector inherently improves with the continuous technology evolution. This integration allows further signal processing functions on the same chip. Many optoelectronic applications can benefit from this new detector and its integration with CMOS circuitry including parallel and serial optical receivers, Compact Disc reading heads and automotive applications.

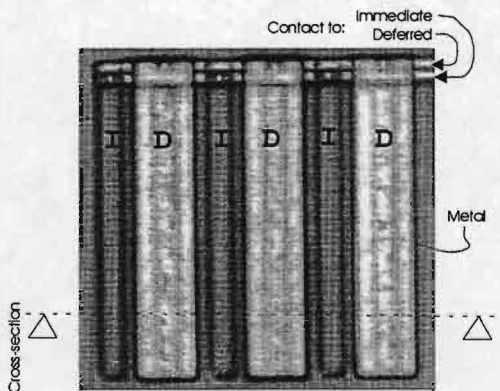


Figure 1. Top view of the Spatially Modulated Light detector. Three Immediate and three Deferred detector fingers form respectively the Immediate and the Deferred detector structure.

Principle of operation

The device [3] consists of a substrate wherein the light being absorbed is spatially modulated. This is accomplished by adding a metal shadow mask which spatially modulates the incident, and consequently, the absorbed light (Fig. 1, 2). By measuring the magnitude of the spatial frequency component in the minority carrier distribution (Fig. 2), a fast detector is conceived. The structure which is not shielded by the shadow mask is called the Immediate detector, the other one the Deferred detector.

Assume we apply a Dirac-like light pulse (Fig. 3) on the detector. At t_0 , the minority

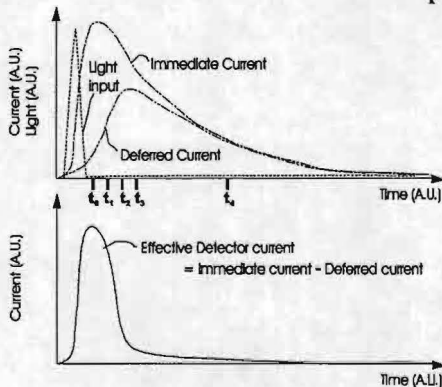


Figure 3. Typical CMOS-detector current (for a short light pulse) is like the Immediate current shown: relative fast rise and slow recovery times. Subtracting the deferred from the Immediate current delivers a shorter pulse (faster recovery), defined as the Effective detector current.

In general, photo-generated carriers live long but their spatial modulation disappears with time. This allows the detector to respond faster than the lifetime of the photo-

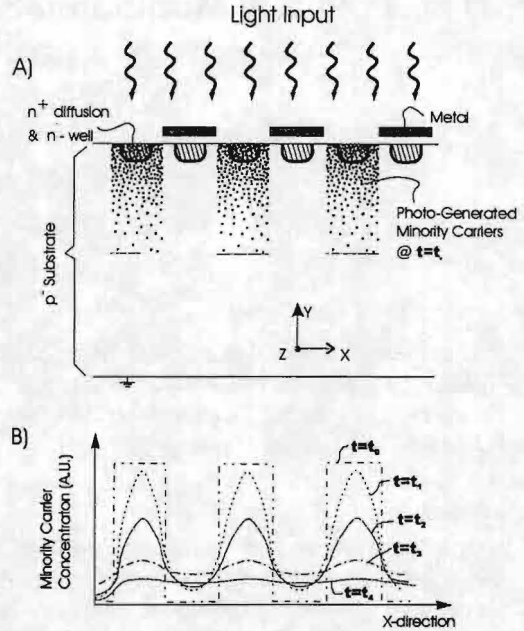


Figure 2. (a) Cross-section. (b) Evolution of photo-generated carriers in time.

carrier concentration is then a spatial block-form (Fig. 2b). Electron-hole pairs are only created in and below the immediate detector. Light incident on the metal is reflected such that there are no carriers present at the deferred detector. The block-form is smoothing out by diffusion (t_1 , t_2 , t_3) to the moment in time (t_4) when no spatial information is left. The effective signal is the difference between the Immediate and the Deferred detectors (Fig. 3) and is a measure for the spatial modulation of the carriers. This difference initially gives a fast response due to the Immediate detector and will return to zero once the Deferred detector receives carriers. The conventional CMOS-detector output would be like the Immediate signal. The turn-off time of the difference-signal is shorter than that of the Immediate alone.

generated carriers. Similarly, carriers originating at a neighboring detector will loose their spatial modulation resulting in low cross talk between multiple detectors.

From an electrical point of view, this type of detector has several advantages. Firstly, though only a single light input signal is required, from the detector on, analog signal processing can be achieved fully differentially. Subsequently, a good power supply rejection ratio (PSRR) can be expected which is necessary when mixing with digital circuits on the same chip. Secondly, the complete compatibility with standard CMOS technology and the elimination of hybridization steps avoids supplementary bonding-pad capacitance, bonding-wire inductance and associated signal degradation. Last, due to the finger shape, a very low detector capacitance yields high voltage readout of the detector. This facilitates further amplification and conversion to digital signal levels.

Experimental results

The tested devices are fabricated with a 0.8-micron 5 V CMOS technology by AMS. The detector area was approximately $70 \times 70 \mu\text{m}^2$ and has a capacitance of 50 fF (and an additional 70 fF of the measuring circuit). The finger pitch is $12 \mu\text{m}$. We used a semiconductor laser at 860nm as the light source. The experiment was done at a bit rate of 200 Mbit/s NRZ. After biasing the detector, a sequence of light pulses was applied to the detector. When biasing the detector at 3.8 V (not critical), responsivities of 0.05 A/W at 860 nm and 0.132 A/W at 635 nm were achieved. This corresponds to 6.9 % and 25 % external quantum efficiency respectively. The higher quantum efficiency at shorter wavelengths corresponds to the shorter absorption length. Figure 4 shows how the voltages at the Immediate and the Deferred detector change. Notice that, although both detector outputs continue to change, the difference does not if there is no incident light. The photo-current is achieved by differentiating the difference signal and a multiplication with the 120 fF capacitance value of the spatially modulated detector structure.

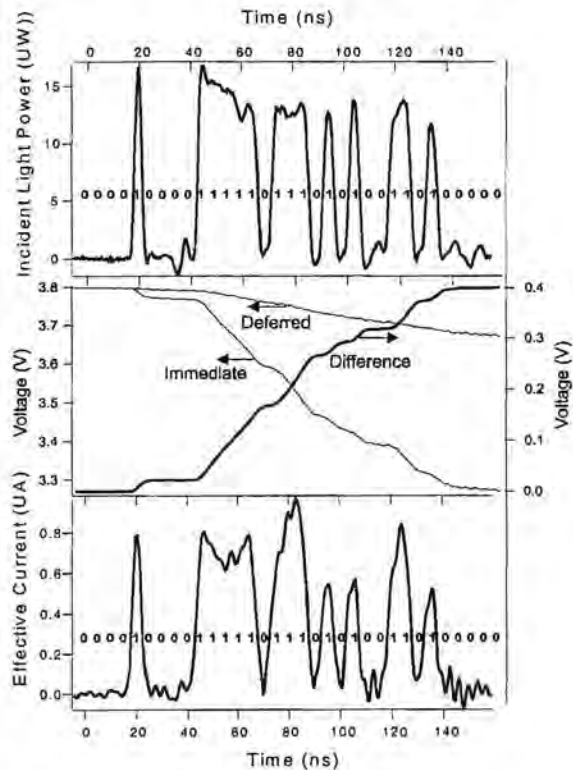


Figure 4. Incident light-pulse at 200 MHz NRZ (top); Voltage response at Immediate, Deferred detector and calculated Difference (middle); Reconstructed effective current showing initial bit sequence (bottom).

Conclusion

We demonstrated the operation of the novel spatially-modulated light detector. First measurements showed light detection at 200 Mbit/s. At 860 nm, the detector with $70 \times 70 \mu\text{m}^2$ area yielded a responsivity of 0.05 A/W with 50 fF device capacitance. At 635 nm, 0.132 A/W was measured.

Acknowledgements

The authors thank for partial funding the following institutions: ESPRIT IV-MELARIOIC, FWOV, IUAP IV/13, GOA 20325 and IWT (Brussel).

References

- [1] Massimo Ghioni, Franco Zappa, Vijay P. Kesan, James Warnock, "A VLSI-Compatible High-Speed Silicon Photodetector for Optical Data Link Applications", IEEE Transaction on Electron Devices, vol. 43, pp.1054-1060, NO.7, July 1996 *and references therein*.
- [2] L.D.Garret, J. Qi, C. L. Schow, J.C. Campbell, "A silicon-Based Integrated NMOS-p-I-n Photoreceiver", IEEE Transactions on Electron devices, vol.43, pp. 411-416, No 3, March 1996.
- [3] Patent pending.

Integrated optical sensor system for detection of chemical concentrations

R.G. Heideman, P.V. Lambeck
MESA Research Institute, Universiteit Twente
P.O. Box 217, 7500 AE Enschede, the Netherlands

Abstract

The "on-line" measurement of chemical concentrations is very important in a variety of application fields. The recent developments in both integrated optical circuitry and "easy-to-use" fiber-to-chip interconnects enable the fabrication of remote optical sensors. Both developments will be discussed.

1. Introduction

In several areas such as process technology, health care, environmental control, biotechnology, etc. [1,2], chemical sensors are required. These sensors generally should be very sensitive, small, fast, cheap, and reliable. Furthermore, they should have the option of remote sensing [3]. An attractive solution fulfilling all these requirements are formed by integrated optical sensors [4].

As initiated by the Dutch Innovative Research Programme (IOP) "Electro-Optics", TNO-FEL (Physics and Electronics Laboratory) and the University of Twente collaborate in the development of hybrid, silicon based integrated optical sensors. In this collaboration, the TNO-FEL research is focused on physical sensors, while the University of Twente restricts itself to integrated optical sensors for detecting chemical concentrations.

2. Basic sensor components

The basic component of integrated optical sensors is the optical channel waveguide. This waveguide consists of several thin (typically $\leq 1 \mu\text{m}$) layers of dielectric materials with different refractive indices, grown on top of a silicon substrate. An example is given in Fig.1. In the sensing region the waveguiding configuration is structured in such a way that external (physical and chemical) parameters will influence the propagation properties of the guided light. This is serving as the basis for sensing. Using an appropriate optical read-out system, this effect is converted in an intensity change, see e.g. the section *Mach-Zehnder interferometer*.

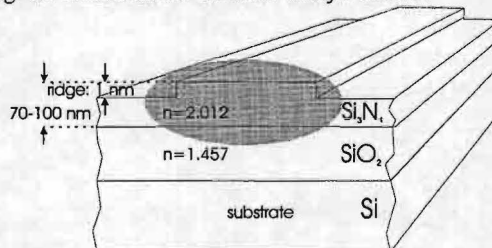


Figure 1. Schematic of a silicon based channel waveguide. The shown configuration is typical for sensing applications [5,6]. The intensity profile of the guided light is shown in grey.

The fabrication of integrated optical chips consisting of these basic optical channel waveguides starts from the well known processes in IC and optical telecommunication industries. This technological base is often replenished by incorporation of materials, that are sensitive to specific (physical or) chemical parameters.

The passive optical chip has to be connected to light sources (e.g. LED's or (diode)lasers) and photo detectors, and (if necessary) external electronics. In the IOP "Electro-Optics" project, both the external (electro-)optical components as well as the electronics are hybridly connected to the optical chip. This approach enables a large flexibility but requires the development of proper connection techniques [8,9], see section "*Fibre-to-chip interconnect*".

3. Mach-Zehnder interferometer

The general sensing principle of integrated optical sensors is often based on the interaction of the evanescent tail of the guided wave with the analyte to be measured, see Fig. 2.

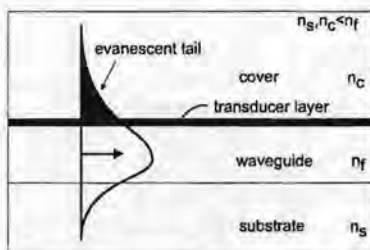


Figure 2. The evanescent tail of a guided wave can interact with the analyte to be detected, thereby changing the effective index (ΔN) of this wave.

Most often, the specific selectivity is obtained by applying a thin cover layer on top of the waveguide layer, in which receptor molecules are immobilised, capable to bind selectively to the analyte in a reversible way. Due to this complexation optical parameters, like the refractive index, the absorption coefficient, or the emission properties, are changed.

We restrict ourselves to refractive index based sensors [12], wherein (the binding of) the analyte changes the refractive index of the cover layer. This causes a change (ΔN) in the effective refractive index N of the guided wave. This latter change should be converted to an intensity change using an appropriate optical read-out system. Some well known read-out principles are the Surface Plasmon Resonance (SPR) [13], the grating in/outcoupling concept [14], and the Mach-Zehnder interferometer (MZI) [6], see Fig. 3.

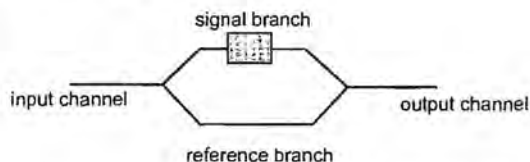


Figure 3. Top view (schematic) of a Mach-Zehnder interferometer with (a part of) the signal branch subject to the external parameter to be detected.

The MZI is generally supposed to show the highest potential and indeed it can be very sensitive [14]: in addition the intrinsic balance due to the incorporation of a reference branch (see Fig. 3) makes it insensitive for many perturbing effects.

Despite of its high potential, until now the MZI is hardly used in commercial applications. Probably, this is caused by two major problems. The first problem is specific for the interferometer. To exploit its high sensitivity potential, the MZI has to be actively (phase)modulated. Effective phase modulation however, often put requirements to waveguiding materials and/or structures, which are contradictory to those set by an optimal transduction of the chemical concentration into changing waveguiding properties. Secondly, there is the general problem of connecting the optical chip to external parts (e.g. the light source and the detection unit) in an economical way. A solution to this problem will be treated in section "Fibre-to-chip interconnect".

The first mentioned MZI-problem can be solved by the introduction of a vertical tapering technique. This technique, which is part of a patent application [11], enables to optimise all individual components on the optical chip independently. In Fig. 4, a (schematic) cross-section of a such a waveguide is shown.

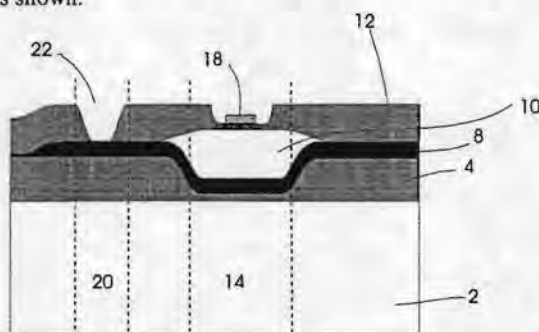


Figure 4. Schematic cross-section of a waveguide configuration (reprinted from [11]), showing individually optimised optical components using vertical tapering.

Using this vertical tapering system, 2π phase modulation can be obtained using low voltage levels (typically 10 Volt).

At the conference the relevant details concerning this vertical tapering technique will be discussed.

4. Fibre-to-chip interconnect

For a commercial application, especially the connection of the light source to the integrated optical circuitry is of crucial importance.

Recently, a lot of progress has been obtained in the connection of the light source to optical chip: both by TNO-FEL with the diodelaser-to-chip connection [10] and the UT with the reusable fibre-to-chip interconnect [5], see Fig. 5.

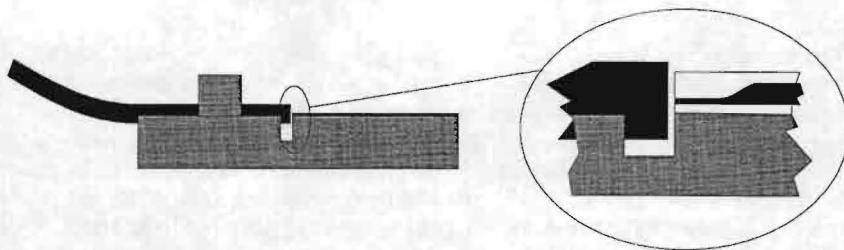


Figure 5. Cross-section (schematic) of the (patented) fibre-to-chip interconnect.

Due to V-grooves fabricated in the optical chip, and an incorporated "eye-of-a-needle" fibre guide, the interconnect is self-aligning and easy to use. Furthermore it is reusable, and shows an adjustable coupling efficiency ranging from zero to typically 50%, as is amply sufficient for sensor applications. This relatively high coupling efficiencies are obtained using loose-mode waveguides [5,9], exploiting the previously discussed vertical tapering technique.

The important aspects concerning this fibre-to-chip interconnect, which are also incorporated in the patent application [11], will be discussed in detail at the conference.

References

- [1] P.V. Lambeck, "Integrated opto-chemical sensors", *Sensors and Actuators B*, 8, p.103-116.
- [2] O.Parriaux, in: O.S. Wolfbeiss (ed.), *Fiberoptic chemical sensors and biosensors*, Ch.4., CRC press, 1991.
- [3] F.W.H. Kampers et.al., "Sensors for agricultural production in the 21st century", proceedings of the 2nd Dutch Conference on Sensor Technology, april 1996.
- [4] R.G. Heideman, G.J. Veldhuis, E.W.H. Jager, P.V. Lambeck, "Fabrication and packaging of integrated chemo-optical sensors", *Sensors and Actuators B*, vol. 35-36, p.234-240, 1996.
- [5] R.G. Heideman, P.V. Lambeck, "Simple and reusable fibre-to-chip interconnect with adjustable coupling efficiency", proceedings, European Symposium on Lasers and Optics in Manufacturing, Munchen, Germany, to be published, 1997.
- [6] R.G. Heideman, R.P.H. Kooyman and J. Greve, "Performance of a highly sensitive optical waveguide Mach-Zehnder interferometer", *Sensors and Actuators B*, vol.10, p. 209-217, 1993.
- [8] J. Joppe, A. de Krijger and O. Noordman, "Hybrid integration of laser diode and monomode high contrast slab waveguides on silicon", *Electron.Lett.*, vol.27, p.162-3, 1991.
- [9] R.G. Heideman, E. Jager, P.V. Lambeck, "Loose-mode fibre-to-chip couplers", proceedings, IEEE/LEOS Symposium, Enschede, p.316-319, 1996.
- [10] A.J.T. de Krijger en H.H.P.Th. Bekman, "Hybrid Coupling of Laser Light sources to Silicon (Oxy)Nitride Based Waveguides", proceedings, European Symposium on Lasers and Optics in Manufacturing, Munchen, Germany, to be published, 1997.
- [11] Octrooiaanvrage NL 1006323, "Geïntegreerd optisch golfgeleider systeem", code MM97-06/7694, juni 1997.
- [12] P.V. Lambeck, R.G. Heideman and T.J. Ikkink, "Phase-modulated Mach-Zehnder Interferometer for sensor applications", *Medical and Biological Engineering*, vol.34 Suppl. 1 Part 1, p.145-6, 1996.
- [13] J. van Gent, "Surface Plasmon Resonance-based Chemo-Optical Sensors", Ph.D.thesis, University of Twente, 1990.
- [14] W. Lukosz, "Principles and sensitivities of integrated optical and surface plasmon sensors for direct affinity sensing and immunosensing", *Biosensors & Bioelectronics*, vol. 6, pp.215-225, 1991.

Polymeric integrated optical components for add-drop multiplexing

M.B.J. Diemeer¹, E. Rikkers², D.T. van Veen³, G.J.M. Krijnen^{2,4,5}, M.J. Gilde², J.L. Joppe⁶, A.F. Bakker^{4,5}, M.K. Smit⁴, R.M. de Ridder², A. Driessen², A.M.J. Koonen⁷

¹ Akzo Nobel Central Research, P.O. Box 9300, 6800 SB Arnhem, The Netherlands
Tel. +31-263662685, Fax +31-263662193, E-mail: diemeer@akzo.nl

² University of Twente, MESA Research Institute, P.O. Box 217, 7500 AE Enschede

³ University of Twente, CTIT Research Institute, P.O. Box 217, 7500 AE Enschede

⁴ Delft University of Technology, Mekelweg 4, 2628 CD Delft

⁵ BBV Software, Hengelsestraat 705, 7521 PA Enschede

⁶ TNO-FEL, Electro-optics group, P.O. Box 96864, 2509 JG Den Haag

⁷ Lucent Technologies, P.O. Box 18, 1270 AA Huizen

Polymeric integrated optic components for fiber-compatible add-drop multiplexers have been realized. Switch matrices (4x4) with cascaded 1x2 thermo-optic digital optical switches will be connected with (8x8) phasars in a fold-back architecture to obtain optimal performance of the add-drop mux.

Introduction

Solid state optical space switches based on the thermo-optic (t.o.) effect in polymeric optical waveguides have now reached the commercial stage [1]. These components are marketed under the trade name BeamBoxTM by Akzo Nobel Photonics. Their application is in network protection and network reconfiguration functions for fiber optic communications systems. The requirements for these applications include polarization and wavelength independence, low insertion loss, low cross talk, low drive power with step-like response, millisecond switching times and small size. Polymeric t.o. digital switches can meet these requirements due to the exceptional thermal and t.o. effects of polymers combined with their tunability and processing versatility. Polarization sensitive phased arrays for 1550 nm based on the BeamBoxTM technology have been reported earlier [2]. In the framework of the Dutch collaboration program IOP Electro-Optics/Polymers supported by the Ministry of Economic Affairs, the BeamBoxTM technology has been applied to realize polarization insensitive phasars. These will be combined with digital switch arrays to obtain a reconfigurable add-drop multiplexer for the EDFA window.

Polymeric thermo-optic switches

For routing application where the required response times are of the order of milliseconds, t.o. control of optical waveguide devices is attractive from the viewpoint of simplicity and flexibility. The t.o. effect is polarization independent and present in all practically used waveguide materials. This allows materials with good waveguide characteristics (low loss and cost) to be selected for fiber-compatible t.o. component realization. Important examples of such materials are polymers and silica. The silica components are derived from the well-established silica-on-silicon technology for passive waveguide components, whereas the polymer components are primarily developed for t.o. space switching applications utilizing the high t.o. coefficient of polymers.

Switching between waveguide channels can be induced by creating a difference in their effective refractive indices. This can be done by activating one of the resistive stripe

heater electrodes that are deposited above the waveguides on top of the cladding layer. In the commercially available t.o. components silicon wafers are used as substrates because of their compatibility with standard IC process equipment, their good surface quality and their excellent heat conduction. The latter property is for t.o. components important as it provides them with a nearly perfect heatspreader. Through that, the rise in temperature of the heater electrode is proportional with the dissipated electrical power density and inversely proportional with the thermal conductivity, λ , of the waveguide material. For glassy polymers $\lambda \sim 0.2$ W/m.K, while for silica $\lambda \sim 1.4$ W/m.K. Therefore to induce the same difference in the temperatures of the channel waveguides, it takes for a silica-on-silicon waveguide 7 times more power than for a polymer waveguide on silicon. In addition, the temperature distribution in the waveguide layer for a given heaterstripe temperature is independent of its thermal conductivity. Since the relatively large t.o. coefficient for polymers of about $-10^{-4}/^{\circ}\text{C}$ is an order of magnitude larger than for silica ($+10^{-5}/^{\circ}\text{C}$), it can be concluded that takes about two orders of magnitude less power to induce in polymer waveguides the same difference in (effective) indices as in silica-on-silicon waveguides.

There are two different waveguide switch types that can be used in practical t.o. devices. These are the Mach Zehnder interferometer (MZI) and the Digital Optical Switch (DOS). The operation of the DOS is based on the adiabatic evolution of the (system) mode of the two waveguides in the branching section to the (fundamental) mode of the output channel. The output channel will be the channel with the highest effective index. For a polymeric DOS this is the unheated branch because the t.o. coefficient in polymers is negative. The mode evolution in the DOS results in a "digital" switch behavior. Fig. 1 shows this in a switch curve of a typical 1x2 switch.

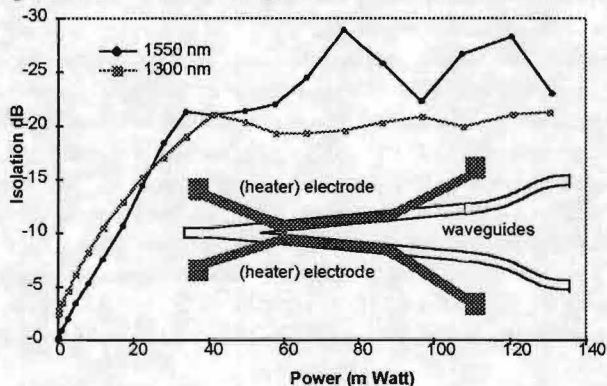


Fig. 1 1x2 polymeric t.o. DOS and its switch curve.

When the switch is powered further than required, the light remains in the intended output channel with high isolation, typically < -20 dB. The advantage of the DOS over the MZI switch is this non-recursive character which makes it insensitive for drive power fluctuations and, associated with that, for temporal refractive index changes caused by for example by water desorption or material relaxation phenomena. In addition to that, the DOS principle results in wavelength (fig. 1) and polarization insensitivity ($\text{PDL} < 0.2$ dB). Typical insertion loss (dual window) for a pigtailed and packaged polymeric 1x2 DOS is < 2 dB and the switching time is < 2 milliseconds. All these features makes the DOS highly compatible with optical fiber systems where low-loss operation in both windows is often required and the polarization state is

random. A disadvantage of the DOS as compared with the MZI is its higher power required for switching. This is typically an order of magnitude higher. However, the switch power for a polymeric DOS is only 50-100 mW (fig. 1) due to the strong t.o. effect in polymers. A silica-on-silicon DOS would require 5W, which is extremely high and excludes the practical use of the DOS principle in t.o. silica-on-silicon switches.

Polymeric phased array

At this moment silica-based phased arrays or phasars are commercially offered by several companies. Like the BeamBoxTM polymeric phasars, these suffer from stress-induced birefringence due to the difference in thermal expansion coefficients of the silicon substrate and the waveguide film, combined with elevated deposition/annealing temperatures of waveguidelayers. This birefringence results in polarization dependent transmission characteristics that cannot be tolerated in fiber-optic transmission systems. In the BeamBoxTM polymer waveguidelayers are not (yet) optimized for low birefringence; their birefringence is typically $2.5 \cdot 10^{-3}$, leading to a polarization dependent shift of about 2.5 nm at 1550 nm.

To remove this, we have integrated a polymeric half-wave compensation film in a phasar of the type as reported in [2]. This was done by dicing a 15 μm wide groove in the middle the (8x8) phasar and inserting the thin (6 μm) film oriented at 45 degrees with the waveguide plane in the groove and fixing using a UV-curing glue.

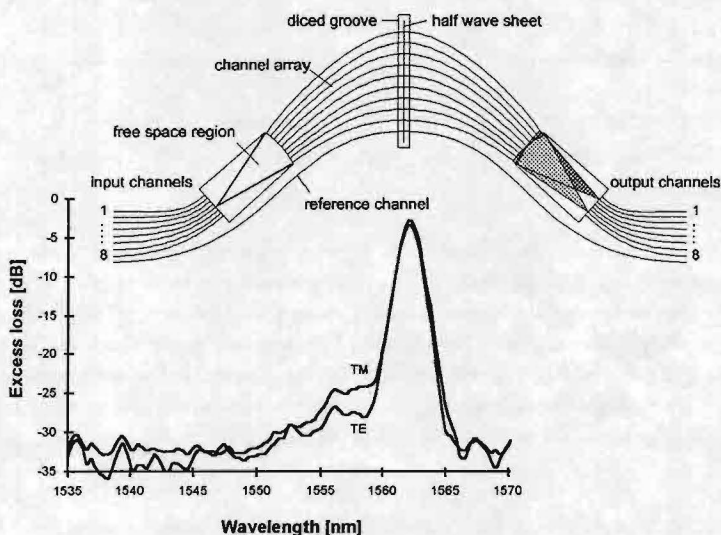


Fig. 2 Phasar with half-wave compensation film and wavelength response (ch.1 to 1) for TE and TM polarization. Excess loss is relative to the reference channel.

Measurements show nearly complete elimination of the TE-TM shift of 2.3 nm (fig.2) without noticeable increase of the insertion loss. The insertion loss for all 8 output channels using input channel 4 is between 8 and 10 dB. Crosstalk is <-20 dB. Channel spacing and free spectral range are 3.2 nm and 30.8 nm respectively.

In practical devices, temperature control is not only required for the stabilization of the central wavelength but also for tuning of the transmission peaks at the required wavelength grid. Typical stabilization is at the level of 0.1 nm, corresponding to

(effective) refractive index changes of 10^{-4} . This requires a temperature control within 1°C for a polymeric phasor whereas for silica phasors 10°C is sufficient. Tuning at the grid follows from the required control over the index at a level of 10^{-4} , which is impossible to achieve directly in the waveguide fabrication process since variations in the (effective) index of polymer layers and silica layers is $\sim 10^{-3}$. This means that the temperature control should be capable to tune the index over a range of 10^{-3} . The high t.o. coefficient of polymers allows for tuning of all realized components as the tuning range is only 10°C . For silica devices the tuning range would be 100°C which is unrealistic in practice and other techniques have to be applied for tuning at the grid.

Reconfigurable add-drop multiplexer

4x4 switch matrices based on polymeric t.o. DOS switches have been designed. These will be connected to the 8x8 phasor in a fold-back architecture to obtain a 4-channel reconfigurable add-drop multiplexer. This architecture is preferred from crosstalk analysis [3]. A further improvement of the crosstalk will be obtained by using for the add-drop switch two cascaded 1x2 DOS's per channel rather than a 2x2 switch (see fig3). The 2x2 functionality is not really needed because the path from add to drop will not be used. Advantages are the reduced number of switches and the absence of a waveguide crossing, eliminating near-end crosstalk and improving the crosstalk figures for signals from In to Out.

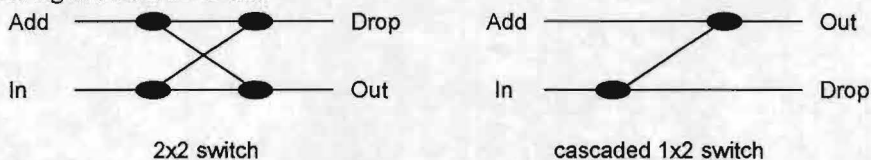


Fig. 3 Symbolic representation of a conventional 2x2 switch (four 1x2's) and a cascaded 1x2 switch (two 1x2's).

Because the (low contrast) standard BeamBox™ technology has been selected for component realization, integration of the phasor and the switch matrix on a 4" wafer was not feasible due to the minimal allowable bend radius for low-loss of $\sim 25\text{ mm}$. Therefore, switches and phasors have been realized on separate wafers and will be connected through fiber pigtailed. Current research is aimed towards the development of a more compact technology in order to integrate the phasor and the switch matrix on one chip for a full polymeric reconfigurable add-drop multiplexer.

Conclusion

It can be concluded that polymeric integrated optic components possess attractive properties for reconfigurable add-drop multiplex applications.

Acknowledgment

Senter (IOP) is acknowledged for its financial support and R.van Heuven (AN) for the waveplate integration.

References

- [1] T. Tumolillo et al., IEEE Commun. Mag., Feb. 1997, pp. 124-130.
- [2] M.B.J. Diemeer et al., Electron. Lett., 32 (12), 1132 (1996).
- [3] H. Takahashi et al., Electron Lett., 30 (24), 2053 (1994).

Tuneable WDM add-drop multiplexer using cascaded Mach-Zehnder wavelength filters

Bertrik H. Sikken, René M. de Ridder, Kerstin Wörhoff,
G.J.M. Krijnen, René G. Heideman, Alfred Driessen

University of Twente, MESA Research Institute
P.O. Box 217, 7500 AE Enschede, The Netherlands
Telephone: +31 53 4892712, e-mail: R.M.deRidder@el.utwente.nl

A thermo-optically tuned Mach-Zehnder wavelength filter has been realised in optimised silicon oxynitride (SiO_xN_y) technology. Several filter elements can be cascaded to obtain an 8-channel WDM add-drop multiplexer with 1 nm channel spacing in the 1550 nm transmission window.

Introduction

Add-drop multiplexers are very important elements in WDM networks. They can be used to isolate a signal in a single wavelength channel from a fibre and substitute it with another signal, while leaving the other channels undisturbed. Ideally an add-drop multiplexer should have low cross-talk, low attenuation and should be polarisation independent. An add-drop multiplexer can be implemented by using well-known [1,2] Mach-Zehnder interferometer (MZI) structures with unequal branches (figure 1). The length difference in the branches causes a wavelength dependent phase shift resulting in a transfer function that is periodic in optical frequency. Through the thermo-optical effect a small additional phase shift can be induced by heating one of the branches. This causes the periodic transfer function to shift with respect to optical frequency and thus to switch the device from the cross to the bar state for a certain wavelength.

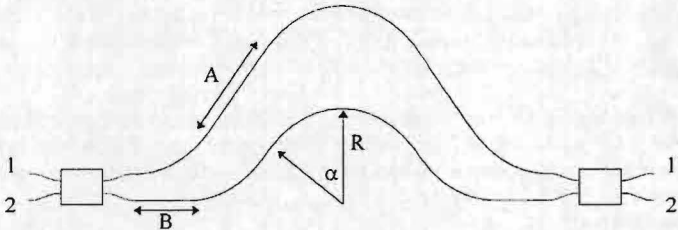


Figure 1. Diagram of a thermally tuneable Mach-Zehnder interferometer wavelength filter. All bends in the interferometer branches have the same bending radius R and the same total subtended angle of arc α , so that the path length difference is given by $2(A-B)$. The rectangular structures are 3-dB couplers based on the multimode interference principle. For thermo-optical tuning, heater electrodes are overlayed on the upper branch of the interferometer.

Several of these MZI's can be cascaded to form an add-drop multiplexer (ADM) as shown in fig. 2, where the periods of MZI's of types A, B and C have to be chosen in proportions 1:2:4 in order to (de)multiplex 8 equally spaced wavelength channels.

This type of ADM scales well with increasing number of wavelength channels since only two additional MZI's are needed for doubling the number of resolvable channels.

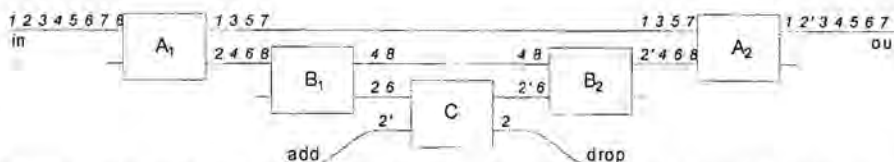


Figure 2. 8-Channel (numbered 1..8) Add-Drop Multiplexer. Each rectangle stands for an MZI as shown in fig. 1 (3 different types A, B, C). This example shows adding and dropping channel 2.

The remainder of this paper will concentrate on the design, realisation and testing of the thermo-optically tuneable MZI-elements that are the building blocks of the ADM.

Design

The general lay-out of a thermo-optically tuneable MZI is shown in fig. 1. The required optical path length difference is introduced by using bent waveguides. In both branches the bend radii and arc lengths are chosen to be equal in order to cancel out any bend-related effects. Two 3-dB 2x2 Multi-Mode Interference (MMI) couplers are used to split and recombine the light of the branches.

The device is to be designed for fabrication in a silicon oxynitride (SiON) waveguide system, which is described in more depth in a companion paper [3]. At 1550 nm wavelength, the channels consisting of a square 3x3 μm cross-section core, embedded in a SiO_2 background, are single-moded and have an effective index of 1.47 and a minimum bending radius of about 2 mm.

The channel spacing was chosen to be 1 nm, which means a free spectral range of 2 nm and in this case a path length difference of 820 μm .

The design of the MMI-couplers resulted in a structure supporting 9 modes and having dimensions 35 μm width and 920 μm length. The bends were chosen to have a safe 7 mm radius. The angle α , subtended by the bends was optimised in such a way that, under the constraint of the output channels being in line with the input channels, the total MZI filters had minimum dimensions for a given path-length difference.

The heaters for actuating the thermo-optical tuning mechanism were made from a thin gold layer deposited on top of the 5 μm thick SiO_2 cladding layer. The non-optimised dimensions were chosen to be 20 μm wide and 200 nm thick, which at a length of 4.5 mm results in a 26 Ω heater resistance.

Experimental results

Wavelength dependent measurements were performed with a tuneable laser having a tuning range of 1470..1580 nm and a line width less than 500 MHz (< 4 pm).

The light is end-fire coupled onto the cleaved facets of the wafer using microscope objectives. The light coming out can be projected onto a CCD camera for alignment purposes, or measured with a photodetector.

The transmission from each input port to each output port was measured by stepping the tuneable laser in 0.05 nm increments. The result for a typical device is shown in figure 3.

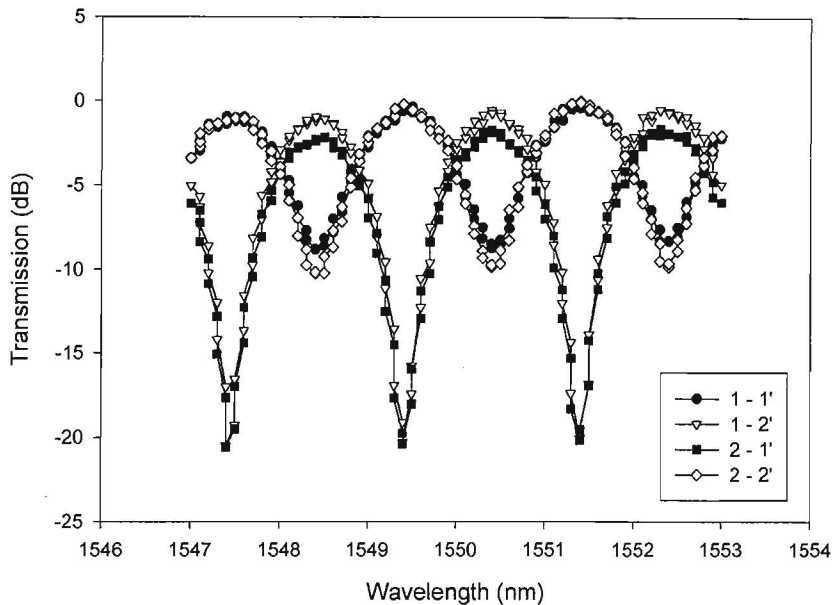


Figure 3. Measured transmission functions of an MZI-filter. The transmission functions for the cross-ports is given by the 1-2' and 2-1' curves. The two remaining curves are from the bar ports.

The free spectral range (FSR) was measured to be 2 nm which is in excellent agreement (within the experimental accuracy of 0.05 nm) with the designed value.

The cross-talk for the bar-ports is -10 dB and for the cross-ports it is -20 dB.

The devices could be thermo-optically tuned over several FSR's. With a heating power of 0.8 W the device was tuned over one FSR, giving a tuning sensitivity of 0.4 W/nm (for a non-optimised heater design). The heaters were found to have a resistance of 120 Ω which is significantly larger than designed.

Discussion

The different values of the cross-talk as measured at the cross and bar output ports respectively are somewhat unexpected at first. A possible asymmetry in the MMI-couplers would reduce the attainable cross-talk, but this would affect both outputs to the same degree. The same holds for asymmetric input to the output-MMI, caused by different optical attenuation in the channels forming the interferometer branches. It can be shown however, that the simultaneous occurrence of both MMI asymmetry and different channel attenuation can explain the measured effect. Calculations show that an asymmetry in the power distribution of the MMI of 40/60 and a power balance at the input of the output MMI of 30/70 would explain the measured cross-talk of -20 dB at the cross-port and -10 dB at the bar port. The theoretical transfer functions for an otherwise loss-less device is shown in figure 4.

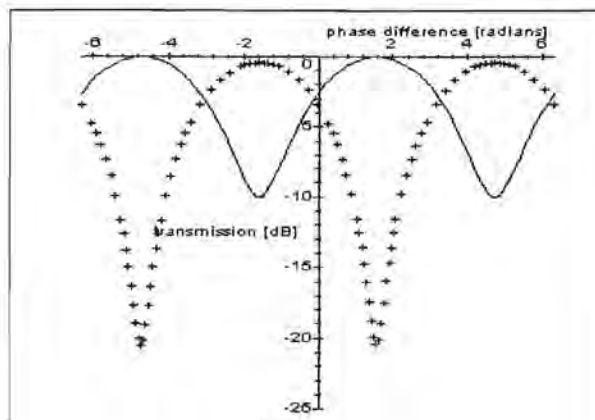


Figure 4. Theoretical transfer functions of MZI wavelength filter with both asymmetrical MMI (power imbalance 40/60) and unequal attenuation in the interferometer channels (power imbalance 30/70).

Although the required imbalance for explaining this behaviour is quite large, measurements on separate MMI's confirmed an imbalance of approximately 40/60. The channel attenuation necessary for arriving at the large power imbalance at the input of the second MMI is however unrealistically large.

Conclusion

Operation of a device with about -20 dB cross-talk in the cross state has been demonstrated. The difference in measured cross-talk for the bar state could be theoretically explained with asymmetry of the MMI-couplers and channel attenuation.

The FSR of 2 nm was measured to be in excellent agreement with the designed value.

The device could be thermo-optically tuned over several FSR's with a tuning power of 0.4 W/nm.

Acknowledgement

We would like to thank Lucy Hilderink and Peter Linders for their assistance in the fabrication of the devices and Erwin Rijkers for help with the experimental set-up.

References

- [1] Verbeek et al., "Integrated four-channel Mach-Zehnder multi/demultiplexer fabricated with phosphorous doped SiO₂ waveguides on Si", *J. Lightwave Technol.*, vol. 6, pp. 1011-1015, (1988).
- [2] Takato et al., "128-channel polarization-insensitive frequency-selection-switch using high-silica waveguides on Si", *IEEE Photonics Technol. Lett.*, vol. 2, pp. 441-443, (1990).
- [3] K. Wörhoff et al., "Application of silicon oxynitride in telecommunication devices", *in these proceedings*.

A COMPACT INTEGRATED SINGLE PHASAR OPTICAL CROSSCONNECT ON InP

C.G.P. Herben, C.G.M. Vreeburg, D.H.P. Maat*, X.J.M. Leijtens, Y.S. Oei,
F.H. Groen*, J.J.G.M. van der Tol*, P. Demeester#, and M.K. Smit

Faculty of Electrical Engineering, Delft University of Technology, PO Box 5031,
NL-2600 GA, Delft, The Netherlands, herben@et.tudelft.nl

*Research Group for Optics, Delft University of Technology, The Netherlands

*KPN-Research, Royal PTT Netherlands N.V., Leidschendam, The Netherlands

#University of Gent-IMEC, Department of Information Technology, Belgium

We report the first InP-based integrated optical crossconnect. The device can crossconnect signals at four wavelengths independently from two input fibers to two output fibers. Total on-chip loss is less than 13 dB. Device size is $7 \times 9 \text{ mm}^2$.

I. Introduction

Wavelength selective switches such as optical crossconnects (OXC's) and add-drop multiplexers (ADM's) play a key role in advanced WDM-networks [1]. Devices presently used in network experiments are assembled from a large number of discrete components, which makes them costly and voluminous. Integration will be necessary to reduce both cost and volume. First integrated wavelength selective switches reported were based on silica technology [2]. We have reported the first reconfigurable InP-based ADM [3]. This device showed good loss and crosstalk properties, but it was not polarization independent. To obtain a polarization independent wavelength selective switch both the PHASAR and the switches have to be insensitive to the polarization.

In this paper we report the first integrated InP-based polarization-independent crossconnect. The device, which can crossconnect signals at four wavelengths independently from two input fibers to two output fibers, has been realized by integrating a polarization dispersion compensated 16×16 PHASAR as reported by Vreeburg [4] with four polarization independent Mach-Zehnder Interferometer switches. Experimental results are found to be in good agreement with simulation results obtained with an advanced photonic circuit simulator [8].

II. Design

The OXC consists of a single 16-channel polarization dispersion compensated PHASAR [4] and four Mach-Zehnder Interferometer space switches connected in a fold-back configuration. The 2×2 electro-optical Mach-Zehnder Interferometer switches have phase sections orientated 28° from the [011]-direction (perpendicular to the small flat of the wafer) towards the [011]-direction to obtain polarization independent

operation. In Fig. 1 the layout of the device is depicted. The channel spacing is 400 GHz (3.2 nm) and the device size is $8.5 \times 6.4 \text{ mm}^2$.

The fold-back configuration using a single PHASAR has been chosen to avoid additional losses caused by misalignment of the wavelength responses of the demultiplexer and the multiplexer due to non-uniformities of the wafer. Small thickness and composition non-uniformities will change the central wavelength of the PHASAR, a 2% variation in the layer-thicknesses results in a shift of the central wavelength of a few tenths of a nanometer, yielding a loss penalty of 1 dB [7].

III. Fabrication

The PHASAR was fabricated in a MOVPE grown layer stack as shown in Fig. 1. A 100 nm thick PECVD-SiN layer served as an etching mask for the waveguides. The pattern was defined using contact illumination with positive photoresist and transferred in the SiN-layer by CHF_3 reactive ion etching. The waveguides were etched employing an optimized CH_4/H_2 etching and O_2 -descumming process [6]. After removal of the SiN-layer, metallisation windows in photo-sensitive polyimide were made on the phase shifting sections of the switches. TiAu contacts on top of the phase shifting sections are fabricated by vacuum evaporation and lift-off with image reversal photo-resist. The PHASAR has been made polarization independent by removing part of the top-layer of the waveguides in the triangular birefringence compensation section (see Fig. 1) down to a Q(1.3) etch stop layer using a selective etch ($\text{HCl}:\text{H}_3\text{PO}_4=1:4$). After removal of photo-resist the wafer processing was finished.

IV. Experiments and Simulations

The OXC was measured using the spontaneous emission spectrum of an EDFA as a broadband light source and a polarizer to select the polarization. Light was coupled in the chip by using microscope objectives, coupled out of the waveguides by a single mode tapered fiber and analyzed using an optical spectrum analyzer. Straight reference waveguides with a width of 3 μm showed a propagation loss of 1.5 dB/cm.

Figure 2 shows the measured polarization independent response of the OXC. The total on-chip loss is only 13 dB for TE and 16 dB for TM-polarization. It is composed as follows: PHASAR (which is passed twice) 2x3 dB (2x3.5 dB), MZI-switch 1.5 dB (2.5 dB), crossings 6x0.2 dB, 3 cm waveguide 3x1.5 dB/cm (3x1.7 dB), (Values between brackets are for TM-polarization). The inter-band crosstalk level is low: <-40 dB indicating good performance of the PHASAR.

The main problem in the performance is the high intra-band crosstalk level of -13 dB. We analyzed the background of this crosstalk using the recently developed 16x16 PHASAR simulation module of our photonic circuit simulator [8]. With this tool, which is based on HP's Microwave Design System (MDS) we analyzed a number of different crossconnect configurations, two of which are shown in Fig. 3. In the simulations we used a conservative crosstalk value of -20 dB for the PHASARs and a state-of-the-art value of -40 dB for (dilated) switches. The figure shows a great difference in performance. Analysis of the results reveals that in configuration A the crosstalk consists of three main contributions; one from the switch, one from the multiplexer (pass 1) and one from the demultiplexer (pass 2). Because all signals are routed through the same PHASAR they will interfere with each other, which is visible in the oscillating character of the response. In configuration B the crosstalk is drastically reduced by

applying two 8x8 PHASARs. In this configuration each crosstalk contribution contains only the switch crosstalk or at least twice the PHASAR-crosstalk, which leads to much better results.

Fig. 4 shows the measured and simulated results for TE-polarization, using a value of -20 dB for the switch crosstalk, which is typical for our single-stage devices. It is seen that the coherent interference increases the predicted crosstalk of -20 dB to -16 dB.

V. Discussion and Conclusions

A polarization independent integrated four-channel 2x2 crossconnect on InP is reported. This integrated OXC is realized using a single low-loss polarization dispersion compensated PHASAR [4] and Mach-Zehnder Interferometer electro-optical switches with special oriented phase shifting sections [9] to cancel the polarization dependence of earlier designs [5]. The use of a single PHASAR both as demultiplexer and multiplexer was chosen to avoid loss penalties originating from misaligned wavelength responses of separate (de)multiplexers. Simulations show that this configuration results in a crosstalk penalty. Simulations predict a much better performance using two 8x8 PHASARs in stead of a single 16x16 one.

VI. Acknowledgments

This work was partly supported by the ACTS AC-065 project BLISS. Anja Suurling and Adrie Looyen are acknowledged for EBPB mask fabrication and vacuum evaporation, respectively.

VII. References

1. C. Brackett, A. Acampora, J. Sweitzer, G. Tandon, M. Smith, W. Lennon, K. Wang, and R. Hobs, "A scalable multiwavelength multihop optical network: a proposal for research on all-optical networks," *IEEE J. of Lightwave Technol.*, vol. 11, no. 5/6, pp. 736-753, 1993.
2. K. Okamoto, M. Okuno, A. Himeno, and Y. Ohmori, "16-channel optical add/drop multiplexer consisting of arrayed-waveguide gratings and double-gate switches," *Electron. Lett.*, vol. 32, no. 16, pp. 1471-1472, 1996.
3. C. Vreeburg, T. Uitterdijk, Y. Oei, M. Smit, F. Groen, E. Metaal, P. Demeester, and H. Frankena, "First InP-based reconfigurable integrated add-drop multiplexer," *IEEE Photon. Technol. Lett.*, vol. 9, no. 2, pp. 191-193, 1997.
4. C. Vreeburg, C. Herben, X. Leijtens, M. Smit, F. Groen, J. van der Tol, and P. Demeester, "An improved technology for eliminating polarization dispersion in integrated PHASAR demultiplexers," *Proc 23rd Eur. Conf. on Opt. Comm. (ECOC '97)*, Edinburgh, UK, pp. 3.83-3.85, 1997.
5. T. Uitterdijk, D. Maat, F. Groen, H. van Brug, C. Vreeburg, J. Pedersen, and I. Moerman "Dilated, polarisation insensitive InP-based space switch," *Proc. 8th Eur. Conf. on Int. Opt. (ECIO'97)*, Stockholm, Sweden, pp. 551-554, 1997.
6. Y. Oei, L. Spiekman, F. Groen, I. Moerman, E. Metaal, and J. Pedersen, "Novel RIE-process for high quality InP-based waveguide structures," *Proc. 7th Eur. Conf. on Int. Opt. (ECIO'95)*, Delft, The Netherlands, pp. 205-208, 1995.
7. N.N. Khrais et al., "Effect of cascaded misaligned optical (de)multiplexers on multiwavelength optical network performance," *OFC/IOOC '96 Technical Digest*, San Jose USA, pp. 220-221, 1996.
8. X.J.M. Leijtens, P. Le Lourec, and M. Smit, "S-matrix oriented CAD-tool for simulating complex integrated optical circuits," *IEEE J. on Selec. Topics in Quant. Electron.*, vol. 2, no. 2, pp. 257-262, 1996.
9. R. Krähenbühl, R. Kyburz, W. Vogt, M. Bachmann, T. Brenner, E. Gini, and H. Melchior, "Low-loss polarization insensitive InP/InGaAsP optical space switches for fiber optical communication," *IEEE Photon. Technol. Lett.*, vol. 8, no. 5, pp. 632-634, 1996.

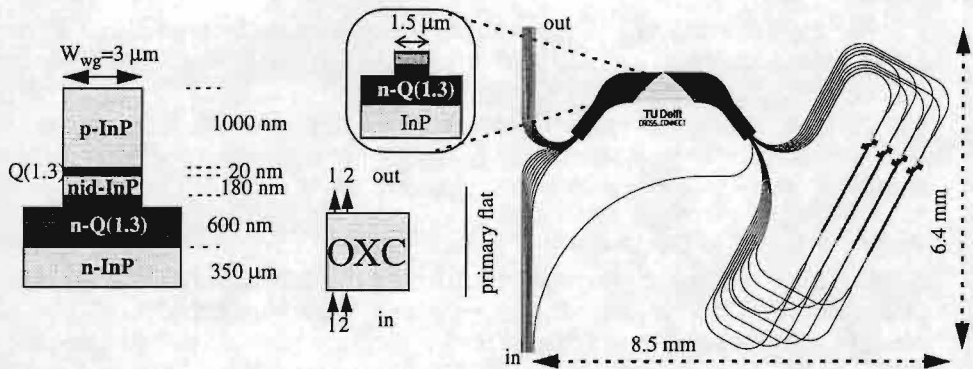


Fig. 1. Layout of the OXC and dimensions of the waveguide structures used.

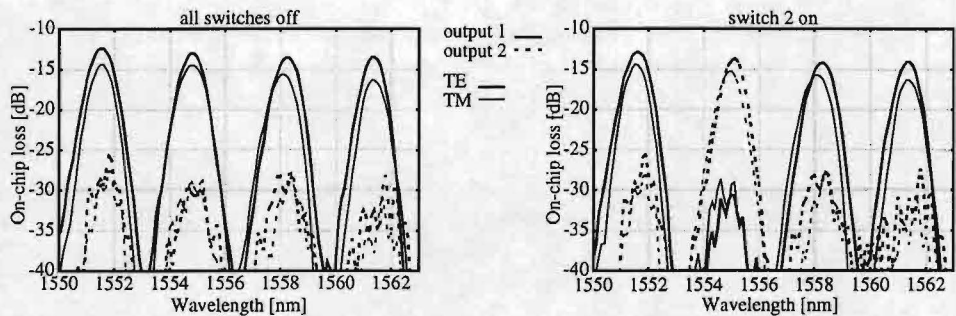


Fig. 2. Measured polarization independent response with all switches off (left) and with switch 2 on (right)

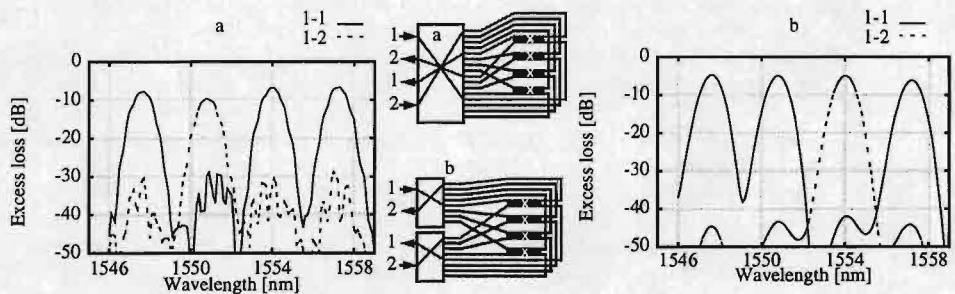


Fig. 3. Simulated response with a) single PHASAR and b) two PHASARs using dilated switches.

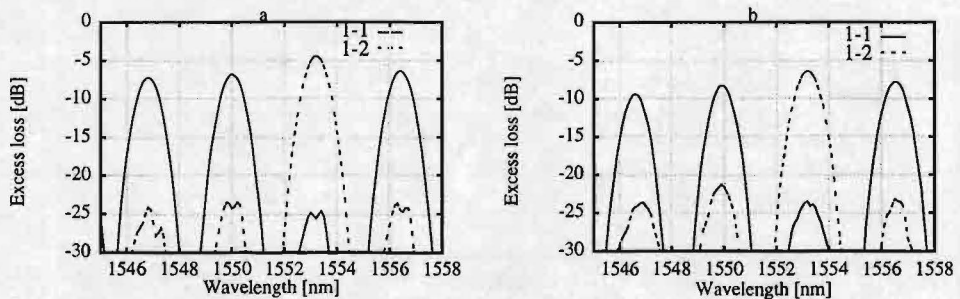


Fig. 4. Response of the OXC with switch 3 on, a) simulated and b) measured.

Monolithic integration using selective area Chemical Beam Epitaxy

C.A. Verschuren^{a*}, P.J. Harmsma^b, Y.S. Oei^b, M.R. Leys^a, H. Vonk^a and J.H. Wolter^a

COBRA Inter-University Research Institute, P.O. Box 513, 5600 MB Eindhoven, the Netherlands

^a Eindhoven University of Technology, Department of Physics

^b Delft University of Technology, Department of Electrical Engineering

* phone: +31 40 2474872; fax: +31 40 2453587; e-mail: c.a.verschuren@phys.tue.nl

We present our recent results on the lateral butt-coupling of InP/InGaAs MQW waveguides using selective area CBE, with coupling losses as low as 0.2 dB/interface for both [011] and [01 $\bar{1}$] directions.

1. Introduction

The fabrication of monolithic InP-based Photonic Integrated Circuits (PIC) operating at 1.55 μm is increasingly important for applications such as WDM networks. An attractive way for the production of such PICs is embedded selective area epitaxy. Using CBE, high quality structures can be grown in the (Ga,In)(As,P) materials system at low temperatures (500-530 $^{\circ}\text{C}$) [1]. This is an advantage for multiple step epitaxy. Moreover, by masking the substrate with a SiN_x pattern, growth is restricted to the uncovered areas of the wafer with perfect selectivity and very good uniformity, which is independent of the mask design [2]. Thus, by localized growth in etched recesses, different vertically aligned structures with lateral butt-couplings can be realized on a single InP chip, combining freedom in device design with an optimal overlap of the optical modes. These lateral couplings are the regions of interest with respect to the complex growth behaviour, the optical properties and the resulting coupling loss. Here, we present our results on integrated InP/InGaAs multiple quantum well (MQW) structures.

2. Experimental procedure

In the first epitaxy step, an MQW waveguide is grown on a 2" (100) InP substrate, 0.5 $^{\circ}$ misoriented towards (111)B. The waveguiding core consists of 60 periods of 2-3 nm lattice matched $\text{Ga}_{0.47}\text{In}_{0.53}\text{As}$ quantum wells and 6 nm InP barriers, resulting in a room temperature photoluminescence at 1350-1400 nm. The top cladding layer of InP is 300 to 800 nm. After PECVD deposition of 100 nm SiN_x , a mask pattern, illustrated in fig. 1, is defined by photolithography on quarter wafers. The windows have lengths ranging from 100 to 900 μm , in steps of 200 μm and are aligned either in the [011] or the [01 $\bar{1}$] direction. Using an alternate CH_4/H_2 : Q RIE process [3], recesses are etched in the windows, through the WG core and about 200 nm into the InP buffer. After cleaning, the sample is briefly etched in diluted $\text{Br}_2/\text{CH}_3\text{OH}$, which gives a slight underetch below

the SiN_x mask. If properly applied, this prevents the formation of so-called 'ears'. In the second growth step, the recesses are filled with a similar WG structure using identical CBE growth conditions as for the original structure. Following the regrowth, 10 nm long waveguide stripes of 2 - 4 μm width are defined in SiN_x for Fabry-Perot transmission measurements. As indicated by the dashed lines in fig. 1, each stripe runs through 1 to 4 regrown recesses, i.e. the number of lateral interfaces is from 2 to 8. Also, reference WG stripes are defined, which only run through the original material. The stripes are then used to etch shallow WG ridges, 100 nm into the core.

3. Results

3.1 Waveguide substrates

Our 60 period MQW waveguide structures show bright luminescence and a high material quality, as indicated by e.g. the 4K PL linewidth of 7 to 9 meV and mirror-like morphology with low defect density. Similar structures grown on exactly oriented or 2° towards (110) misoriented (100) substrates either show numerous defects or broader PL (17-20 meV) and rougher morphology. As discussed in [4], the presence of the chemically active B type surface steps strongly reduces the number of defects, whereas the simultaneous presence of A type steps easily gives rise to a roughening of the surface. Based on these results we selected a misorientation of 0.5° towards (111)B.

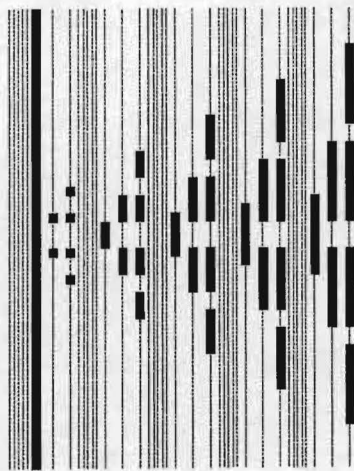


Fig. 1. Mask layout for regrowth (rectangles) and waveguide definition (dashed lines).

3.2 Integration results

Fig. 2 shows cross-sectional views of the integrated waveguides in both perpendicular

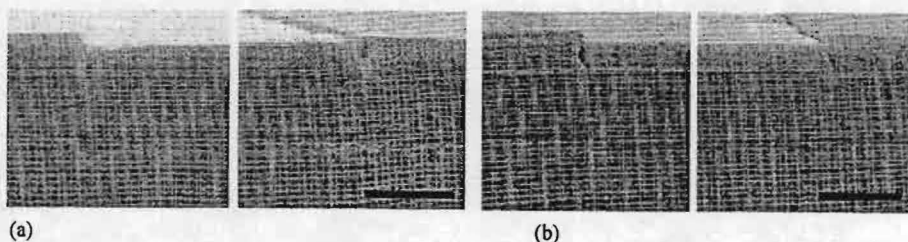


Fig. 2. SEM cross-section of WG-WG integration looking on a) (01T), b) (011). The bar indicates 1 μm .

directions. The regrown waveguide is in the middle, the nitride layer (dark) on top of the original waveguide is still present. It is clear that in both cases the vertical alignment and the flatness of the layers is excellent. The absence of air gaps and a transition over only about $0.1 \mu\text{m}$ suggest low coupling loss at the lateral interfaces. Although surface diffusion and incorporation are slow in the $[011]$ direction, the coupling in fig. 2.a (along $[011]$) looks surprisingly good. In the perpendicular $[0\bar{1}1]$ direction, the combination of fast surface diffusion and chemically active B type steps helps to compensate shadowing effects of the chemical beams at the recess side walls [4]. Therefore, the coupling in fig. 2.b looks somewhat better.

The slight asymmetry that can be seen in fig. 2.b is inevitable due to the 0.5° towards $(111)\text{B}$ substrate misorientation. However, when higher misorientation angles are used or misorientations containing also A type steps, this asymmetry becomes much more pronounced [5]. Then, the formation of large air gaps and/or discontinuous layers can be prevented only under a narrow range of growth conditions (see e.g. [2]).

In order to check the material properties, a spatially resolved PL (SRPL) setup was used with an Ar^+ laser focused to a spot of about $5 \mu\text{m}$ and a He-flow cryostat which can be moved by two stepping motors with $0.1 \mu\text{m}$ step resolution. For the original WG we find no degradation or shift of the optical properties after regrowth. Both PL position and linewidth are the same within the experimental error of about 1 nm . The regrown material has PL intensities and linewidths which are uniform over the wafer and are comparable to that grown on $2''$ epi-ready substrates.

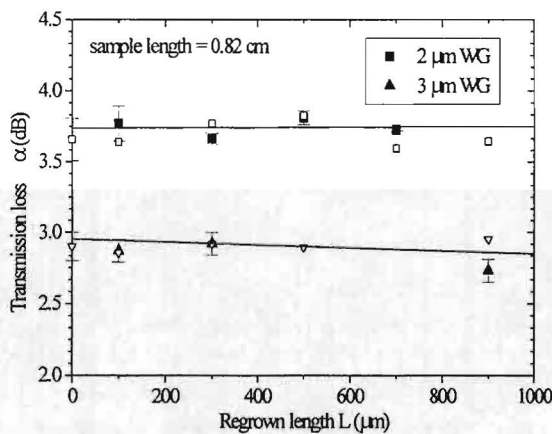


Fig. 3. Waveguide transmission loss versus the length of the regrown area (closed symbols). The open symbols represent the corresponding reference waveguides. The solid lines are linear fits to the data.

which can be achieved by varying the length of the regrown part of the waveguide ridge. Extrapolating the measured transmission loss to a length of zero, and subtracting the reference's transmission loss, yields the loss due to the lateral interfaces only.

Using a Fabry-Perot setup, the transmission loss at 1530 nm (TE polarization) was measured for all waveguide ridges. Fig. 3 shows the results for the sample in fig. 2.a

For the feasibility of PICs, the signal loss due to the lateral coupling of devices must be sufficiently low. This coupling loss (dB) can be obtained by processing the regrown wafer into waveguide ridges and measuring the transmission loss for both reference and partly regrown waveguides. For accurate and straightforward measurements only passive structures should be used. Additionally, the influence of a difference in material propagation loss must be eliminated,

with coupling in the $\langle 011 \rangle$ direction. It is clear that the loss values for both reference and regrown waveguides are equal within the accuracy of the experiment. This yields a *maximum* coupling loss as low as 0.1 ± 0.04 dB/interface. For two samples with coupling along $\langle 01\bar{1} \rangle$ somewhat higher values of 0.18 ± 0.02 and 0.3 ± 0.1 dB/interface are found. In both cases this is due to accidental technological imperfections, as confirmed by SEM and a deconvolution analysis of SRPL scans over the lateral couplings. However, these results show that coupling losses around 0.1 dB/interface can be reproducibly achieved in both crystallographic directions.

4. Conclusions

We have investigated the monolithic integration of passive MQW structures by selective area Chemical Beam Epitaxy. Our results show that using $0.5^\circ - (111)\text{B}$ misoriented (100) InP substrates instead of the 'standard' $2^\circ - (110)$ wafers significantly improves both material properties and lateral integration. Moreover, successful regrowth is obtained under identical growth conditions as for planar growth, with the same morphological and PL quality. SEM and Fabry-Perot measurements reveal very good coupling results with excellent uniformity in both perpendicular crystallographic directions. Loss values around 0.1 dB/interface can be realized for both $\langle 011 \rangle$ and $\langle 01\bar{1} \rangle$ directions, which is extremely attractive for applications in the integration of photonic devices.

Acknowledgements

This work was financially supported by the Dutch Ministry of Economic Affairs (IOP) and the ACTS programme of the European Union. Special thanks to Geraldine O'Donovan for carrying out the spatially resolved photoluminescence measurements.

References

- [1] R.T.H. Rongen, M.R. Leys, P.J. van Hall, C.M. van Es, H. Vonk and J.H. Wolter, "Investigations on Indium Phosphide grown by chemical beam epitaxy", *J. Electron. Mater.* 24, 1391-1398, 1995.
- [2] M. Wachter, U. Schöffel, M. Schier and H. Heinecke, "Lateral coupling of InP/GaInAsP/InP structures by selective area MOMBÉ", *J. Cryst. Growth* 175/176, 1186-1194, 1997.
- [3] Y.S. Oei, C. van Dam, F.P. van Ham, L.H. Spiekman, B.H. Verbeek, F.H. Groen, E.G. Metaal and J.W. Pedersen, in *Proc. 18th State of the Art Program on Compound Semiconductors*, 134-138, 1993.
- [4] C.A. Verschuren, M.R. Leys, Y.S. Oei, C.G.M. Vreeburg, H. Vonk, R.T.H. Rongen and J.H. Wolter, "Surface morphology of InP/InGaAs in selective area growth by chemical beam epitaxy", *J. Cryst. Growth* 170, 650-654, 1997.
- [5] C.A. Verschuren, M.R. Leys, Y.S. Oei, P.J. Harmsma, H. Vonk and J.H. Wolter, "On the influence of surface steps on the (a)symmetry in InP Selective Area Chemical Beam Epitaxy", in *Proc. EWMOPVE VII*, Berlin, Germany, 1997.

Experimental demonstration of "GIRO-gratings"

S. Goeman, B. Dhoedt, K. Caekebeke, S. Verstuyft, R. Baets, P. Van Daele

N. Nieuborg*, J. Stiens**, H. Thienpont*, R. Vounckx**

Department of Information Technology (INTEC), University of Ghent-IMEC,
Sint-Pietersnieuwstraat 41, B-9000 Gent, Belgium

Tel: +32 9 264 3316

Fax: +32 9 264 3593

e-mail: goeman@intec.rug.ac.be

*Department of Applied Physics, Vrije Universiteit Brussel,
Pleinlaan 2, B-1050 Brussels, Belgium

**Electronics Department, Laboratory for Microelectronics and Technology,
Vrije Universiteit Brussel, Pleinlaan 2, B-1050 Brussels, Belgium

Abstract

This paper presents the first experimental result of the GIRO-principle (Giant Reflectivity to 0 order) of a semiconductor-air diffraction grating with high TM reflectivity and low TE reflectivity under normal incidence, as predicted by theory.

1.Introduction

Diffraction optics, and in particular the field of sub-wavelength gratings[1], is gaining importance for the fabrication of new optical components. In [2] we proposed a new concept for a special linear sub-wavelength grating, called GIRO-grating (Giant Reflectivity to 0 order), with high reflectivity, upon normal incidence from the high refractive index material side, for TM polarization and low reflectivity for TE polarization. In [2] we have proposed that such structures can be used as a mirror in VCSELs. In section 2 of this paper we will shortly discuss the working principle and design rules of these gratings while section 3 presents experimental demonstration of the GIRO principle for gratings designed in the wavelength region of a tunable CO₂-laser (9-11 μm).

2.Grating Design

In the first part of this section, the working principle and the design rules of these GIRO-gratings will be explained. Fig.1 shows a surface relief grating between a high index material (n_1) and low index material (n_2). A plane wave is incident normal to the grating plane from the high index side. In general, due to diffraction in the grating layer, this plane wave can couple to the following waves: zero order in reflection[a], zero order in transmission[b], higher order in reflection[c], higher order in transmission [d] (fig.1). By a proper choice of the grating parameters (shape, filling factor f , period Λ , depth h) it is possible to cancel all unwanted orders thereby coupling all optical power to the zero order specular reflection. Thinking in terms of optical modes, we state that 2 modes(ψ_0 and ψ_2) exist in the grating region with approximate effective indices $n_{e,0} = \sqrt{n_1^2 - (\lambda / \Lambda)^2}$, $n_{e,2} \approx n_2$ and mode profiles as in fig.1. The zero order mode is highly concentrated in the material with refractive index n_1 and the second order mode is highly concentrated in the material with refractive index n_2

(fig.1). Expressing that the two modes interfere destructively at interface 2 and constructively at interface 1 and allowing a phase error φ at interface 2 (and consequently a phase error 2φ at interface 1) leads to following design rules[2]:

$$\text{Filling factor } f=50\%, \quad \frac{d}{\lambda} = \frac{3/2}{\sqrt{3n_1^2 + n_2^2 - n_2}}, \quad \frac{\Lambda}{\lambda} = \frac{2}{\sqrt{n_1^2 - n_2^2}}$$

In view of the approximations used to arrive at these design rules diffraction calculations were done, using a model based on RCWA[2][3], to predict the coupling of optical power to the zero order in reflection for TM- and TE-polarisation. Calculations were performed over a large grating period and depth region and the results are shown in fig.2. These figures show a large region of high TM reflectivity ($R>90\%$) while the TE reflectivity is much lower ($R<40\%$). This allows to obtain a high polarisation selectivity and high TM reflectivity with the same grating. Further optimising the grating design, taking into account limitations imposed by optical lithography, resulted in the following grating parameters: grating period= $6\mu\text{m}$, grating depth= $3\mu\text{m}$ and filling factor= 50% for the wavelength of $9.4\mu\text{m}$.

3.Experiment

These gratings have been fabricated in undoped GaAs using optical contact photolithography and subsequent reactive ion etching. Since we have to measure the grating reflectivity from the high refractive index material side, the samples were polished under a wedge angle to avoid multiple beam interference. This allows to measure the reflectivity of the polished interface and the grating interface, through the substrate, separately. By comparing these two measurements it is possible to determine the reflectivity of the grating itself.

Surface profile measurements based on optical interferometry and SEM pictures(fig.3) revealed that a duty cycle of 40% rather than 50% was achieved resulting in a reduced polarisation selectivity and a wavelength shift of the maximum TM reflectivity(fig.4).

Optical measurements are done with a CO_2 -laser tunable in the wavelength region of 9-11 μm . Fig.5 shows measurements for TE and TM polarization and a comparison with theoretical calculations. The theoretical calculations agree with the measurement within $\pm 5\%$, as indicated by the error bars. The measurements show a high TM reflectivity in excess of 90% for wavelengths around 9 μm . Over the entire wavelength region, the TM reflectivity remains 3 to 7 times higher than the TE reflectivity.

4.Conclusion

Based on simple design rules, we have fabricated GIRO-gratings for the wavelength region of 9-11 μm . Although the fabricated gratings differ from the designed gratings, we have demonstrated high TM reflectivity, in excess of 90%, and low TE reflectivity in agreement with the theory.

Acknowledgement

This work is partly funded by the European ACTS024-VERTICAL project and the Belgian DWTC-project IUAP-13. S. Goeman, N. Nieuborg and B. Dhoedt also acknowledge financial support of the Flemish IWT.

Reference

- [1] A. Vasara, M.R. Taghizadeh, J. Turunen, J. Westerholm, E. Noponen, H. Ichikawa, J.M. Miller, T. Jaakkola, S. Kuisma, "Binary surface-relief gratings for array illumination in digital optics", *Applied Optics*, vol. 31, no. 17, pp. 3320-3336, 1992
- [2] B. Dhoedt, S. Goeman, B. Demeulenaere, B. Baekelandt, D. De Zutter, and R. Baets, "GIRO gratings: a novel concept for mirrors with high reflectivity and polarisation selectivity", *Diffraction Optics and Micro-Optics*, post-deadline paper JTUB30, 1996
- [3] B. Dhoedt, "Theoretical and Experimental Study of Free-Space Optical Interconnections Based on Diffractive Lens Arrays", Ph.D dissertation, University of Ghent
- [4] M.G. Moharam, D.A. Pommet, E.B. Grann, T.K. Gaylord, "Stable implementation of the rigorous coupled-wave analysis for surface-relief gratings: enhanced transmittance approach", *J. Opt. Soc. Am. A*, Vol. 12, No. 5, pp 1077-1086, May 1995

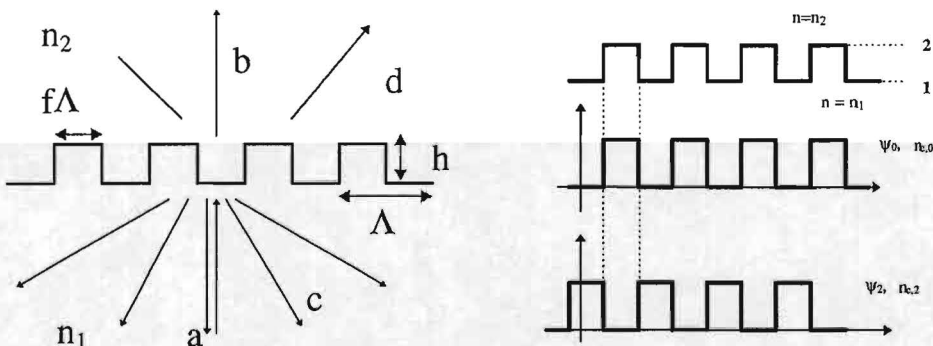


Fig.1: grating and grating parameters

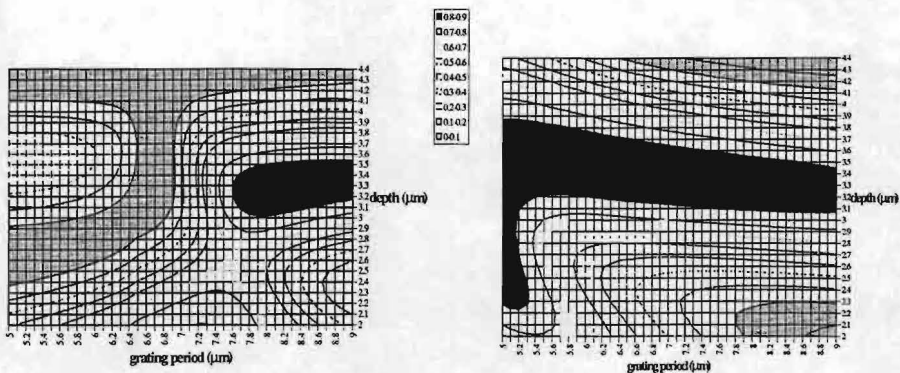


Fig.2: Contour plots of the zero-order TM-reflectivity (right) and TE-reflectivity(left) over a large grating depth(2μm-4.5μm) and period(5μm-9μm). High TM reflectivity regions ($R > 90\%$) and TE reflectivity regions ($R > 80\%$) are black while low TM reflectivity regions ($R < 20\%$) and TE reflectivity regions ($R < 10\%$) are gray.

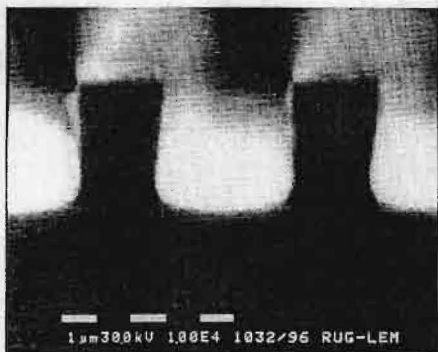


Fig.3: SEM picture of GIRO-grating test structure indicating a filling factor of 40%.

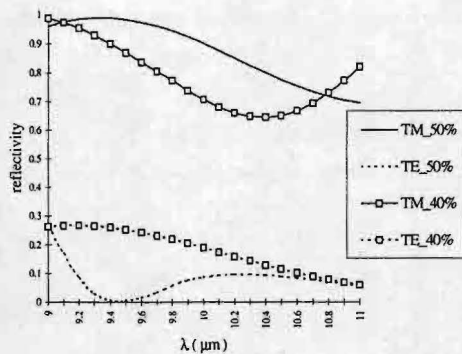


Fig.4: calculations of the TE and TM zero order reflectivity of the designed grating(TE_50%,TM_50%) compared with fabricated grating(TE_40%,TM_40%)

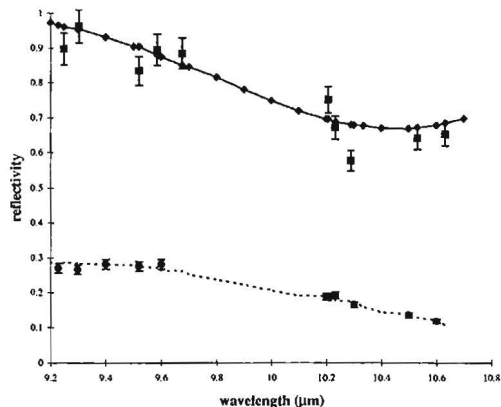


Fig.5: Comparison between measurements (TM,TE) and theoretical calculated reflectivities (theory_TM,theory_TE) for zero order TM and TE-polarisation

Polarization-dependent Saturation in Semiconductor Vertical-Cavity Lasers

M.P. van Exter, A. Al-Remawi, and J.P. Woerdman

Huygens Laboratory, Leiden University, P.O. Box 9504, 2300 RA Leiden, The Netherlands

We discuss how linear and nonlinear anisotropies affect the polarization fluctuations in a laser and apply this to semiconductor vertical-cavity lasers. We focus on the nonlinear anisotropies, or the polarization dependence of the optical saturation, which were demonstrated and quantified in three different experiments, via: (i) a nonlinear spectral redshift, (ii) an extra four-wave mixing peak in the optical spectrum, and (iii) correlations between the polarization fluctuations.

The polarization of light emitted by a laser is determined by its linear and nonlinear optical anisotropies. *Linear* anisotropies are independent of laser power; they usually originate from deviations from the ideal cylindrical symmetry of the optical cavity. *Nonlinear* anisotropies increase with laser power; they reflect the polarization dependence of optical saturation, or the fact that the saturation power can be quite different for linearly-polarized and circularly-polarized light.

The nominal cylindrical symmetry of most vertical-cavity surface-emitting laser (VCSELs) makes their optical polarization both interesting and fragile. In practical VCSELs the dominant anisotropy was found to be linear birefringence, caused by stress acting via the elasto-optic effect [1] and by internal electric fields acting via the electro-optic effect [2]. We have now measured the much weaker nonlinear anisotropies, or the polarization dependence of the optical saturation, using the polarization fluctuations of the laser light as a diagnostic tool.

The polarization of laser light is never 100 % pure; the polarization always fluctuates a little bit as spontaneous emission continuously perturbs the laser away from its equilibrium polarization. For many lasers the optical is approximately linearly polarized and the optical field can be written as $|\vec{E}|(\vec{e}_x - (\phi + i\chi)\vec{e}_y)e^{-i(\omega t + \varphi)}$. Polarization fluctuations come in two varieties: changes in the polarization angle $\phi(t)$ and changes in the ellipticity $\chi(t)$ ($\phi, \chi \ll 1$).

A study of the polarization fluctuations in principle allows one to separate the various linear and nonlinear anisotropies. To demonstrate this idea Fig. 1 shows the (hypothetical) noise-free evolution of the polarization state, for the most general class A laser. The shape of the dashed spiral contains all anisotropies: its rotation rate is a measure for the combined linear and nonlinear birefringence $\Delta\nu$, or the frequency difference between x- and y-polarized emission; its "shrinkage rate" is a measure for the combined dichroism, or polarization preference; finally, the flattening or elliptical shape of the spiral shows the presence of a counter-rotating term and is solely due to nonlinear anisotropies.

The experiments were performed on proton-implanted $\text{Al}_x\text{Ga}_{1-x}\text{As}$ quantum-well VCSELs operating at a wavelength of 850 nm. Nonlinear anisotropies were observed in three different experiments, the results of which are summarized as Figs. 2, 3 and 4.

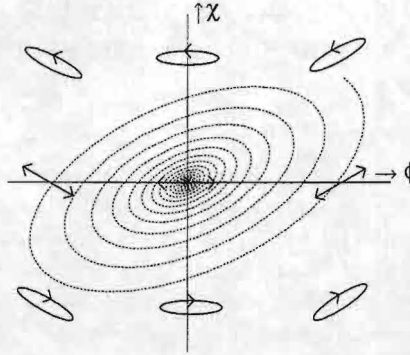


FIG. 1. Polarization fluctuations around the equilibrium x -polarized state can be presented by a time trace $(\phi(t), \chi(t))$, where $\phi(t)$ represent the polarization direction and $\chi(t)$ the ellipticity

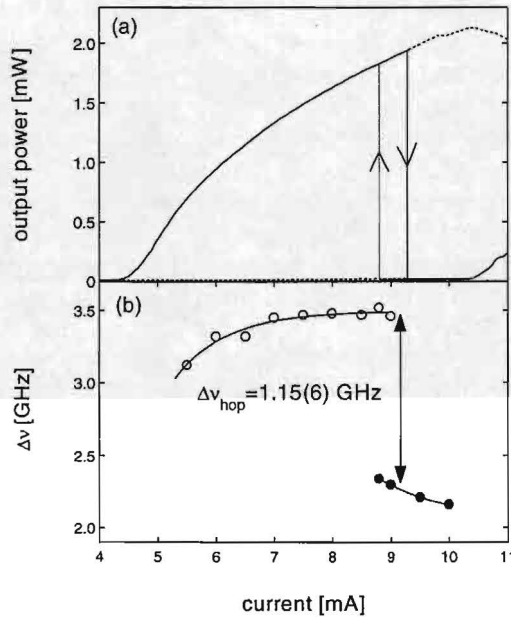


FIG. 2. Polarization-resolved output power (Fig. 2a) and effective birefringence $\Delta\nu$ (Fig. 2b) as a function of current. At low current the emission is dominantly x -polarized (solid curve, open circles); at higher currents the laser switches to y -polarized emission (dashed curve, dots). Note the sudden change in $\Delta\nu$ at the polarization switch.

The first manifestation of nonlinear anisotropies comes from a study of the optical spectrum. Figure 2a shows the (polarization-resolved) output power of one of our VCSEL as function of input current (solid and dashed curves for x - and y -polarization). At $I \approx 9$ mA this VCSEL exhibits a polarization switch, as the dominant polarization suddenly switches

from x to y . Fig. 2a shows that the optical output was not perfectly linearly polarized, but contained typically 1 % in the orthogonal polarization, as a result of formentioned polarization fluctuations. In the optical spectrum these fluctuations show up as a weak y -polarized spectral peak, which is shifted and broadened with respect to the dominant x -polarized peak [3]. Figure 2b shows how the frequency splitting $\Delta\nu$ (measured with a planar Fabry-Perot interferometer) changed as a function of current. When the laser polarization switched, $\Delta\nu$ was found to jump from 3.45 GHz for dominant x -polarized emission to 2.30 GHz for dominant y -polarized emission. We attribute this change to the nonlinear contribution to the birefringence, which is expected to change sign upon a polarization switch.

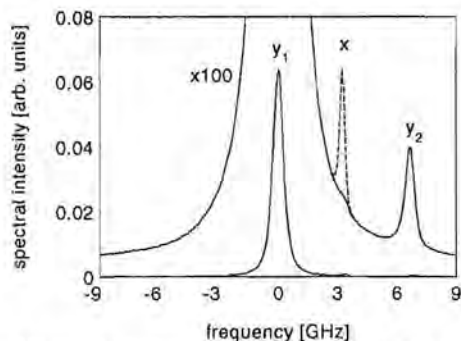


FIG. 3. A detailed view of the optical spectrum at $I = 9.0$ mA. The symbols denote the suppressed lasing mode (x), the nonlasing mode (y_1), and the FWM peak (y_2).

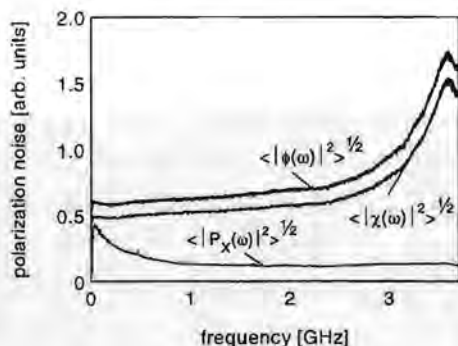


FIG. 4. The frequency-dependent intensity and polarization noise (see text)

The second manifestation of nonlinear anisotropies is an additional four-wave mixing peak in the optical spectrum. This is demonstrated in Fig. 3, which gives a detailed view of the optical spectrum at $I = 9.0$ mA. The x -polarized lasing mode (peak x), which by itself peaks at 40 on this scale, was suppressed to about 10^{-5} for the dashed curve (to serve as a frequency marker) and to less than 10^{-6} for the solid curves. The 100x magnification clearly shows the presence of a weak FWM peak (peak y_2), being the mirror image of the usual "nonlasing" peak (peak y_1). The relative strength of this FWM peak y_2 , as compared to the

other y -polarized peak y_1 , was 0.6 %. The FWM peak is intimately related to the flattening of the spiral sketched in Fig. 1; it is the counter-rotating component that together with the co-rotating “nonlasing” mode produces the flattening of the spiral.

As a third manifestation of nonlinear anisotropies we have compared the fluctuations in the polarization direction and ellipticity of the emitted light. Experimentally this was done by passing the light through a (rotateable) $\lambda/4$ plate and polarizer, to project onto a (selectable) polarization state, and by measuring the intensity fluctuations in that projection with a fast photodiode and RF-analyzer. The $\lambda/4$ plate and polarizer allow projections on any polarization state, so that we can observe fluctuations in $\phi(t)$ or $\chi(t)$ or any combination of the two. The lower curve in Fig. 4 shows the noise spectrum for projection, with a polarizer only, onto the dominant x -polarization, so that we observe the intensity noise in the x -polarization, $\langle |P_x(\omega)|^2 \rangle > \frac{1}{2}$. The upper and middle curve show the noise spectrum for projection onto the $x + y$ (45° linear) and $x + iy$ (circular) polarization, respectively. As the noise level in the mixed projections is much larger than that in the x -projection, the extra noise must originate from *polarization* instead of *intensity* fluctuations. The fact that the fluctuation in the polarization direction (upper curve) are large than those in the ellipticity (middle curve) is our third proof for the existence of nonlinear anisotropies in VCSELs.

In conclusion we have demonstrated the existence of nonlinear anisotropy in VCSELs using a detailed study of the polarization fluctuations as a diagnostic tool. From Figs. 2, 3 and 4 we have deduced the strength of the nonlinear anisotropies, via respectively: (i) the observed frequency jump, (ii) the relative strength of the FWM peak, and (iii) the anisotropy of the polarization noise. We compare these results with a simplified version of the model of San Miguel et al. [4], from which the spin dynamics has been adiabatically eliminated. [5] This elimination reduces the polarization dynamics of a VCSEL to that of a class A (gas) laser [6], and allows for simple analytic solutions. Within experimental errors the three measurements gave the same results. At an output power of 2 mW, the strength of the nonlinear anisotropy was found to be about 0.5 GHz, to be compared with a linear birefringence of typically $\nu_0 \approx 10$ GHz. This shows that VCSEL have a mild intrinsic preference for linearly-polarized emission, the saturation power for linearly-polarized light being only about 1 % larger than for circularly-polarized light. The spin dynamics must therefore be very fast; we estimate that the spin flip rate Γ (normalized to the inversion decay rate) is a few 100. In hindsight this validates the adiabatic elimination of the spin dynamics.

-
- [1] A.K. Jansen van Doorn, M.P. van Exter, and J.P. Woerdman, Appl. Phys. Lett. **69**, 1041 (1996).
 - [2] M.P. van Exter, A.K. Jansen van Doorn, and J.P. Woerdman, Phys. Rev. A. **56**, 845 (1997).
 - [3] A.K. Jansen van Doorn, M.P. van Exter, A.M. van der Lee, and J.P. Woerdman, Phys. Rev. A. **55**, 1473 (1997).
 - [4] M. San Miguel, Q. Feng, and J.V. Moloney, Phys. Rev. A **52**, 1728 (1995).
 - [5] M.P. van Exter, R.F.M. Hendriks, and J.P. Woerdman, submitted to Phys. Rev. A.
 - [6] W. Van Haeringen, Phys. Rev. **158**, 256 (1967).

Self-Pulsation and Mode-Locking in Narrow Stripe Lasers

J. L. A. Dubbeldam, and D. Lenstra

*Department of Physics and Astronomy, Vrije Universiteit
De Boelelaan 1081, 1081HV Amsterdam*

Abstract

We give a new explanation of self-sustained pulsation phenomena as the envelope of many mode-locked pulses. By starting with the round-trip equations and making suitable identifications between the mode-locking and narrow stripe laser equations, we show that it is possible to map in some approximate sense the evolution equations describing the narrow stripe laser on the mode-locking evolution equations. The self-pulsations show up as relaxation oscillations of the pulse energy, having a sub-structure on the round-trip time scale that arises from the mode-locking mechanism.

Self-sustained pulsation phenomena were first observed in degraded lasers. It was always considered to be a non-profitable characteristic of these devices, but later it turned out to be a useful feature in e.g. CD-players. Narrow stripe lasers also show this self-pulsating behavior. It is possible to produce stable self-pulsations with these devices, which can be used to reduce noise in injection lasers. Although, rate-equation models predicting the self-pulsations exist, a more physical explanation of the self-pulsations is still lacking. Since self-sustained pulsations can also be obtained in structures with an unpumped region in the longitudinal direction of the laser, which then acts as a saturable absorber, the connection with saturable absorber mode-locking is tempting. In Fig. 1 the models are shown schematically. The gain is pumped by a positively biased DC voltage in both models and in the Haus model there is the additional possibility to apply a negatively biased DC voltage to the saturable absorber.

The mode-locking model we will consider was first put forward by Haus [1]. In the case of stable mode-locking the model, which we modified by introducing a finite absorber relaxation time [3], predicts short pulses of about 1 ps, in agreement with experiment. In the mode-locking model only the temporal profile is assumed to be relevant. The equation that describes

the pulse envelope (a_n) after n round-trips is given by

$$a_{n+1}(t) = a_n(t) + QG_T(t)a_n(t) + Q\frac{1}{\omega_C^2}\frac{d^2}{dt^2}a_n(t) \quad (1)$$

where Q is the total loss due to the finite reflectivity of the end mirrors, and the gain and absorption coefficients are defined relative to Q . The net gain $G_T(t)$ is defined by

$$G_T(t) = g(t) - q(t) - 1 \quad (2)$$

Here $q(t)$ models the saturable absorber, which is time dependent, since it saturates during passage of the pulse. Its time evolution is modeled by the rate equation

$$\frac{dq}{dt} = -\frac{q(t) - q_0}{T_a} - \frac{|a(t)|^2}{E_{A,sat}}q(t) \quad (3)$$

where T_a is the absorber relaxation time, $E_{A,sat}$ the saturation energy of the absorber, and q_0 the small signal absorber loss. There is a similar equation describing the gain evolution. The saturation energy of the gain, $E_{G,sat}$ is larger than $E_{A,sat}$ in order to accomplish stable mode-locking. Furthermore the small signal gain $g_0 > 1 + q_0$ and the gain relaxation time denoted by T_1 is comparable to the round-trip time T_R . The gain and the absorption are frequency dependent. The effect of this on the pulse envelope is accounted for by the last term on the right-hand side in Eq.(1), where ω_C is the bandwidth of the net gain.

The most common approach to describe the evolution of the laser intensity in a cavity is by means of rate equations. Here we will use a model of Yamada, which predicts self-pulsations. In order to keep the number of parameters limited we lumped some parameters together. The evolution of both the photon number S , the number of carriers in the gain region N_1 , and the number of carriers in the absorber region N_2 are governed by the following equations

$$\frac{dS}{dt} = [g_1(N - N_{t1}) + g_2(N_2 - N_{t2}) - \Gamma_0] S \quad (4)$$

$$\frac{dN_1}{dt} = J - \frac{N_1}{\tau_s} - \frac{N_1 - \nu N_2}{T_{12}} - g_1(N_1 - N_{t1}) S \quad (5)$$

$$\frac{dN_2}{dt} = -\frac{N_2}{\tau_s} - \frac{\nu N_2 - N_1}{T_{12}} - g_2(N_2 - N_{t2}) S \quad (6)$$

where τ_s is the carrier lifetime. This time the differential absorption and gain are given by g_2, g_1 . The coupling between the absorber and the gain is

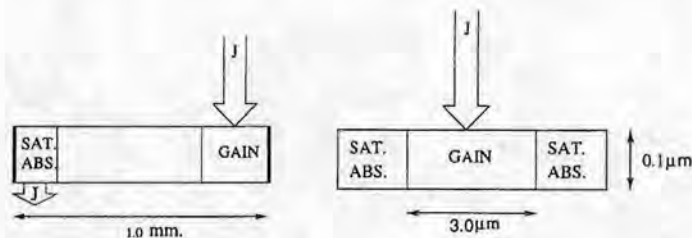


Figure 1: On the left-hand side the configuration in the case of saturable absorber mode-locking is shown, whereas the right-hand side shows the configuration for the narrow stripe laser. In the left-hand picture the pulses propagate from right to left and are confined to the cavity by mirrors (reflectivity of approximately 90%) on each side. The pulses in the narrow stripe model propagate perpendicular to the page and are confined to the cavity in a similar way.

modeled by the parameter ν , and T_{ij} is the characteristic diffusion time for electrons from region i to j . The mirror loss is represented by Γ_0 .

When one compares Eqs. (1) and (2) with Eqs. (4)-(6), it is immediately noticed that the diffusive term in Eq. (1) has no counterpart in the narrow stripe equation (4). Similarly the carrier diffusion term is not present in Eq. (2). Since we want to predict self-pulsations by the mode-locking equation (1), we limit ourselves to the case in which the times T_{ij} are much larger than the round-trip time so that carrier diffusion between the two regions can be neglected. The rate equations describing the narrow stripe laser are valid for time scales on the order of the round-trip time. The round-trip equation with the diffusive term, which limits the widths of the mode-locked pulses, is valid on a much smaller time scale and in this sense thus more general. In Fig. 2 we show that the self-pulsations can also be explained by Eqs. (1)-(3), and predict a substructure due to mode-locking. Experiments performed on these lasers also show some kind of substructure, but the commonly hold opinion is that this originates from the presence of several lateral modes. We, however, try to give an explanation of this phenomenon by extending the round-trip equation model and showing that in this case a substructure arises from the presence of several longitudinal modes in the cavity.

This work is part of the research program of the 'Stichting voor Funda-

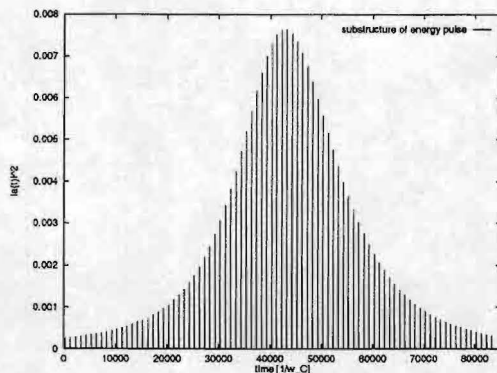


Figure 2: One self-pulsation with a substructure on the round-trip time scale. One can see a pulse within each round-trip. The pulses are very short; the pulse duration $t_p \approx 30/\omega_C$, which corresponds to 3 ps for an inverse net gain bandwidth of 0.1 ps. The parameters were chosen in such a way that apart from the diffusive term there is complete correspondence between the mode-locking and narrow stripe laser equations.

menteel Onderzoek der Materie (FOM)', which is financially supported by the 'Nederlandse Organisatie voor Wetenschappelijk Onderzoek (NWO)'.

References

- [1] H. A. Haus, IEEE J. Quantum Electron. **11**, 736, (1975).
- [2] M. Yamada, IEEE J. Quantum Electronics **29**, 1330, (1993).
- [3] J.L.A. Dubbeldam, J.A. Leegwater, D. Lenstra, Appl. Phys. Lett. **70**, 1938, (1997).

Active mode locking of a p-Ge hot hole laser

J.N. Hovenier, T.O. Klaassen and W.Th. Wenckebach,

Department of Applied Physics and DIMES, Delft University of Technology,
P.O. Box 5046, 2600 GA Delft, The Netherlands,

and

A.V. Murav'jov, S.G. Pavlov and V.N. Shastin,

Institute for Physics of Microstructures, Russian Academy of Sciences, GSP- 105,
Nizhny Novgorod 603600, Russia.

Abstract

Active mode locking of a p-Ge hot hole laser has been achieved by electrical intracavity modulation of the gain, that results in the generation of a train of sub-nanosecond pulses of far-infrared radiation.

Introduction

The operation of the p-Ge hot hole laser¹ is based on the existence of two types of holes; heavy holes and light holes with effective masses of m_{hh}^* and m_{lh}^* respectively. When these holes are accelerated in crossed electric and magnetic fields $\vec{E} \perp \vec{B}$ at cryogenic temperatures ($T \approx 4-20$ K), the maximum values for momentum and kinetic energy of

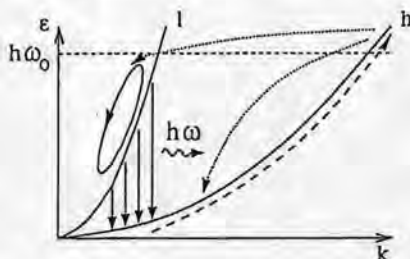


Fig. 1. Mechanism for the population inversion; the light (l) and heavy (h) hole bands are shown in an energy-momentum diagram. The pumping cycle is indicated.

the holes are given by $\hbar k = 2m^*(E/B)$ and $E = 2m^*(E/B)^2$ respectively. Because $m_{hh}^* \gg m_{lh}^*$ the values of E and B can be chosen such that $2m_{hh}^*(E/B)^2 \gg \hbar\omega_{LO} \gg 2m_{lh}^*(E/B)^2$, with $\hbar\omega_{LO}$ the optical phonon energy ($= 37$ meV in Ge). The heavy holes are strongly scattered under emission of optical phonons, in part into the light hole band (see fig. 1). Because of the low temperature, no thermal optical phonons are present that can scatter the light holes, they accumulate on closed trajectories below the optical phonon energy and a population inversion results between the light hole and the heavy hole band that leads to optical

emission in the far-infrared region. The applied magnetic field causes the hole bands to split up in Landau levels. As the life time of the heavy holes is very short, the hh-Landau levels are smeared out into a continuous band, whereas for the light holes, with a much longer life time, the quantisation into discrete Landau levels has to be taken into account. Therefore two types of radiative transitions have to be distinguished. Transitions between a lh-Landau level and the hh- band - intervalence band (IVB) transitions - and transitions between two lh- Landau levels - cyclotron resonance (CR) transitions. In fig. 2 the experimentally observed (E,B) field regions and the corresponding frequency regions for both the IVB- and the CR laser are shown². Clearly, the frequency of both types of lasers can be tuned by changing the values of E and B .

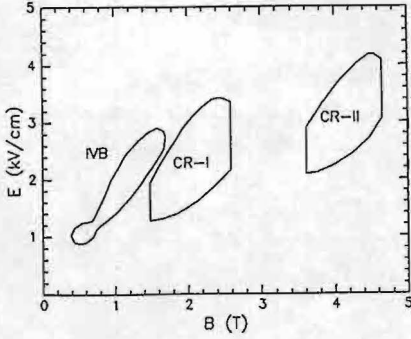


Fig.2a. (E, B) field region for the IVB and CR laser.

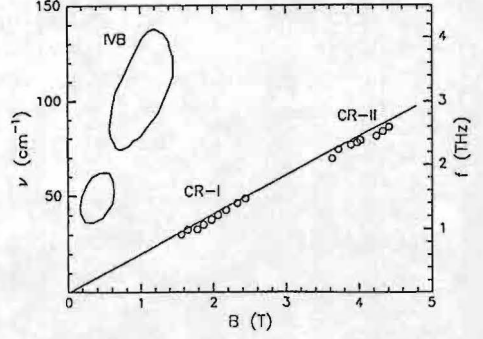


Fig.2b. Corresponding frequency regions versus B .

Mode locking.

As the intrinsic gain width of the IVB laser is extremely large, up to 1 THz^3 , this laser can be used for the generation of very short pulses of far-infrared radiation through mode locking. Monte Carlo simulations have shown that gain modulation of the IVB laser can be achieved by applying a radio frequency (rf) electric field $\parallel \vec{B}^4$, as such a periodic field causes a periodic acceleration of the light holes in the direction of \vec{B} leading to a strong increase of the maximum energy of the light holes. The resulting possibility of optical phonon emission leads to a decrease of the population inversion and thus to a periodic lowering of the gain³.

Experimental details

The active laser sample used in the present experiments (Fig. 3) was cut from a single crystal of Ga doped Ge, with $N_{Ga} = 7.10^{13} \text{ cm}^{-3}$, in the form of a rectangular parallelepiped of $5 \times 7 \times 49.46 \text{ mm}^3$. The high voltage electric excitation field is applied to ohmic contacts covering two opposite lateral surfaces of the sample. The magnetic field is applied perpendicular to the long axis and to \vec{E} (Voigt configuration) using an iron core electromagnet. For the modulation of the gain an rf electric field parallel to \vec{B} is applied to additional ohmic contacts of $1 \times 10 \text{ mm}^2$. Two gold mirrors, evaporated on sapphire substrates and isolated by $10 \mu\text{m}$ Teflon films are attached to the ends of the sample. The entire system is immersed in liquid helium. At the side of the smaller mirror laser radiation is coupled out and detected with a fast GaAs Schottky diode detector (Faran Technology). The signal is displayed using both a 1 GHz bandwidth, 5 Gb/s oscilloscope to monitor the overall pulse envelope and a 6 GHz bandwidth real-time scope allowing for a detailed study of the waveform of individual short pulses.

The high electrical current ($\approx 200 \text{ A}$) through the crystal causes severe heating effects. Therefore, in the present experimental set up, the excitation is limited to pulses with a duration of a few microseconds and a repetition rate of a few Herz.

The rf modulation field, with a frequency of 386.1 MHz, is applied in short pulses too, synchronized with the excitation pulses. Because the gain reaches a minimum at maximum instantaneous amplitude of the rf field, the gain is modulated at $2 \times 386.1 \text{ MHz} = 772.2 \text{ MHz}$, which equals the laser cavity roundtrip frequency.

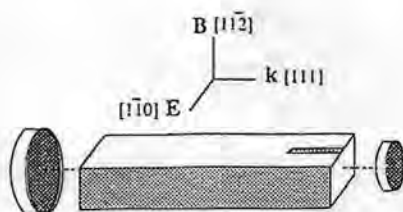


Fig. 3. p-Ge laser design.

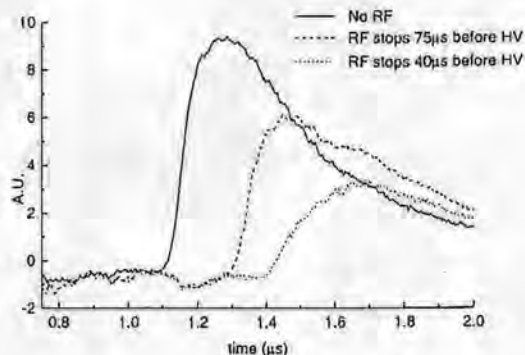


Fig. 4. Effect of rf heating on pulse delay.

Results

In a recent publication we reported on the first experimental observation of short pulses resulting from active mode locking in the high field region of the IVB laser⁵. Applying about 200 W of rf modulation power, a train of sub-nanosecond pulses, separated by the roundtrip time of about 1.3 ns, were obtained; the shortest pulse duration observed was 140 ps.

Here we report on the influence of temperature and of intensity of the rf field on the operation of the IVB laser.

We did increase the temperature of part of the crystal by applying a short pulse of rf field just *before* the start of the excitation pulse. As a result, the region in between the rf electrodes is initially heated from 4.2 K up to about 11 K. This local temperature rise decreases because of the heat conduction to the rest of the crystal, depending on the time delay between the end of the heating pulse and the subsequent excitation pulse. In fig. 4 the experimentally observed laser emission is given for delays of 75 and 40 μ s and also in the *absence* of a heating pulse. It is evident that with an increase of the temperature in part of the crystal at the start of laser action (short time delay) the overall gain of the laser drops: the delay of the optical pulse w.r.t. the excitation pulse at $t=0$ increases and both the risetime and the maximum intensity of the optical pulse decrease. As this effect results from the input of only 20 mJ/cm³ in just a small part of the crystal, it is to be expected that a similar, but stronger effect will result from the laser excitation pulse itself. The energy input of this high voltage pulse is much higher: 80 mJ/cm³ over the whole crystal in a time interval of 0.8 μ s between the start of the excitation and the moment that the laser output reaches its maximum intensity. Clearly, this continuous heating will cause the (small signal) gain of the laser to be time dependent.

The upper trace in fig. 5 shows the optical pulse observed with the rf field on during laser excitation: the modulation of the output intensity resulting from the gain modulation is clearly visible. Compared to the pulse shown in the lower trace, obtained *without* rf field, under otherwise equal conditions, two differences are observed. The delay between excitation pulse and the start of the optical signal is larger for the mode locked pulse, most probably due to the additional heating effect from the rf field. However, the pulse envelope under mode lock conditions shows a steeper increase with time and

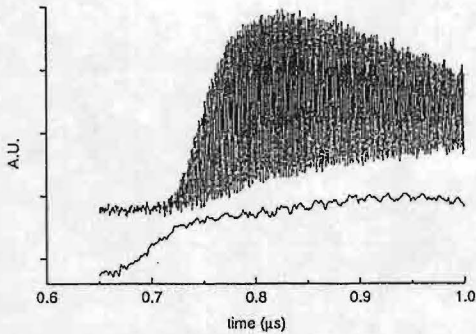


Fig. 5. p-Ge laser pulse obtained with 1 GHz oscilloscope. Upper trace: with modulation field, lower trace: without modulation field.

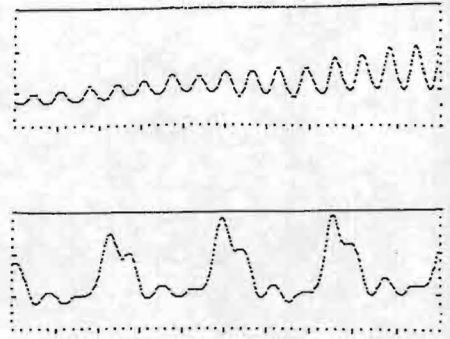


Fig. 6. p-Ge laser pulse obtained with 6 GHz oscilloscope. Upper trace (2 ns/div) : start of laser action, lower trace (0.5 ns/div): end of laser action.

reaches a higher maximum than the un-modulated pulse. This latter effect seems to indicate that, although the population inversion with rf field is smaller than without, nevertheless the gain for the short pulses is larger. The upper trace in fig. 6, obtained with the 6 GHz bandwidth oscilloscope, shows a typical shape of individual pulses at the start of the laser action. A regular train of pulses with a 1.3 ns separation; the amplitude increases and the width decreases slowly with time. From this trace a gain per roundtrip of about 7.5% is derived. The lower trace shows irregularities in the pulse shapes that are observed typically in the descending part of the pulse envelope where often also the modulation depth decreases. These effects may be related to - longitudinal and transversal - mode competition, partly driven by the time and wavelength dependent gain. Also, the simple cavity design may play a role here.

The authors thank M.J.W. Vermeulen from the Delft Interfaculty Reactor Institute for the use of the high frequency oscilloscopes and the help with the data acquisition.

References

1. E. Gornik and A.A. Andronov, editors, *Far-infrared Semiconductor Lasers*, Special issue of Opt. Quantum Electron. **23**(1991) S111-S349.
2. V.N. Shastin, *Hot-hole inter-sub-band transition p-Ge FIR laser*, Opt. Quantum Electron. **23**(1991) S111-S131.
3. A.V. Murav'jov, A.V. Nevedov, I.M. Pavlov and V.N. Shastin, *Tunable narrow band laser that operates on interband transitions of hot holes in germanium* Quantum Electronics **23**(1993)119-24.
4. R.C. Strijbos, J.G.S. Lok and W.Th. Wenckebach, *A Monte Carlo simulation of mode-locked hot hole laser operation*, J.Phys.Condens.Matter **6**(1994)7461-8.
5. J.N. Hovenier, A.V. Murav'jov, S.G. Pavlov, V.N. Shastin, R.C. Strijbos and W.Th. Wenckebach, *Active mode-locking of a p-Ge hot hole laser*, Appl. Phys. Lett. **71**(1997)443-5.

Thermal lateral waveguiding in gain-guided, low confinement laser diodes

M.Buda, G.A.Acket, T.G. van de Roer, W.C. van der Vleuten, E.Smalbrugge

*COBRA Interuniversity Research Institute on Communication Technology
Eindhoven University of Technology, Electronic Devices Group (EEA)*

Abstract: Unusually large delays (500 ns - 5 μ s) between electrical and optical pulses are reported for low confinement, gain guided laser diodes. These peculiar effects are attributed to thermal waveguiding and are noticeable in low-contrast index-guided devices also.

1) Introduction

Laser diodes with low confinement are promising devices for high power applications, if the required optimization of the layer structure is achieved [1,2]. In principle, also the lateral modal behavior could be improved, if compared to usual GRIN-devices, due to the reduced influence of carrier induced antiguiding. For gain-guided devices, the temperature gradient along the stripe width becomes the leading factor in deciding the lateral behavior of the beam, through its influence on the lateral effective refractive index. This leads to unexpectedly large delays (500 ns - 5 μ s) between the optical and electrical pulse and to peculiar shapes of the optical pulse. A similar effect is also noticeable in low-contrast index guided laser diodes, when the temperature induced lateral waveguiding becomes comparable to the built-in profile, in the form of a ripple superposed on the normal rectangular optical pulse. These effects are found in GaAs/AlGaAs as well as in InGaAs/AlGaAs low confinement QW structures, symmetric or asymmetric. The purpose of this paper is to present some of these results and to propose an explanation for a few of them.

2) Experimental results

Although the same type of behavior is noticed for all QW low confinement laser structures, symmetric or asymmetric, with GaAs or $\text{In}_{0.2}\text{Ga}_{0.8}\text{As}$ active regions, we present here only results measured on a DQW, symmetrical structure, for gain guided devices.

The refractive index profile in the transverse direction, i.e. perpendicular to the active region, and the optical field distribution are presented in Fig. 1. The active region consists of two 55 Å QW's and the computed confinement factor is 7.5×10^{-3} per well. Due to the poor carrier confinement and subsequent current leakage in barrier and confinement layers, the resulting threshold current density is about 2 500 A/cm² for a device length $L = 1.5$ mm. This value is measured in pulsed conditions, and depends considerably on pulse width. The same type of behavior was noticed for lower threshold structures, i.e. with threshold current densities of 600-900 A/cm². The thickness of both confinement layer is in total $2 \times 3.10 \mu\text{m}$.

The photolithographically defined stripes of 8 and 16 μm are etched in such a way that the total step height is 2 μm . The lateral difference of the refractive index then is less than 2×10^{-4} , so that we can consider these devices as gain guided. For the case of the low-contrast index guided devices, the 80 Å SQW structure is asymmetric and the computed lateral index step is $\Delta n_{\text{eff}} \approx 10^{-3}$. The devices are mounted p-side up or p-side down on silicon submounts.

Measurements are made in pulsed conditions, at room temperature. If the period between pulses is larger than 1 ms for pulse widths less than 1 μs and larger than 10 ms for pulse widths in the range of 10-30 μs respectively, the optical pulse shape is not influenced by the repetition rate. The threshold current density, wavelength at threshold and changes in the far field are recorded as a function of pulse width and amplitude. Electrical pulses always have a rectangular shape.

Typical results are presented in fig. 2 and for 8 μm stripe devices mounted p-side up and in fig. 3 for 16 μm stripe laser diodes mounted p-side down, respectively. In all cases the device length is 1.5 mm.

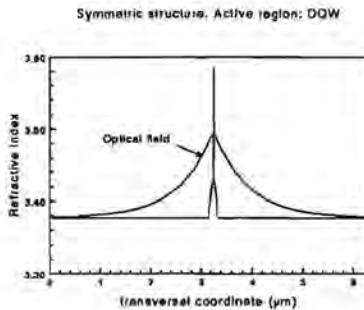


Fig. 1

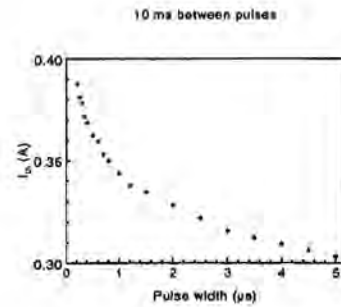
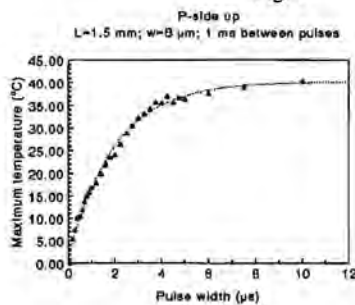
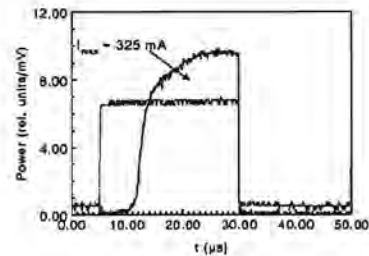


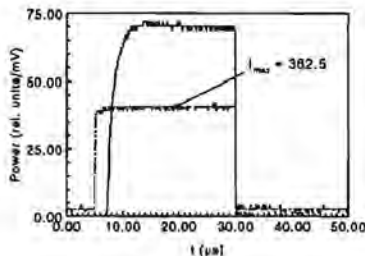
Fig. 2 a)



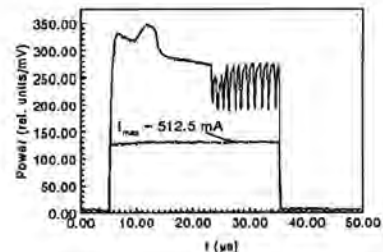
b)



c)



d)



e)

Fig. 2. Stripe width $w = 8 \mu\text{m}$. Device length $L = 1.5 \text{ mm}$. 10 ms between pulses. P-side up mounting.

a) Threshold current density and b) temperature at threshold as a function of pulse width.

c)-e) Optical pulse shape for different injection levels at constant pulse width of 20 μs .

3. Discussion

3.1. Delay between the optical and electrical pulse

Looking at fig. 2 and 3 we observe in all cases delays as large as 5 μs between the beginning of the electrical and optical pulses, depending on the injected current. We propose the following explanation: In the first moments after initiating the electrical injection, the carrier induced antiguiding defocuses the optical mode, causing extra losses in the lateral direction and lower gain. In the time range of a few microseconds, the thermal waveguide builds up and as a consequence, the

lateral mode loss decreases, and at a certain time gain equals losses and laser emission occurs. For all cases, the optical pulse shape is rounded at the beginning with a time constant in the range of a few microseconds.

The time constant theoretical predicted for a transversal dimension of the order of magnitude of $3 \mu\text{m}$, i.e. the thickness of the confinement layer (d_c), is $\tau = d_c^2/D$ [3], where D is the thermal diffusivity. For representative values we obtain a time constant of $1.5 \mu\text{s}$. The agreement is reasonable, taking into account the distribution of the two main heat sources at threshold: ohmic heating mostly in the p-contact layer and spontaneous emission absorbed in the p^{++} contact layer and substrate.

Delays of the same order of magnitude were reported earlier for different semiconductor laser diodes [4.5] and qualitatively attributed to thermal effects.

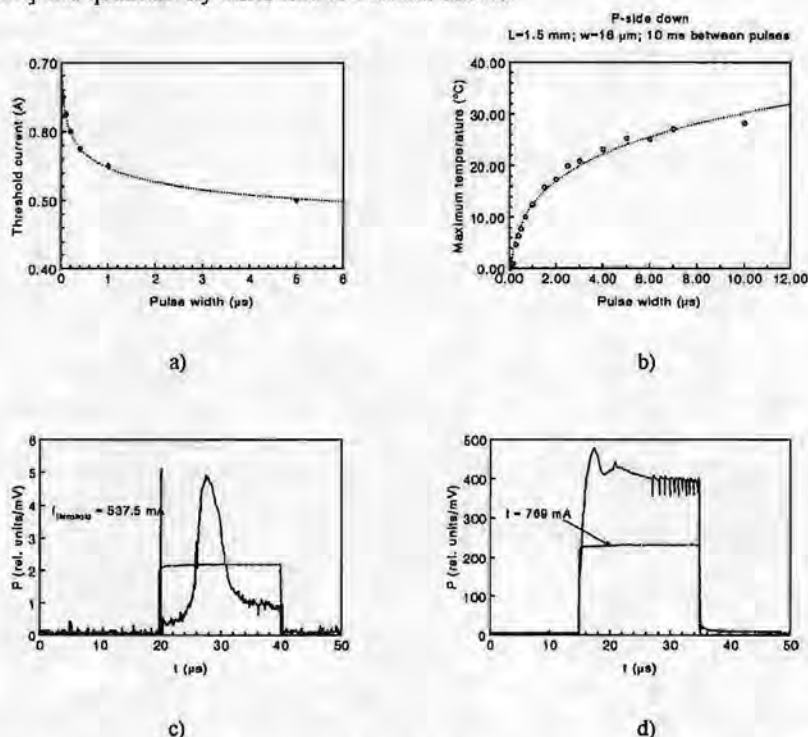


Fig.3. Stripe width $w = 16 \mu\text{m}$. Device length $L = 1.5 \text{ mm}$. 10 ms between pulses. P-side down mounting.

a) Threshold current density and b) temperature at threshold as a function of pulse width.

c),d) Optical pulse shape for different injection levels at constant pulse width of $20 \mu\text{s}$.

3.2. Maximum temperature of the active region and thermal waveguiding in the stripe region

If we investigate the spectral response of the device, we can deduce information related to the maximum temperature in the active region, while if we look at the lateral far field distribution the important parameter is the thermal waveguiding in the stripe region. The spectra at threshold (not shown) are shifting when the pulse width increases. We assume that these shifts reflect entirely changes due to temperature rise in the active region and use a value of $d\lambda/dt$ equal to 0.254 nm/K [6] for translating recorded wavelengths into temperature changes. The plots can be seen in fig. 2b and 3b respectively. For a stripe width of $16 \mu\text{m}$, the maximum temperature corresponding to a $10 \mu\text{s}$ pulse at threshold is 28°C for p-side down mounting. For a stripe width of $8 \mu\text{m}$, mounted p-side up the corresponding temperature rise is 38°C .

In all cases, the lateral far field has a half-width value of 4° and the filament width is $8 \mu\text{m}$, even for the $16 \mu\text{m}$ wide stripes. If we consider a step-like effective index profile in the lateral

direction, this value of the far-field corresponds to a lateral step value $\Delta n_{\text{eff}} \approx 10^{-3}$, i.e. 2.5°C temperature difference between the middle and the edge of the stripe, assuming a value $dn_{\text{eff}}/dT = 4 \times 10^{-4} \text{ K}^{-1}$. The devices with $16 \mu\text{m}$ wide stripes are much more sensitive with respect to thermal waveguiding.

In all cases, after a few microseconds, the optical pulse decreases in magnitude. We attribute this effect to the perturbation of the thermal waveguide due to the beginning of lasing. At longer times and larger injection, oscillation between lateral modes are also possible, as seen in figs. 2e, 3e.

We tried to model the temperature behavior at threshold, taking into consideration first a one dimensional heat source with a semi-infinite medium in the lateral direction, and then a 2D constant ohmic source in the confinement layers and two delta-sources located in the p^{++} GaAs contact layer and substrate. In the latter case, the temperature was assumed to be constant at the heat sink, the heat flux zero at the other edges of the device and the heat conductivity uniform. Both models predict temperature differences between the middle and the margin of the stripe close to values deduced from measurements, i.e. 2.5°C in the case of $8 \mu\text{m}$ wide stripe and 2.75°C for a $16 \mu\text{m}$ wide one, for a $1 \mu\text{s}$ pulse width. For longer pulse widths, the predicted thermal waveguiding is significantly larger for the $16 \mu\text{m}$ wide stripes and may explain the larger instabilities observed in these conditions.

4. Conclusions

-Unusual large delays ($500 \text{ ns} - 5 \mu\text{s}$) are between the beginning of the electrical and optical pulse are noticed for low confinement QW laser diodes;

-These peculiar effects are attributed to lateral thermal waveguiding;

-An attempt is made to estimate the maximum temperature in the active region and the magnitude of the thermal waveguide from experimental data and to explain it using a theoretical model;

-For a thermal load given by a threshold current density of 2500 A/cm^2 the stable filament width is $8 \mu\text{m}$ and the estimated thermal difference between the middle and the margin of the stripe is $\Delta T \approx 2.5^\circ\text{C}$. The corresponding thermal waveguiding is $\Delta n_{\text{eff}} \approx 10^{-3}$.

References:

- 1) "Design of a 1W, Single Filament Laser Diode", I.B.Petrescu-Prahova, M.Buda, T.G. van de Roer, IEICE Trans. on Electr., vol E77-C no. 9, 1994, p.1472;
- 2) "Analysis of 6-nm AlGaAs SQW low-confinement laser structures for very high power operation", M.Buda, T.G.van de Roer, L.M.F.Kaufmann, Gh.Iordache, D.Cengher, D. Diaconescu, I.B.Petrescu-Prahova, J.E.M.Haverkort, W. van der Vleuten, J.H. Wolter, IEEE Sel. Topics in Quant. El., vol. 33, no. 2, p.173;
- 3) "Waveguiding in high power short wavelength semiconductor lasers", M.F.C. Schemmann, Ph.D. thesis report, TUE, 1994;
- 4) "Long delay time for lasing in very narrow graded barrier SQW lasers", F.C.Prince, N.B.Patel, D.Kasemset, C.S.Hong, Electron. Lett., vol. 19, no. 12, 1983, p. 435;
- 5) "Anomalous temporal response of gain guided surface emitting lasers", N.K.Dutta, L.W.Tu, G.Hasnain, G.Zydzik, Y.H.Wang, A.Y.Chao, Electron. Lett., vol. 27, no. 3, 1991, p.208;
- 6) "Time-resolved emission studies of GaAs/AlGaAs laser diode arrays on different heat sinks", M.Voss, C.Lier, U.Menzel, A.Barwolff, T.Elsaesser, J.Appl. Phys., vol. 79, no. 2, 1996, p.1170;

Resonator design for a long pulse XeCl excimer laser

R.M. Hofstra^a, M.J. Zwegers^b, F.A. van Goor^a and W.J. Witteman^{a,b}

^a Twente University, P.O. Box 217, 7500 AE Enschede, The Netherlands

^b Nederlands Centrum voor Laser Research (NCLR), P.O. Box 2662
7500 CR Enschede, The Netherlands

Abstract

A nearly diffraction limited output beam is obtained from a hard edge confocal positive branch unstable resonator. Partial hard edge outcouplers and gaussian outcouplers result in an improved far field energy distribution.

1 Introduction

For the application field of the 1 kHz, 1 kW long pulse excimer laser developed by the Nederlands Centrum voor Laser Research (NCLR) [1], the beam divergence of the optical beam is of utmost importance. The active medium of this laser has large discharge dimensions relative to the size of the fundamental gaussian mode of a stable plano-concave resonator. The beam from such a resonator is therefore multimode with a relatively poor beam divergence. To decrease the divergence of this laser the number of modes has to be decreased to, preferably, one fundamental mode which fills the whole gain volume. This can be done with an unstable resonator. For our system a positive branch unstable resonator is found to be the best choice. In this paper we present a detailed experimental study of different unstable resonators for a low gain, long pulse XeCl excimer laser.

2 Experimental configuration

The experiments have been performed with a XeCl laser system having a 2.5×2

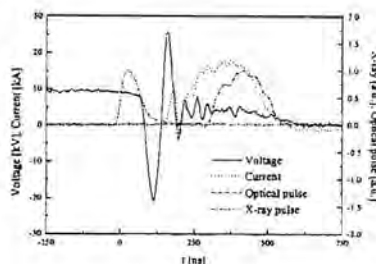


Figure 1: Typical waveforms of the discharge voltage, discharge current, x-ray preionisation pulse and optical output pulse.

$\times 60 \text{ cm}^3$ (electrode distance \times discharge width \times discharge length) x-ray preionised high pressure discharge [2]. The gas mixture (1 mbar HCl, 10 mbar Xe and 5 bar Ne) is excited by a spiker-sustainer circuit, which is operated in the resonant overshoot mode [3]. To reach optimal efficiency conditions and to avoid electrode wear the system is operated under matched discharge conditions, i.e. the voltage on the sustainer circuit is twice the steady state voltage of the discharge. Figure 1 shows some typical waveforms of the laser.

The near and far field energy distributions are measured using a scintillator and a gated image intensified CCD camera.

For the near field measurement the (attenuated) beam is transported away from the laser with a relay imaging system and for the far field measurement the beam is attenuated and subsequently focussed using a 10 m radius of curvature mirror.

3 Stable resonators

The simplest type of resonator is the stable resonator. Good energy extraction from the gain medium can easily be obtained if proper feedback is used. With a 1.5 m long plano-concave resonator consisting of a plane 50 % outcoupling mirror and a concave full reflector with a radius of curvature of 10 m as the back mirror a homogeneous, nearly square beam of 23 mm x 22 mm, having a pulse energy of about 500 mJ is obtained. The problem of stable resonators is their divergence. In our system the discharge dimensions are much larger than the dimensions of the fundamental mode hence the beam is multimode. This results in a large divergence. We measured 7 mrad beam divergence from the above mentioned stable resonator, while a diffraction limited beam of this size would have a divergence of about 30 μ rad.

4 Hard edge unstable resonators

The size of the fundamental mode can be increased with an unstable resonator. An unstable resonator reaches this fundamental mode earlier if the magnification is larger [4]. Therefore the magnification should be chosen as large as possible within the constraints of the gain medium. With stable resonators we found a minimum value for the resonator feedback of about 20 %. This minimum value determines the choice for the magnification of the unstable resonator which is given by

$$M = -\frac{R_2}{R_1} \quad (1)$$

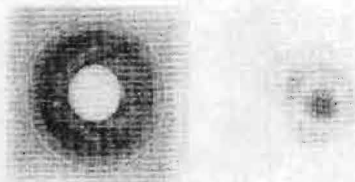


Figure 2: Near field profile (left) and focus profile (right) of the beam from a hard edge unstable resonator ($M = 2.4$) with a central HR spot of 8 mm diameter, focussed by a 10 m radius concave mirror.

where R_1 is the radius of curvature of the outcoupling convex mirror and R_2 is the radius of curvature of the concave rear mirror. The feedback of an unstable resonator is given by

$$\gamma = \frac{1}{M^2} \quad (2)$$

Hence we used an unstable resonator with a magnification of 2.4 to have enough feedback (18 %).

Hard edge unstable resonators are resonators in which the outcoupling mirror shows a step in the reflectance profile. Figure 2 shows typical near field and far field profiles from a hard edge unstable resonator. The outcoupler in this experiment had a central reflectivity of 100 %. As can be seen in the figure the focus field shows a rather strong ring structure. Calculations have shown that the energy in this ring structure can be reduced by making the reflecting spot on the outcoupler partially transmitting. Figure 3 shows the focus energy distributions for three resonators with the same magnification, but with different reflectivities for the spot on the outcoupling mirror. The 72 % spot reflectivity clearly leads to an improved focus profile; less energy is lost in the side lobe. Further reduction of the reflectiv-

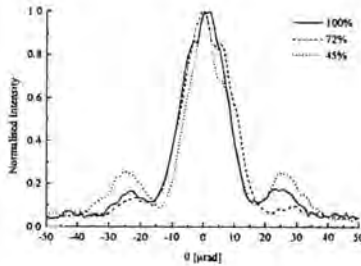


Figure 3: Focus energy distributions from resonators with different central reflectivities (100, 72 and 45 %). The magnification $M = 2.4$ for all resonators.

ity to 45 % results in a huge side lobe. This sudden increase instead of decrease as expected from calculations is caused by the outcoupling mirror. When the beam passes through the outcoupling mirror a phase difference occurs between the part of the beam that passes through the reflecting spot and the part that passes outside the reflecting spot. This phase difference results in a worse focus profile. Interferometric measurements on the outcoupling mirrors have shown that the 72 % mirror yields a phase difference of only 0.3π and the 45 % mirror a phase difference of π .

This phase difference can be decreased using a special coating design: the phase unifying mirror [5,6]. Experiments have shown that with a phase unifying mirror the side lobe is further reduced.

5 Soft edge unstable resonators

A hard edge outcoupler will always result in a side lobe because of diffraction at the hard edge. A focus spot without side lobes requires a soft edge unstable resonator. A soft edge unstable resonator



Figure 4: The near field spots of two gaussian resonators. Left: $M = 2.4$ and $R_c = 65\%$. Right: $M = 2.0$ and $R_c = 25\%$.

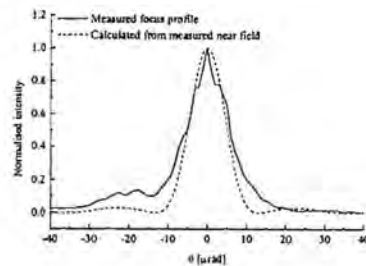


Figure 5: Measured and calculated focus energy distributions for the high central reflectivity gaussian resonator ($M = 2.4$ and $R_c = 65\%$).

is a resonator where the outcoupling mirror shows a smooth reflectance profile. We used nearly gaussian mirrors because these can easily be analysed mathematically. In our experiments we used different magnifications and central reflectivities for the gaussian mirror to be able to study the influence on the beam.

This central hole still leads to a small side lobe in the focus field as can be seen from figure 5. Figure 4 shows two typical near field spots from two different gaussian unstable resonators. A high central reflectivity for the gaussian outcou-

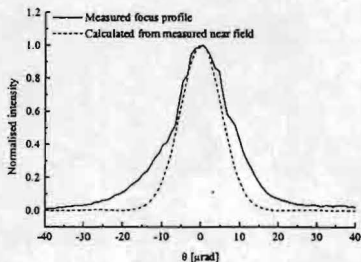


Figure 6: Measured and calculated focus energy distributions for the high central reflectivity gaussian resonator ($M = 2.0$ and $R_c = 25\%$)

pler (shown on the left in figure 4) results in a beam with a smooth edged central hole in the near field. Calculations have shown this to be in accordance with theory.

The spot shown on the right in figure 4 is from a gaussian resonator where the outcoupler is designed to result in a maximally flat output beam, i.e. no central hole in the near field. Even from this resonator a very small side lobe is expected from theory. The experiments show a slightly larger focus with a low however wide shoulder as shown in figure 6.

6 Performance comparison

When we compare the output energy of the different resonators we find that the high reflectivity gaussian resonators result in an output energy that is comparable to the energy from a stable resonator. The hard edge resonators result in output energies that were about 25 % lower. Hence the gaussian resonators lead to maximal energy extraction and a good beam quality.

7 Conclusions

In this paper we presented results from measurements on different resonator designs for a long pulse, low gain XeCl excimer laser. With a stable resonator a homogeneous, nearly square, beam can be obtained, however with a large divergence. A hard edge unstable resonator leads to a nearly diffraction limited beam, but with a rather strong side lobe. The best resonator in our view is the gaussian resonator as it combines the good properties of both resonators: good energy extraction and a good beam quality.

Acknowledgements

The present work has been supported by the Netherlands Technology Foundation (STW).

References

- [1] F.A. van Goor, W.J. Witteman, J.C.M. Timmermans, J. van Spijker and J. Couperus, *High-Average power XeCl laser with x-ray pre-ionization and spiker-sustainer excitation*, in: *High-Power Gas and Solid State Lasers*, M. Bohrer, T. Letardi, D. Schuöcker and H. Weber, eds., Proceedings Europto Series 2206, p. 30-40, SPIE, 1994.
- [2] J.C.M. Timmermans, *Double discharge XeCl laser*, PhD thesis, University of Twente, Enschede, the Netherlands, 1995.
- [3] J.W. Gerritsen, A.L. Keet, G.J. Ernst and W.J. Witteman, *High-efficiency operation of a gas discharge XeCl laser using a magnetically induced resonant voltage overshoot circuit*, *Journal of Applied Physics* 67 (7), p. 3517-3519, 1990.
- [4] P.E. Dyer, *Unstable resonators*, in: *The physics and technology of laser resonators*, D.R. Hall and P.E. Jackson, eds., ch. 2, p. 21-39, Institute of Physics Publishing, Techno House, Redcliffe Way, Bristol BS1 6NX, England, 1992.
- [5] V.B. Kaul', S.V. Mel'chenko, M.R. Perrone, A. Piegari and V.F. Tarasenko, *Near diffraction limited output from a 100 ns XeCl laser fitted with a phase unifying cavity*, *Journal of Modern Optics* 42 (11), p. 2229-2238, 1995.
- [6] M.R. Perrone, *On the performance of a phase-unifying unstable resonator for excimer lasers*, *Optics Communications* 116 (1-3), p. 101-108, 1995.

On the dynamics of solitons in randomly birefringent optical fibers

H.J.S. Dorren and J.J.B. van den Heuvel

Department of Electrical Engineering, Eindhoven University of Technology, PO Box 513,
5600 MB Eindhoven, The Netherlands

Abstract

A novel method to compute exact solutions of nonlinear partial differential equations is used to find an analytical expression for the decay of an initially localized pulse in a randomly birefringent optical fiber. The result is in close agreement with experimental data.

1 Introduction

In an ideal nonlinear optical fiber, the nonlinear Schrödinger equation describes the electromagnetic field envelope in a single polarization case. Actual optical fibers however, have the property that there is a difference in the propagation velocity for the two different polarization states of the electromagnetic field. This property is called birefringence. The effects of birefringence are almost never steady, but they vary randomly, in both magnitude and orientation. The random birefringence will ensure that an initially localized pulse will eventually disintegrate. This effect is called Polarization Mode Dispersion (PMD). It is widely believed that PMD is described by the following set of coupled nonlinear differential equations [1]:

$$\begin{cases} i(u_x + \delta u_t) + \mu u + \frac{1}{2}u_{tt} + (|u|^2 + \alpha|v|^2)u = 0 \\ i(v_x - \delta v_t) - \mu v + \frac{1}{2}v_{tt} + (|v|^2 + \alpha|u|^2)v = 0. \end{cases} \quad (1)$$

In Eq.(1), the (scaled) electromagnetic field envelopes of the polarization states are described by u and v respectively. The parameter α describes a material property of the optical fiber. The parameter μ in Eq.(1) represents the phase-velocity birefringence, whereas the parameter δ describes group velocity birefringence. In the limit $\delta \rightarrow 0$ and $\mu \rightarrow 0$, the well-known Manakov equation is retained. Ueda and Katz have argued that the parameters δ and μ are actually random parameters with zero mean [2]:

$$\langle \delta \rangle = 0, \quad \langle \mu \rangle = 0. \quad (2)$$

As a result of this, Eq.(1) is a stochastic differential equation. In the following, we treat the parameters δ and μ as the half-differences of the group-velocity and the phase-velocity between local principal birefringence axes. It has been shown by Zakharov and Schulman that the set of equations (1) cannot be solved by Inverse Scattering Techniques (IST) [3]. Recently, a novel method for solving nonlinear partial differential equations has been developed [4]. This method which is more universal than IST, transforms the nonlinear partial differential equation into an ordinary linear differential equation. In this paper these techniques are applied to find (special) soliton solutions of Eq.(1).

2 A linearizing transformation for the PMD-equations

It is convenient to reformulate Eq.(1) into the following matrix form:

$$i(Iw_x + Dw_t) + Lw + \frac{1}{2}Mw_{tt} = Aw. \quad (3)$$

In Eq.(3), \mathbf{I} represents the unity matrix and the vector \mathbf{w} is given by $\mathbf{w} = (u, v, q, r)^T$. Furthermore, the matrices \mathbf{D} and \mathbf{M} and \mathbf{L} in Eq.(3) are given by:

$$\mathbf{D} = \begin{pmatrix} \delta & 0 & 0 & 0 \\ 0 & -\delta & 0 & 0 \\ 0 & 0 & \delta & 0 \\ 0 & 0 & 0 & -\delta \end{pmatrix}, \quad \mathbf{M} = \begin{pmatrix} 1 & 0 & 0 & 0 \\ 0 & 1 & 0 & 0 \\ 0 & 0 & -1 & 0 \\ 0 & 0 & 0 & -1 \end{pmatrix}, \quad \mathbf{L} = \begin{pmatrix} \mu & 0 & 0 & 0 \\ 0 & -\mu & 0 & 0 \\ 0 & 0 & -\mu & 0 \\ 0 & 0 & 0 & \mu \end{pmatrix} \quad (4)$$

respectively. Finally, all the nonlinearity's in Eq.(3) are contained in the matrix \mathbf{A} , which is defined by the following relationship:

$$\begin{pmatrix} uq & \alpha ur & 0 & 0 \\ \alpha vq & vr & 0 & 0 \\ 0 & 0 & -uq & -\alpha vq \\ 0 & 0 & -\alpha ur & -vr \end{pmatrix} \begin{pmatrix} u \\ v \\ q \\ r \end{pmatrix} = \mathbf{A} \mathbf{w}. \quad (5)$$

If we put $q = -u^*$ and $r = -v^*$, Eq.(3) transforms into Eq.(1). We proceed by decomposing each component of the vector function $\mathbf{w}(x, t)$ into an infinite sum of functions $\mathbf{f}^{(n)}(x, t)$:

$$\mathbf{w}(x, t) = \sum_{n=1}^{\infty} \mathbf{f}^{(n)}(x, t). \quad (6)$$

In the following, we develop a method to solve $\mathbf{f}^{(n)}(x, t)$. If Eq.(6) is substituted into Eq.(3), we find that the four coupled differential equations (3) transform into the following expression:

$$\sum_{n=1}^{\infty} \left(i\mathbf{I}\partial_x + i\mathbf{D}\partial_t + \mathbf{L} + \frac{1}{2}\mathbf{M}\partial_{tt} \right) \mathbf{f}^{(n)}(x, t) = \sum_{k=1}^{\infty} \sum_{l=1}^{\infty} \sum_{m=1}^{\infty} \mathbf{s}^{(klm)}(x, t), \quad (7)$$

where the vector function $\mathbf{s}^{(klm)}(x, t)$ is given by:

$$\mathbf{s}^{(klm)}(x, t) = \begin{pmatrix} f_1^{(k)} f_1^{(l)} f_3^{(m)} + \alpha f_1^{(k)} f_2^{(l)} f_4^{(m)} \\ f_2^{(k)} f_2^{(l)} f_4^{(m)} + \alpha f_1^{(k)} f_2^{(l)} f_3^{(m)} \\ -f_1^{(k)} f_3^{(l)} f_3^{(m)} - \alpha f_2^{(k)} f_3^{(l)} f_4^{(m)} \\ -f_2^{(k)} f_4^{(l)} f_4^{(m)} - \alpha f_1^{(k)} f_3^{(l)} f_4^{(m)} \end{pmatrix}. \quad (8)$$

The left-hand side of Eq.(7) consist of a linear partial differential operator. We will try to linearize the right-hand side of Eq. (7) by using similar procedure as developed in Ref.[4]. Following the machinery presented in this reference, we can solve Eq.(7) by comparing the terms of order n on the left-hand side of Eq.(7) to terms of order of $n = k + l + m$ in $\mathbf{s}^{(klm)}(x, t)$: We then obtain the following result:

$$\begin{aligned} & \left(i\mathbf{I}\partial_x + i\mathbf{D}\partial_t + \mathbf{L} + \frac{1}{2}\mathbf{M}\partial_{tt} \right) \mathbf{f}^{(1)}(x, t) = 0; \\ & \left(i\mathbf{I}\partial_x + i\mathbf{D}\partial_t + \mathbf{L} + \frac{1}{2}\mathbf{M}\partial_{tt} \right) \mathbf{f}^{(2)}(x, t) = 0; \\ & \left(i\mathbf{I}\partial_x + i\mathbf{D}\partial_t + \mathbf{L} + \frac{1}{2}\mathbf{M}\partial_{tt} \right) \mathbf{f}^{(3)}(x, t) = \mathbf{s}^{(111)}(x, t); \\ & \left(i\mathbf{I}\partial_x + i\mathbf{D}\partial_t + \mathbf{L} + \frac{1}{2}\mathbf{M}\partial_{tt} \right) \mathbf{f}^{(4)}(x, t) = \mathbf{s}^{(211)}(x, t) + \mathbf{s}^{(121)}(x, t) + \mathbf{s}^{(112)}(x, t); \\ & \vdots \end{aligned} \quad (9)$$

In Ref.[4], it has been shown that it is useful to introduce a kernel $G(x, t|x', t')$ according to the following ansatz:

$$\mathbf{s}^{(klm)}(x, t) = \mathbf{M} \int_{-\infty}^{\infty} \int_{-\infty}^{\infty} G(x, t|x', t') \mathbf{f}^{(k+l+m)}(x', t') dx' dt'. \quad (10)$$

If we can find a satisfactory kernel $G(x, t|x', t')$, we can solve all the equations in ((9) simultaneously. In Ref.[4], it shown for the Korteweg-de Vries equation that choice of the kernel leads to a constraint on the solution space. In fact

Eq.(10) acts as a boundary condition. If Eq.(10) is substituted into Eq.(9), we obtain the following result:

$$\begin{cases} (i\partial_x + iD\partial_t + L + \frac{1}{2}M\partial_{tt}) f^{(1)}(x, t) = 0; \\ (i\partial_x + iD\partial_t + L + \frac{1}{2}M\partial_{tt}) f^{(2)}(x, t) = 0; \\ (i\partial_x + iD\partial_t + L + \frac{1}{2}M\partial_{tt}) f^{(3)}(x, t) = M \int_{-\infty}^{\infty} \int_{-\infty}^{\infty} G(x, t|x', t') f^{(3)}(x', t') dx' dt'; \\ \vdots \\ (i\partial_x + iD\partial_t + L + \frac{1}{2}M\partial_{tt}) f^{(n)}(x, t) = K(n) \int_{-\infty}^{\infty} \int_{-\infty}^{\infty} G(x, t|x', t') f^{(n)}(x', t') dx' dt'; \\ \vdots \end{cases} \quad (11)$$

In Eq.(11), we have used that the matrix $K(n)$ is given by:

$$K(n) = \frac{1}{2}(n-1)(n-2)M. \quad (12)$$

If we apply the following Fourier transformation onto Eq.(11):

$$f^{(n)}(x, t) = \frac{1}{2\pi} \int_{-\infty}^{\infty} \tilde{f}^{(n)}(k) e^{ikz} dk, \quad z = t - \frac{\omega(k)}{k}x, \quad \tilde{g}^{(n)}(z, k) = \tilde{f}^{(n)}(k) e^{ikz}, \quad (13)$$

and if we use that the linear dispersion relationship associated with Eq.(11) is given by:

$$L\omega(k) = \frac{1}{2}Mk^2 + Dk - L, \quad (14)$$

we find that Eq.(1) transforms into the following linear problem:

$$\begin{aligned} D \left(\frac{d}{dz} + ik \right) \tilde{g}^{(n)}(z, k) &= K(n) \tilde{G}(k) \tilde{g}^{(n)}(z, k); \\ s^{(klm)}(x, t) &= M \int_{-\infty}^{\infty} \int_{-\infty}^{\infty} G(x, t|x', t') f^{(k+l+m)}(x', t') dx' dt'. \end{aligned} \quad (15)$$

In Ref.[5] soliton solutions are constructed by solving Eq.(15) using an iterative method. It has been shown that the system (15) has the following special solutions:

$$\begin{aligned} u(x, t) &= \frac{\frac{1}{2}bAe^{i(\frac{1}{2}\delta^2 + \mu)x}}{\sqrt{[A^2 + \alpha B^2]}} \operatorname{sech}[bt_1 + \chi_1], \\ v(x, t) &= \frac{\frac{1}{2}bBe^{i(\frac{1}{2}\delta^2 - \mu)x}}{\sqrt{[B^2 + \alpha A^2]}} \operatorname{sech}[bt_2 + \chi_2], \end{aligned} \quad (16)$$

$$\chi_1 = \frac{1}{2} \log \left(\frac{[A^2 + \alpha B^2]}{b^2} \right), \quad \chi_2 = \frac{1}{2} \log \left(\frac{[B^2 + \alpha A^2]}{b^2} \right). \quad (17)$$

In Eq.(16), the coefficients A and B have to be determined by the initial condition. The coefficient b is the imaginary part of the wavenumber k . It follows from Eq.(16) that the non-zero coefficient α makes that both the polarization states $u(x, t)$ and $v(x, t)$ can not propagate independently. The solutions (16) are defined with respect to the transformed coordinates:

$$\begin{aligned} t_1 &= t - \delta x; \\ t_2 &= t + \delta x, \end{aligned} \quad (18)$$

where $\hat{t}_1 = t_1 - t$ and $\hat{t}_2 = t_2 - t$. This implies that with respect to the transformed coordinates the both the polarization states propagate with a relative velocity $1/2\delta x$. An example is given in Figure 1. If we take a solitonic pulse and assume that both the polarization states have equal amplitude, we find that after a time Δx both polarization states have separated with a distance equal to half of the pulse width:

$$\Delta x = \frac{\gamma}{2b\delta\sqrt{1+\alpha}}, \quad \gamma = \log \left(\frac{2+\sqrt{3}}{2-\sqrt{3}} \right). \quad (19)$$

If we apply the values given for δ and b given in Ref.[6] and if we also apply the rescaling given in the same reference, we find that the for a 20 psec pulse this distance lies around 500 km. This result is in agreement with experimental data [6].

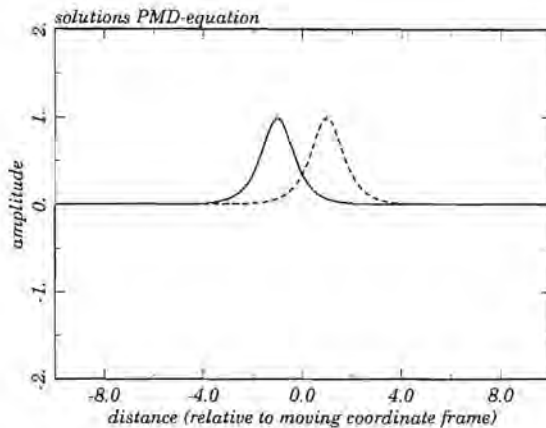


Figure 1: The solutions $u(x, t)$ (solid) and $v(x, t)$ (dashed) of Eq.(16) plotted at $t = 1$. We have chosen $A = B = 1$ and $\alpha = \mu = \delta = b = 1$.

3 Conclusions

It is shown that we are able to derive analytical soliton solutions of the PMD-equations. It is concluded that both the distinct polarization states propagate with a relative velocity $1/2\delta t$. This result enables us to present a simple formula for the decay of an initially localized pulse. The result is in close agreement with experimental data.

Acknowledgments

Huug de Waardt and Djan Khoe are greatly thanked for commenting this manuscript. H.J.S. Dorren is with the KPN-TUE partnership.

References

- [1] A.L. Berkhoer and V.E. Zakharov, *Self-excitation of waves with different polarizations in nonlinear media*, Sov. Phys.-JETP, **31**, 486-490, 1970.
- [2] T. Ueda and W.L. Kath, *Dynamics of optical pulses in randomly birefringent fibers*, Physica D **55**, 166-181 (1992).
- [3] V.E. Zakharov and E.I. Schulman, *To the integrability of the system of two coupled nonlinear Schrödinger equations*, Physica 4D, 270-274 (1982).
- [4] H.J.S. Dorren, *A linearization method for the Korteweg-de Vries equation; generalizations to higher dimensional S-integrable differential equations*, submitted to J. Math. Phys.
- [5] H.J.S. Dorren and J.J.B. van den Heuvel, *An exact analysis of solitons in randomly birefringent optical fibers*, In preparation.
- [6] C.R. Menyuk, Opt. Lett. **12**, 614 (1987); J. Opt. Soc. Am. B **5**, 392 (1988).

How does optical cross-talk depend on the network topology?

J. Siffels, I. Tafur Monroy, H. de Waardt and H.J.S. Dorren
Eindhoven University of Technology

Telecommunication Technology and Electromagnetics
P.O. Box 513, 5600 MB Eindhoven, The Netherlands

Abstract— The influence of in-band cross-talk on the error performance of all optical networks with different topologies is studied. We present a network topology having the best performance while using the largest transmission path.

I. INTRODUCTION

ALL-OPTICAL networks offering a large transport capacity, are regarded as a promising solution to the increasing demand of bandwidth in future telecommunication systems. In these networks routing, switching and amplification is performed in the optical domain. In Fig.1, a diagrammatic representation of an optical multi-wavelength cross-connect is presented.

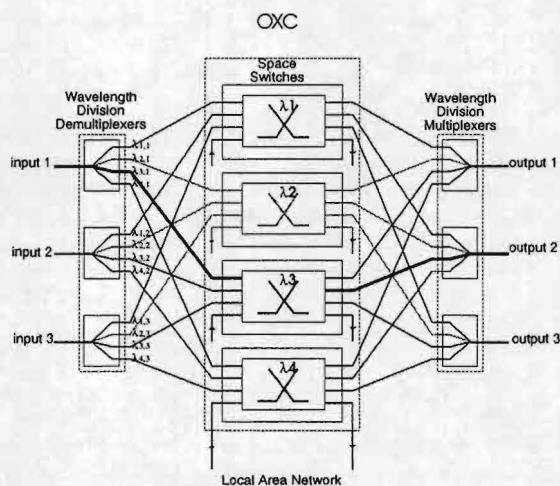


Figure 1. Optical Cross Connect

Suppose we consider a signal at wavelength λ_3 which is switched from input 1 to output 2. It is well-known that due to an imperfect switching array, the output signal is corrupted with contamination of other input signals. This phenomena is called cross-talk. Transparent optical networks impose strict requirements on the cross-talk performance of the network elements involved [1]. We restrict ourselves by considering the situation that the contamination has the same wavelength as the signal (in-band cross-talk). This type of cross-talk can not be removed by using optical filters and it is therefore necessary to design optical networks with an optimum cross-talk performance. In

this paper we focus on cross-talk accumulation which takes place when a signal passes through different nodes in a network. An example is given in Fig.2. Suppose we have a fixed distribution of nodes which are connected to each other by four different configurations. It is clear that the cross-talk performance is related to the topology involved. In this paper we want to investigate which of the topologies has the best performance with respect to cross-talk accumulation. We approach the problem by using numerical simulation techniques in which is accounted for the data-statistics, linear random polarisation and a non-perfect extinction ratio. The main result of the paper is that we will show that introducing additional links in a network leads to a decreased cross-talk performance. We will consider two situations. In the first case we consider ideal networks, while in the second case we assume that link failures take place.

This paper is structured as follows: Sec.II introduces four different network topologies. The mathematical model which used to compute the cross-talk is explained in Sec.III. The simulation results are presented in Sec.IV. The paper is concluded with a short discussion.

II. ANALYSIS

The considered networks consist of a core-network which is connected to a number of sub-networks (Fig.2). We assume that every node in a sub-network is connected to an access network. We search for the largest transmission path in these networks. With this we mean that we compute the set of shortest paths between all possible pairs of nodes in the network. From this set of shortest paths we select the path with the maximum length. From physical point of view this means that we have selected the largest possible connection between two nodes in the network.

The next step is to calculate the total number of cross-talk sources. We will use this number as a measure for comparing the four studied topologies. The number of cross-talk sources is determined by counting the number of interfering channels. In the following we assume that this number equals the number of fibres connected to the node minus one (which represents the incoming signal).

The first network of Fig.2 we discuss in detail is *Topology 1* which represents five interconnected ring networks. This implies that every node has a connection to its left-hand-side neighbour and to the right-hand-side neighbour. Rings are commonly used because of the possible alterna-

tive routing (self-healing) when a failure occurs. The number of needed connections (fibres) is equal to the number of nodes. Each sub-network has only one connection to the core-network. This can be an unwanted situation because of the absence of a backup route. From this topology, it follows that the nodes in the core-network have two sources of cross-talk. Since it is assumed that the sub-networks are connected to access networks, it follows that every node in the sub-network has two possible sources of cross-talk, except the node with the connection to the core-network. The latter has three sources of cross-talk.

Topology 2 is similar to *Topology 1*, but in the core-network two extra links are introduced (Fig.2b). With these extra links the core-network is fully connected. With this we mean that every node in the core-network is interconnected to every other node. This implies that by passing the core-network only two nodes have to be visited. On the other hand the number of cross-talk sources in each node of the core-network is increased from two to three.

We proceed by considering *Topology 3*. In this topology the sub-networks are interconnected to each other. This implies that only *Topology 3* has an alternative for re-routing between two sub-networks. The largest path consists of six nodes. However there are two possible routes, one using the core-network and one using the outer-ring. The difference between these two routes is that the route through the core has fourteen cross-talk sources, while the route using the outer ring has nineteen sources of cross-talk.

The last network of Fig.2 we consider is *Topology 4*. This network consists of a fully connected core-network and fully connected sub-networks. The largest route in this network consists of six nodes, but the number of crosstalk sources has increased to twenty.

III. CROSSTALK MODEL

We assume that N sources of cross-talk are present and we assume that $p(\mu)$ is the probability of μ cross-talk sources being simultaneously a "digital one". Furthermore, the average error probability P_e , given a detection threshold α , is given by a weighted statistical average of the error probability $P_r(\alpha, \mu)$ for each value μ :

$$P_e = \sum_{\mu=0}^N p(\mu) P_r(\alpha, \mu) \quad (1)$$

In Eq.(1) we assume that $p(\mu)$ is a binomial distribution

$$p(\mu) = \frac{N!}{(N-\mu)!\mu!2^N} \quad (2)$$

We proceed by making the following assumptions:

- Perfect signal and cross-talk bit-alignment.
- Extinction ratio is denoted by φ .
- It is assumed that m photons per bit are received for a transmitted "one" while φm are for transmitted "zero".
- The ratio of leakage crosstalk to signal power is denoted by ϵ .

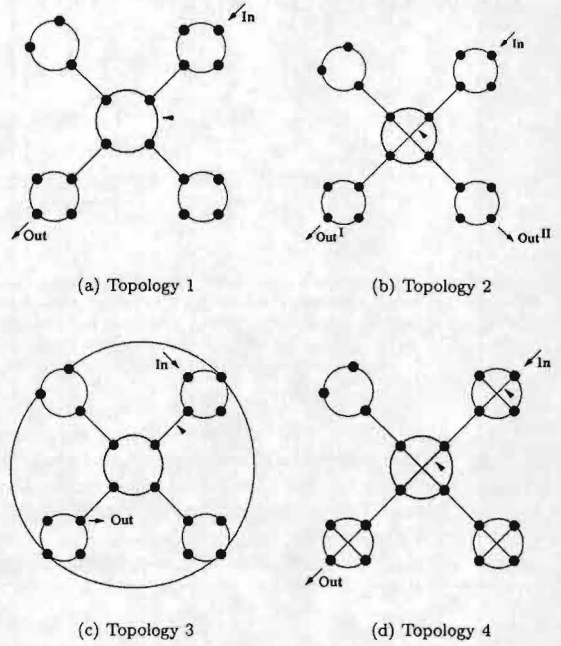


Figure 2. The topologies studied in this paper

- We assume that each interferer has the same relative crosstalk power ϵ .
 - The cross-talk statistics is assumed to be Gaussian having zero-mean and having a normalised variance which is equal to 1/2. This assumption is reasonable for a large number of cross-talk sources [1].
 - The signal and cross-talk polarisation are linearly random and its induced intensity noise is assumed to be Gaussian with zero-mean and with a normalised variance which is equal to 1/2.
 - The post-detection filter is of the "integrate-and-dump type".
 - The detection threshold is fixed to be a midway point between the signal level for a transmitted "zero" and "one".
 - The receiver thermal-noise is considered to be Gaussian distributed, zero-mean and with variance σ_{th}^2 .
- We proceed by following Ref.[2]. Following this reference we use that $P_r(\alpha, \mu)$ can be written as:

$$P_r(\alpha, \mu) = \frac{1}{2} Q\left(\frac{E_1 - \alpha}{\sigma_1}\right) + \frac{1}{2} Q\left(\frac{\alpha - E_0}{\sigma_0}\right) \quad (3)$$

In Eq.(3), E_1 and E_0 represent the mean value of the receiver decision variable for a transmitted "one" and a transmitted "zero" respectively. σ_1 and σ_0 are the corresponding standard deviations. The Q-function represents the normalised Gaussian probability tail. Its precise definition can be found in Ref.[3]. For the case of a transmitted "digital one" E_1 and σ_1^2 are given by Eq.(4) and Eq.(5) respectively. Similar expressions are also easily obtained

when a binary symbol "zero" is transmitted.

$$E_1 = m + \epsilon m (\mu + (N - \mu)\varphi) \quad (4)$$

$$\begin{aligned} \sigma_1^2 = & \mu (2m\sqrt{\epsilon})^2 \frac{1}{4} + (N - \mu) (2m\sqrt{\varphi\epsilon})^2 \frac{1}{4} + \\ & + (2m\epsilon)^2 \frac{\mu(\mu - 1)}{8} + (2m\sqrt{\varphi\epsilon})^2 \frac{1}{4} \mu(N - \mu) + \\ & + (2m\epsilon\varphi)^2 \frac{(N - \mu)(N - \mu - 1)}{8} + E_1 + \sigma_{th}^2 \end{aligned} \quad (5)$$

All possible cross-talk-cross-talk, signal-cross-talk binary bit combinations are covered in the model.

In Fig.3 the bit-error-rate as a function of the number of cross-talk sources for different values of ϵ is presented. The extinction ratio is $\varphi = 8$ dB while $m = 1.3 \cdot 10^4$ photons/s. This corresponds to a signal power of -24dBm for a receiver with responsivity equal to 1 A/W, operating at a wavelength of 1.55 μ m, and at a bit-rate of 2.5 Gb/s. The receiver resistance load is equal to 50 Ω .

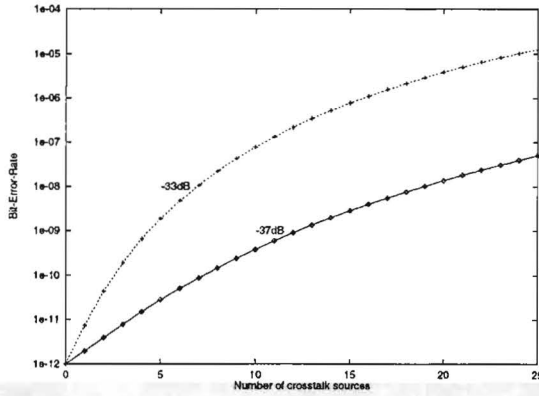


Figure 3. BER dependence on the number of cross-talk sources for values $\epsilon = -33$ dB (dotted line) and $\epsilon = -37$ dB (solid line). The extinction ratio $\varphi = 8$ dB.

IV. RESULTS

As mentioned in Sec.1, we consider two situations. In the first situation the case without link failures is considered. In the second case we assume that link failures in the network are present. The place of the link failures are indicated by the \blacktriangle in Fig.2. We firstly discuss the case without link failures.

A. Without link failures

Table I presents the performance results for network operating without link failures.

The first column in Table 1 represents the topology as indicated in Fig.2. As discussed in Sec.2, *Topology 3* has two alternative routes, indicated by the upper-index I and II. Column 2 gives the number of nodes in the largest route, while in column 3 the number of cross-talk sources are presented. Finally in column 4 the corresponding BER is given.

topology	nodes	sources	BER
1	9	20	$3.8 \cdot 10^{-6}$
2	8	20	$3.8 \cdot 10^{-6}$
3 ^I	6	14	$5.2 \cdot 10^{-7}$
3 ^{II}	6	19	$2.9 \cdot 10^{-6}$
4	6	20	$3.8 \cdot 10^{-6}$

TABLE I
CHARACTERISTICS OF THE LARGEST ROUTES. ^I ROUTE USING THE CORE-NETWORK. ^{II} ROUTE USING THE NEW LINKS.

topology	nodes	sources	BER
1 ^I	9	19	$2.9 \cdot 10^{-6}$
1 ^{II}	10	20	$3.8 \cdot 10^{-6}$
2	9	21	$5.0 \cdot 10^{-6}$
3	6	19	$2.9 \cdot 10^{-6}$
4 ^{III}	7	21	$5.0 \cdot 10^{-6}$
4 ^{IV}	7	22	$6.5 \cdot 10^{-6}$

TABLE II
CHARACTERISTICS OF THE LARGEST ROUTES. ^I USING THE SAME ROUTE. ^{II} USING A NEW LONGEST ROUTE. ^{III} REMOVED LINK IN THE CORE-NETWORK. ^{IV} REMOVED LINK IN A SUB-NET.

It can be concluded from Table 1 that *Topology 3* has the best error performance. This is related to the fact that this topology has the lowest number of interfering cross-talk sources.

B. With link failure

In the second case we consider the situation that link failures take place. As reflected in Table 2, link failures will affect the largest route. Similarly as in Table 1, the first column in Table 2 describes the topology discussed.

In *Topology 1* the link failure will not introduce an extra node in the route, but one source of cross-talk is removed. This situation is indicated in Table 2 by the upper-index I. Additionally, another route has become the largest path. This "new largest path" starts in the node marked as "in" and ends in the node marked as "out II". This situation is indicated in Table 2 by the upper-index II. It follows from Table 2 that this route has one additional node. The BER-performance of both cases are presented in Table 2.

In *Topology 4* there are two places where a link failure can occur without blocking the route. The situation marked with upper-index III indicates a link failure in the core-network, while in situation IV the failure occurs in a sub-network. The BER-performance of both situations are given in Table 2.

The second column of Table 2 contains the number of nodes in the largest routes. If we compare this result to the result presented in Table 1, we can conclude that "in average" the number of nodes has increased. As a result of this the number of cross-talk sources has also increased. This results is presented in the third column of Table 2. Finally, in column 4 the resulting BER is given.

V. CONCLUSIONS

We can conclude that inserting just a few, wisely placed, extra connections in the ring-only network (*Topology 3*) improves the operation reliability with respect to crosstalk. Introducing more links will make the route even shorter, but more sources of crosstalk can contaminate the signal.

In general these results indicate that a balance between the number of links and the error-performance with respect to cross-talk exists. It should be noted that it is crucial in the design of future all-optical networks to find an optimum topology with respect to in-band cross-talk.

VI. ACKNOWLEDGEMENTS

H.J.S. Dorren is with the KPN-TUE partnership.

REFERENCES

- [1] E. Goldstein and L. Eskildsen, "Scaling limitations in transparent optical networks due to low-level crosstalk," *IEEE Photon. Technol. Lett.*, vol. 1, no. 1, pp. 93-95, 1995.
- [2] I. Tafur, "Xtalk, analysis of crosstalk in optical crossconnect systems." Report on research at the Eindhoven University of Technology, Januari 1997.
- [3] M. Abramowitz and I. Stegun, *Handbook of Mathematical Functions with Formulas, Graphs, and Mathematical Tables*. Dover Publications, 1965.

Theoretical consideration on bandwidth and chirping in injection-locked semiconductor lasers

G. YABRE

COBRA, Interuniversity Research Institute
Eindhoven University of Technology, TTE Department, EH-12
PO Box 513 - 5600 MB Eindhoven - The Netherlands
G.Yabre@ele.tue.nl

1 Introduction

Microwave-millimeter wave (mw/mmwave) fiber/radio communications systems have recently emerged as an important application of lightwave technology [1]. The need for these high speeds arises mainly from the spectral congestion at lower frequencies and the increasing demand on transmission capacity. Since metallic cables exhibit extremely large losses at high frequencies, the direct electrical transportation of signals over distances of several kilometers as desired is roughly an impossible task. Electronic amplifiers may be used as countermeasure to reach the objectives. But this method may increase system cost and reduce reliability as electronic amplifiers are active devices. On the other hand, single-mode optical fibers offer an enormous bandwidth together with a very low attenuation allowing to carry mw/mmwave signals without regeneration through the distances of interest. Moreover, several different sites can be easily served from the same transmitter, which will contribute to reduce system installation and maintenance costs. It is also worth mentioning the electromagnetic interference (EMI) free transmission ability of optical fibers as an additional advantage over metal. Combining optical fiber with microwave technology is obviously an attractive alternative to supply customers with broadband services through wireless multiaccess links.

Future fiber/radio communications systems are intended to use an architecture in which the mw/mmwave signals are generated at a central switch (CS) and optically carried to base-stations (BS's) for wireless radiation to remote (fixed or nomadic) terminals. Therefore, using this technique, a large range of applications may be envisaged including mobile communications (mobile telephone, portable computer...), cordless links between a central server and workstations, and traffic guidance. An interesting option also exists for a mw/mmwave-link replacement of the so-called 'one last mile', thereby avoiding individual wiring from a central donor site. Another possible application of fiber-to-wireless transmissions systems is the provision of satellite entrance links through the deployment of a proper satellite-antenna at the CS. Because most the expected services require a bidirectional exchange, the proposed technology will be designed to permit full-duplex communications between the remote terminals and the CS. A simpler one-way exchange system may be implemented for pure distributed applications like television, but in considering the general trend to the integration of services, the full-duplex option should be adopted as the preferred choice.

Previous wireless multiaccess distribution services have typically operated in the neighborhood of 2.5 GHz. It is now commonly accepted to shift to frequency bands in the range of 26-70 GHz or more. It is clear that such high frequencies will put new requirements on the lightwave components which have to be used. One of the important requirements is a large modulation bandwidth in the transmitter laser diode as well as a low chirp in order to minimize dispersion-induced distortion in fiber. However, in addition to nonlinear distortion and noise,

conventional semiconductor lasers suffer from serious speed limitation and generally exhibit a tremendous frequency chirping. To by-pass these impairments within the downlink path, the mw/mmwave signals can be electrically generated and used to externally modulate a CW laser beam. Similarly, a large bandwidth external modulator may be employed in the transmitter module of the uplink scheme. Such modulators exist, but are, for instant, very expensive as a result of their manufacturing difficulty. An interesting option consists of all-optically generating the microwaves in the central switch. Several method may be implemented at this objective such as an adequate injection-locking of FM side modes [2] or the use of a WDM coupler in conjunction with a twin frequency optical source which emits at two wavelengths separated by the desired mw/mmwave frequency [1]. This approach effectively solves the problem of transmitter intrinsic bandwidth and chirp in the transmitting path from the CS. In the return path, however, both problems remain present when the remote user signals arriving at the BS have to be optically transported towards the CS. A solution has been proposed that aims at firstly lowering the frequency of uplink signals before their application to the laser diode [1]. Unfortunately, among other things, this will inevitably increase system cost and affect its reliability because additional active devices are required in the mixing technique. Obviously, it is of great interest if the system can be made less complex in circuit configuration. One way to achieve that is to make it possible the direct transmission of the mw/mmwave signals to the central switch without having recourse to the mixing solution. This is ideally feasible if the laser bandwidth and chirp can be, respectively, increased and reduced at the same time.

In this paper, we have theoretically shown that a proper external CW light injection into the cavity of the transmitting laser may flatten the frequency response and greatly enhance the modulation bandwidth available. Depending on the injection parameters, we have demonstrated that an increase in the bandwidth of more than a factor 2.8 may be practically achieved. This occurs most probably as a result of the coherent addition of the injected optical field with the laser optical field within the cavity, rather than by the increase in photon density. On a related matter, our analysis equally shows that as long as the parameters are adjusted to improve bandwidth, this is accompanied by a considerable broadband reduction in the chirp-to-power ratio (CPR). This result is also quite in line with the needs.

2 Computation results

For clear demonstration, numerical results will be given using the same theoretical model and physical parameters as displayed in [3, 4]. We consider a single-mode laser diode supposed to be biased at twice above its threshold current for oscillation. As far as optical injection-locking is concerned, the main parameters include the so-called injection level and the frequency detuning between the injected light and transmitted light in the solitary operation regime. Simulations of the laser in the locking condition are obtained for two injection levels of $s_i/s_0 = 0.2, 0.4$ and for a constant frequency offset $\Delta\nu_0 = -20$ GHz which is chosen in the dynamically stable locking range.

Simulation results of the normalized power transfer function are displayed in fig. 1 showing a comparison between the solitary laser and the same laser in two different locking conditions. As can be seen, the higher the injection level, the flatter the frequency response. The modulation bandwidth (defined as the frequency at which the response drops to -3 dB) is also found to greatly increase relative to the free-running operation case. Considering the curve obtained with the highest injection level in fig. 1 ($s_i/s_0 = 0.4$), we note a modulation bandwidth of 20.3 GHz against 7.3 GHz for the laser in the free-running condition. This approximately corresponds to a broadening factor of 2.8. But, at this regard, it must be precised that this number is certainly

not the maximum limit achievable. In fact, as pointed out in [3, 5], higher bandwidths can be obtained in the locking range for higher injection levels and less negative detunings. Through the use of commercially available laser diodes whose bandwidths cover 15 to 20 GHz or more, it should be possible, when operating the same lasers under optical injection, to extend this range to 26-70 GHz (or more), which is required for fiber-wireless communications systems as described earlier.

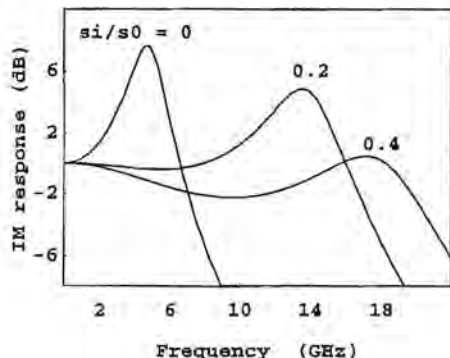


Fig. 1 Power responses normalized to the zero frequency value: Comparison between the solitary laser ($s_i/s_0 = 0$) and the same laser under two different injection-locking conditions for a fixed frequency detuning $\Delta\nu_0 = -20$ GHz.

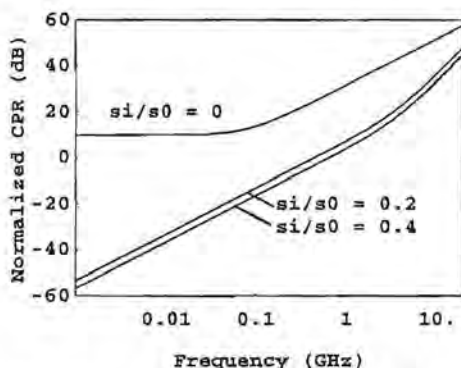


Fig. 2 Normalized chirp-to-modulated power ratio (CPR) as a function of the modulation frequency: Comparison between the free-running regime ($s_i/s_0 = 0$) and the injection-locked regimes of fig. 1.

Plots of the normalized chirp-to-modulated-power (CPR) are reported in fig. 2 as decibels versus the modulation frequency showing the effect of the injection levels in the same conditions as in fig. 1. The comparison between CPRs in absence and in presence of light injection is of great interest. Fig. 2 shows that the CPR significantly reduces when the laser operation is shifted from the free-running regime to an injection-locking state. It can be observed that the reduction in CPR is much more important in the low frequency region where the free-running characteristic is seen to settle at a constant value. Nevertheless, considering the characteristic obtained using an injection level of 0.4, we note a broadband reduction in CPR of more than 18 dB over the plotrange up to modulation frequencies above 10 GHz.

3 Conclusions

Theoretical investigations have been reported showing that the modulation bandwidth available in semiconductor lasers can be greatly enhanced by strong optical injection-locking. The chirp-to-modulated power (CPR) characteristics have also been considered as an important performance parameter. Our analysis reaches the conclusion that the CPR can be simultaneously improved as the injection parameters are chosen to achieve higher bandwidth. This is

equally a relevant result, meaning that an mw/mmwave signal can be transmitted through direct modulation of the laser diode without attracting the problem of dispersion-induced distortion in fiber. Optical injection technique is, therefore, ideally suited as an alternative to the speed limitation of semiconductor lasers.

It is worth mentioning that the above conclusions have been experimentally verified [5, 6]. In addition to bandwidth enhancement and chirp reduction offered by injection-locking, we expect that, by suitably choosing the parameters, it may be possible to reduce intrinsic intermodulation distortion [4]. It is also hoped that the locking regime will practically allow the reduction of intensity noise as the external lightwave to a large extent determines the noise characteristics [7]. This feature can be utilized at improving link performances or upgrading the capabilities of systems. Although earlier comments given in this paper were specifically focused on using injection-locking in fiber-to-cordless communications systems, the advantages offered by the technique can be extended to many other areas of applications of semiconductor lasers. We believe that implementation of the technique in future WDM or coherent lightwave systems may significantly contribute to enhance the transmission capabilities of the transmitter modules. Further work is to be undertaken to evaluate these potentials when injection-locking is implemented within real communications systems where the combined effect of the overall components involved in link can be addressed.

Acknowledgement

This work is done within the framework of the Dutch research project IOP Electro-Optics ongoing in COBRA, Interuniversity Research Institute, Eindhoven University of Technology. Helpful discussions with Prof. G. D. Khoe on the subject are acknowledged.

References

- [1] J. J. O'Reilly *et al.*, "Race R2005: microwave optical duplex antenna link," *IEE Proceedings-J.*, Vol. 140, pp. 385-391, 1993.
- [2] L. Goldberg, H. F. Taylor, J. F. Weller and D. M. Bloom, "Microwave signal generation with injection-locked laser diodes," *Electron. Lett.*, Vol. 19, pp. 491-493, 1983.
- [3] G. Yabre, "Effect of relatively strong light injection on the chirp-to-power ratio and the 3 dB bandwidth of directly modulated semiconductor lasers," *J. Lightwave Technol.*, Vol. 14, pp. 2367-2373, 1996.
- [4] G. Yabre and J. Le Bihan, "Reduction of nonlinear distortion in directly modulated semiconductor lasers by coherent light injection," *IEEE J. Quantum Electron.*, Vol. 33, pp. 1132-1140, 1997.
- [5] T. B. Simpson and J. M. Liu, "Enhanced modulation bandwidth in injection-locked semiconductor lasers," *IEEE Photon. Technol. Lett.*, Vol. 9, pp. 1322-1324, 1997.
- [6] S. Mohrdiek, H. Burkhard and H. Walter, "Chirp reduction of directly modulated semiconductor lasers at 10 Gb/s by strong CW light injection," *J. Lightwave Technol.*, vol. LT-12, pp. 418-424, 1994.
- [7] N. Schunk and K. Petermann, "Noise analysis of injection-locked semiconductor injection lasers," *IEEE J. Quantum Electron.*, Vol. 22, pp. 642-650, 1986.

Pulse Collision in Wavelength Division Multiplexed Optical Communication System

Hong Wang

Department of Electrical Engineering, Eindhoven University of Technology, PO Box 513
5600 MB Eindhoven, The Netherlands

Abstract: Several nonlinear factors limiting the capacity of a Wavelength-Division-Multiplexed system, such as Four-wave Mixing (FWM), Stimulated Raman Scattering (SRS) and Cross Phase Modulation (XPM), which all occur during the collision of pulses in different channels, are studied both in linear and soliton transmission system. Formula describing the power reduction and frequency shift caused by these three nonlinear effects during collision are derived and numerical calculation results are given.

1 INTRODUCTION

In recent years, optical multi-channel transmission system has been extensively studied because it is a practical and simple way to utilize the bandwidth of optical fiber and upgraded the constructed lines. Higher transmission power, low losses and dispersion are required to fully utilize the capability of silica fiber. In order to minimize dispersion and transmission loss penalties, dispersion shifted fiber is used. However, all these attempts can result in severe performance degradation due to optical nonlinearity in a single mode fiber, and it ultimately imposes a fundamental limitation on the capacity of optical system. The nonlinear effects are of particular concern in WDM system since these processes arise from the interaction between WDM channels.

In WDM systems, the simultaneous requirements of high launched power and low dispersion lead to the generation of new frequencies by FWM. These generated new frequency waves can produce inter channel interference and the frequencies of signal pulse are affected. The generated spurious side modes cause the depletion of the optical signal and the crosstalk. The system performance will be degraded when the fiber input power is high and/or the channel spacing is too small.

Besides FWM, the other nonlinear processes, SRS and XPM, also occur during collision between pulses with different wavelength. SRS not only provide gain to the longer wavelength channels at the expense of the shorter wavelength channels, but also provide gain to the higher frequency components at the expense of the lower-frequency components within one pulse. Consequently crosstalk between channels and signal frequency shift is induced. XPM can induce frequency shift of signal pulse

because the refractive index is intensity dependent. Frequency shifts of signal pulse caused by the three nonlinear process will lead to timing jitter at the transmission end. Most of previous studies on FWM were based on continuous wave theory. In fact, FWM during a collision between pulses is much more complicated than that of continuous waves. So we study the three nonlinear effects through pulse-pulse collision. In this paper, analytic expressions describing variance of power and frequency shift of signal pulse due to FWM, SRS and XPM for both soliton and Gaussian pulses are derived. Some useful conclusions and discussion are given.

2 THEORETICAL TREATMENT

For simplicity, we study only a pair of pulses with different wavelength traveling together along the fiber. In our model, lumped Erbium-doped fiber amplifiers (EDFA) are used to compensate for the transmission loss. The two pulses of different wavelength travel in the fiber with different velocity. During their collision (when the slower one is in the front of the faster one), mutual interaction involving FWM, XPM and SRS occur. One of the coupled normalized wave envelop equations describing the evolution the two pulses' system are as following:

$$i \frac{\partial u_1}{\partial z} - \frac{1}{2} \frac{\partial^2 u_1}{\partial t^2} + B^2(z) |u_1|^2 u_1 - C_x - C_F - C_S = 0 \quad (1)$$

We can get the equation for the other pulse u_2 by exchange the subscribe 1 and 2, $\Delta\beta$ and $\Delta\beta'$. u_1 and u_2 are the envelop functions of the two pulses and C_F , C_S and C_X represents the FWM, SRS and XPM effects respectively. The third term in above equation represents the self-phase-modulation (SPM) effects. It is well known that SPM leads to spectral broadening of optical pulse. In this paper, we only pay our attention to the other three effects (XPM, FWM and SRS) which occur in WDM system. According to the typical value of SRS gain spectrum, we have $\delta=0.00297/t_c$, in which t_c is the time unit, $t_c=\tau_{FWHM}/1.763$. $B(z)$ is a periodic function satisfying:

$$dB(z)/dz = P(z)B(z) \quad (2)$$

$$B^2(z) = \sum_{n=M}^N H(z - nL_a) \quad (3)$$

and $H(z)$ is given by

$$H(z) = \frac{2\Gamma L_a \exp(-2\Gamma z)}{1 - \exp(-2\Gamma L_a)} \quad (0 \leq z < L_a) \quad (4)$$

$$C_S = \delta B^2(z) [u_1 \frac{\partial}{\partial t} |u_1|^2 + u_1 \frac{\partial}{\partial t} |u_2|^2 + u_2 \frac{\partial}{\partial t} (u_1 u_2^*)] \quad (5)$$

$$C_F = -\frac{B^4(z)}{\Delta\beta L_D} [(1 + \frac{iP(z)}{\Delta\beta L_D}) |u_2|^4 u_1 + \frac{i}{\Delta\beta L_D} u_2^2 \frac{\partial}{\partial z} (u_2^* u_1)] \\ - \frac{2B^4(z)}{\Delta\beta' L_D} [(1 - \frac{iP(z)}{\Delta\beta' L_D}) |u_1|^2 |u_2|^2 u_1 \\ - \frac{i}{\Delta\beta' L_D} u_1^* u_2 \frac{\partial}{\partial z} (u_1^2 u_2^*)] \quad (6)$$

$$C_S = \delta B^2(z) [u_1 \frac{\partial}{\partial t} |u_1|^2 + u_1 \frac{\partial}{\partial t} |u_2|^2 + u_2 \frac{\partial}{\partial t} (u_1 u_2^*)] \quad (7)$$

$$C_x = -2B^2(z) |u_2|^2 u_1 \quad (8)$$

Where L_a is the amplifier spacing, Γ is the normalized fiber loss coefficient, z is the normalized transmission distance. $\delta(x)$ is the Dirac delta-function, M and N are determined by the initial and end position of the collision. We assume that neither of the frequencies of signal channels is located at the zero-dispersion point $P(z)$ is the periodic function representing the fiber loss and periodically lumped amplification.

$$P(z)U_{1,2} = -\Gamma U_{1,2} [\exp(\Gamma L_a) - 1] \times \\ \sum_{n=M}^N \delta(z - nL_a) U_{1,2}(nL_a - 0, t) \quad (9)$$

1. Frequency shift and power variance:

Since one pulse can be characterized by the amplitude and frequency, the variance of them can show the effects of nonlinearity and higher order dispersion on the system

The normalized central frequency of signal pulse u_1 is:

$$\Omega_c = \frac{\int_{-\infty}^{\infty} \text{Im}(\partial u_1^* u_1) dt}{\int_{-\infty}^{\infty} |u_1|^2 dt} \quad (10)$$

The central frequency shift of pulse u_1 with transmission distance is [2]:

$$\frac{d\Omega_c}{dz} = -\frac{i}{2} \frac{d}{dz} \int_{-\infty}^{\infty} (u_1 \frac{\partial u_1^*}{\partial t} - u_1^* \frac{\partial u_1}{\partial t}) / \int_{-\infty}^{\infty} |u_1|^2 dt \Big|_{z=0} \\ = -2 \int_{-\infty}^{\infty} \text{Re}[h \frac{\partial u_1^*}{\partial t}] / \int_{-\infty}^{\infty} |u_1|^2 dt \Big|_{z=0} \quad (11)$$

where

$$h = C_F + C_S + C_x - B^2(z) |u_1|^2 \quad (12)$$

The power change is [2]:

$$\frac{dP}{dz} = \frac{d}{dz} \int_{-\infty}^{\infty} |u_1|^2 dt / \int_{-\infty}^{\infty} |u_1|^2 dt \Big|_{z=0} \\ = 2 \int_{-\infty}^{\infty} \text{Im}(h u_1^*) dt \quad (13)$$

2. Soliton system:

The solution of Eqn.(1) with $C_F=0$ and $C_S=0$ is expressed approximately as:

$$u_1(z, t) = \text{sech}(t + \Omega z + T_0) \exp(-i\Omega t + i\phi) \quad (14)$$

$$u_2(z, t) = \text{sech}(t - \Omega z - T_0) \exp(i\Omega t + i\phi) \quad (15)$$

where 2Ω is the normalized angular frequency difference between the two solution pulses, T_0 is the initial position of pulses on time frame and

$$\frac{d\phi}{dz} = B^2(z) - (1 + \Omega^2)/2 \quad (16)$$

After taking (14) and (15) into (11) and (13), we obtain the expressions for the frequency shift and power variance due to FWM., SRS and BPM respectively.

$$\frac{d\Omega_{S,x}}{dz} = -4B^2(z)g_1 \quad (17)$$

$$\frac{d\Omega_{S,F}}{dz} = \frac{B^4(z)}{3L_D^2\Delta\beta^2} [4(\Omega + \frac{L_D\Delta\beta}{\Omega})g_1 + \\ (\frac{5\Delta\beta L_D}{4\Omega^2} - 1) \frac{\partial^2 g_1}{\partial z^2} + 8P(z)\Omega g_2 - 2P(z) \frac{\partial g_1}{\partial z}] \quad (18)$$

$$\frac{d\Omega_{S,S}}{dz} = -\delta B^2(z) \left[\frac{8}{15} + \frac{2}{3}(6\Omega^2 + 1)g_2 + \frac{11}{6\Omega}g_3 \right] \quad (19)$$

$$\frac{dP_{S,F}}{dz} = -\frac{B^4(z)}{3L_D^2\Delta\beta^2} \times [4g_1 - 8P(z)g_2 + 2\frac{P(z)}{\Omega}\frac{\partial g_1}{\partial z} + \frac{1}{\Omega}\frac{\partial g_1^2}{\partial z^2}] \quad (20)$$

$$\frac{dP_{S,S}}{dz} = -8\delta\Omega B^2(z)g_2 \quad (21)$$

(17), (18) and (19) are the frequency shift of the soliton pulse u_i caused by XPM, FWM, and SRS. (20) and (21) are the power variance with transmission distance of the same pulse due to FWM, and SRS.

3. Gaussian pulses:

The solution of Eqn. (1) For a Gaussian pulses transmission system is expressed approximately as :

$$u_1(z,t) = \exp\left[-\frac{1}{2}\left(\frac{t+\Omega z+T_0}{\tau}\right)^2\right] \exp(-i\Omega z+i\phi) \quad (22)$$

$$u_2(z,t) = \exp\left[-\frac{1}{2}\left(\frac{t-\Omega z-T_0}{\tau}\right)^2\right] \exp(i\Omega z+i\phi) \quad (23)$$

where τ is the pulse width. Similarly we have the following expressions :

$$\frac{d\Omega_{G,X}}{dz} = -\frac{2\sqrt{2}z}{\tau^2} B^2(z) \exp(-2\Omega^2 z^2/\tau^2) \quad (24)$$

$$\frac{d\Omega_{G,F}}{dz} = \frac{B^4(z)}{3\sqrt{3}\tau^2\Delta\beta^2 L_D^2} \exp\left(-\frac{8\Omega z}{3\tau^2}\right) \times [3P(z)\Omega\tau^2 - 8(L_D\Delta\beta + \Omega^2)\Omega z] \quad (25)$$

$$\frac{d\Omega_{G,S}}{dz} = -\frac{1}{\sqrt{2}} \delta B^2(z) \left[\frac{1}{\tau^2} + (2/\tau^2 - 4\Omega^2 z^2/\tau^4 + 4\Omega^2) \times \exp(-2\Omega^2 z^2/\tau^2) \right] \quad (26)$$

$$\frac{dP_{G,F}}{dz} = \frac{B^4(z)}{\sqrt{3}\Delta\beta^2 L_D^2} \left[P(z) - \frac{8\Omega^2 z}{3\tau^2} \right] \exp\left(-\frac{8\Omega z}{3\tau^2}\right) \quad (27)$$

$$\frac{dP_{G,S}}{dz} = -2\sqrt{2}\delta\Omega B^2(z) \exp(-2\Omega^2 z^2/\tau^2) \quad (28)$$

(24), (25) and (26) are the frequency shift of the Gaussian pulse u_i caused by XPM, FWM and SRS. (27) and (28) are the power variance with transmission distance of the same pulse due to FWM and SRS. XPM only affect the pulse on frequency field.

3. CALCULATION RESULT AND DISCUSSION:

The frequency shift caused by FWM is a short-range process because it only occurs during the collision period. The signal pulse gives power to the spurious contemporary pulse, which is composed of the new mixing frequency components. After collision, the signal pulse not only loss a little power, but also has a frequency shift. The frequency shift caused by SRS consists of two parts, one parts is the self-frequency shift, which is a long-range process and occurs between the frequency components of one pulse itself. The higher frequency components give some power to the lower frequency components and finally cause the central frequency to shift. It exist all along the whole transmission line and shift the pulse central frequency to red evenly and continuously. The other part is a short-range process caused by the mutual interaction between pulses. The pulse at higher frequency give a little power to the pulse at lower frequency and its central frequency shifts. XPM is also a short-range process, which only exist during the collision between pulses of different channels, and induce frequency shift of signal pulse [1]. The mutual interaction is sensitive to the severe change of pulse power, such as lumped amplifying. FWM, short-range SRS and XPM affects the pulse frequency and power differently in the approaching close course and the departing apart course. The amplifier appeared during collision course affect the final frequency shift and power variance. In practical system, it is impossible to keep the relative position between amplifier and collision center constant. So the frequency shifts and power variances of different collision are different and varied randomly within a range. Here we just give one collision as an example.

By use of above equations (17) -(28), we calculate the frequency shift and power variance of the pulse with higher frequency of the colliding pulse pair in one collision. We assume that the collision is complete, in other words, initially the two pulses are separate completely. In a practical transmission line except that at the beginning and the end, all collision are complete.

Fig.1-a and 1-b shows the frequency shift of a solution and Gaston pulse due to F.M. in one collision respectively. Fig.2 and Fig.3 shows the frequency shift and power variance of a solution pulse due to SR. The specific parameters used are: pulses FWHM width $\tau_{FWHM}=10$ ps, channel spacing $\Delta\lambda=0.6$ nm, wavelength

$\lambda=1.55\mu\text{m}$, fiber dispersion $D=1.0\text{ps/km/nm}$, fiber loss coefficient $\alpha=0.25\text{dB/km}$ and amplifier spacing $L_a=30\text{km}$, which is almost the same as the collision length (33km). The collision center is at about 5.0 (normalized).

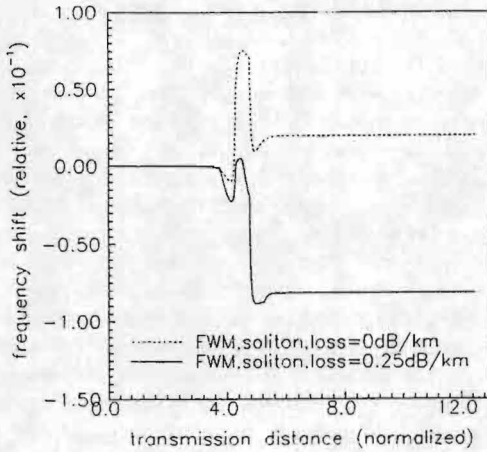


Fig.1-a The frequency shift of soliton pulse due to FWM during a collision.

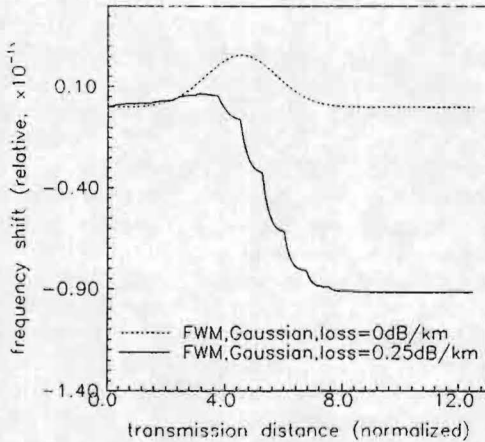


Fig.1-b The frequency shift of Gaussian pulse due to FWM during a collision.

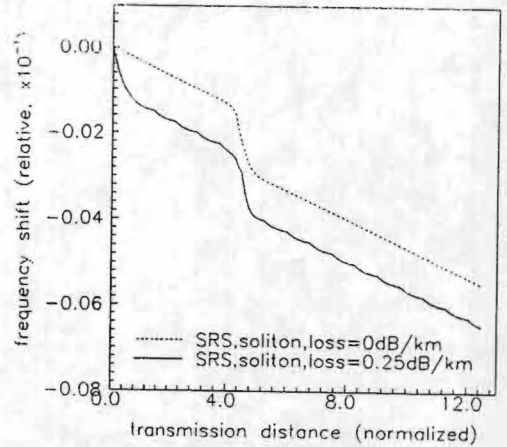


Fig.2 The frequency shift of soliton pulse due to SRS during a collision.

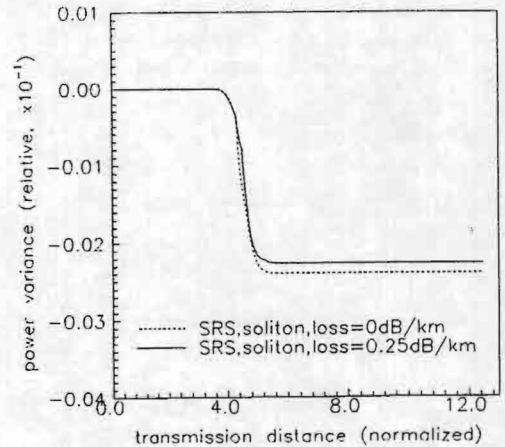


Fig.3 shows the power variance of a soliton pulse due to SRS during a collision.

4.CONCLUSION

We analyzed the collision between pulses of different channel, which is unavoidable in WDM system and involve three important nonlinear process: FWM, SRS and XPM. Formula describing frequent shift and power variance of signal pulses experienced during collision are given .

REFERENCE:

- [1]L.F.Mollenauer and S.G.Evangelides et al.J.Ligh. Tech. Vol. 9, No.3, March 1991.
- [2] Yuji Kodama et. Al. IEEE J. QE Vol. QE-23, No. 5, May 1987.

Crosstalk analysis of an OXC based on a broadcast and select optical space switch

Tim Gyselings, Geert Morthier, Roel Baets

Department of Information Technology, University of Gent - IMEC,

Sint-Pietersnieuwstraat 41, B-9000 Gent, Belgium

Tel: +32 9 2643316 - fax: +32 9 2643593

email: tim.gyselings@intec.rug.ac.be

We present the results of a crosstalk analysis for an optical WDM cross connect based on a broadcast and select principle. The analysis is based on analytical calculations and verified with numerical simulations. Dependencies on individual components and possible optimisations are discussed.

I. Introduction

Optical WDM networks make use of optical cross connects (OXC) to route the signals through the network. In this all optical component, a lot of signals and wavelengths come together and interact with each other. These interactions cause crosstalk ([1], [2]).

Crosstalk seems to be one of the major problems in the OXC, resulting in signal degradation. Because of the complexity of an OXC, different sources of crosstalk exist, which makes it difficult to optimise the component parameters for minimum total crosstalk. In this paper an analytical equation is presented which describes the output power of a broadcast and select optical space switch as a function of the input powers and the component parameters. The results are compared with results obtained with numerical simulations. In the last part the influence of the two major component parameters on the crosstalk is studied.

II. OXC Topology

Several topologies exist for all optical cross connects. The topology we discuss here is based on a broadcast and select optical space switch without wavelength conversion (*Figure 1*). The N input fibres are routed to the desired N output fibres, each carrying M wavelength channels. A $N \times NM$ space switch is used to route the signal to the desired output fibre. This switch is based on passive splitters (N), gates ($N^2 \times M$) and combiners ($N \times M$) (*Figure 2*). The gate is implemented as a gain-clamped semiconductor optical amplifier (GC-SOA). After this switching part, the correct wavelength is selected with a Fabry-Perot filter. Finally, N time M filter outputs with a different central wavelength, are combined into the N output fibres.

III. Crosstalk Sources

Crosstalk results in a reduction of the signal quality. The gate adds crosstalk due to non perfect gain clamping in the amplifier, because the gain dynamics of the GC-SOA depend on the total input power. The output of the gate can be modelled as $P_{out} = P_{in} + P_{cros}$ if the amplification of the gate is neglected. The crosstalk power at wavelength i is given by:

$$P_{cros,i} = X_{sw} P_{in,i} \sum_{k=1}^M P_{in,k} \quad (1)$$

with X_{sw} the crosstalk parameter of the GC-SOA [3]. At the combiner after the gates crosstalk is added due to a non perfect blocking of the gate (on/off ratio). The filter suppresses the other channels, but the resulting power interferes with the signal power at the last combiner, resulting in crosstalk.

If signals with the same wavelength are combined, they can interfere coherently or non coherently depending on their phase difference. In this paper two situations are studied. First the case of non coherent interference. It is assumed that the different input channels interfere non coherently, but the power of one channel which is split up at the input and combined at the output combines coherently. In the second case the assumption is made that all channels with the same wavelength interfere coherently. We will call this full coherent interference.

IV. Analytical Expression of the Crosstalk

We present an analytical expression which gives the output power as a function of the input power and of the component parameters. Based on such an equation the influence of a certain parameter on the crosstalk can be studied easily.

The signal power is defined by P_i^j , where i designates the wavelength and j the number of the fibre. The fibre which contains the signal under study is indicated j_0 , the wavelength i_0 . For this equation, we suppose that all powers on channels different from the channel under study $P_{i_0}^{j_0}$ are equal. $M' + 1$ wavelengths from fibre j_0 are switched to the same output fibre. Losses and gains are not taken into account. The on/off ratio of the gate is given by R_{sw}^{-1} . The suppression of an other wavelength by the filter is given by T_F^{-1} .

Below the equation is given in the case of full coherent crosstalk. The equations in the other case can be easily derived from this one.

$$\begin{aligned}
 P_{i_0}^{out} = & P_{i_0}^{j_0} + \\
 & + P_{i_0}^{j_0} \{ X_{sw} ((M-1)P_{i_0}^{j_0} + P_{i_0}^{j_0}) + M' T_F [1 + X_{sw} ((M-1)P_{i_0}^{j_0} + P_{i_0}^{j_0})] \} + \\
 & + P_{i_0}^j \{ (N-1)R_{sw} + (M-M'-1)T_F [1 + X_{sw} M P_{i_0}^j] + 2R_{sw} \left(\sum_{i=1}^{N-2} t \right) + \\
 & + (M-M'-1)2T_F \sqrt{R_{sw}} (N-2) + 2T_F \left(\sum_{i=1}^{N-2} t \right) \} + \\
 & + \sqrt{P_{i_0}^{j_0}} \sqrt{P_{i_0}^j} \{ 2\sqrt{R_{sw}} (N-1) + 2M' (N-1)T_F \sqrt{R_{sw}} + \\
 & + 2(M-M'-1)T_F \sqrt{R_{sw}} \} + \\
 & + \sqrt{P_{i_0}^{j_0}} \{ 2M' \sqrt{T_F} \sqrt{[P_{i_0}^{j_0} + 2\sqrt{R_{sw}} (N-1) \sqrt{P_{i_0}^{j_0}} \sqrt{P_{i_0}^j}]} + \\
 & + \sqrt{P_{i_0}^j} \{ 2(M-M'-1) \sqrt{T_F} \sqrt{[P_{i_0}^{j_0} + 2\sqrt{R_{sw}} (N-1) \sqrt{P_{i_0}^{j_0}} \sqrt{P_{i_0}^j}]} \}
 \end{aligned} \tag{2}$$

The first term contains the input power. The output power would be equal to the input power if no interaction with the other channels existed. The second term contains the crosstalk of the GC-SOA and a contribution due to the other possible routing ways. The third term contains contributions due to the input channels with the same wavelength on other input fibres. The coherent interference in the combiners results in the other three terms. It can be remarked that the first part of the fifth term holds the coherent interference which is taken into account in the non coherent case.

V. Results

The crosstalk value obtained with the equations is compared to results of numerical simulations. The crosstalk is calculated as the output of a simulation / analytical calculation with all input powers minus a simulation / analytical calculation with only one signal at the input divided by the output with only one signal at the input. The parameters used for the calculations are given in *Table 1*.

R_{sw}	- 40 dB	M	4
X_{sw}	- 0.1 mW ⁻¹	M'	1
T_F	- 25 dB	N	2
P input (1)	-15 dBm		

Table 1

The input power for a one is chosen very low. This is because no gain or loss is taken into account, but the crosstalk due to the GC-SOA depends on the absolute power value. The power value of -15 dBm is a normal input value for a gate. We expect higher analytical crosstalk than numerical crosstalk because in the simulation the suppression of non adjacent channels is higher. In our simulations there was one non adjacent channel (four wavelengths and the crosstalk was calculated at one of the centre wavelengths).

Figure 3 gives the crosstalk as function of the input power for non coherent (two lines at the bottom) and full coherent crosstalk (two lines at the top). The crossed lines are the results of simulations, the ringed lines the analytical results. These values are statistical values. M' has been varied between M-1 and 0, and the number of ones in the other channels has also been varied. The results presented in *Figure 3* are the average.

The first effect which can be mentioned from *Figure 3* is that the crosstalk declines for higher input power. This is due to the crosstalk of the GC-SOA, which compensates for the other crosstalk sources. The saturation of the GC-SOA has not been included in the calculations however.

Further more, it can be seen that as expected the crosstalk predicted by the equations is higher than the results of the simulations. To check the statement that this is due to the filter, the result of a calculation with three wavelengths is also shown in *Figure 3* (normal line). The simulated crosstalk is between this result and the result with four wavelengths, which proofs the statement.

More important is the big difference between coherent and non coherent crosstalk. Some of the coherent terms in equation (2) are only reduced by a factor of $\sqrt{T_F}$ and they give rise to high coherent crosstalk. But this coherent crosstalk is due to interference of channels of different input fibres and can strongly be reduced if the channels are not phase matched.

The effect of the filter parameter on the crosstalk is given in *Figure 4*, for different on/off ratios (analytical crosstalk). The calculation is done with M' = 1 and all ones at the other channels. The crossed lines are for full coherent crosstalk, the other are for non coherent crosstalk. One can conclude that as expected from equation (2) the filter parameter has a large impact on the coherent crosstalk and the suppression should be as large as possible. The on/off ratio is less important in terms of crosstalk as long as it is higher than 40 dB.

VI. Conclusion

An analytical equation was derived for the crosstalk of an OXC based on the broadcast and select principle. Good qualitative agreement between the analytical approach and more detailed numerical simulations have been demonstrated. The absolute crosstalk value is overestimated in the analytical approach.

A big difference between coherent crosstalk and non coherent crosstalk has been observed. To reduce this coherent crosstalk, filters with high suppression of the other wavelengths are required. If this is not enough, phase scramblers should be placed before the combiner.

VII. References

- [1] A. M. Hill, D. B. Payne, "Linear crosstalk in wavelength-division-multiplexed optical fibre transmission systems", Jour. Lightwave Tech., Vol LT-3, N 3, June 1995.
- [2] J. Zhou, et. al., "Crosstalk in multiwavelength optical cross connect networks", Jour. Lighthwave Tech., Vol 14, N 6, June 1996.
- [3] J. Sun, G. Morthier, R. Baets, "Numerical and theoretical study of the crosstalk in gain clamped semiconductor optical amplifiers", to be published, Jour. Selected Topics in Quantum Electronics

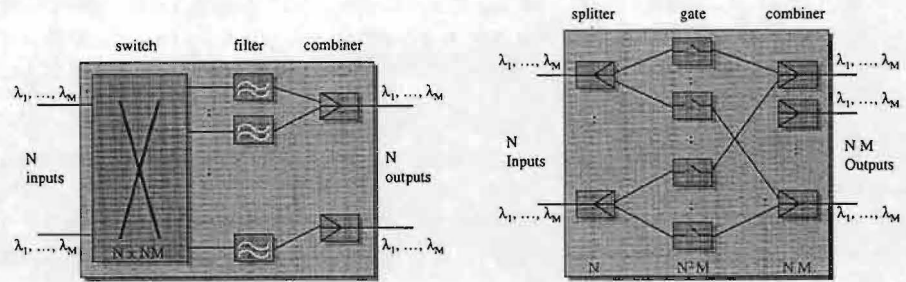


Figure 1: Left: Topology of a broadcast and select optical space switch

Figure 2: Right: Topology of the space switch based on splitters, gates and combiners.

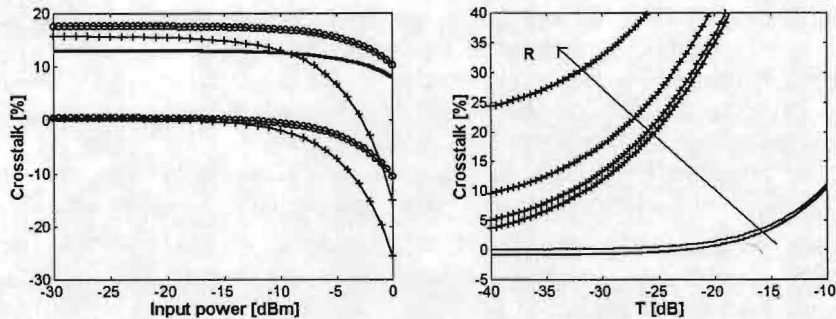


Figure 3: Left: Crosstalk as function of the input power. The crossed lines are the simulation results, the ringed lines the analytical results. The two lines with the highest crosstalk are for full coherent crosstalk. The two bottom lines are for non coherent crosstalk. The single line is for the case of $M=3$.

Figure 4: Right: Crosstalk (analytical) as function of the filter parameter for different on/off ratios ($R = -20$ dB, -30 dB, -40 dB and -50 dB). Crossed lines are for full coherent crosstalk, normal lines for non coherent crosstalk.

Meshed Wavelength Division Multiplexed Networks partially equipped with wavelength converters

W. Van Parys, B. Van Caenegem, B. Vandenberghe, P. Demeester

Department of Information Technology, University of Gent - IMEC

Sint-Pietersnieuwstraat 41, B-9000 Gent, Belgium

Tel: +32 9 264 34 46, Fax: +32 9 264 35 93, E-mail: wim.vanparys@intec.rug.ac.be

Abstract

The impact on the network performance by putting a limited number of wavelength converters in the optical cross-connect is assessed. A major conclusion is the good performance of an optical cross-connect architecture with a limited "pool" of wavelength converters.

Introduction

A lot of work has been reported on the use of wavelength converters (WCs) in Wavelength Division Multiplexed (WDM) Networks. Recent research indicates that for a wide variety of applications the use of WCs in WDM networks results only in modest improvements in throughput, compared to networks without WCs¹. It has been observed that a limited set of nodes equipped with WCs can give almost equal performance as a Virtual Wavelength Path Network, where all nodes are fully equipped with WCs². Furthermore, it has been shown that already a limited form of wavelength conversion can enhance the performance of WDM ring networks³. Former work indicates that a limited number of converters should be sufficient to provide decent performance⁴. This paper reports the impact of two different architectures for the optical cross-connect (OXC), containing a limited number of WCs, on the performance of meshed WDM networks.

Approach and Assumptions

Two architectures for the OXC, embedding a limited number of wavelength converters, are considered:

- (1) an OXC containing a "pool" of WCs, where a free WC can be used by any incoming channel (Type I, see figure 1a)
- (2) an OXC where the WCs are dedicated to a particular channel, conversion occurs before the signal is multiplexed on the outgoing fibre. (Type II, see figure 1b)

In case of the WC-pool two types of WCs are considered :

- (1) a “coloured” WC for which the inlet signal on a random wavelength is converted to a fixed outlet wavelength. Note that this type is the only choice for the second OXC architecture (figure 1c)
- (2) a “white” WC able to convert any incoming wavelength to any outgoing wavelength, within the range of operation. (figure 1d)

The technical implications of both OXC architectures and WC types are beyond the scope of this work, we focus on the impact of these options on the performance of the network.

In general, the difference in network performance is small between a Wavelength Path network (no WCs) and a Virtual Wavelength Path network (with WCs) for an optimised routing under static traffic conditions¹. Because of this, the impact of the options mentioned above is evaluated on a static routing problem for a worst-case⁵ topology and corresponding traffic, as depicted in figure 2. A simple routing strategy exploring the K (e.g. 5, 10) shortest paths, trying to minimise the usage of the WCs while maximising throughput, is used. The routing evaluates sequentially for all connections the availability to accommodate the request on a Wavelength Path, i.e. a path using the same wavelength on all links, before evaluating the availability of a path making use of one or more WCs.

Discussion of results

The results are shown in figure 3. The network performance, represented by the throughput of the load, is depicted as a function of the percentage of WCs in the nodes for the options considered. Increasing the number of “coloured” WCs is done systematically by adding a WC converting to wavelength 0, then one converting to wavelength 1,... Nodes with a type II architecture offer limited routing flexibility, as a result only small improvement is noted for a substantial percentage of WCs. Contrary, the type I architecture with the pool of converters performs well, maximum throughput is achieved for 1/3 of “coloured” WCs. This corresponds with a complete set of converters, one for each wavelength used in the network. Inherent to a pool of “coloured” WCs, a mismatch in “colour” occurs when the “colour” of a free WC does not match the required “colour” to set-up a connection. Consequently, only a part of the “coloured” WCs in the pool is used and equal performance is achieved for a substantial smaller number of “white” WCs.

Conclusions

In conclusion, we observed, based on a worst-case topology, that a limited pool of WCs can significantly improve the network performance. A further reduction on the number of converters required in the pool can be achieved by making use of “white” WCs.

Acknowledgement

The ACTS projects AC066 OPEN and AC084 PHOTON are acknowledged.

Figures

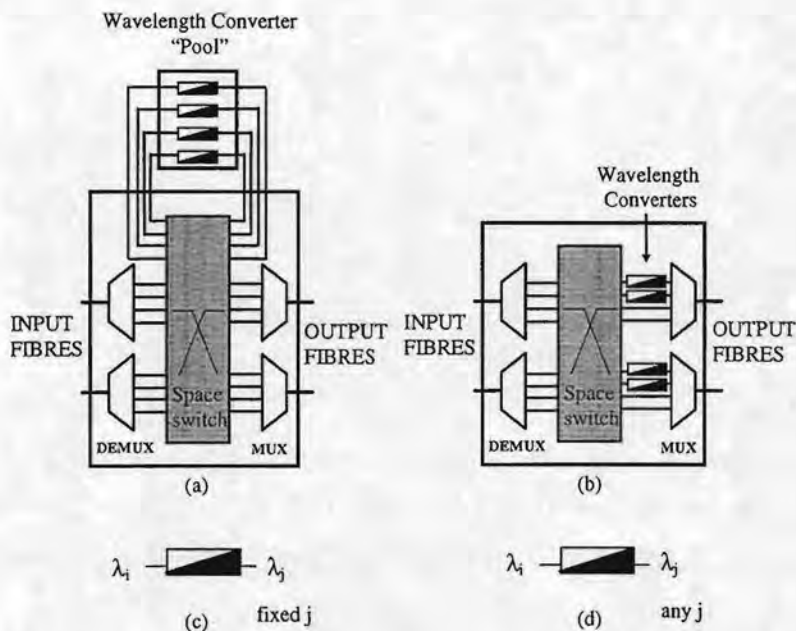


Figure 1: Two optical cross-connect architectures with a limited set of wavelength converters (a) and (b). Figure (c) shows a “coloured” wavelength converter able to convert a signal on a random inlet wavelength to a fixed outlet wavelength and figure (d) shows a “white” wavelength converter able to convert any incoming wavelength to any outgoing wavelength.

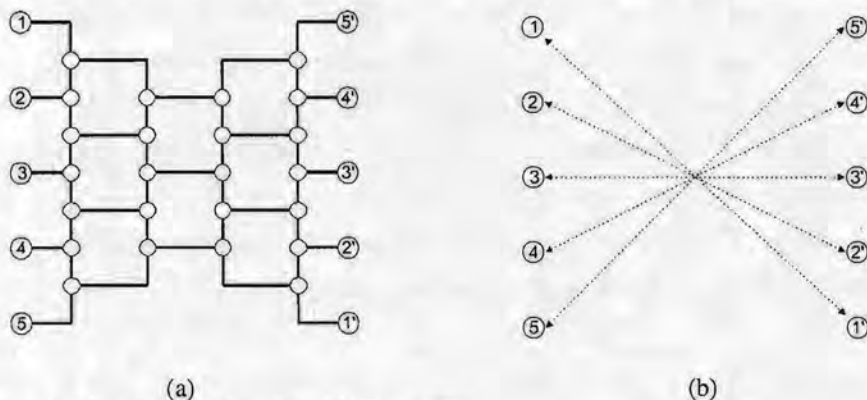


Figure 2 : Worst-case network and load pattern.

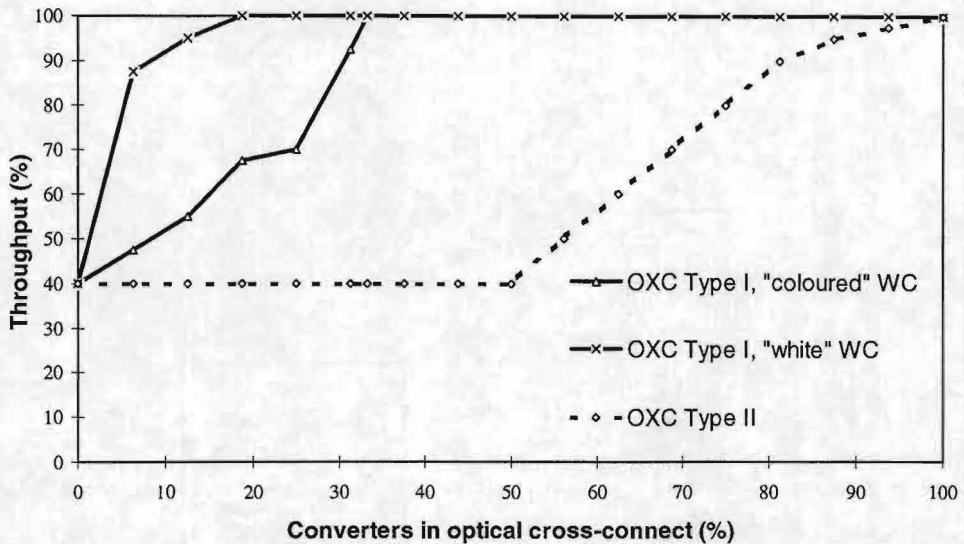


Figure 3 : Results for the described routing strategy applied on the worst-case network with 16 wavelengths per fibre and a load with capacity 8 for all connections. A limited set of wavelength converters in a pool configuration gives Virtual Wavelength Path performance.

References

1. N. Wauters, P. Demeester, "Wavelength Translation in optical multi-wavelength multi-fibre transport networks", Journal of Optoelectronics, Vol 11, No 1, pp 53-70, '97
2. N. Wauters, W. Van Parys, B. Van Caenegem, P. Demeester, "Reduction of wavelength blocking through partitioning with wavelength converters", OFC '97, pp122-123, Feb '97
3. R. Ramaswami, G. H. Sasaki, "Multiwavelength Optical Networks with Limited Wavelength Conversion", Infocom 97, April '97
4. K. C. Lee, V. Li, "A wavelength-convertible optical network", IEEE Journal of Lichtwave Technology, Vol 11. NO. 5, pp 962-970, 1993
5. A. Aggerwal et all, "Efficient routing and scheduling algorithms for optical networks", in proc. 5th Annual ACM-SIAM Symp on Discrete Algorithms, pp. 412-423

Implementation approaches for spare capacity in meshed WDM transport networks

B. Van Caenegem, B. Jacobs**, P. Demeester**

**Dep. of Information Technology, Univ. of Gent - IMEC,
Sint-Pietersnieuwstraat 41, B-9000 Gent, Belgium*

Tel: +32 9 264 34 46, Fax: +32 9 264 35 93,

E-mail: bart.vancaenegem@intec.rug.ac.be

***Deutsche Telekom, Technology center*

Am Kavalleriesand 3, 64295 Darmstadt, Germany

Tel: +49 6151 83 6842, Fax +49 6151 83 4572

Abstract

Two implementation approaches for spare capacity in a meshed WDM transport network are compared in terms of required resources and operation. One approach is based on overlaying spare rings, the other approach on spare channels.

Introduction

Today's transport networks are based on SDH and the transmission is done on optical fibre, however mostly in a single channel with bitrates up to 2.5 Gbit/s (STM-16). Thanks to the Wavelength Division Multiplexing (WDM) technology, several channels can be multiplexed together in one single fibre. Commercially available systems using 32 channels are announced for the near future. As traffic is increasing fast nowadays, operators are upgrading the capacity in the transport network often by adopting WDM for the transmission because it is more economical or there is a shortage of fibres in the existing links. Lab experiments have shown the feasibility of transmitting 2.6 Tbit/s (i.e. 132 channels, each carrying 20 Gb/s information) through a single fibre [1]. As traffic increases, optical switching will be used in the crossconnects as well to better cope with the high throughputs in the nodes.

By using WDM a lot of traffic is carried through one fibre which makes a fibre break already dramatic. Therefore, effective survivability means must be applied to recover from network failures. In [2] survivability strategies are described. Protection as well as restoration can be used, either adjacent to the failure or rather end to end by path.

In this paper we discuss two technical options to implement spare capacity in a WDM meshed network. One is based on overlay rings with spare fibers. The other is based on spare capacity in the meshed network.

Network architecture

In general, ring structures are very attractive for its simple node architectures and its built-in survivability features (protection). However the resources' usage is less efficient as is the case in meshed structures. We consider a meshed network with routed traffic. Figure 1.a shows four nodes and three links of the network. We assume bidirectional links, using one fibre per direction; in each link 1, 2 and 3 one fibre pair is present. The node architecture of the bold node looks like in figure 1.b. The links are folded out in a way that the input fibers can be shown at the left handside, the output fibres at the right handside of the space switch. Local traffic can be added and dropped.

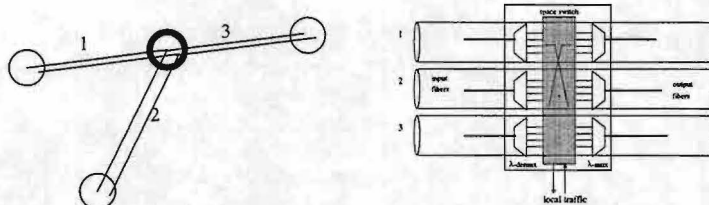


Figure 1: a. part of network and b. OXC architecture

We assign spare capacity for restorability in case of single link failures. To benefit from the ring structure, the spare capacity can be implemented in rings overlaying the meshes. The ring can be realised using the same links as the meshed network. In figure 2.a the ring is laid in links 1 and 2. In case that link 1 breaks, the complementary part to link 1 of the spare ring is used for restoration. Complete fibres are switched to the spare ring. A practical node implementation is shown in figure 2.b. Notice the simple implementation, using 1 by 2 switches. In normal conditions the spare ring is connected through in every node, and no intermediate configuration of switches is required. Restoration with this implementation is only valid for link restoration of complete fibres.

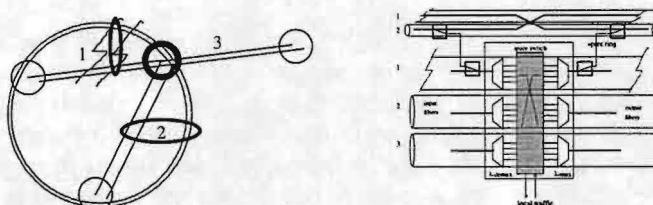


Figure 2: a. part of network and b. OXC architecture with overlaying spare ring

Another approach for implementing the spare capacity is embedding the spare channels in the meshed structure of the network. In this case, the node switch must be dimensioned for both working and spare channels. The node architecture is shown in figure 3, under the assumption that in link 3 a spare fibre pair is required.

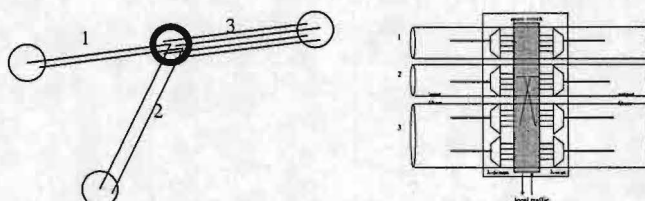


Figure 3: a. part of network and b. OXC architecture with spare channels

With this implementation spare capacity can also be used for other purposes as for accomodating traffic growth for instance, since the spare capacity can be used as flexibly as the normally used capacity. Link restoration as well as path restoration can be applied. Configuration of intermediate nodes is however required.

For the first option spare capacity can be added after network implementation. For the second option, spare capacity must be rather assigned at the time of network implementation as it has consequences for the node dimensioning.

Case study

As case study, the spare capacity requirement is compared for both spare capacity implementation options.

In an initial topology with 20 nodes and 43 candidate links, a load is planned with 232 entries and 240 capacity units. The planning is done for an optical WDM network using 8 wavelengths per fibre and without wavelength conversion in the nodes. The optimisation is done using Integer Linear Programming [3]. The dimensioning resulted in 47 used fibre pairs in 34 links (Figure 4).

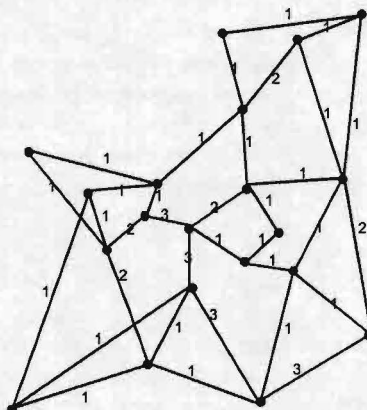


Figure 4: planned topology with capacity (in fibre pairs)

On top of this topology spare capacity is assigned according to both implementation options described above.

When assigning the spare fibres to one overlaying ring connecting all 20 nodes and using already used links, 60 spare fibre pairs are required (3 spare fibre pairs per link, as the most heavily loaded link on the ring uses 3 fibre pairs) (Figure 5.a). A drawback of this option is that the restoration route can be rather long. Consider for instance a link on the ring that fails. This section is restored via the other end of the ring, i.e. 19 links. In an optical network with a large diameter, regeneration would certainly be required. When judiciously choosing the rings, we might end up with 5 rings, only using 39 fibre pairs (Figure 5.b). The restoration routes are now shorter than in the first case. The rings are chosen heuristically by hand.

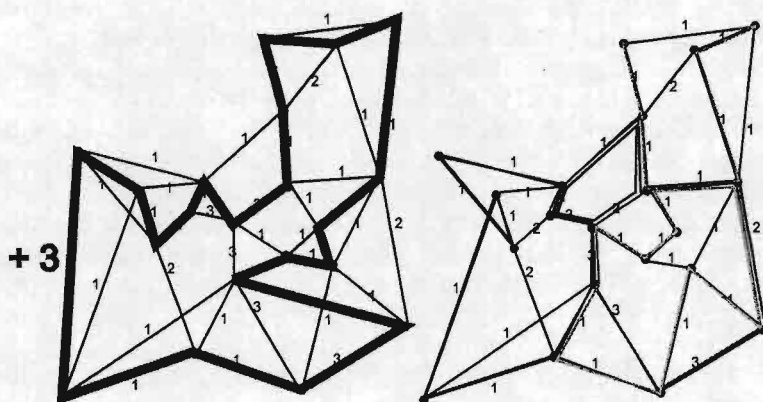


Figure 5: overlaying rings for survivability purposes (a and b)

When using more rings, less capacity is required as the heaviest loaded links can be made protected by shorter rings and eventually multiple rings. Thus, due to a different fibre load in the links, a higher sharing factor of the spare capacity amongst the used capacity, can be obtained by overlaying multiple rings on the meshed network. In addition the network is even more survivable. Failures that is protected for by different rings, may happen at the same time. For the second implementation option, spare channels are assigned in the meshed structure of the network in an optimised way using Integer Linear Programming [4]. The optimised assignment resulted in 33 fibre pairs, yielding a higher sharing factor of the spare capacity. For this assignment link restoration is applied considering the 5 shortest restoration routes. With this planning approach the length of the restoration routes can be better controlled. With the same crossconnect architecture, path restoration could be applied too. With this restoration strategy, a higher sharing factor can be obtained as the restoration happens using spare capacity wider distributed over the network. So, even less spare fibre pairs are required (only 16 for this case study). And the length of the restoration routes can be controlled even better end to end.

Conclusion

In this paper a simple implementation of spare capacity by using overlaying rings was presented. The drawback however, is that the length of the restoration paths is not easy to control and that the provided spare capacity cannot simply be used for other purposes. The approach of spare channels has the advantage that the spare capacity is more flexible to use, but the disadvantage is that it requires more configuration and control when restoring a failure and larger dimensioned crossconnects.

Acknowledgement

The first author thanks the Fund for Scientific Research - Flanders (Belgium) (FWO-V) for a research fellowship. Part of this work has been supported by the ACTS project PHOTON (Panneuropean Photonic Transport Overlay Network).

References

- [1] Y.Yano et al., "2.6 Terabit/s WDM Transmission Experiment using Optical Duobinary Coding", ThB.3.1, *ECOC'96*, Oslo, Sept. 16-19 1996.
- [2] T.H. Wu, "Emerging technologies for fiber network survivability", *IEEE Communications Magazine*, February 1995, pp 58-74
- [3] B. Van Caenegem, P. Demeester, "Planning of the fibre- and path layer of WDM networks", *Proc. of European Conference on Networks and Optical Communications 1997 (NOC'97)*, pp. 95-102, Antwerp, Belgium, June 17-20, 1997
- [4] B. Van Caenegem, F. De Turck and P. Demeester, "Restoration and Spare Capacity Assignment in WDM Networks", *Proc. of 2nd Optoelectronics & Communications Conference (OECC'97)*, pp. 424-425, Seoul, Rep. of Korea, July 8-11, 1997

InP-based LED emitting at 1.55 μ m with 6.8% external QE

We present a MOCVD-grown 3QW InGaAsP microcavity LED structure emitting at 1.55 μ m, achieving an external quantum efficiency of 6.8%. A spectral linewidth of 20nm is demonstrated.

Bart Depreter, Johan Blondelle, Ingrid Moerman, Roel Baets, Peter Van Daele, Piet Demeester

University of Gent, INTEC-IMEC.

St.-Pietersnieuwstraat 41, B-9000 Gent BELGIUM.

Introduction

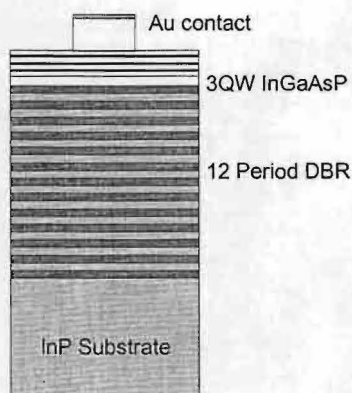
The light emitting diode (LED) has already earned its right of existence in the short and medium distance telecommunications industry, because of its low cost, high reliability and temperature insensitivity. However, ordinary LEDs suffer from low efficiency and a broad spectrum, which limits possible transition distances over fiber due to chromatic dispersion. Additionally, their emission profile is comparable to a standard Lambertian source. This necessitates lenses in order to efficiently couple the light from a classical LED into a fiber.

It has been shown in the GaAs system, that the use of a microcavity structure may improve certain unfavorable LED-properties [1,2]. Spectral linewidth is reduced, and the modulation bandwidth is increased, thus improving performance in fiber communication. This reduces the limits posed by chromatic dispersion of a signal sent over a few kilometers of optical fiber. Moreover, the far field emission profile of a microcavity LED can be much narrower than a standard Lambertian source, which may facilitate fiber coupling.

Finally, external quantum efficiencies of over 20% were obtained recently with InGaAs/(Al)GaAs LED's using microcavity structures[3,4].

Transferring these results to the InP material system, with its industrially relevant wavelengths of 1.55 μ m and 1.3 μ m, is not straightforward. The small refractive index contrast in the InP material system has hindered the realization of a DBR with high reflectivity. That is why monolithic VCSELs operating at these long wavelengths are extremely difficult to achieve. When designing a microcavity LED, the DBR mirror through which the light is extracted preferably has a relatively low reflectivity. This limits the total number of periods in the DBR and enables us to grow an InP microcavity LED monolithically with MOCVD. In this paper a working InP microcavity LED is reported.

Device Design and Fabrication



The microcavity LED is designed to be a bottom emitter (i.e. through the substrate). The optical cavity is formed in between two mirrors. The top mirror is metallic; the bottom mirror through which the light is coupled out is a semiconductor DBR. In order to take advantage of the microcavity effect, the quantum wells must be placed on the antinode positions of the optical cavity. This will enhance spontaneous emission in the direction perpendicular to the substrate, thus improving extraction efficiency.

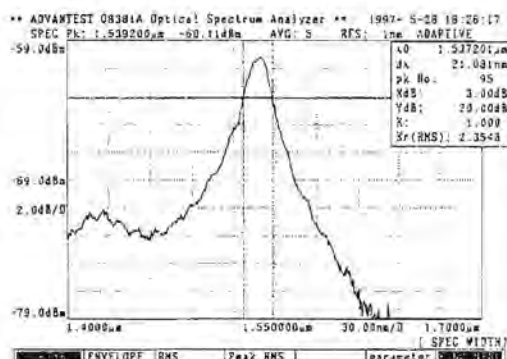
Our device was grown with MOCVD in two steps on an exact n-type InP substrate. The use of two steps enables us to tune the properties of the optical cavity. First the n-doped DBR and the active layers were grown at low pressure, afterwards the p-type layers were grown at atmospheric pressure, because this guarantees better p-type dopant incorporation. The active region of the microcavity LED consists of 3 7.5nm $\text{In}_{0.84}\text{Ga}_{0.16}\text{As}_{0.74}\text{P}_{0.26}$ quantum wells embedded in 15nm $\text{In}_{0.75}\text{Ga}_{0.25}\text{As}_{0.54}\text{P}_{0.46}$ barriers, emitting at $1.55\mu\text{m}$. They are placed inside a λ -cavity defined by an Au-mirror, which also serves as the p-contact, and a 12 period $\text{InP}/\text{In}_{0.66}\text{Ga}_{0.34}\text{As}_{0.73}\text{P}_{0.27}$ DBR.

On the p-side 200nm Au was evaporated to serve as the top mirror and as the p-contact. A circular mesa was etched to assure current confinement. Afterwards the substrate was thinned to minimize free carrier absorption. It was also polished to prevent scattering losses and to enable us to perform meaningful measurements of the far field emission.

The processing scheme we have used is very simple and allows us to individually probe and test different devices on die before packaging.

Experimental Results

Different LED's were individually probed and tested. The spectrum was analyzed using a lensed fiber connected to an Advantest Q8381A optical spectrum analyzer. The emission varied from 1534nm to 1552nm across a 2-inch wafer. The spectral width was about 20nm, which corresponds to 10meV. This narrow spectrum compared to a classical LED will limit dispersion losses when the microcavity LED is coupled into a fiber.

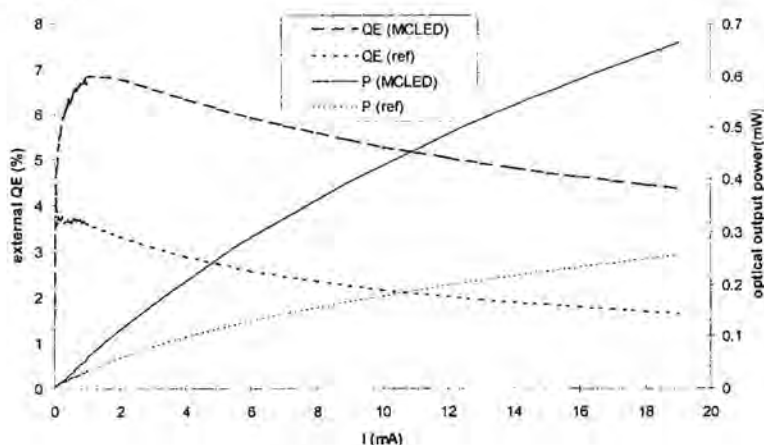


The measurements of the optical power indicate an external quantum efficiency as high as 6.8% for a driving current of 1mA. An increase in efficiency is still to be expected after applying an AR coating.

In order to estimate the advantage a microcavity structure has over a more conventional approach, a reference LED was also grown. This reference LED has exactly the same structure as the microcavity LED but lacks the 12-period DBR mirror. The reference LED is processed in the exact same way as the microcavity LED described above.

From the optical power measurements it is clear that the microcavity structure is drastically improving efficiency. The microcavity LED constantly delivers twice the power as the classical reference LED.

The saturation that currently occurs may be avoided by using more than 3 quantum wells. This will reduce the band filling that is partly responsible for the saturation, and will also narrow down the emission spectrum and may, in the case of the microcavity LED, even further improve efficiency.



Conclusion

An InP microcavity LED emitting at 1.55 μm has been successfully grown using MOCVD. The device shows a narrow spectral linewidth and a high external quantum efficiency that may be improved further after subsequent processing. It is clear that the microcavity structure offers an advantage over a classic multi quantum well LED.

Acknowledgments

The authors would like to thank S. Verstuyft, K. Vandeputte and D. Radomska for device processing.

References

- [1] N.E.J. Hunt, E.F. Schubert, R.F. Kopf, D.L. Sivco, A. Y. Cho, and G.J. Zydzik: "*Increased fiber communications bandwidth form a resonant cavity light emitting diode emitting at $\lambda = 940\text{ nm}$* ", Appl. Phys. Lett., 1993, 63, (19), pp. 2600-2602
- [2] E.F. Schubert, N.E.J. Hunt, R. J. Malik, M. Micovic, and D. L. Miller: "*Temperature and Modulation Characteristics of Rsonant-Cavity Light Emitting Diodes*", Journal of Lightwave Technology, 1996, vol.14, no.7, pp. 1721-1729
- [3] H. De Neve, J. Blondelle, P. Van Daele, P. Demeester, R. Baets, G. Borghs: "*Planar substrate emitting microcavity light emitting diodes with 20% external QE*", SPIE Photonics West, 10-14 February 1997, San Jose, California, US
- [4] H. De Neve, J. Blondelle, P. Van Daele, G. Borghs, P. Demeester, R. Baets: "*Recycling of guided mode light emission in planar microcavity LEDs*", Applied Physics Letters, vol. 70 (7), 1997

High Efficiency InGaAsP/InP Phase Modulator at 1.06 μm .

G. Flamand*, J. Hendrix, K. Jacobs, I. Moerman, B. Dhoedt, R. Baets, P. Demeester,
P. Van Daele

University of Gent-Imec, Department of Information Technology (INTEC)
Sint-Pietersnieuwstraat 41, B-9000 Gent, Belgium
(Tel. ++32 9 264 33 16; Fax ++ 32 9 264 35 93)

* e-mail : gflamand@intec.rug.ac.be

We present an MOVPE grown InGaAsP/InP based phase modulator, exhibiting propagation losses of 4 dB/cm and an excellent phase modulation efficiency of better than 15 $^{\circ}$ /V.mm at a wavelength of 1.06 μm .

Introduction

An increasing number of future space projects will make use of optical technologies for a wide range of applications such as remote sensing, earth observation, space science and communications. The requirements on size, weight and reliability of such optical components and equipment are very stringent, creating a need for waveguide based Photonic Integrated Circuits (PICs).

We are currently studying the feasibility of the InGaAsP/InP technology, used in telecommunications for fiber transmission at 1.3 μm and 1.55 μm , for the realization of a PIC for phase control of optical radiation at 1.06 μm . This PIC is to be integrated in an Optical Phased Array telescope system, acting as a receive terminal in geostationary orbit for advanced intersatellite free-space laser communications (using Nd:YAG lasers) [1].

As a first step towards the realization of such a PIC, we have successfully realized a phase modulator showing very good loss and modulation characteristics at the desired wavelength.

Design and Fabrication

Efficient waveguiding calls for a core (InGaAsP) material with a bandgap wavelength which needs to be, on one hand, sufficiently higher than that of the (InP) cladding layers, to obtain a high confinement of the light in the waveguide core, while on the other hand, it needs to remain appreciably smaller than the wavelength of the guided light, to avoid high absorption losses. Since our structure needs to guide Nd:YAG light with a wavelength of 1.06 μm , and the InP-cladding layers have a bandgap wavelength of 0.92 μm , this will place very stringent restrictions on the composition of the waveguiding layer. From modeling and a number of waveguide test structures, it was found that the best results are expected with a waveguiding layer exhibiting a bandgap wavelength between 0.98 and 1.00 μm (composition between

170 nm p++ InGaAs contacting layer
700 nm p+ InP top cladding layer
300 nm p InP top cladding layer
400 nm un InP top cladding layer
700 nm un (or n-) 0.98 μm InGaAsP core layer
1000 nm n InP bottom cladding layer

Figure 1. Layer structure for the realisation of an InGaAsP/InP phase modulator at 1.06 μm .

pin) structure, required to make use of the well-known electro-optic and carrier effects to achieve phase modulation [2][3]. The layer structure is capped of with a highly p-doped InGaAs contacting layer.

The above described layer structure was grown using LP-MOVPE. The source materials are PH_3 , AsH_3 , TMI, and TMG, and H_2S and DEZ for resp. n- and p-doping. We used an elevated growth temperature of 700 $^\circ\text{C}$, where the higher PH_3 -cracking efficiency enables us to use a higher AsH_3 -flow than is the case at the standard growth temperature of 625 $^\circ\text{C}$. Thus we obtain a better control on the composition of the (low As-content) quaternary guiding layer. The reactor pressure is 76 Torr, except for the InGaAs contacting layer, where we use a higher pressure (700 Torr) to obtain a higher doping level. The structure was grown on a $[100] + 2^\circ$ off-oriented, n-doped InP substrate.

After growth of the layer structure the phase modulator ridges are etched. Following the deposition of a SiO_x -layer on the structure by means of PECVD, the mask pattern is defined by photolithography. This is followed by the dry etching of the dielectric layer and the removal of the resist layer with O_2 -plasma etching (PE). After this the actual modulator ridges are RIE-etched, and the remaining oxide layer is removed. The modulator ridges have widths between 1.75 μm and 4.5 μm , and are separated by 80 μm interspacings.

After this, a polyimide layer is spinned over the sample, which is opened above the waveguide ridges with an O_2 -PE, resulting in via-stripes needed for contacting. A Ti/Au deposition for p-contacting is then performed above the via stripes. The metallisation stripes are 20 μm wide, and are divided into 900 μm long parts, separated by 100 μm openings. At these openings there is neither polyimide nor metallisation in order to allow easy cleaving and hence only the InGaAs layer is responsible for conducting the applied electrical signal. At every 900 μm zone three 40 $\mu\text{m} \times 40 \mu\text{m}$ contacting blocks are provided. The Ti/Au contacts are Au-plated to reduce the serial resistance of the structure. The polyimide is then removed in an O_2 -PE run, using the Ti/Au and Au layers as a mask. Finally, AuGe/Ni is deposited on the back of the substrate, resulting (after an alloying step) in ohmic back contacts. The resulting phase modulator structure and the layout of the metallisation mask are shown in figure 2.

$\text{In}_{94.8}\text{Ga}_{5.2}\text{As}_{11.4}\text{P}_{88.6}$ and $\text{In}_{93.2}\text{Ga}_{6.8}\text{As}_{15.0}\text{P}_{85.0}$). Further modeling resulted in a layer structure as shown in figure 1.

The InGaAsP core layer has a thickness of 700 nm, resulting in monomodal waveguiding for ridge widths up to 1.8-2.5 μm (depending on etch depth). The guiding layer is placed between an n-doped bottom and p-doped top cladding layer, where the latter is separated from the core layer by an undoped cladding layer, in order to reduce additional losses due to the strong absorption of the optical mode in a p-doped layer. This way we obtain a piin (or

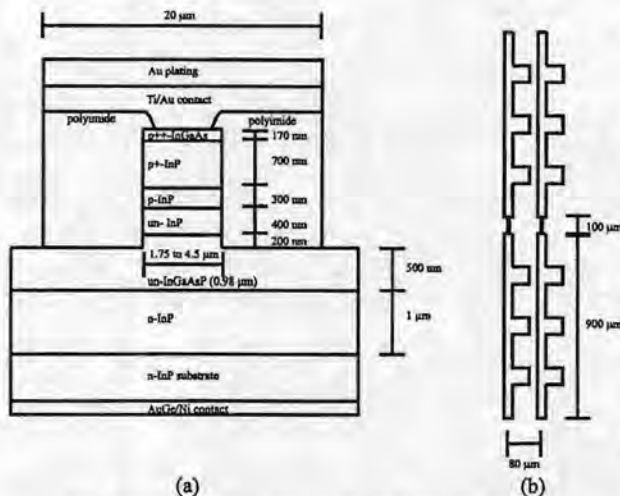


Figure 2 (a) Phase modulator structure (b) Metallisation mask layout

CCD-camera (for alignment and study of the modal behavior), or onto a detector, connected with an x-t writer for data-output. The studied sample had a length of 8 mm, and held a number of waveguides with ridge widths between 1.75 and 4.5 µm (series of 5 waveguides with the same width).

Propagation losses were measured using the well-known Fabry-Perot resonance principle [4]. Heating of the DUT causes a change in the path length, causing Fabry-Perot resonances. The loss in the waveguide is then calculated using the formula

$$\alpha = -\frac{10}{\ln 10 \times L} \times \ln \left(\frac{1}{R} \times \frac{\sqrt{K} - 1}{\sqrt{K} + 1} \right), \text{ where } K \text{ is the ratio of the reflection maxima and minima, } R \text{ is the reflection coefficients of the waveguide facets, and } L \text{ is the length of the DUT.}$$

Phase modulation efficiencies are measured by applying a reverse voltage difference over the pin structure. Changing of the applied voltage causes a change in refractive index, and thus a phase shift, due to electro-optic and carrier depletion effects [5]. This results in a sinusoidal varying signal, from which the phase modulation

efficiency is calculated using the formula $\eta_{\text{mod}} = \frac{\Delta\phi / 2}{\Delta V \cdot L}$, where ΔV is the change in applied voltage and $\Delta\phi$ is the resulting phase shift of the outgoing signal.

The best modulation efficiencies so far were obtained with half-deeply etched modulators (200 nm of the quaternary layer being removed) having ridge widths of 2 and 2.25 µm. These exhibited (average) propagation losses of respectively 4.8 and 3.9 dB/cm, with best values of resp. 3.0 and 3.6 dB/cm. Modulation efficiencies as high as 18.2 °/V.mm and 16.5 °/V.mm, for resp. the 2 and 2.25 µm wide modulators, were measured at reverse bias voltages of approximately 6.2 V (no higher reverse voltages were applied, since initial tests-measurement of the diode characteristics of the pin structure-showed breakdown voltages of approximately 10 V). Over a longer voltage range (from 2.5 V to 7.5 V), modulation efficiencies amounting to about resp. 11.0 °/V.mm and 10.1 °/V.mm were measured. To our knowledge, these results (figure of

Measurement Results

The measurements were performed using a Nd:YAG laser ($\lambda_{\text{emission}} = 1.064 \mu\text{m}$) with an output power of 100 mW. After passing through an attenuator disk (attenuation variable between 0 and 25 dB) the laserlight is coupled into a modulator using a microscope objective. The outgoing light is focused, either onto a

merit of about 25 $^{\circ}$ /V.dB) are comparable to the results reported so far in this material system, especially at the specified wavelength of 1.06 μ m.

Meanwhile, initial measurements have been performed on shallowly etched modulators with a comparable layer structure. Due to the reduction of the overlap of the electrical and the optical fields, lower modulation efficiencies were observed. We measured an average values of about 7 $^{\circ}$ /V.mm (voltage range: from 1.5 V to 13 V) for 1.75 μ m wide (monomodal) waveguides. The measurement of the diode characteristics of these modulators showed reverse breakdown voltages above 20 V, with peak values of 45 V.

Conclusion

We have demonstrated an InGaAsP/InP phase modulator, exhibiting very good loss and modulation characteristics at a wavelength of 1.06 μ m. We are confident that this will be the first step towards the extension of the InGaAsP/InP PIC technology, from its current optical fiber communications wavelength range (1.3 - 1.55 μ m), to the intersatellite free-space laser communications wavelength of 1.06 μ m.

Acknowledgments

This work was performed under ESA-ESTEC/contract No. 11450/95/NL/PB. The authors would wish to acknowledge Steven Verstuyft and Kristien Caekebeke for their work on the device processing.

References

- [1] W.M. Neubert and K.H. Kudielka, "Coherent Optical Self-Phasing Array Antenna for Space Communication Receivers", Proc. Of ECOC'93, p. 501
- [2] W.K. Marshall and J. Katz, "Waveguide PIN junction electrooptic phase modulators: theoretical analysis and design criteria", Applied Optics, vol. 24, no. 11, p. 1996, 1985
- [3] J. Vinchant et. al., "InP/GaInAsP Guided-Wave Phase Modulators Based on Carrier-Induced Effects : Theory and Experiment", Journal of Lightwave Technology, vol. 10, no. 1, p. 63, 1992
- [4] R.G. Walker, "Simple and accurate loss measurement technique for semiconductor optical waveguides", Electronic letters, vol. 21, no. 13, p. 581, 1985
- [5] J.G. Mendoza-Alvarez et. al., "Analysis of Depletion Edge Translation Lightwave Modulators", Journal of Lightwave Technology, vol. 6, no. 6, p. 793, 1988

OLIMPEX : measurement and parameter extraction tools for advanced laser diodes

P. Verhoeve[°], G. Diet[°], G. Sarlet[°], G. Morthier[°], R. Baets[°], T. Farrell^{*}

[°] University of Gent, dept. of Information technology (INTEC), St. Pietersnieuwstraat 41, B-9000 Gent, Belgium, email : verhoeve@intec.rug.ac.be

^{*} University college Dublin, Opto electronics Research Centre, Rm331, Eng. Bldg., Belfield, Dublin 4, Ireland, email : tfarrell@ollamh.ucd.ie

Abstract :

Advanced laser diodes such as tuneable multi section devices, require advanced characterisation and parameter extraction tools in order to effectively feed device information back to both device fabrication and system use. To this end, a versatile software framework (called OLIMPEX) has been developed.

1. Introduction

Advanced laser diodes such as tuneable multi section devices used for WDM transmission normally have multiple sections and a complex behaviour. The system designers need an accurate description to use/control the components in an efficient way. The manufacturer of the component has a similar problem : he needs accurate characterisation in order to select the best devices and have feedback to the processing methods.

Due to the combination of multiple sections and a complex behaviour, regular characterisation is far from obvious. Furthermore, most of the parameters which determine the laser output characteristics can no longer be measured directly. As a result, there is a need for advanced characterisation tools to be able to characterise the component in an efficient way.

Within the European ACTS project BLISS (AC065) a set of software tools was created, to enable advanced component characterisation : OLIMPEX which stands for Opto eLEctronic Integrated Measurement and Parameter EXtraction tools. First an overview of the characterisation strategy and the resulting boundary conditions for the tools will be given (sections 2 and 3), following that a brief overview of the software methods used to achieve the goals (section 4) and finally an overview of the tools will be given in section 5.

2. The characterisation strategy

A component description always starts off with measuring the device. To reduce the size of the measurement data there are three options : fit the data to physical models, fit the data to mathematical models or a combination.

Using mathematical models is merely a data reduction procedure, the end result is a set of parameters which describe the device and can only be used as information to system designers. The use of physical models on the contrary is more than data reduction, it provides information on the device itself. By comparing the extracted parameters (e.g. coupling coefficient of a grating) with the original design values, the fabrication process can be evaluated. Figure 1 shows the process to get from measurement data to a parameter set which in turn is used for performance estimation and feedback to system designers as well as the fabrication process.

The parameter extraction process can be rather straightforward (e.g. the calculation of threshold current and efficiency) or more complex when a model for an amplified spontaneous emission (ASE) spectrum is to be fitted with the corresponding measurement result.

By combining information present in the different measurements, a more complete, more accurate and consistent description of the device is possible. [1] This is due to the fact that some parameters can be extracted from more than one measurement and some measurements are determined by almost all parameters (e.g. threshold current).

The same principle of combination can also be taken one step further : by combining information from several devices instead of just several measurements an even description of a fabrication process can be derived. The combination of Fabry-Perot and DFB lasers of a similar active layer and with varying parameters (e.g. length, facet coating, ...) is quite promising for this purpose.

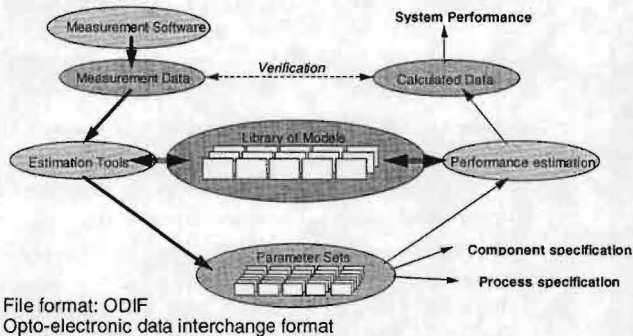


Fig. 1 : processing measurement data

3. Need for advanced tools

When dealing with an advanced characterisation scheme as described in the previous section, there is a big risk that most of the manpower is spent on the configuration and the combining of the different programs and data formats. Having the right tools for the job, i.e. tools that can achieve the complex task without the need for complex (re)programming is a condition for success.

The tools need to accomplish the measurements and parameter extractions in a comfortable way; they must be fairly straightforward to use yet be powerful enough to cope with the complexity of the characterisation process. At the same time the software must be designed such that further automation and extension remains possible. E.g. replacing an instrument in a measurement set up should not impose drastic software modifications to all applications. Similar to the physical measurement instrument being connected to the set up, the instrument driver software needs to be plugged into the application.

In the field of parameter extraction the need for flexibility is even bigger : all the fitting processes to obtain parameters are a combination of a mathematical model describing the measurement result, an optimisation algorithm and an expression for the error (cost function) between the calculated and the measured data. The tools need to allow different combinations of these components (model, cost function and algorithm), especially in the development phase of the overall fitting procedure. Changing the optimisation algorithm or adding an extra term to the cost function must not be a time consuming issue, nor may it require a large programming effort. In a matter of speaking changing a software component (e.g. an optimisation algorithm) may not be more complex than replacing a current source instrument in a measurement set up.

Besides the software tools, the data storage method is equally important : since the strategy is to combine measurement results, all tools should be able to interpret

each others result files. These files should not only contain the raw measurement data but also descriptions of the device and the results to the parameter extraction. By introducing a data format that enables storing and manipulation of all this data in a hierarchical fashion while always keeping the interpretation of the numbers clear, it will not only be possible to combine the results in a comfortable way, but the data format will also help to reduce the number of possible errors due to misinterpretation of numeric data.

4. Short overview of the implementation methods

For the instrument drivers, an abstract approach called "functional instrument drivers" was developed and implemented. This technique allows the addition and removal of instrument drivers on a plug-in base which minimises the programming effort when a new instrument is added.

The chosen file format for data storage is ODIF (developed within the European COST240 project[2]), a hierarchical data format designed to store measurement, modelling and extraction data on opto electronic components.

In order to cope with the complexity and needs for flexibility of models and algorithms, an object oriented analysis of the parameter extraction problem was made. This resulted in a framework implemented in C++ and linked to LabVIEW which provided the graphical user interface for the end application. All other tools were implemented using the same LabVIEW environment from National Instruments.

5. The OLIMPEX environment

The OLIMPEX environment contains tools for the most common measurements performed on laser diodes. OLIMPEX can measure the diode characteristic, the output power and the optical spectrum with tools like LIV and OSAview. The parameters originating from these measurements are either extracted by the application itself (e.g. threshold) or they can be extracted using a second application where the user can input the necessary extra information (e.g. refractive index to calculate the internal loss).

More advanced characterisation of the laser diode can be done with RINoise and Tune4, tools to respectively measure the relative intensity noise (RIN) and the tuning characteristics of a multi section laser diode. The measurement results of RINoise can serve as input for the RINfit application, which extracts the resonance frequency, damping and differential gain.

OLIMPEX also offers an application which realised parameter extraction by fitting an analytical model for the amplified spontaneous emission (ASE) of a DFB laser to a measurement. Amongst others this process can be used to obtain a value for the coupling coefficient of the grating and the phase of the facet reflectance.

Figure 2 gives the complete list of current OLIMPEX applications, figures 3 to 5 give examples of the graphical user interface of two applications.

6. Conclusion

A versatile software framework (called OLIMPEX) has been developed to cope with the specific needs for characterisation of advanced laser diodes. Currently the tools are used to test the proposed characterisation method on a set of Fabry-Perot and DFB lasers.

Acknowledgement

The authors wish to acknowledge to European ACTS program and the BLISS project (AC065) for funding this work.

References

- [1] G. Morthier, P. Verhoeve, R. Baets, R. Schatz, "Extraction of a large set of laser parameters from different measurements", ISLC96
- [2] Book on "Techniques for modelling and measuring advanced photonic telecommunication components" to be published by the COST240 consortium, or internet : <http://intec.rug.ac.be:8080/www/u/162/odif>

Measurement applications :

- **LIV** : laser drive current vs. output light power and laser voltage
- **RINoise** : measurement of Relative Intensity Noise
- **Tune4** : peak wavelength., SMSR and power up to 4 driving currents
- **OSAvie** : optical spectrum analyser on the PC
- **ESAvie** : electrical spectrum analyser on the PC

Figure 2a : OLIMPEX measurement tools

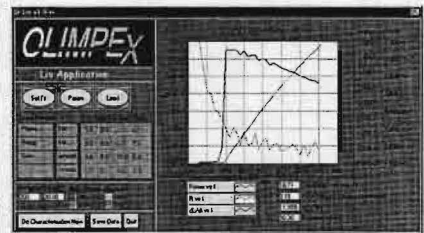


figure 3 : GUI of LIV application

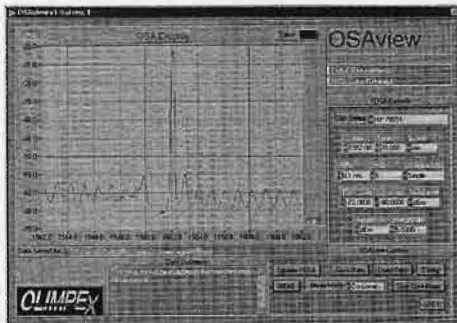


figure 4 : GUI of OSAview application

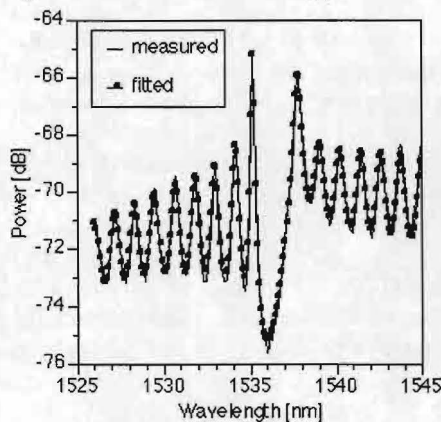


figure 5 : Results of ASE fit for DFB laser

Extractions :

- **IntLoss & TempChar** : I_{th} , η_{ext} , R , α_m , and T_0
(based on LIV measurement)
- **RINfit** : f_r , γ , dg/dn , K , and ϵ
(based on RIN measurement)
- **ASEfit** : R_1 , R_2 , ϕ_1 , ϕ_2 , κ_1 , κ_2 , v_g , gain for DFB laser
(based on ASE spectrum meas.)
- **FPgain** : modal gain and loss
based on laser spectra or waveguide measurement (Hakki & Paoli)

Figure 2b: OLIMPEX extraction tools



Figure 6 : GUI of ASEfit application

Termination and Coupling Experiments for a 1x12 Small Diameter (125 μm) Plastic Optical Fibre Array and POF Coupling to Microcavity LEDs

An Van Hove, Ronny Bockstaele, Thierry Coosemans, Bart Dhoedt, Roel Baets, Peter Van Daele,
University of Gent / IMEC - Department of Information Technology (INTEC)
St. Pietersnieuwstraat 41, B-9000 Gent, Belgium

Tel: +32-9-264 33 16, Fax: +32-9-264 35 93, email: an.vanhove@intec.rug.ac.be

Introduction

Currently, the use of Plastic Optical Fibres (POF) is restricted to large core (500-1000 μm) single fibre links for short haul (<100m) interconnections. Applications in this field are optical LANs, inter- and intra-office connections at distances up to 100 m, where electrical solutions, based on twisted pair or coaxial cables are reaching their limit in terms of distance, speed and cost. As a result there is a lot of interest in competitive optical solutions where the driving force, because of the "end user" character of these short link applications, is cost inspired.

Because of the need for highly accurate, and thus expensive connectors and alignment schemes, the use of glass fibres is less advantageous in the short link applications. Polymer Optical Fibres have the potential to be a suitable candidate. The large core of POF makes the alignment much more tolerant and consequently, the accuracy of the connectors is more relaxed, reducing the cost considerably. Another advantage is the increased flexibility of the optical fibre. Depending on the size of the polymer fibres, the bending radius can be much smaller (down to a few mm) compared to glass fibres, due to the mechanical characteristics of POF and the higher numerical aperture offered. Last but not least, the termination cost to obtain an acceptable optical facet can be severely reduced. Techniques like hot plate flattening and hot knife cutting can replace the expensive and time-consuming polishing of glass optical fibres and have the real potential to be cheap.

In this application area of short distance optical interconnects, parallelism is very often exploited to increase aggregate bitrate and to reduce latency caused by serialisation. This parallelism, also applicable for POF, has also implications on costs, as a further cost reduction can be realised because of the reduced assembly cost and the use of less material. To reduce lateral dimensions there is however the need for plastic fibre arrays with small pitch and compatibility with standard 250 μm pitched source- and detector arrays should be pursued. Because of the increased alignment tolerances and the high N.A. of POF, a parallel interconnection with VCSEL- or LED-arrays is extremely promising.

It is the purpose of this paper to investigate the potential of 125 μm plastic optical fibre in coupling applications and in parallel datacom applications. To this end, an 125 μm polymer optical fibre was coupled with a microcavity LED (section 1) and the termination of small diameter (125 μm) POF in a 1x12 array has been investigated (section 2), which seems to be the main prohibiting factor for practical use today.

Transmission measurements were performed at a wavelength of 633 nm on a number of small diameter POF arrays. MTTM terminated POF arrays were coupled with respect to each other. Additionally, measurements on lateral misalignment tolerances were carried out (section 3).

1 Microcavity LEDs and coupling to 125 μm POF

Conventional planar LEDs have a low external quantum efficiency due to total internal reflection at the semiconductor - air boundary. For a semiconductor refractive index of 3.5 only 2 % of the emitted light escapes to the 2π solid angle into air. Furthermore only 25 % of this externally emitted light falls within a numerical aperture of 0.5. The methods used in display LED's to enhance this efficiency are not applicable in dense parallel optical interconnect applications. In recent years it has been demonstrated that the microcavity effect allows to enhance the external efficiency [1] and to decrease the spectral width. However, interconnect applications demand high efficiency in the NA of the waveguide. Using a dedicated model, simulations were carried out to study the effect of the cavity parameters on the efficiency and the beam divergence of microcavity LED's. Devices as shown in fig 1 were fabricated with a 6-pair DBR. The layer structure was grown on GaAs in a MOCVD reactor. After growth, Au mirrors, also serving as p-contact, with a diameter of 50 μm were deposited. The substrate was thinned to 250 μm to reduce substrate absorption and an anti-reflective coating was deposited on the back surface. An efficiency of 3.9 % into a numerical aperture of 0.5 has been obtained in 85 μm diameter MCLEDs with 3 InGaAs quantum wells [2].

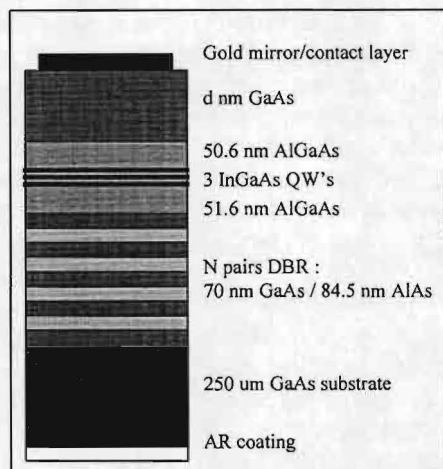


Fig 1 : structure of MCLED

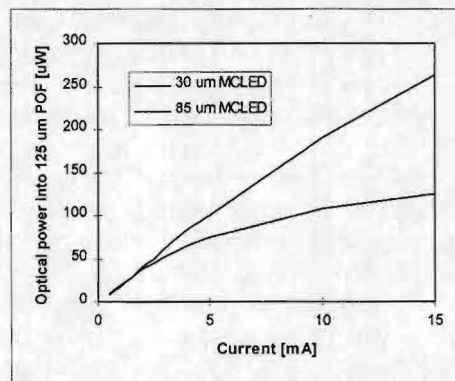


Fig 2 : power in POF for 30 μm and 85 μm MCLED

The coupling efficiency into POF with different diameters was investigated experimentally. First, we measured the absorption of the POF at 980 nm, the central emission wavelength of the MCLEDs, which was about 11 dB/m. Taking this value into account, we measured the power into the fibre for different fibre-diameters and MCLED diameters. The maximal QE into fibre is 2.14 %. The difference to the 3.9% (calculated from the far field curves) can be explained by the partial geometric overlap and the reflections at the fibre facet.

2 MTTM terminated 1x12 POF array

Three termination techniques for the 1x12 125 μm POF array were investigated: hot knife cutting, polishing and hot plate flattening. In all three cases, the fibres are fixed in the V-grooves of a standard MTTM ferrule.

With the hot knife technique, the fibres are fixed in the ferrule so that no epoxy is protruding at the front facet of the ferrule. A holder, which accurately aligns the MT ferrule was used to fix the ferrule, and placed on a z-translation stage.

By applying a translation, the protruded fibres are cut off one by one with the hot knife which is guided by the facet of the ferrule. By selecting the right temperature, the right cutting speed and force applied when cutting, an adequate facet can be obtained. This procedure has the advantage of being fast, which decreases strongly the cost of termination. An example of a hot knife terminated POF facet can be seen in Fig3. The small roughness, due to the knife facet, can be removed by 10s polishing with CeOx. (Fig 4)



Fig 3 Hot knife cut POF

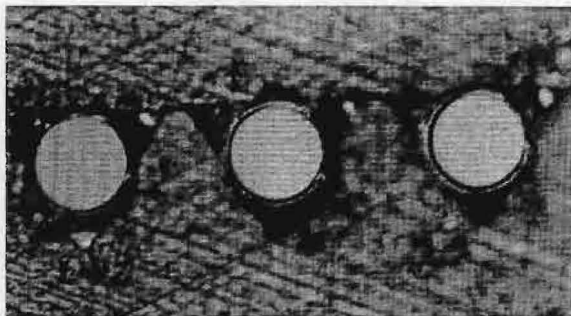


Fig 4 Hot knife, finished with 10 s polishing

The polishing procedure is similar to the procedure used for MTTM glass fibre ferrules using three polishing stages with decreasing grain size (16 μ m, 5 μ m, 1 μ m). The procedure is however considerably shorter due to the polymer character of POF. In Fig 5 polishing is terminated with a buffering cloth.

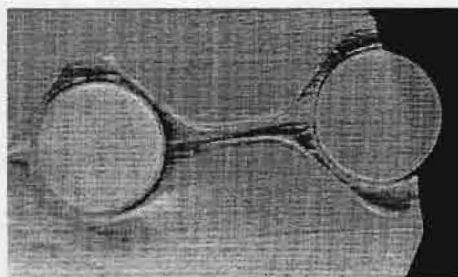


Fig5: Polished fibres, terminated with a buffering stage

With the hot plate technique the protruding fibres are brought during a brief moment in contact with a heated plate. The shape of the hot plate is copied into the facet of the POF array and therefore this plate has to be very flat. Parameters like contact time, temperature and protrusion are critical here. Initially a small protrusion (~0.5 mm) is required which is obtained by cutting the fibres with the hot knife. This procedure has also the advantage of being fast.

3 Transmission measurements and alignment tolerances

For the evaluation of the different termination techniques transmission measurements were performed. The MTTTM ferrules were brought in physical contact with each other while the power transmission per channel was measured. Polishing without buffering stage yielded an average loss of 0.7 dB and the hot plate technique 0.4 dB per channel. Hot knife cutting generated an average loss of 0.9 dB per channel. However, a short polishing (10s) after the cutting reduces the losses to 0.5 dB per channel. Finally radial alignment tolerances were measured and compared with theoretical by shifting the MT ferrules laterally with respect to each other.

Ray tracing predicts the following behaviour of the transmission in function of radial offset for step index fibres [3] :

$$T = \frac{2}{\pi} \left(\arccos\left(\frac{d}{a}\right) - \frac{d}{a} \sqrt{1 - \left(\frac{d}{a}\right)^2} \right)$$

with d half the offset and a the radius of the fibre core.

As can be seen from fig(5) the experimental results are still lower than the theoretical model and especially for small misalignments the divergence between theory and measurement is clear. Further improvements in termination technology are expected to bring both curves closer together.

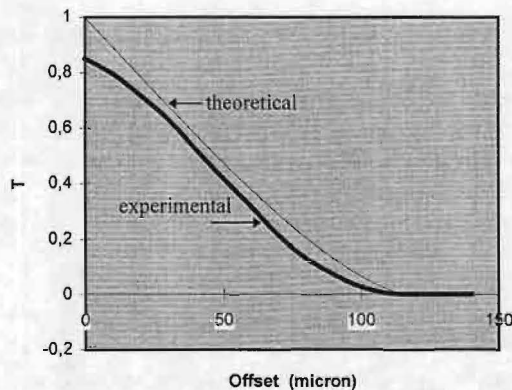


Fig 5: Transmission in function of radial offset of polished 107/125 SI-POF

Conclusion

We evaluated different termination techniques for POF arrays. All three of these are considered to be very promising regarding time/cost aspects and transmission performance. Preliminary measurements have shown that hot plate flattening yields the lowest losses. This, together with the high tolerance to misalignment and the bending flexibility, suggests the strong potential of using 125 μ m POF for short distance parallel interconnects.

Acknowledgements: The authors thank the Flemish IWT for partial support as well as the ESPRIT project OIIC

[1] H. De Neve et al, Applied Physics Letter, Vol 70 no 7, p 799 (feb 1997)

[2] R. Bockstaele et al, LEOS Summer Topical Meetings 1997 Vertical-Cavity Lasers, Montreal, p 69

[3] Wim van Etten and Jan van der Plaats: Fundamentals of Optical Fibre Communications, Prentice Hall, 1991

POLYMERIC WAVEGUIDE BASED OPTICAL INTERCONNECT FOR DATACOM APPLICATIONS

Johan E. van der Linden, Peter P. Van Daele, Peter M. De Dobbelaere*, Mart B. Diemeer*

IMEC / University of Gent, Dept. of Information Technology, B-9000 Gent, Belgium

*AKZO NOBEL Central Research, NL-6800 SB Arnhem, The Netherlands

Abstract

We report on the development of dedicated integration technologies for photonic components with wafer-scale single-mode polymeric waveguide circuits. The use of passive alignment techniques based on micromachining, enables to achieve high performance at low cost.

Introduction

The advantages of optical interconnect for high-speed digital systems include increased I/O density, higher bandwidth, reduced cross-talk, ease of impedance control, insensitivity to EMI, and reduced weight. Deployment of planar polymeric waveguide technology for board level optical interconnect is particularly interesting in terms of potential assembly labour/cost as compared with fibre optics. Most of the currently developed board-level interconnect demonstrators involving polymers, make use of multimode waveguides as to compromise some performance aspects for lower cost [1-5]. For future multiprocessor computer systems, however, high-speed massive fan-out synchronous clock distribution will eventually even become difficult with multimode optical waveguide architectures [6-7]. Optical interconnect based on single-mode waveguide circuits will additionally enable efficient integration of active polymeric guided-wave devices, thus enhancing the circuit functionality and allowing reconfigurable interconnection applications. Moreover, suitably designed single-mode polymeric waveguides can achieve butt coupling losses of 0.1dB or less with standard single-mode fibre (SMF), which is important from the viewpoint of interface compatibility for possible direct telecom system connection.

Most single-mode optoelectronic components, though, still require a mounting technology with submicron accuracy in order to accomplish an acceptable insertion loss. Active alignment can render high coupling performance, but powering of the components during the assembly stages significantly complicates the process and contributes to excessive packaging costs. Hence, further development of available passive and cost-effective assembling technologies with high performance and reliability is of crucial importance [8-10].

Photo-diode Integration

At the receiver end, the use of surface illuminated photo-detectors allows to reduce the alignment problem to two dimensions, of which the tolerances primarily depend on the detector sensitive area size. Although specially designed multimode guided-wave detectors for which alignment is less critical are currently under development [11], the commercial availability of top illuminated photo-diodes makes them particularly favourable. The utilisation of single-mode optical waveguide circuits comprising a small NA will render small spot sizes on the detectors, additionally enabling both a larger lateral alignment tolerance or application of small active area detectors which exhibit a larger bandwidth.

The implementation of surface illuminated photo-diodes, however, demands for a vertical coupling structure as to direct the light emerging from the waveguides onto their sensitive area. We previously investigated the fabrication of mirror-type vertical coupling structures into the polymeric waveguides by embossing [12]. Moreover, when the out-of-plane coupling is carried out by a structure integrated in the polymeric layer stack, the top illuminated detector chip needs to be mounted on the substrate by means of high flip-chip bumps which decrease the planar alignment accuracy [13].

In our novel concept [14], the required beam deflection is obtained by mirroring onto a micromachined silicon structure that simultaneously serves as a submount for the photo-diode chip (fig.1). A prototype integrated receiver module comprising a 4-channel Si detector-chip with sensitive area diameters of $200\mu\text{m}$, was passively aligned with a complementary structured polymeric waveguide array. For this module, a coupling loss of 3.4dB and an average optical cross-talk of -12.1dB to adjacent channels was observed at 633nm [15]. An important part of the occurring optical cross-talk could be attributed to beam scattering caused by the surface roughness of the reflecting planes. It has been demonstrated that optimisation of the anisotropic etching technique can render the silicon mirroring planes very smooth, and the cross-talk contribution due to topographic scattering can be reduced [16]. Moreover, the large sensitive area of the applied photo-diodes also attributed to the cross-talk. The relevant parameter in the detector layout is the ratio δ of the sensitive area diameter to the channel pitch, which was 0.4 in this case. By matching the size of the photo-diodes to the deflected optical spot, reduction of the cross-talk can be achieved without introducing a coupling efficiency penalty.

Additional backside processing of the submount structure has allowed high-density detector integration to perform signal monitoring [17]. For optical interconnect purposes, this operation enhances the circuit design flexibility by the possibility of terminating an arbitrary selection of channels without interrupting other channels (fig.2). A prototype detector module comprising an 8-channel InGaAs/InP photo-diode chip with sensitive area diameters of $70\mu\text{m}$ ($\delta=0.28$) was fabricated. Calculation of the coupling efficiency sensitivity still rendered a 1.0dB alignment tolerance of $22\mu\text{m}$ in this case. Hence, a low-cost thermo-compression flip-chip assembly technology could be applied for mounting the photo-detector chip onto the submount structure. The integrated module exhibited a coupling efficiency of about -2.6dB and an average cross-talk value of -21.3dB to adjacent channels at 1300nm (fig.3).

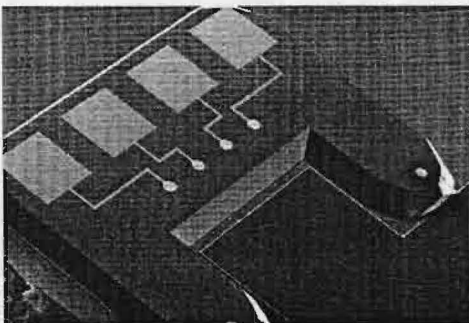


Fig.1 Detector submount passively aligned with a complementary polymeric waveguide array

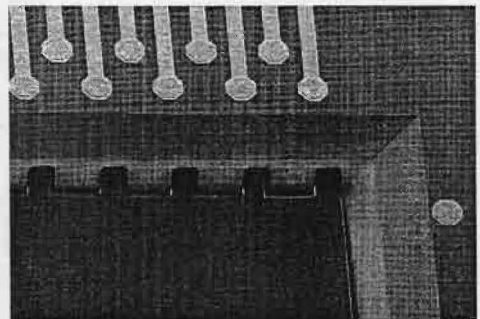


Fig 2. Detector submount comprising backside grooves for selective channel deflection

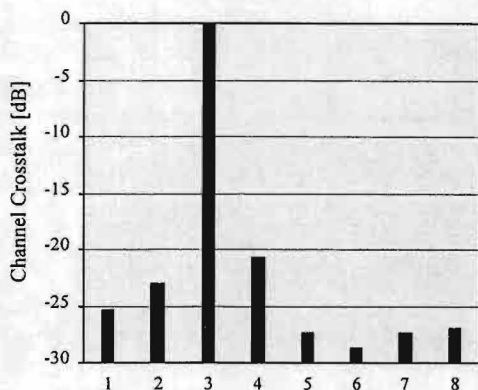


Fig.3. Channel cross-talk for input fibre coupling to a typical waveguide channel

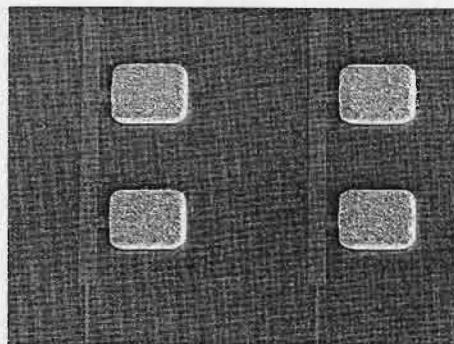


Fig.4. Nucleation and plated bump pattern for passive laser-diode array integration

Laser-diode Integration

There is a trend towards the use of surface emitting lasers for short distance parallel optical interconnect because of their potential channel density and low integration cost [18]. The previously described photo-detector integration concept is also suitable for VCSEL array mounting on the emitter side. For this purpose, however, 45° mirroring planes are to be revealed in the submount structure [19] in order to achieve a sufficiently high coupling efficiency with small NA single-mode waveguides. The integration of driver circuits can simultaneously be accommodated by the submount.

Although the alignment requirements are more stringent for guided-wave light sources [20], the development of spot-size converted laser-diodes has enabled to realise SMF coupling losses around 2.0dB and increased the 1.0dB alignment tolerance to about $8\mu\text{m}$ [21-22]. Since the mode profile of the applied polymeric waveguides is very close to this of a standard SMF, similar coupling efficiencies can be achieved to planar waveguide circuits. This allows to apply thermo-compression flip-chip technology even for the mounting of the emitters. In applications where the development cost of these laser-diodes cannot be justified and more standard designs with a large divergence are to be used, tapering of the polymeric waveguide section is a valuable option as to improve the coupling efficiency [23].

Another problem which has to be overcome during the integration of edge-emitting laser-diodes with polymeric waveguides (next to the mode-mismatch) is the large height difference between the core waveguide layer and the active layer of a flip-chipped laser-diode, which reaches about $13.5\mu\text{m}$ in our case. Although solder bumps have the potential of accurate three dimensional chip positioning [24], their utilisation can suffer from compatibility restrictions put on the reflow temperature or applicable solder flux by the polymer. Because plating thick thermo-compression flip-chip bumps does not allow precise control of both their height and lateral dimensions, a thick-resist lithography process was developed as to firmly border an electroplated pattern of high Au-bumps. We obtained patterns (thickness $>10\mu\text{m}$) with sharp edge profiles of good quality with commercially available photoresist. A fine stripe-pattern was implemented in the nucleation layer to serve as a lateral positioning reference for both the polymeric waveguide definition and the laser-diode mounting, thereby allowing passive alignment (fig.4). The mask design for the definition of the polymeric coupling facet could additionally comprise features with the purpose of altering the field distribution in the final waveguide section and improve the mode overlap with the laser-diode.

In this approach, though, the thick resist lithography has to be performed on a non-planar substrate comprising polymer layers with deeply etched coupling facets, or alternatively, spin-coating of the polymer layers needs to be carried out on a substrate onto which a high Au-bump pattern is plated. Accurate definition of the bump or waveguide pattern will therefore only be possible at a certain distance from the previously processed structures. Due to this inconvenience, we started the development of an alternative process in which the polymer bottom cladding layer itself is used to border the electroplated bump pattern.

Conclusion

We have demonstrated the feasibility of a cost-effective hybrid integration concept which allows passive alignment of top illuminated photo-detector arrays with planar polymeric waveguides by means of a micromachined submount. Integration concepts for VCSEL and spot-size converted laser-diode arrays have also been proposed.

Acknowledgements

We like to thank H.Melchior of ETH-Zürich for providing the InGaAs/InP photo-diodes and M.Vrana of the University of Gent / ELIS for his assistance during the flip-chip mounting.

References

- [1] K.Jelley et al., *Phot.Techn.Lett.* 4(10), Oct 1992, pp.1157-1159.
- [2] J.Thomson et al., *Optical Engineering* 33(3), March 1994, pp.939-945.
- [3] Y.Liu et al., Organic Thin Films for Photonic Applications, Portland, Sept 1995, pp.14-17.
- [4] B.Booth et al., Optoelectronic Packaging Conf., San Jose, Feb 1996, pp.2-8.
- [5] L.Robitaille et al., *Phot.Techn.Lett.* 8(12), Dec 1996, pp.1647-1649.
- [6] T.Li et al., Optoelectronic Interconnects & Packaging Conf., San Jose, Feb 1997, pp.128-135.
- [7] H.Davidson, Photonics in Switching Conf., Stockholm, Apr 1997, pp.94-95.
- [8] S.Koike et al., *Components, Packaging & Manufacturing Techn.* 19(1), Feb 1996, pp.124-130.
- [9] P.Haugsjaa, IPR, Boston, May 1996, pp.350-353.
- [10] Y.Nakasuga et al., ECTC, Orlando, May 1996, pp.20-25.
- [11] J.Yoshida, OFC, Dallas, Feb 1997, pp.275-276.
- [12] P.De Dobbelaere et al., CLEO/Europe, Amsterdam, Aug 1994, pp.178-179.
- [13] W.Lin et al., *Components, Packaging & Manufacturing Techn.* 18(3), Aug 1995, pp.543-551.
- [14] J.van der Linden et al., Organic Thin Films for Photonic Appl., Orlando, Aug 1996, pp.366-367.
- [15] J.van der Linden et al., Networks & Optical Comm. Conf., Antwerp, June 1997, pp. 286-291.
- [16] T.Kwa et al., *J.Electrochemical Society* 142(4), April 1995, pp. 1226-1233.
- [17] J.van der Linden et al., MOC/GRIN, Tokyo, Oct 1997, pp.11-14.
- [18] S.Joiner, OSA Annual Meeting, Long Beach, Oct 1997, pp.170-171.
- [19] Y.Bäcklund et al., Solid-State Sensors & Actuators Conf., Yokohama, June 1993, pp.1031-1033.
- [20] N.Bouadma et al., *Phot.Tech.Lett.* 6(10), Oct 1994, pp.1188-1190.
- [21] I.Moerman et al., *Electr.Lett.* 31(6), March 1995, pp. 452-454.
- [22] T.Yamamoto et al., MOC/GRIN, Tokyo, Oct 1997, pp.104-107.
- [23] D.Goodwill et al., ECTC, San José, May 1997, pp.788-796.
- [24] T.Hayashi, *Components, Hybrids, and Manufacturing Techn.* 15(2), Apr 1992, pp.225-230.

Polarization Switching in VCSEL's Due to Thermal Index guiding

Krassimir Panajotov¹, Boris Ryvkin², Jan Danckaert, Michael Peeters,

Hugo Thienpont, and Irina Veretennicoff

Vrije Universiteit Brussel, Applied Physics Department (TW-TONA),

Pleinlaan 2, B-1050 Brussels, Belgium

Tel. +32 2 629 3613

Fax +32 2 629 3450

e-mail kpanajot@vub.ac.be or jandan@vub.ac.be

Vertical Cavity Surface Emitting Lasers (VCSEL's) usually emit linearly polarized light oriented in a specific crystallographic direction. This has been attributed to an inherent birefringence caused by stresses unintentionally induced during manufacturing [1]. Moreover, it has also been observed that this linear polarization can switch between two orthogonal states [2],[3]. The switching takes place at currents of 10 to 50% above the threshold current, i.e. in the region of the fundamental (Gaussian) transverse mode of the laser. The origin of this switching has been identified to be the spectral shift of the gain maximum relative to the cavity resonance's for the two polarizations caused by the current heating [2]. Alternative mechanisms leading to polarization switching have also been proposed recently [4],[5].

Here, we experimentally demonstrate another mechanism for polarization switching in VCSEL's and provide an explanation based on the effect of thermal lensing in combination with waveguide anisotropy. The lasers used in these experiments are proton - implanted GaAs/AlGaAs multiple-quantum-well VCSEL's from VIXEL Corporation, operating around 850nm [6]. In fig.1 we show a typical optical output power versus current characteristic for both direct current (DC) and short pulse injection current at a fixed substrate temperature of 25 °C. For DC injection, when the active region temperature increases with current, polarization switching takes place. However, for short pulse injection (22ns) at low frequency (1kHz), chosen such that no current heating occurs, polarization switching is not observed. With a prebias close to the switching point, polarization switching has been observed by sinusoidal small current modulation at frequencies of up to about 50MHz, yielding a polarization contrast ratio of 20:1. From polarization resolved measurements we have observed that the shorter wavelength corresponds to the linear polarization at which the VCSEL starts lasing (see Fig.2 right). The wavelength splitting between the two orthogonal polarisation modes was measured to be less than 1 Angstrom.

The measured threshold current dependence on the substrate temperature is presented in fig.2 (left). One can see that both in the DC and in the pulsed regime the threshold current increases monotonically with the substrate temperature. This is a clear indication that the laser operates on the short - wavelength side of the gain maximum for the region of temperatures at hand. Therefore, since the material gain for longer wavelengths is larger and our VCSEL's switch from shorter to longer wavelength with increasing current, *the polarization switching of our VCSEL's is not related to the relative spectral alignment of the laser gain and the cavity mode* [2].

On the other hand, the threshold current in short pulsed current operation (when the temperature of the active layer remains *equal* to the substrate temperature) is larger than for CW

¹ Permanent address: Institute of Solid State Physics, 72 Tzarigradsko Chaussee blvd., 1784 Sofia, Bulgaria.

² Permanent address: A.F. Ioffe Physicotechnical Institute, 194021 St. Petersburg, Russia.

operation. This could be evidence for current heating in the VCSEL's under consideration leading to the formation of a thermal lens and therefore to a decrease of the threshold current [7]. So we measured the dependence of the threshold current on the dissipated power P_{dis} (which was varied by changing the DC current prebias) for short current pulses (22ns), showing clearly that the DC current prebias induces a thermal lens[8].

We will now explain how thermal lensing in combination with a slight cavity anisotropy can induce polarisation switching even when the laser operates at the short wavelength side of the gain maximum. To verify this conjecture we applied the work of Dutta *et al.* [7] for the case of a slightly anisotropic surface emitting laser. They showed that *current heating of the VCSEL active region changes the transverse refractive index profile by a thermo-optic effect and leads to a creation of a waveguide*. As a result, the modal gain G_m for the fundamental Gaussian transverse mode was given by [9]:

$$G_m = g - \frac{\Delta g}{S k_0} (2n_0 \Delta n)^{-1/2} \quad (1)$$

Here g is the gain in the center of the active region with a circular symmetry. Δg and Δn are the gain and the refractive index differences between the center and the edge of the effective contact [9] due to respectively the carrier spreading and the thermal lensing. S is the radius of the effective contact, n_0 is the effective refractive index and $k_0 = 2\pi/\lambda_0$, where λ_0 is the wavelength in free space. The quantity Δn is mainly determined by the temperature change, $\Delta n = (dn/dT)\Delta T$ [7] (ΔT being the temperature difference between the center and the edge of the effective contact and $\Delta T = A P_{dis}$, P_{dis} being the power dissipated in the VCSEL. Formula (1) was obtained assuming that $\Delta n \gg \Delta g/k_0$, i.e. it holds at sufficiently large P_{dis} . Due to the residual stress birefringence VCSEL's have two slightly different refractive indices for the two orthogonal polarizations [1]. As a result, two different linear polarizations of light with slightly different wavelengths λ_{01} and λ_{02} could be supported by the laser resonator (see Fig.2 right). In the steady state, the VCSEL will generate that state of linear polarization which corresponds to the largest modal gain.

The difference in the modal gains $\delta G = G_{m1} - G_{m2}$ for the two linear polarizations with different resonant wavelengths can be written as follows [8]:

$$\delta G = (g_2 - g_1) - \frac{K}{\sqrt{\Delta T}} (g_2 \sqrt{\lambda_{02}} - g_1 \sqrt{\lambda_{01}}) \quad (2)$$

where g_1 and g_2 are the gain coefficients at wavelengths λ_{01} and λ_{02} , respectively. The modal gain difference therefore decreases with increasing ΔT : for weaker wave guiding (smaller ΔT) the difference in the confinement of the two modes is more pronounced. *As a result, for small ΔT (i.e. small P_{dis}) the shorter wavelength mode may experience larger modal gain despite the fact that when operating on the shorter wavelength side of the gain maximum the material gain g for this mode is smaller.* Now, with increasing P_{dis} (i.e. ΔT) waveguiding becomes stronger, the difference in the confinement weaker, and the modal gain for the longer wavelength mode becomes larger. The switching point ($\delta G=0$) can be determined from Eq.(2). The constant K can be obtained experimentally from the dependence of the VCSEL's threshold current on the dissipated power [8].

As a conclusion, we demonstrated polarization switching in proton-implanted GaAs/-AlGaAs multiple-quantum-well VCSEL's, operating around 850nm. The experiments were performed at the cavity resonance wavelength at the short - wavelength side of the gain curve. We showed that this polarization switching is due to the creation of a thermal lens and to subsequent competition of the modal gains for the two orthogonal and linearly polarized modes coexisting in the slightly anisotropic laser resonator.

ACKNOWLEDGMENTS:

KP and BR resp. acknowledge the support of the Belgian Office for Scientific, Technical and Cultural affairs and "Research in Brussels" for their fellowships as visiting researchers. JD acknowledges a postdoctoral fellowship from FWO. This work was performed in the framework of the IUAP13 "Photonic Information Systems", FWO, Concerted Research Action "Photonics in Computing" and Research Council (OZR) of the Vrije Universiteit Brussel. The authors also acknowledge fruitful discussions with Thomas Erneux (Université Libre de Bruxelles).

REFERENCES:

1. A.K.Jansen van Doorn, M.P. van Exter, and J.P.Woerdman, "Elastooptic anisotropy and polarization orientation of VCSEL's", *Appl. Phys. Lett.*, vol.69, pp.1041-1043, 1996.
2. K.D.Choquette, D.A.Richie and R.E.Leibenguth, "Temperature Dependence of Gain-guided of Vertical -Cavity Surface Emitting Laser Polarization", *Appl. Phys. Lett.*, vol.64, pp.2062-2064, 1994.
3. K.D.Choquette, K.L.Lear, R.E.Leibenguth and M.T.Asom, "Polarization Modulation of Vertical -Cavity Laser Diodes", *Appl. Phys. Lett.*, vol.64, pp.2767-2769, 1994
4. J.Martin-Regalado, M.SanMiguel, N.B.Abraham and F.Prati, "Polarization Switching in Quantum-Well Vertical -Cavity Surface Emitting Lasers", *Opt.Lett.*, vol.21, pp.351-353, 1996; J.Martin-Regalado, J.L.A. Chilla, J.J. Rocca and P.Brusenbach, "Polarization switching in Vertical-Cavity Surface Emitting Lasers observed at constant active region temperature", *Appl. Phys. Lett.*, Vol. 70, pp.3350-3352, 1997.
5. A.Valle, L.Pesquera and K.S.Shore, "Polarization Behaviour of Birefringent Multitransverse Mode Vertical -Cavity Surface Emitting Lasers", *IEEE Phot.Techn.Lett.*, vol.9, pp.557-559, 1997.
6. Vixel Corporation, 325 Interlocken Parkway, Bromfield, CO 50021.
7. N.K.Dutta, L.W.Tu, G.Hasnain, G.Zydzik, Y.H.Wang, and A.Y.Cho, "Anomalous temporal response of gain guided surface emitting lasers", *Elect. Lett.*, vol.27, pp.208-210, 1991.
8. K. Panajotov, B. Ryvkin, J. Danckaert, M. Peeters, H. Thienpont and I. Veretennicoff, "Polarisation Switching in VCSEL's due to Thermal Lensing", *Phot. Techn. Lett.*, v.10, No.1, 1998.
9. N.K.Dutta, "Analysis of current spreading, carrier diffusion, and transverse mode guiding in surface emitting lasers", *J.Appl.Phys.*, vol.68, pp.1961-1963, 1990.

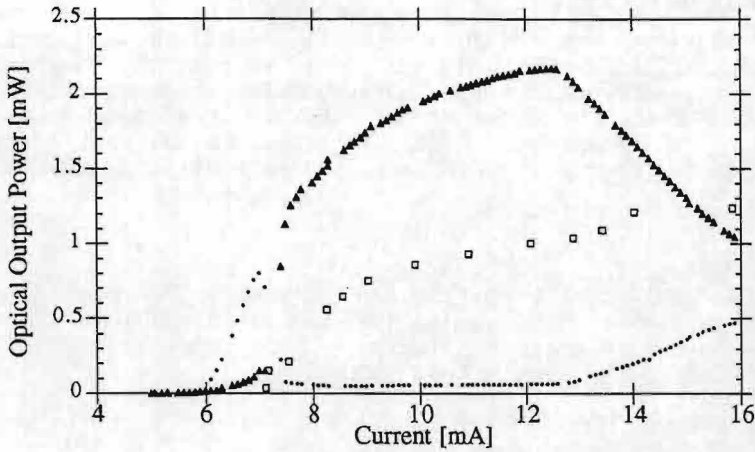


Fig.1. The VCSEL's optical output power as a function of the injection current at a fixed substrate temperature of 25 °C. The circles (triangles) corresponds to linear short (long) wavelength polarization emission in CW operation. The diamonds correspond to linear short wavelength polarization for short pulsed current (22ns, 1kHz) operation.

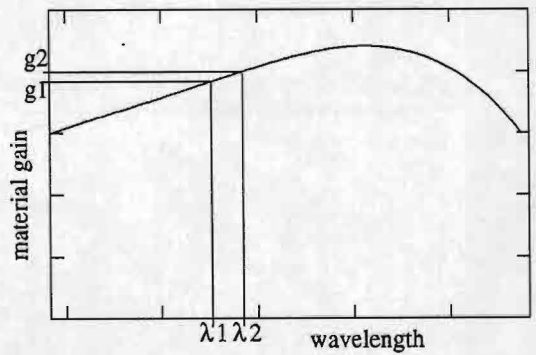
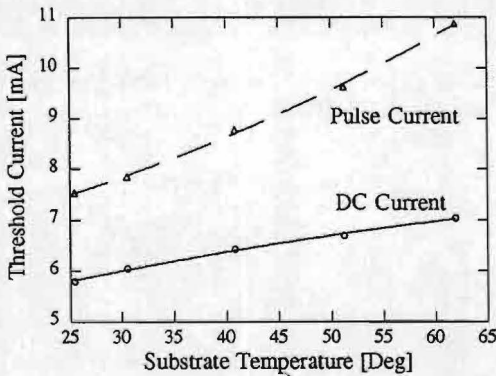


Fig.2. Left: threshold current dependence on the substrate temperature for DC and pulsed drive currents. Right: schematical dependence of the material gain on the wavelength. Polarization switching corresponds to transition from shorter wavelength towards longer wavelength as the current increases.

Reconfigurable optical interconnects in free-space optical processing modules using polarization-selective diffractive optical elements

N Nieuborg¹, A Goulet¹, H Thienpont¹, *Member IEEE*, A Kirk³, P Koczyk¹, P Heremans⁴,
Member IEEE, M Kuijk⁴, *Member IEEE*, C De Tandt², W Ranson², R Vounckx²
 and I Veretennicoff¹, *Member IEEE*

¹Laboratory for Photonic Computing and Perception, ²Laboratory for Microelectronics and Technology, Department of Applied Physics (TW-TONA), Vrije Universiteit Brussel, B-1050, Brussel, BELGIUM

Tel. +32 2 629 3451 Fax +32 2 629 3450 e-mail nnieubor@vub.ac.be

³Photonic Systems Group, Department of Electrical Engineering, McGill University, 3840 University Street, Montreal, Quebec, H3A 2A7, CANADA

⁴IMEC, Kapeldreef 75, B-3001 Leuven, BELGIUM

Abstract – We demonstrate a reconfigurable data transparent optical fanout element and a switchable digital optical logical inverter between planes of optical thyristors using polarization-selective diffractive optical elements in combination with a liquid crystal polarization controller.

1. Introduction

Free-space optical interconnects have been widely used in parallel optical information processing systems [1]. The growing complexity of the desired routing configurations has created an urgent need for data transparent, reconfigurable and flexible interconnections. Polarization has always played an important role in the realization of such interconnects, because of the possibility to route the optical data via an electro-optic control of its state of polarization.

In this paper we demonstrate the use of polarization-selective diffractive optical elements for the realization of reconfigurable optical interconnects in parallel free-space optical information processing modules. In these modules a liquid crystal variable retarder is used as a polarization controller and arrays of differential pairs of optical thyristors [2] serve as optoelectronic processing planes. These differential pairs of optical thyristors may be used as dual-rail optoelectronic transceivers in digital

information and image processing systems [3, 4]. Differential competition ensures that if a voltage above the break-over voltage ($V_{BR} = 5V$) is applied after illumination, that side which received the greatest optical energy will emit light while the other will remain switched off. The emitted light is of a Lambertian nature and has a spectral full width half maximum of 45nm centered around 860nm.

Recently we have demonstrated array-to-array data transcription with a static fanout of 3 [3]. Therefore we built a compact and modular free-space imaging system (fig. 1).

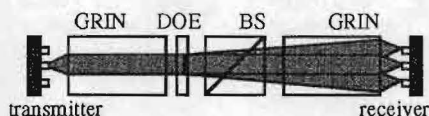


Figure 1. Optical system used for the data transcription between planes of optical thyristors; BS – beam-splitter.

Light emitted from the transmitter plane was collimated through a 0.2 pitch GRIN-lens. The collimated beam was then diffracted into 3 beams by a diffractive optical element and focussed onto the receiver plane by a second identical GRIN lens [5]. The advantage of this optical system is that its Fourier plane is situated between the two GRIN lenses,

allowing us to insert shift invariant diffraction based fanin and fanout elements.

In this paper we will show that it is possible to increase the functionality of this interconnection system by replacing the diffractive optical element with a polarization-selective diffractive optical element [6] in combination with a polarizer and a polarization controller.

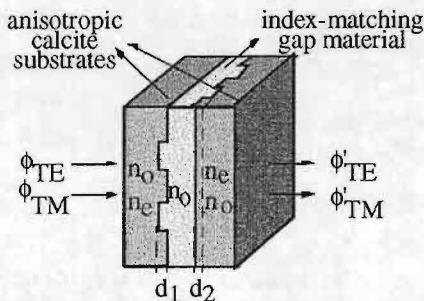


Figure 2. Polarization-selective diffractive optical elements consisting of two etched anisotropic substrates, joined together by an index-matching polymer.

Polarization-selective diffractive optical elements are elements which can fulfill two different functions dependent on the polarization of the incident beam. For the fabrication of such elements we use two wet etched calcite (CaCO_3) plates, which we align orthogonally to one another and join together using an index-matching thermoplast (Cargille Meltmount 1.662) (see fig. 2). For such a structure a TM polarized beam will only see the phase pattern etched in the first substrate, whereas a TE polarized beam will only see the pattern in the second substrate. Typical first order diffraction efficiencies of these binary elements are 30-40%, and polarization contrast ratios up to 1000:1 have been demonstrated.

As examples of how to implement these ADOEs for reconfigurable interconnects we will bring forward two demonstrators. A first makes use of an on/off switchable binary grating that performs the logical NOT operation. The other allows to establish a reconfigurable 1 to 4 / 1 to 5 / 1 to 9

interconnection pattern between the emitting and the receiving plane.

2. Switchable digital optical logical inverter

Differential pairs of optical thyristors can be used as optical logic gates, by using the convention that a logical 1 corresponds to an emitting left hand thyristor, whereas a logical 0 corresponds to an emitting right hand thyristor [4]. Hence to perform a NOT operation within a dual-rail logic system it is necessary to interchange the signals of the left and right channels. Such a cross-over can be achieved through the use of a diffraction grating. By the choice of a suitable grating pitch the +1 diffracted beam from the left-hand transmitter channel can be made coincident with the right-hand receiver channel while the -1 diffracted beam from the right-hand transmitter can be coincident with the left-hand receiver. The gratings are designed such that the other orders fall outside the active area of the receivers. Fig. 3 shows the setup that was used to perform the reconfigurable inversion. The spacing between two thyristors in the receiver plane is $45\mu\text{m}$, resulting in a grating period of $304\mu\text{m}$. An individually electrically addressable pair of optical thyristors in the transmitter plane can be switched such that either the left or right hand side of the pair will emit light. A polarizer is used to polarize the light vertically (TE) (see fig. 3).

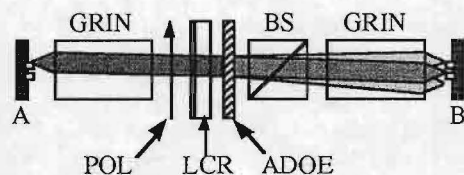


Figure 3. Integration of a switchable digital logical inverter between planes of optical thyristors; POL – polarizer; LCR – liquid crystal retarder; ADOE – anisotropic diffractive optical element.

An electrically controllable liquid crystal retarder (LCR) is used to switch the polarization state between TE and TM. The polarization-selective grating was designed such as to simply transmit the light for TE polarization (yielding transcription without

inversion), and to diffract it for TM polarization (yielding transcription with inversion). Fig. 4 shows the results of the switchable inversion. The first two traces show the voltage applied to the left and the right transmitter elements. The third trace shows the output of the left thyristor of the receiver differential pair. The results show that dependent on the voltage applied on the LCR transcription with or without inversion is realized. The reconfiguration rate of this system is limited by the switching speed of the LCR, which is 20Hz in the case of a nematic liquid crystal retarder. In the case of a ferroelectric LCR this can be increased up to 20kHz.

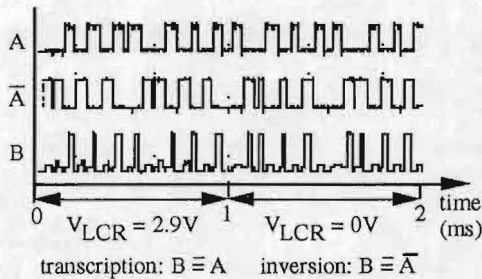


Figure 4. Demonstration of the NOT operation

3. Reconfigurable fanout element

The same principle of combining ADOEs together with liquid crystal polarization controllers can be used to realize more complicated reconfigurable interconnection schemes. In this paragraph we present a reconfigurable fanout element that, dependent on the polarization of the incident

beam, connects either to 4, to 5 or to 9 nearest-neighbours in the receiver plane (see fig. 5).

In order to achieve this functionality we have designed two crossed gratings for the 1 to 4 and the 1 to 5 interconnect respectively. The spacing between the differential pairs in the receiver plane was $96\mu\text{m}$ in the horizontal direction and $100\mu\text{m}$ in the vertical direction, resulting in grating periods of $144\mu\text{m}$ and $137\mu\text{m}$ respectively. These resulting grating patterns are combined in one polarization-selective diffractive optical element, that can realize the 1 to 4 interconnect for horizontally, and the 1 to 5 interconnect for vertically polarized light. For circularly polarized light a combination of the two functionalities is obtained and so a 1 to 9 interconnection will be established.

Fig. 5b shows the response of ADOE and fig. 6 shows the corresponding response of the receiver plane for the three different polarization states when the left-hand (a) and the right-hand (b) transmitter element were switched on. When the left-hand transmitter element is switched on the left-hand thyristors of the addressed differential pairs in the receiver plane will switch on (i.e. emit light), whereas the other elements of the receiver plane will not be addressed optically, and will therefore switch at random. We can see that the fanout is correctly realized. We should however note here that the higher the fanout the lower the intensity of the individual optical channels, resulting in a trade-off between the fanout of the grating and the switching speed of the thyristors in the receiver plane.

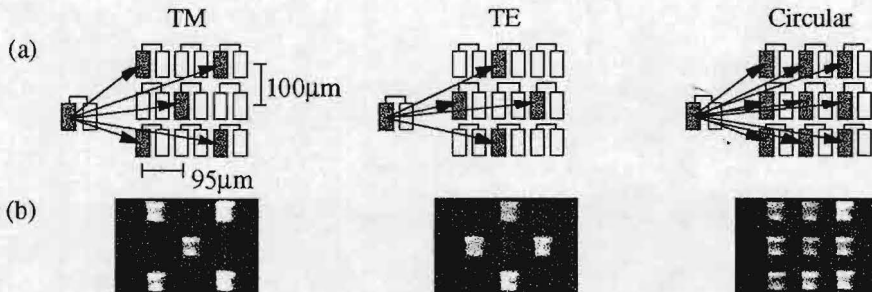


Figure 5. Desired interconnection scheme (a) and experimentally obtained output (b) for the reconfigurable polarization-based fanout-element when the polarization of the incident beam is vertical, horizontal or circular.

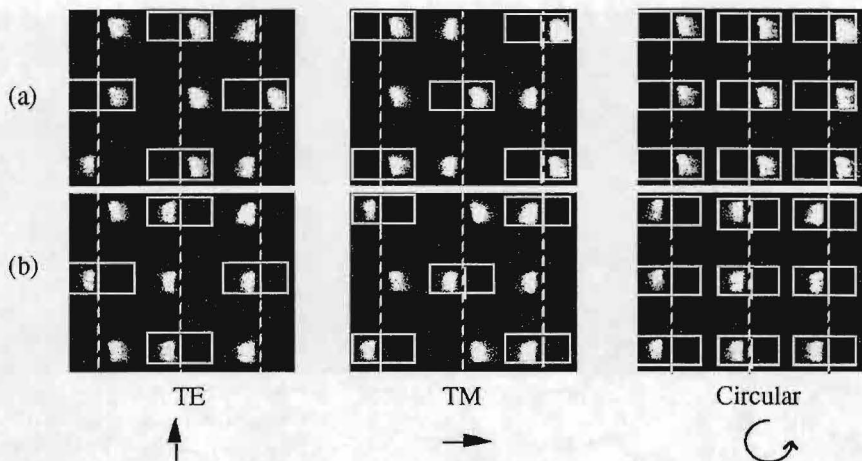


Figure 6. Output from differential pair receiver for input to the left (a) and to the right (b) for the different possible polarization states.

4. Conclusion

We have shown that we can increase the functionality of a free-space digital parallel optoelectronic data transcription system based on differential pairs of optical thyristors by use of polarization-selective diffractive optical elements and polarization controllers. We have demonstrated the application of a switchable diffractive grating as a logical inverter, and we have demonstrated that it is possible to realize reconfigurable 1 to 4, 1 to 5 and 1 to 9 fanout operations. Finally it is important to notice that we can easily change the functionality of the ADOE by altering its design or by replacing it with a polarization-selective computer-generated hologram [7], and that the techniques that have been presented here are also generally applicable to other types of opto-electronic transceiver elements.

Acknowledgements

Nancy Nieuborg thanks the IWT for her research grant. Pawel Koczyk thanks TEMPUS for his grant. Hugo Thienpont thanks the FWO for sponsoring the purchase of the polarization analyzer. This work has been carried out in the framework of a broad project supported by IUAP 13, Geconcerteerde Onderzoeksactie GOA "Photonics in Computing", FWO "Micro-Optics and Parallel Photonic Information Processing" and the Onderzoeksraad OZR of the Vrije Universiteit Brussel.

References

- [1] H. S. Hinton, An introduction to photonic switching fabrics, Plenum Press, New York, 1993.
- [2] M. Kuijk, B. Knüpfer, P. Heremans, R. Vounckx, G. Borghs, "Down-scaling differential pairs of depleted optical thyristors," *IEEE Photon. Technol. Lett.*, vol. 7, no. 6, pp.646-648, 1995.
- [3] A.G. Kirk, H. Thienpont, A. Goulet, P. Heremans, G. Borghs, R. Vounckx, M. Kuijk, I. Veretennicoff, "Parallel Optoelectronic Data Transcription with Fan-Out Between Planes of PnpN Optical Thyristors," *IEEE Phot. Techn. Lett.*, vol. 8, no. 3, pp.464-466, 1996.
- [4] A.G. Kirk, H. Thienpont, A. Goulet, P. Heremans, G. Borghs, R. Vounckx, M. Kuijk, I. Veretennicoff, "Demonstration of Optoelectronic Logic Operations with Differential Pairs of Optical Thyristors," *IEEE Phot. Techn. Lett.*, vol. 8, no. 3, pp.467-469, 1996.
- [5] A.G. Kirk, A. Goulet, H. Thienpont, N. McArdle, K.-H. Brenner, M. Kuijk, P. Heremans, I. Veretennicoff, "Compact optical imaging system for arrays of optical thyristors," *Applied Optics*, vol. 36, no. 14, pp. 3070 - 3078, 1997.
- [6] N. Nieuborg, A. Kirk, B. Morlion, H. Thienpont, I. Veretennicoff, "Polarization-selective diffractive optical elements with an index-matching gap material," *Applied Optics*, vol. 36 (20), pp. 4681-4685, 1997.
- [7] F. Xu, Y. Fainman, J.E. Ford, A.V. Krishnamoorthy, "Optoelectronic-VLSI packaging with polarization-selective computer-generated holograms," *Optics Letters*, vol. 22, no. 14, pp.1095-1097, 1997.

Optical performance analysis of free-space and guided-wave optical pathway blocks for intra-MCM interconnects

V. Baukens, G. Verschaffelt, P. Tuteleers, P. Vynck, H. Ottevaere, M. Kufner, S. Kufner, H. Thienpont, I. Veretennicoff, B. Dhoedt¹ and R. Baets¹.

Vrije Universiteit Brussel, Applied Physics Department (TW-TONA), Pleinlaan 2,B-1050, Brussel, Belgium, Tel. +32 2 629 3451, Fax. +32 2 629 3450, vbaukens@vub.ac.be

¹Rijksuniversiteit Gent, Departement of Information Technology (INTEC), Sint-Pietersnieuwstraat 41, B-9000 Gent, Belgium

We have simulated, analysed and compared the performances of several free-space and POF-based guided-wave intra-MCM optical interconnection systems for different types of microcavity emitters, resulting in guidelines for the design of practical configurations.

1. Introduction

The performance of future generation data processing systems will be set by intra-MCM interconnect limitations rather than by the processing performance of the CMOS IC's within this module.

Optical I/O over the entire chip area is pursued as a solution to these interconnection problems in the European Community funded ESPRIT project "Optically Interconnected Integrated Circuits" (OIIC). With this approach, two dimensional (2D) parallel data transfer will be made possible through the use of opto-electronic emitter and receiver arrays, flip-chip mounted on CMOS circuitry, and interconnected by passive optical pathway blocks. At the source side of the optical interconnection, both Vertical Cavity Surface Emitting Lasers (VCSELs) and Micro-Cavity Light Emitting Diodes (MCLEDs) [1] are considered.

For the optical pathways, two approaches are explored. As a principal choice in this project, a 2D array of small diameter Plastic Optical Fibers (POFs) is used as a flexible transmission medium. The large numerical aperture of these fibers makes high coupling efficiencies possible with both types of emitters. Furthermore its small bending radius allows for a compact assembly such that low headroom optical interconnection modules become possible. Finally its large core diameter allows for a highly tolerant mechanical alignment of the optical pathway block with respect to the emitter/receiver chips. As an alternative to this POF guided-wave interconnection approach the construction of a free-space optical pathway block is pursued. Here we apply deep proton irradiation as a deep etch lithographic technique to fabricate PMMA-based, manufacturable, chip-compatible and high-precision monolithic micro-optical pathway blocks [2]. They integrate microlenses and micromirrors to optically interconnect the flip-chip mounted surface-normal transmitters and receivers.

In this paper we simulate and analyse the performances of the guided-wave optical interconnection system for different POF characteristics and different microcavity emitters. We also study the performances of the free-space interconnection systems for VCSEL sources. In both cases we derive guidelines for the design of practical configurations.

2. The POF optical pathway block.

The optical pathway block under study consists of a plastic plate with a 2D-array of holes into which POF ribbons are inserted. (See Fig 1) The advantages of POFs over glass fibers are their lower cost and their higher flexibility. There are two requirements that have to be fulfilled before we can consider the OPB as a possible candidate for optical intra-MCM interconnections. First of all we cannot allow cross-talk between the optical data channels. Secondly the transmission efficiency has to be high enough such as to satisfy the receiver sensitivity. This will assure a very low bit error ratio, required for this kind of data transmission links. For this POF approach we have modeled both the optical transmission efficiency and the cross-talk.

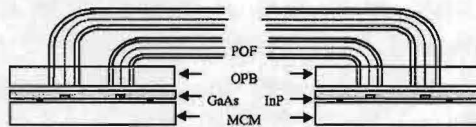


Figure 1. Schematic drawing of the guided-wave optical intra-MCM interconnect

Fig 2 shows a schematic model of the configuration. The optical system consists of three main parts. First we have the emitter followed by an optical input module (OPB_{in}), secondly the light guiding POF and as a last part the output module (OPB_{out}) and the receiver. We have divided the optical system in these three parts because this allows investigating them on efficiency and cross-talk individually. From these results we can draw conclusions on the overall efficiency of the OPB and on the working distances between the emitter or receiver surfaces and the OPBs so as not to have cross-talk. For each of these three parts of the optical system, we can make a list of the parameters, which affect the cross-talk and the efficiency. (See fig 2 and table 1) Two different micro-emitters are used: a MCLED and a VCSEL. The characteristics of these sources and detectors are according to the specifications of the OIIC project. We have also investigated two different device pitches. Although the device pitch within the OIIC project is 250 μm , also a smaller pitch of 125 μm has been investigated to check whether the system is scalable. In our model we consider small diameter POFs with a core diameter of 120 or 60 μm , each of which could have a numerical aperture of 0.25 or 0.50. Both the emitter and detector side has been simulated via ray tracing and radiometric calculations. The simulations do not taken into account the reflection losses. Inside the POF we have assumed a perfect optical transmission, which comes down to neglecting the attenuation (att. of less than 0.1dB/cm) as well as the bending losses. (90° bend of a POF with a bending radius of 2 mm does not result in extra losses larger than 0.3 dB at 633 nm [3].)

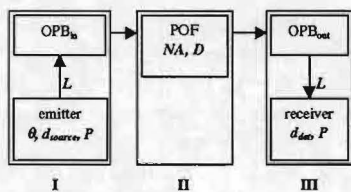


Figure 2. Schematic model of the simulated optical system

	I		II	III
	MC-LED*	VCSEL*	POF	Detector*
Substr. Thick.	T=150 μm			T=150 μm
Diameter	$d_{\text{source}}=50 \mu\text{m}$	$d_{\text{source}}=15 \mu\text{m}$	$D=60 \wedge 120 \mu\text{m}$	$d_{\text{det}}=150 \mu\text{m}$
NA	$\theta_{\text{FWHM}}=100^\circ$	$\theta_{\text{FWHM}}=12^\circ$	$NA=0.5 \wedge 0.25$	$d_{\text{det}}=75 \mu\text{m}$
Pitch	$P=125 \wedge 250 \mu\text{m}$			
Working dist.	L			L

Table 1. Characteristics of sources and detector (*Through substrate emitter/receiver).

I. Results at the emitter side

Since we want to avoid cross-talk between neighboring fibers, we have to limit the working distance L. The maximum value for this working distance, as derived from an analytic study of the optical system, is given by

$$L_{\text{max}} = \frac{P - d_{\text{source}}/2 - D/2}{\text{tg}\theta} \quad (1)$$

We also know that once the diameter of the light beam is larger than the diameter of the POF a drop in efficiency will occur. The distance L* for which the beam diameter and the POF diameter are equal is given by

$$L^* = \frac{D/2 - d/2}{\text{tg}\theta} \quad (2)$$

For the MCLED and the VCSEL the meaning of θ in formula (1) and (2) is different. The divergence angle of the MCLED ($\theta_{\text{FWHM}} = 100^\circ$) is larger than the acceptance angle of the POF ($\theta_a = 30^\circ$ for $NA = 0.5$ and $\theta_a = 14.5^\circ$ for $NA=0.25$), which is not the case for the VCSEL. Because of this, that part of the light with an emission angle larger than θ_a can not propagate through the POF. Therefore θ should have the value of the acceptance angle of the POF instead of the divergence angle of the MCLED.

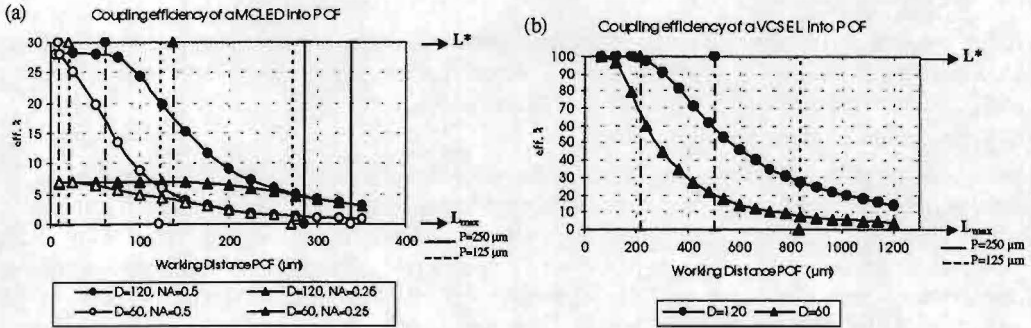


Figure 3. Coupling efficiency of a MCLED (a) and VCSEL (b) into POF.

In our radiometric calculations the source model has a Gaussian angular distribution and a circular geometry with a uniform emittance. The detector is modeled as a multi mode fiber with the corresponding diameter and NA of the POF. The result of these simulations gives us the coupling efficiency of the source in the POF. In fig. 4 we show the efficiency as a function of the working distance for both the MCLED (a) and the VCSEL (b). These curves are calculated for different combinations of the diameter and NA of the POF. The vertical lines are the limits on L for cross-talk. L^* indicates where we expect a drop in efficiency. In case of the MCLED we see that for short working distances, a large NA fiber results in a higher efficiency and the influence of the core diameter is of minor importance. Even for these small working distances the coupling efficiencies are low and do not exceed 30%. However if a VCSEL is used the NA of the fiber does not affect the coupling efficiency because of the small divergence angle of this emitter type. A 100% coupling efficiency can be reached if working distances smaller than 180 μm and 60 μm are applied for a POF diameter of resp. 120 μm and 60 μm .

II. Results at the receiver side.

In analogue way the optical system at the receiver side has been studied. The maximum working distance in order to avoid cross-talk is given by

$$L_{\max} = \frac{P - d'_{\text{det}}/2 - D/2}{\text{tg}\theta} \quad \text{where} \quad (3)$$

$$d'_{\text{det}} = d_{\text{det}} + 2L_{\text{subst}} \cdot \text{tg}(a \sin \frac{NA}{n_{\text{InP}}})$$

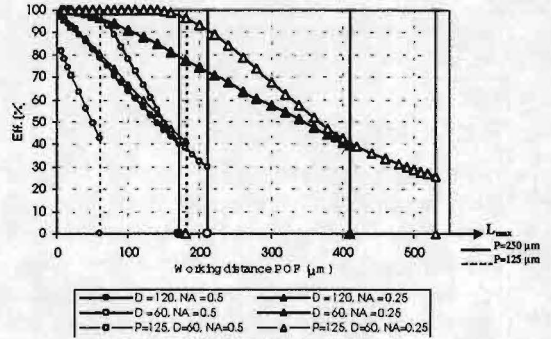


Figure 4. Efficiency at receiver side

III. Overall Efficiency.

The overall efficiencies for several configurations of the optical intra-MCM interconnections are summarised in table 2. We can conclude that if we use a VCSEL as emitter that the efficiency is much higher. The distance L is chosen such that we work in the region where we expect the best efficiency and where cross-talk is avoided both at emitter and receiver side.

Emitter/Receiver	POF	L	Overall eff. %
MCLED/InP det, P=250 μm	D=120 μm , NA=0.5	$\leq 60\mu\text{m}$	26 \rightarrow 22
	D=120 μm , NA=0.25	$\leq 135\mu\text{m}$	7 \rightarrow 6
	D=60 μm , NA=0.5	$\leq 50\mu\text{m}$	26 \rightarrow 20
	D=60 μm , NA=0.25	$\leq 50\mu\text{m}$	7 \rightarrow 6
MCLED/InP det, P=125 μm	D=60 μm , NA=0.5	$< 50\mu\text{m}$	18 \rightarrow 10
	D=60 μm , NA=0.25	$< 50\mu\text{m}$	7 \rightarrow 5
VCSEL/InP det, P=250 μm	D=120 μm , NA=0.5	$< 150\mu\text{m}$	93 \rightarrow 46
	D=120 μm , NA=0.25	$< 200\mu\text{m}$	100 \rightarrow 77
	D=60 μm , NA=0.5	$< 200\mu\text{m}$	100 \rightarrow 96
	D=60 μm , NA=0.25	$< 200\mu\text{m}$	100 \rightarrow 99
VCSEL/InP det, P=125 μm	D=60 μm , NA=0.5	$< 50\mu\text{m}$	71 \rightarrow 49
	D=60 μm , NA=0.25	$< 160\mu\text{m}$	93 \rightarrow 68

Table 2. Transmission efficiencies for optical interconnects

In the last column of table 2 the efficiency for a distance of 20 μm (max. eff.) and the efficiency for a distance L are shown. Working above L would dramatically decrease the overall efficiency and could even introduce cross-talk (see bold, italic values).

3. Free-space optical pathway block

To establish a free-space optical interconnection, we will use a pencil beam approach (see Fig 1). Here a first microlens array, positioned above the array of emitters acts as a beam collimator, while a second microlens array is used to refocus the beams onto the detector array. Each micromirror surface makes an angle of 45° with respect to the optical axes of the lenses in order to deflect the collimated beams by 90° . In this second approach for intra-MCM interconnects we will only consider VCSEL's as sources, because their low divergence angle emitters are imperative to avoid cross-talk between adjacent channels. Due to diffraction of the laser beam, the maximum interconnection distance L_{max} for a lens diameter ϕ_{lens} is limited to

$$L_{\text{max}} = \frac{\pi}{\lambda} \cdot \left(\frac{\phi_{\text{lens}}}{3} \right)^2 \quad (4)$$

In this formula we apply the rule that the laser beam must always be smaller than $2/3$ of the lens diameter so that more than 99% energy throughput through the lenses is achieved. Fig. 5 shows the maximum interconnection length as a function of the lens diameter. To relax the misalignment tolerances, it is better to work with a lens diameter that is a little larger than the diameter given by formula (4).

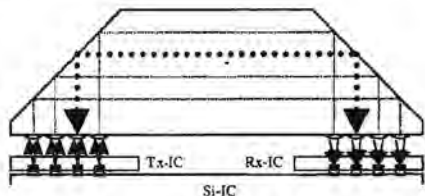


Figure. 4 Schematic drawing of a free-space optical interconnect

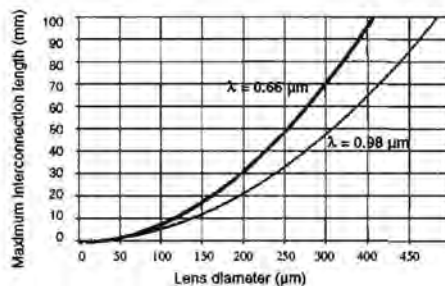


Figure. 5 Maximum interconnection length

4. Conclusions

In this paper we have studied both a free-space and a guided-wave system for intra-MCM optical interconnections. Whereas for dense interconnects the free-space approach is most suited for interconnection lengths up to a few millimeters, the guided-wave solution is more appropriate for distances larger than a centimeter. The choice of the emitter type in case of the guided-wave approach will strongly depend on thermal budget, overall system efficiency, single channel bandwidth, cost and yield of large arrays of both type of devices.

Acknowledgments

The work reported here is funded the European Commission ESPRIT-MELARI project 22641 "OIIIC", by DWTC IUAP 13, by FWO, GOA and the OZR of the Vrije Universiteit Brussel.

References

- [1] H. De Neve, et al., "Planar Substrate-Emitting microcavity Light-Emitting Diodes with 20% External QE", pp. 74-84, SPIE proc., San Jose, California, 1997.
- [2] P. Vynck, et al., "Aspects of Deep Proton Lithography for the Fabrication of Micro-optical Elements", IEEE LEOS BENELUX annual symposium, Eindhoven, 1997.
- [3] A. Neyer, M. Jöhnck, "Connectorized Two-Dimensional Array interconnects using $125 \mu\text{m}$ - POF", Proc. POF'97 conf., pp. 21-22, Hawaii, 1997.
- [4] G. Verschaffelt, et al., "Experimental demonstration of a free-space intrachip micro-optical interconnect", IEEE LEOS BENELUX annual symposium, Eindhoven, 1997.

THE STUDY OF THE STIMULATED LIGHT SCATTERING ACCOMPANIED WITH A TWO-PHOTON DISSOCIATION IN LIQUID ETHANOL AT 308 NM AND 248 NM.

Pastor A.A., Bertsev V.V., Bureiko S.F., Keller A.A., Serdobintsev P.Yu.

Institute of Physics, St. Petersburg State University, Peterhof, St. Petersburg 198904 Russia

Abstract

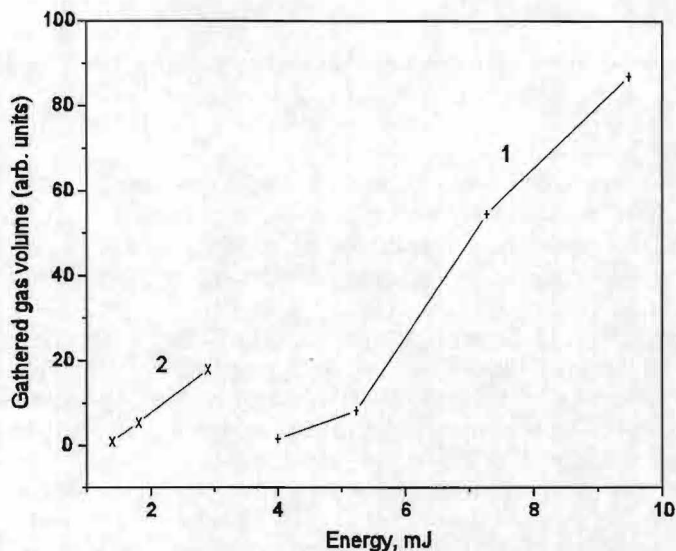
The connection between the stimulated light scattering and two-photon dissociation by excimer laser irradiation of liquid ethanol at 308 nm and 248 nm has been studied experimentally. Our experiments demonstrate the correlation between the intensity of stimulated scattering and the rate of the two-photon dissociation at this wavelengths.

The stimulated Brillouin scattering (SBS) is commonly applied to control temporal and spatial characteristics of laser radiation. The SBS is caused by variations of nonlinear refractive index in an transparent medium by means of the hypersound wave excited by laser radiation. The efficiency of this inertial process significantly depends on spectral purity of laser radiation. It is known that spatial variations of absorption coefficient and refractive index caused by the electronic excitation may be also the reason of the stimulated scattering (SS). Existing methods of the study of SS in linear absorbing media (stimulated temperature scattering (STS) and similar processes) have the defect in the case of so-called strong focusing geometry, when pumping laser beam is focused into nonlinear medium. The linear absorption leads to considerable losses of exciting laser radiation outside the focal zone where the nonlinear scattering occurs.

The aim of our investigations is to study SS processes at pumping laser frequencies lying near the two-photon resonances of transparent optical media. In our previous paper [1,2] we have demonstrated that the two-photon dissociation of liquid CCl_4 by the excimer XeCl laser radiation (308 nm) is accompanied by the stimulated scattering of pumping laser radiation. The performed measurements of the cross section of two-photon dissociation allowed us to estimate the CCl_4 dissociation degree in the focal zone where the stimulated scattering occurs. The dissociation degree is equal to 10% and more at the pumping intensities above the threshold of the SS. It leads to significant intensity-dependent variations in the refraction index and, hence, to the SS of the pumping radiation. In the work of Karpov, Korobkin and Dolgolenko [3] the stimulated scattering of the XeCl laser radiation in liquid hexane has been considered. They did not observe the frequency shift of scattered radiation relative to the pumping radiation at high intensities. This proves that the scattering mechanism of XeCl laser radiation in hexane at high intensities is STS. The authors suggest that the STS exciting mechanism is the two-photon process, because liquid hexane is lineary transparent at XeCl laser frequency.

In the present communication we report the results of simultaneous studies of two photon dissociation of liquid ethanol by XeCl (308 nm) and KrF (248 nm) excimer laser irradiation and the SS of pumping radiation in this liquid. Liquid ethanol is an perspective nonlinear medium for the nonlinear adaptive optical devices in near-UV spectral region because the threshold of the SS of excimer laser radiation in ethanol is relatively low; this liquid is transparent in near-UV and has no losses of pumping radiation by linear absorption. This leads to high efficiency of SS processes of excimer laser radiation in liquid ethanol. On the other hand, SS mechanism of near-UV laser radiation in ethanol is not finally clear. The stimulated scattering connected with the multiphoton absorption of pumping UV laser radiation (such as STS) is also discussed. On contrast to SBS, the STS and other

mechanisms combined with multiphoton absorption don't require of high spectral purity of the pumping UV radiation. Therefore the efficiency of adaptive optic devices based on these mechanisms can be higher in comparison with SBS method.



Our experimental setup utilizes excimer TEA lasers generating 5 ns fwhm pulses of either 308 nm (XeCl) or 248 nm (KrF) unfiltered radiation with the energy up to 60 mJ per pulse and the repetition rate up to 100 Hz. The cavity was formed by the plane totally reflecting mirror and by the flat uncoated quartz output coupler. The laser beam was focused by a spherical quartz lens of $f=2-5$ cm focal length into the quartz cells of 2-5 cm length equipped with BaF_2 windows and filled by the liquid ethanol. Under the irradiation of liquid ethanol, we observed the gas bubble's formation in the focal zone. The bubbles volume measurements were made with special capillary, which was adjusted vertically just over the lens focal zone. At the beginning, the capillary was filled by liquid ethanol. The lower capillary edge was widened and plunged into liquid ethanol, and the upper one was completely closed. The pumping pulses energy measurements were performed by a calorimeter IMO-2.

Fig.1. The dependence of the bubbles formation rate on frequency and intensity of pumping laser radiation. The curves 1 and 2 correspond to the pumping, respectively, by the XeCl (308 nm) and KrF (248 nm) excimer laser radiation.

When XeCl laser pulses with the energy more than 3 mJ were focused by the quartz lens $f=5$ cm into central region of the cell filled with ethanol, we observed an intense bubble's formation in the lens focal zone. It was noticed at once, that the bubbles did not change geometrical sizes when they moved up from the formation region to the liquid ethanol surface, as it should be if they were formed by evaporation. This fact let us to suppose that the bubbles are products of ethanol dissociation under the influence of focused laser beam. This conclusion was confirmed later by the spectral investigation of the gathered gas bubbles. The IR absorption spectra of the gathered gas show the presence of CH_4 which is known to be one of the ethanol dissociation products. Thus the total volume of the bubbles

formed during the fixed time unit was proportional to the ethanol dissociation rate. This fact was used for the measurements of the relative dissociation rates in dependence on frequency and intensity of pumping laser radiation. The relative dissociation rates measurements were made with the method of gathered gas volume estimation for the defined fixed time over the condition of stable process and constant pumping laser radiation parameters.

The dependence of the bubbles formation rate, i.e. dissociation rate dependence, on energy in the laser beam pulse is shown in fig. 1. The curves 1 and 2 correspond to the pumping, respectively, by the XeCl (308 nm) and KrF (248 nm) excimer laser radiation. One can see that these both dependencies are evident nonlinear. Besides, the striking dissociation rate dependence on pumping laser radiation wavelength is seen. The dissociation under XeCl (308 nm) laser radiation begins with lower intensities than under KrF (248 nm) laser radiation.

It is necessary to note that certain accordance of the results obtained with the results of SS investigation in the same medium takes place. When the same excimer lasers (XeCl (308 nm) and KrF (248 nm)) radiation was used in the SS experiments, it was found that the scattering as well as dissociation significantly depend on pumping laser radiation wavelength. When XeCl excimer laser (308 nm) was used as pumping laser the SS was excited easy, whereas when KrF laser (248 nm) was used, the SS was not observed without special linewidth reducing of pumping radiation. The linear losses of pumping radiation at both frequencies in liquid ethanol are negligible.

The observed frequency dependence of the SS probability can be explained scarcely within SBS model, since in that case the scattering probability grows with the increase of the pumping laser radiation frequency. On the other hand, the accordance of the above mentioned dependence with the nonlinear dissociation probability is observed. This fact let us to the conclusion that the SS mechanism as in the case of CCl_4 , is caused by the dissociation of molecules in the focal zone.

Financial support for this work through by the Russian Foundation for Basic Research under grant 96-02-17092a is gratefully acknowledged.

REFERENCES

1. Bertsev V.V., Pastor A.A. and Bulanin M.O., Optics Communications, v. 77, n. 1, 1990, p. 71-74
2. Bertsev V.V., Bulanin M.O., Pastor A.A., Optics and Spectroscopy, v. 70, n. 1, 1991, p. 97-100
3. Karpov V.B., Korobkin V.V., Dolgolenko D.A., Quantum Electronics, v. 18, n. 11, 1991, p. 1350-13

A single channel dropping filter based on a cylindrical micro-resonator

F.C. Blom, H. Kelderman, H.J.W.M. Hoekstra, A. Driessen, Th.J.A. Popma

Centre of Materials Research(CMO) & MESA Research Institute, University of Twente

P.O. Box 217, 7500 AE Enschede, The Netherlands,

Phone X-31-53-4892816, Fax X-31-53-4893343, E-mail: F.C.Blom@tn.utwente.nl

A single channel dropping filter for WDM systems with high selectivity has been realised in planar waveguide technology. It consists of a monomodal high-Q cylindrical micro-cavity between a pair of parallel waveguides.

Introduction

Channel dropping filters that select one channel of a wavelength division multiplexed (WDM) signal, and do not disturb the other channels, are useful elements for WDM communications [1]. Resonant filters are attractive candidates for this purpose because they theoretically drop 100% of the signal with high selectivity. In addition, they can be realised as extremely compact structures. B.E. Little et al.[1] show that a single ringresonator, or several in cascade, allow a large variety of filter responses in accordance with the demands of the network architecture. In this paper we present to our knowledge the first experimental results of such a single channel dropping filter based on a integrated optics cylindrical micro-cavity resonator.

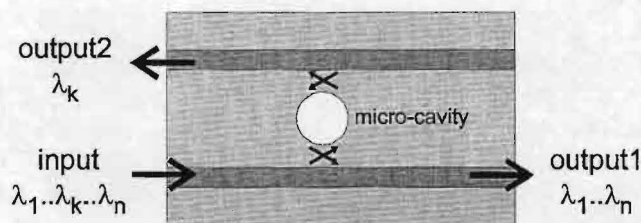


Figure 1: Schematic top view of the single channel dropping filter based on a cylindrical micro-cavity resonator, λ_k is dropped to output2.

The single channel dropping filter

A schematic top view of the channel dropping filter is shown in figure 1. The filter consists of a micro-cavity with a single vertical mode, located between two single mode waveguides. The distance between the waveguide and the micro-cavity is chosen close enough to allow coupling by the evanescent fields of the waveguide and the cavity. As a consequence, resonances in I_{out1} as well as in I_{out2} can be observed as a function of the wavelength. It is possible to drop 100% at resonance when for one roundtrip the losses in the resonator, due to absorption in the resonator and coupling into the upper/probe waveguide, equal the power coupled into the resonator, due to coupling from the

lower/signal waveguide. When the micro-cavity is made of active material, the device can also work as an all-optical switch [2],[3] or a tuneable wavelength filter. Evidently, this device can also be used for efficient addition of a single wavelength by the unused second input on the right side of the device. The filter can be characterised by the Free Spectral Range (FSR) and the Full Width Half Maximum ($\Delta\lambda$) of the resonances (see figure 2).

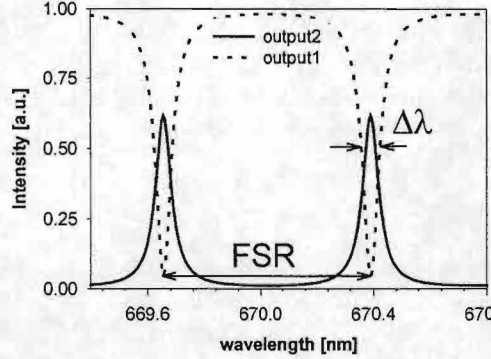


Figure 2: The field intensity of a micro-cavity as a function of the wavelength.

The FSR is simply approximated by

$$FSR \cong \frac{\lambda^2}{2\pi R n_e} \quad (1)$$

where n_e is the effective refractive index of the resonance mode, λ the resonance wavelength and R the radius of the cylinder. So, using our silicon technology and decreasing the micro-cavity radius to 20 μm , it is possible to realise a filter with a FSR larger than 20 nm operating in the third telecommunication window.

The Finesse, which is a measure for the sharpness of the resonance peaks, is given by the FSR divided by $\Delta\lambda$.

The realisation

A cross section of the planar waveguide filter at 670nm is shown in figure 3a. The waveguides are made of Si_3N_4 ($n=2.01$) [4] and the micro-cavity resonator of a polymer ($n=1.6$). Only two lithographic steps are needed for the realisation of the filter, one to define the waveguides and one to define the micro-cavity resonator. With this two step approach it is possible to realise the required different lateral index contrasts for the micro-cavity resonator and the waveguides, *i.e.* $\Delta n=0.13$ and 0.004, respectively. A drawback is the extra critical alignment between the waveguides and the micro-cavity resonator. Even in the case of slight misalignment the coupling coefficients and the behaviour of the filter can change dramatically.

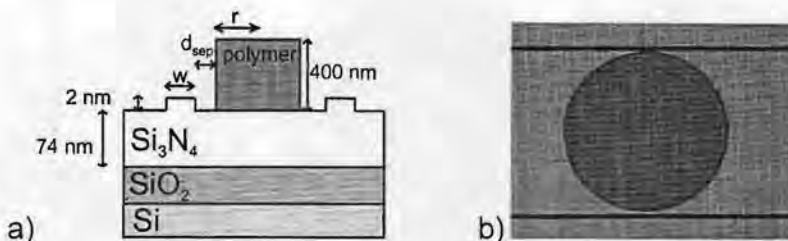


Figure 3: a) Cross-section of the filter showing the layer stack and the dimensions b) photograph of a cylindrical micro-cavity resonator with a radius of 57mm in resist .

Realised dimensions of the fabricated devices up to now are: r between 30 and 80 μm , $w = 2.5 \mu\text{m}$ and $d_{sep} < 1 \mu\text{m}$. As an example of an almost realised filter, a photograph of the device in resist is shown in figure 3b. We present here the resist photograph, because the 2nm step of the waveguides is, compared to the height of the polymer layer, too small to make it visible with any kind of phototechnique. It is clearly visible that the filter is not exactly symmetrical, the resonator is shifted to the upper waveguide.

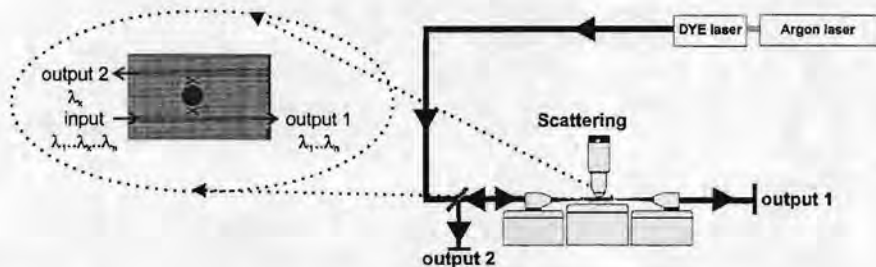


Figure 4: The experimental set-up

The experimental set-up

We have measured the spectral behaviour of the filters in a wavelength region of 660-680 nm using an Argon pumped Dye-laser. The smallest wavelength step of the Dye-laser with a linewidth of about 0.1 nm is 0.03nm. Using this set-up we are able to measure three outputs: the device outputs, *i.e.* output1 and output2, and light scattering from the device. The signal of output2 is obtained by a beamsplitter and the incouple objective. As a consequence, the measured output2 has a large background value due to the back reflection of the input beam on the entrance interface of the wafer. Furthermore, extra spatial Airy rings occur on the diode of output2, probably caused in the objective. The scattering is measured in the vertical direction. Using a pinhole and a microscope we can measure the scattering of a reduced area of the device, the edge of the cylindrical micro-cavity for example.

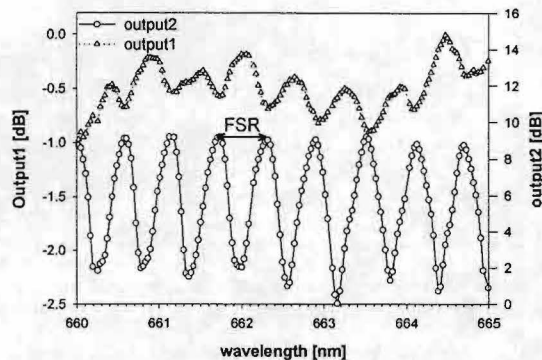


Figure 5: Preliminary results of output1 and output2 as a function of the wavelength.

The experimental results

Figure 5 shows the preliminary results of a single channel dropping filter with a radius of about $78\text{ }\mu\text{m}$. The device has been designed and realised for a number of different purposes, including the demonstration of all-optical switching. For use as a drop filter the FSR of this large diameter device is too small. It demonstrates however the validity of the concept. Without any optimisation for background reduction of output2 or Q enhancement, *i.e.* coupling coefficients, we obtain selectively drop with about 9 dB cross talk in output2 and a Finesse of about 6 for the resonance wavelength.

Conclusions

In this paper we have shown to our knowledge the first results of a single channel dropping filter based on a cylindrical integrated optics micro-cavity. These first experimental results are very promising for the realisation of a single channel nearly 100% dropping filter with a large free spectral range working in the third telecommunication window.

References

- [1] B.E. Little, S.T. Chu, H.A. Haus, J. Foresi, and J.-P. Laine, 'Microring resonator channel dropping filters', *J. Lightwave Technol.*, vol 15(6), pp. 998-1005, 1997
- [2] F.C. Blom, D.R. van Dijk, H.J.W.M. Hoekstra, A. Driessen, and Th.J.A. Popma, 'Experimental study of integrated-optics microcavity resonators: Toward an all-optical switching device', *Appl. Phys. Lett.* vol 71(6), pp 747-749, 1997
- [3] F.C. Blom, D.R. van Dijk, H.J.W.M. Hoekstra, A. Driessen, and Th.J.A. Popma, 'A new integrated all-optical switch based on a micro-cavity', *Proc. CLEO '96*, pp 20, 1996
- [4] K. Worhoff, P.V. Lambeck, H. Albers, N.F. van Hulst, O.F.J. Noordman and Th.J.A. Popma, 'Optimization of LPCVD Silicon Oxynitride growth to large refractive index homogeneity and layer thickness uniformity' *Proc. SPIE 3099*, pp 257, 1997

Integrated optical refractometer based on losses in curved waveguides

G.J. Veldhuis and P.V. Lambeck
MESA Research Institute, University of Twente
P.O. Box 217, 7500 AE Enschede, The Netherlands

A passive integrated optical waveguide refractometer based on bendloss changes in a spiral-shaped channel waveguide is proposed and fabricated in Si₃N₄/SiO₂-technology. The experimentally determined performance and the theoretical predictions, based on a simple model for so called 'Whispering Gallery Modes', agree very well. The minimum detectable refractive index change was measured to be $\Delta n=8 \cdot 10^{-6}$.

Integrated optical sensors for measuring chemical or physical quantities show interesting prospects because of their high sensitivity, small size, low price and the absence of electro-magnetic interference. In the last decade many types of integrated optical sensors have been proposed and fabricated, where devices based on a Mach-Zehnder interferometer are generally considered as the most promising, due to their high sensitivity and intrinsic balancing [1]. Unfortunately, to exploit the full sensitivity potential, these devices often require on-chip modulation to tackle the phase ambiguity in the interference signal [2]. In this paper we introduce a novel passive waveguide refractometer [3], where refractive index changes induce a change in the bendloss of a spiral-shaped channel waveguide. Here no on-chip modulation is required. Measurements on a device fabricated in Si₃N₄/SiO₂-technology are presented and its performance is compared with theory.

The losses of a bent optical waveguide increase strongly with a decrease of either the bending radius or the effective refractive index contrast defining the waveguide [4]. In the sensor we propose a single mode channel waveguide has been used which has a spiral shape as illustrated in figure 1a.

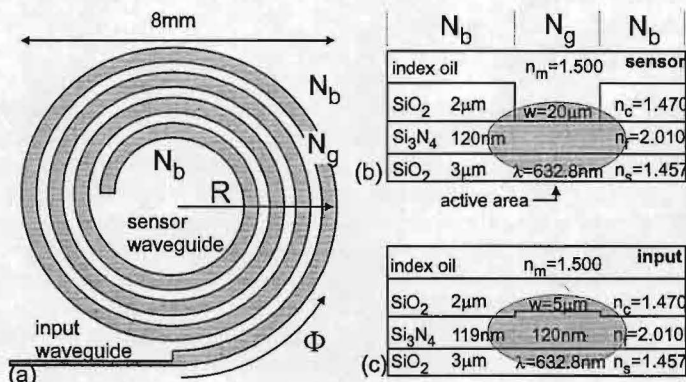


Fig. 1: Schematic representation of the refractometer, with a top-view of the spiral-shaped channel waveguide (a), a side-view of the sensor waveguide (b) and a side-view of the input waveguide (c).

The radius of curvature R of the waveguide decreases in the propagation direction so for a given effective refractive index contrast $\Delta N=(N_g-N_b)$, where N_g and N_b are the refractive

indices of the waveguide and the background respectively, the losses will gradually increase in the propagation direction and at a certain point in the spiral all the light will be lost by the waveguide. The sensor principle is based on the shift of this point in the propagation direction caused by an increasing lateral refractive index contrast. In this way the depth of propagation of the light into the spiral is a direct measure for the refractive index contrast.

In literature simple expressions can be found for the attenuation, A , in bent waveguides which are in the so called Whispering Gallery Mode (WGM) regime [4]

$$A = \frac{2}{\pi} \frac{1}{\sqrt{100\Delta}} \cdot 10^{2.29-2.17R_n-0.58R_n^2} \quad (\text{dB/rad}) \quad (1)$$

$$\text{with } \Delta \equiv \frac{\Delta N}{N_b} \text{ and } R_n \equiv \frac{N_b R}{\lambda} \cdot \Delta^{\frac{3}{2}} \cdot 1137 \Delta^{-0.01}$$

The total power loss in the spiral as a function of the propagated angle, $\alpha(\Phi)$, can be calculated by integrating (1)

$$\alpha(\Phi) = \int_0^\Phi \frac{2}{\pi} \frac{1}{\sqrt{100\Delta}} \cdot 10^{2.29-2.17R_n(\Phi)-0.58R_n^2(\Phi)} \cdot d\Phi \quad (\text{dB}) \quad (2)$$

Using this expression the point where the light is lost by the waveguide, defined as $\Phi_{\alpha=20\text{dB}}$, can be calculated.

The performance of the device will be determined by the choice made for the initial radius, R_0 , and the angular dependency of the radius, $\delta R/\delta\Phi$, together with the waveguide cross section. From (1) it can be deduced that the sensitivity becomes higher with a larger bend radius. Nevertheless the bending radius will be limited by the device size we allow; in our case 1cm^2 . From this we choose a initial radius $R=4\text{mm}$. The optimisation of $\delta R/\delta\Phi$ was done by evaluating a number of different spiral shapes and an attractive spiral shape was found to be

$$R(\Phi) = \frac{4}{1 + \frac{\Phi}{25}} \quad (\text{mm}) \quad (3)$$

For obtaining a sensitive refractometer it is essential to find a waveguide geometry which converts a refractive index change in a sensing layer, Δn_m , efficiently into a change in the effective refractive index contrast, ΔN , i.e. we need a large value for $\delta\Delta N/\delta n_m$. This can be obtained by the waveguide illustrated in fig. 1b. If the refractive index of the index oil (in general the sensing layer showing the Δn_m) changes, only the effective refractive index of the waveguide, N_g , will change, whereas the refractive index of the background, N_b , will remain unchanged because here the optical field does not penetrate the oil. This means that for this type of waveguide optimizing $\delta\Delta N/\delta n_m$ is the same as optimizing $\delta N_g/\delta n_m$, which has been extensively studied earlier [5]. For our sensing device we chose to use a He-Ne laser with a wavelength $\lambda=632.8\text{nm}$ and quasi-TE polarization. For the structure with the parameters as shown in figure 1b, made in the in our laboratory available $\text{Si}_3\text{N}_4/\text{SiO}_2$ -technology [6], we then find $\delta\Delta N/\delta n_m=0.19$.

Using (2) and (3) together with the waveguide geometry (fig. 1b), we can calculate $\Phi_{\alpha=20\text{dB}}$, i.e. how far the light propagates into the spiral before the light is lost, as a function of the applied refractive index difference between the SiO_2 -cladding and the index oil, $n_m - n_c$. This is

the dotted curve in fig. 2. A straight-waveguide attenuation of 0.5dB/cm was incorporated in this analysis. It can be seen that $\delta\Phi/\delta n_m \approx 400 \cdot 2\pi$ rad.

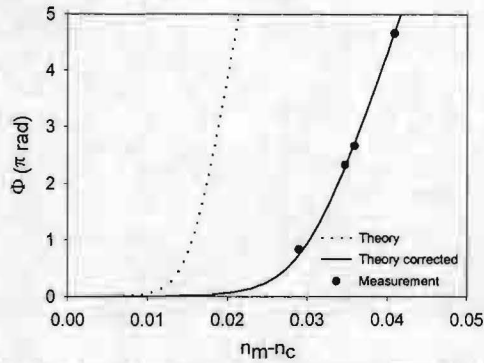


Fig. 2: Penetration angle of the light into the spiral ($\Phi_\alpha = 20\text{dB}$) versus $n_m - n_c$. The dotted line is the theoretical curve, the solid line the theoretical curve for a residual SiO_2 layer of 40nm thickness; the dots are the experimental values.

For demonstrating the feasibility of the sensing principle, measurements on the device were performed with a ccd-camera, allowing a simple determination of the point where the intensity of the light scattered by the waveguide, i.e. the light inside the waveguide, is reduced 20dB with respect to the intensity at the beginning of the spiral. The refractive index n_m was varied using several refractive index oils. Fig. 3 shows the penetration of the light into the spiral for four different values of n_m . The sensing capability of this device is clearly illustrated; the higher the refractive index of the oil the further the light penetrates the spiral (fig. 3a-d).

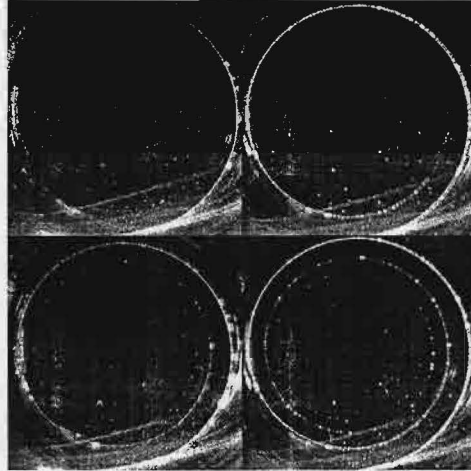


Fig. 3: Scattered light in the spiral for different values of n_m ; $n_m = 1.4990$ (a), 1.5047 (b), 1.5059 (c) and 1.5109 (d). Note that the pictures have an initial rotation of $\pi/12$ rad.

In fig. 2 the dots indicate how far the light penetrates the spiral ($\Phi_\alpha = 20\text{dB}$) as a function of $n_m - n_c$. It is clear that the theoretical curve does not coincide with the experimentally found points. The reason for this was found by Scanning Electron Microscopy to be a 40nm thick residual layer of SiO_2 in the sensing waveguide area, apparently due to a too short etching time in the sensing waveguide defining etch step. The solid line in fig. 2 is the theoretical

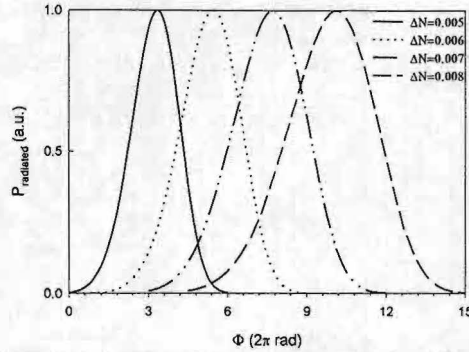


Fig. 4: Power radiated from the spiral versus the penetration angle, for different ΔN .

The resolution of the sensor can be evaluated by plotting the radiated power, $\delta P/\delta \Phi$, versus the penetration angle for different values of ΔN (fig. 4).

$$P_{\text{radiated}} = \frac{\partial P}{\partial \Phi} = -\frac{\partial}{\partial \Phi} \left[10^{-\frac{\alpha(\Phi)}{10}} \right] \quad (4)$$

Figure 4 shows that the sensitivity, $\delta \Phi/\delta N$, stays approximately constant for increasing contrasts whereas the width of the peaks, which determines the resolution, increases. If we assume that the position of the peaks can be measured with an accuracy of 1/1000 of its FWHM, with a detector array or ccd-camera, a sensing resolution of $\Delta n = 8 \cdot 10^{-6}$ can be achieved, while for the originally designed structure a resolution of $\Delta n = 4 \cdot 10^{-6}$ can be calculated. This number can be improved by using a larger initial bend radius for the spiral. Also facilities for compensation of temperature effects can be incorporated. Furthermore the working point, i.e. the sensitivity region, can be adjusted to the specific application. Note here that SiO_xN_y layers can be made with a refractive index in the range $1.45 < n < 2.00$. Device to device reproducibility depends on technological limitations, which should be determined carefully.

In conclusion a novel highly sensitive passive integrated optical spiral-shaped waveguide refractometer was proposed and fabricated in $\text{Si}_3\text{N}_4/\text{SiO}_2$ technology. A resolution in the refractive index of $\sim 8 \cdot 10^{-6}$ is shown, and a value of $4 \cdot 10^{-6}$ is calculated for an even not completely optimized structure. The experimental performance of the device agrees very well with the simple model derived for WGM waveguide bends. The sensor concept is shown to be flexible (the range can be adjusted to practical specifications) and is expected to be well applicable in making useful integrated optical sensing systems.

The authors like to thank Rene Heideman for the valuable discussions on the subject. This research was financially supported by the Dutch Innovative Research Program (IOP) Electro-Optics.

¹ R.G. Heideman, G.J. Veldhuis, E.W.H. Jager and P.V. Lambeck, S&A B 35-36, 234 (1996).

² P.V. Lambeck, R.G. Heideman and T.J. Ikkink, Med. & Biol. Eng. & Comp. 34, 145 (1996).

³ G.J. Veldhuis and P.V. Lambeck, Applied Physics Letters (to be published).

⁴ M.K. Smit, E.C.M. Pennings and H. Block, J. Lightwave Technol. 11, 1737 (1993).

⁵ O. Parriaux and G. J. Veldhuis, J. Lightwave Technol. (to be published).

⁶ K. Worhoff et al., Proc. SPIE 3099, 257 ((1997).

Design method for coplanar waveguides in high-speed integrated electro-optical modulators

Marcel Hoekman, René M. de Ridder, Gijs J.M. Krijnen,
Erwin Rikkers, Alfred Driessen, Arjen Bakker

University of Twente, MESA Research Institute, Lightwave Devices Group, P.O. Box 217, 7500 AE Enschede, The Netherlands, Tel.: +31-53-4892712, E-mail: R.M.deRidder@el.utwente.nl
BBV Software BV, Hengelosestraat 705, 7521 PA Enschede, The Netherlands, Tel.: +31-53-4836340, E-mail: bbv@bbv.nl

Abstract

Travelling-wave electrode structures are necessary in high-speed integrated electro-optical modulators. A method is presented to obtain an explicit relation between electrode dimensions and characteristic impedance of (un)shielded coplanar waveguides on multilayered sub-/superstrates.

Introduction

In high-speed (> 1 GHz) electro-optical modulators the application of travelling-wave electrode structures is often necessary. An important property of such electrodes is the characteristic impedance, which should be matched to the output impedance of the signal source.

Our electro-optical modulator design calls for a coplanar waveguide (CPW) type electrode structure. Although several models for calculating the characteristic impedance of this type of structure have been published [1, 2, 3], none of these was sufficiently general for dealing with a large number of different dielectric sub- and superstrate layers as well as top and bottom shielding conductors. Here we describe how to combine a few basic models into a more general multilayer CPW model.

The model is derived using a well-known conformal mapping technique, which leads to expressions involving elliptical integrals that can only be solved numerically.

The design of the electro-optical modulator requires tapering of the CPW structure; the narrow structure that is necessary for obtaining efficient electro-optical interaction should grow gradually wider in order to facilitate electrical connections to standard SMA-type coaxial connectors. In order to prevent reflections of the RF-signal, the characteristic impedance should be 50Ω in each cross-section along the tapered CPW. In order to design a smoothly tapered structure, we derived a simple function giving the gap width g between the centre electrode and the surrounding ground planes, as a function of the centre electrode width $2s$, while keeping the characteristic impedance constant. This function contains 6 parameters that are determined by curve-fitting to the numerical results of the original model.

Model of an electrical coplanar waveguide

The strategy of the modelling is to transform the complicated waveguide structure shown in Figure 1 into

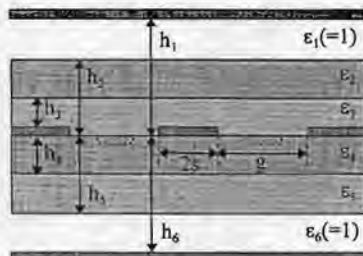


Figure 1: Conductor backed coplanar waveguide with shield electrode and a multilayer substrate. Between the electrodes are two optical waveguides, indicated with a dotted rectangle

an equivalent simple parallel plate waveguide as indicated in Figure 3.c, of which the characteristic impedance is easily calculated. It consists of a central signal electrode (width: $2s$) with two ground electrodes running parallel separated by a gap g . The electrode structure is placed upon a two-layer substrate and has a cover layer on top. The electrodes are considered to be infinitely thin. A structure containing n dielectric layers (air and vacuum included) can be split into n partial structures. Each partial structure i has a capacitance $2C_i$. ($i = 1, 2, \dots, n$; C_i is the capacitance of the right half of the structure only, because the structure has a vertical symmetry axis). All partial capacitances in parallel, together form the capacitance of the total structure: $C = 2 \sum C_i$. There are three types of partial structures:

1. only the CPW in air without a shield electrode;
2. the CPW upon or underneath a dielectric layer with thickness h_i (see Figure 2.b, 2.c, 2.d, and 2.e);
3. the same as type 2, but now the dielectric layer is backed by a conductor (see Figure 2.a and 2.f).

In Figure 2 for every partial structure the effective relative permittivity $\epsilon_{e(i)}$ is shown. For the partial structures that are filled only with air $\epsilon_{e(i)} = 1$ (see Figure 2.a and 2.f). For the other partial structures, $\epsilon_{e(i)} = \epsilon_i - \epsilon_{i-1}$ for cover layers, and $\epsilon_{e(i)} = \epsilon_i - \epsilon_{i+1}$ for substrate layers.

The next step is to transform each structure to a parallel plate capacitor to simplify calculation of the partial capacitance of these structures. Figure 3 shows schematically how the partial structure C_1 is transformed. The width of the ground electrodes is supposed to be half-infinite. First the electrodes are transformed from the z -plane ($z = x + iy$) to an R -plane ($R = t + ir$) (see Figure 3.a and 3.b). This is done with a conformal mapping, using the formula [1]:

$$t = \begin{cases} z^2 & \text{for the half-plane } (h_i \rightarrow \infty) \\ \cosh\left(\frac{\pi z}{2h_i}\right)^2 & \text{for a dielectric layer of thickness } h_i \end{cases} \quad (1.1)$$

After transformation all the electrodes are located on the t -axis. The second step is a transformation from the R -plane to the w -plane ($w = u + iv$) (see Figure 3.b and 3.c), using the Christoffel-Schwartz conformal mapping formula:

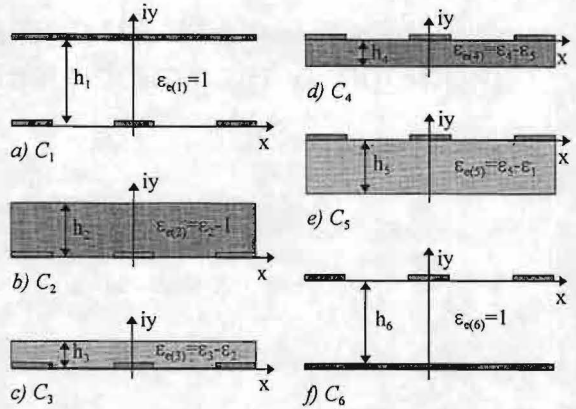


Figure 2: The CPW split into partial capacitances

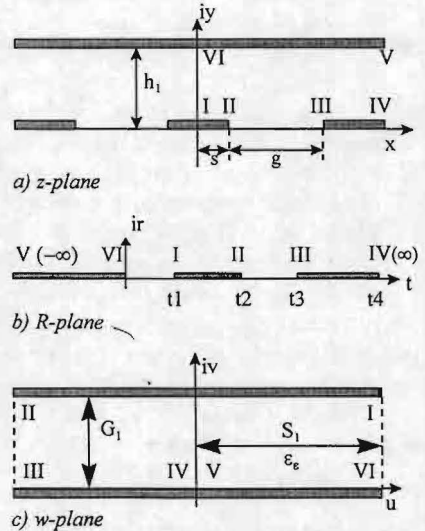


Figure 3: Schematic display of the two conformal mappings for a conductor backed dielectric layer of thickness h_1 (partial structure C_1 of type 3)

$$w = \int_{t_0}^t \frac{dt}{(t-t_1)(t-t_2)(t-t_3)(t-t_4)} = \int_{t_0}^t \frac{dt}{\sqrt{1-t^2}\sqrt{1-k^2t^2}} \quad (2)$$

The parameter k_i depends on the type of the partial structure:

$$k_i = \begin{cases} \sqrt{\frac{t_2}{t_3}} = \frac{s}{s+g} & \text{for partial structures of type 1} \end{cases} \quad (3.1)$$

$$k_i = \begin{cases} \sqrt{\frac{t_2-1}{t_3-1}} = \frac{\sinh\left(\frac{\pi s}{2h_i}\right)}{\sinh\left(\frac{\pi(s+g)}{2h_i}\right)} & \text{for partial structures of type 2} \end{cases} \quad (3.2)$$

$$k_i = \begin{cases} \sqrt{\frac{t_2-1}{t_2} \frac{t_3}{t_3-1}} = \frac{\tanh\left(\frac{\pi s}{2h_i}\right)}{\tanh\left(\frac{\pi(s+g)}{2h_i}\right)} & \text{for partial structures of type 3} \end{cases} \quad (3.3)$$

where h_i are the positions of the interfaces between dielectric layers, s the half centre electrode width, and g is the gap between coplanar electrodes. The integrals of (2) are elliptic integrals which can be rewritten in terms of $K(k_i)$ and $K'(k_i)$ [4]. $K(k_i)$ is the complete elliptic integral of the first kind which cannot be calculated analytically [2], and $K'(k_i)$ is the complementary complete elliptic integral of the first kind which is defined as $K'(k_i) = K(k'_i)$ with $k'_i = \sqrt{1-k_i^2}$. Introducing the effective electrode width $2S_i$ which is proportional to $K(k_i)$, and the effective electrode separation G_i which is proportional to $K'(k_i)$ (see Figure 3.c) the partial capacitance can be written as:

$$C_i = \epsilon_0 \epsilon_{e(i)} \frac{2S_i}{G_i} = \epsilon_0 \epsilon_{e(i)} \frac{2K(k_i)}{K'(k_i)} = \epsilon_0 \epsilon_{e(i)} \frac{2K(k_i)}{K(k'_i)} \quad (4)$$

The total capacitance C can now be calculated as

$$C = 2 \sum_{i=1}^n C_i = 4\epsilon_0 \sum_{i=1}^n \epsilon_{e(i)} \frac{K(k_i)}{K(k'_i)} \quad (5)$$

To derive the characteristic impedance it is useful to use partial filling factors given by:

$$q_i = \frac{K(k_i)}{K(k'_i)} \left[\frac{K(k_1)}{K(k'_1)} + \frac{K(k_n)}{K(k'_n)} \right]^{-1} \quad (6)$$

We can introduce a total effective dielectric permittivity ϵ_e :

$$\epsilon_e = \sum_{i=1}^n q_i \epsilon_{e(i)} \quad (7)$$

The total capacitance can be written as:

$$C = 2\epsilon_0 \epsilon_e \left[\frac{K(k_1)}{K(k'_1)} + \frac{K(k_n)}{K(k'_n)} \right] \quad (8)$$

Finally, the characteristic impedance:

$$Z_0 = \sqrt{\frac{\mu_0}{\epsilon_0 \epsilon_e}} \frac{G}{2S} = \frac{60\pi}{\sqrt{\epsilon_e}} \left[\frac{K(k_1)}{K(k'_1)} + \frac{K(k_n)}{K(k'_n)} \right]^{-1} \quad (9)$$

As all k_i and k'_i are functions of s and g , it is possible to make a contour plot of Z_0 as function of s and g as is shown in Figure 4. The lines in the g , s -plot are iso-impedances. For the desired characteristic impedance one can make a curve-fit by using a root-solver in a mathematical program. A function that approximates the iso-impedance line at 50 Ω very well is:

$$g(s, a) = a_0 \left(\frac{s}{a_1} \right) e^{-a_2 s} + a_3 \left(1 - \frac{s}{a_1} \right) s^{a_4} + a_5 \quad (10)$$

with s the signal electrode half-width and a_0, a_1, \dots, a_5 the curve-fitted parameters. The error of the curve-fit with respect to the iso-impedance line of 50 Ω is $\pm 1 \Omega$.

Application of the model

The application for which this model has been derived is an electro-optical modulator based on a Mach-Zehnder interferometer. The electric field of the microwave travelling along the CPW causes phase shifts of opposite sign in the lightwaves in both electro-optical channels (see Figure 1: inverted ridge waveguides with the ridges indicated by the dotted rectangles), which run in the gaps of the CPW (Figure 5).

Since the CPW electrodes need to cross the optical channels, part of the CPW structure (containing tapered bends) is placed in a different layer. Using equation (10) a CPW electrode configuration with varying signal electrode width and electrode gap, and yielding a constant 50 Ω characteristic impedance could be parametrised and implemented in the commercial lay-out package Prometheus [5], see Figure 5.

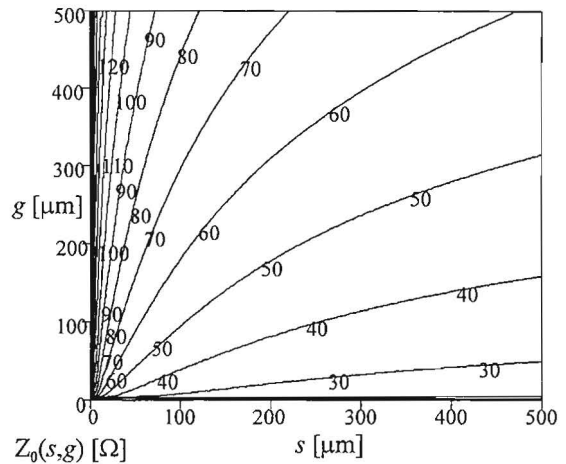


Figure 4: Contour plot of the characteristic impedance Z_0 as function of the electrode half-width s and the electrode gap g

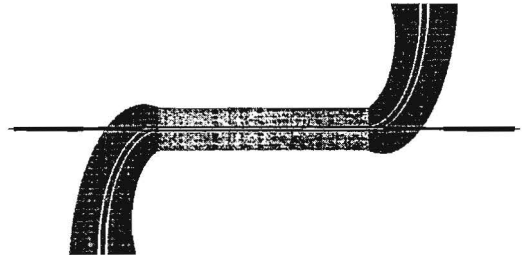


Figure 5: Lay-out of the electro-optical modulator: the optical structure (a Mach-Zehnder interferometer (MZI) using 1x2 multimode interferometers (MMIs)) is coloured black, the CPW which lies in the same layer as the optical structure is coloured light grey, and the tapered and bended CPWs are coloured dark grey. The horizontal and vertical dimensions are not drawn to the same scale (overall device dimensions: 4000 x 50000 μm)

- [1] K.C. Gupta, Ramesh Garg, I.J. Bahl, *Microstrip Lines and Slotlines*, Artech House Inc., Dedham, Massachusetts, USA, 2nd edition, 1996, pp. 375-456;
- [2] Spartak Gevorgian, L.J. Peter Linnér, Erik L. Kollberg, *CAD Models for Shielded Multilayered CPW*, IEEE Transactions on Microwave Theory and Techniques, Vol. 43, No. 4, 1995, pp. 772-779;
- [3] Matthew Gillick, Ian D. Robertson, Jai S. Joshi, *An Analytical Method for Direct Calculation of E & H-Field Patterns of Conductor-Backed Coplanar Waveguides*, IEEE Transactions on Microwave Theory and Techniques, Vol. 41, No. 9, 1993, pp. 1606-1610;
- [4] E.T. Whittaker, G.N. Watson, *A Course of Modern Analysis*, Cambridge University Press, Cambridge, England, 4th edition, 1927;
- [5] BBV Software BV, Hengelsestraat 705, 7521 PA Enschede, The Netherlands, Tel.: +31-53-4836340, E-mail: bbv@bbv.nl, Internet: <http://www.bbv-software.com>.

Beam pointing stability studies on a long pulse XeCl excimer laser fitted with unstable resonators

R.M. Hofstra^a, M.J. Zwegers^b, F.A. van Goor^a and W.J. Witteman^{a,b}

^a Twente University, P.O. Box 217, 7500 AE Enschede, The Netherlands

^b Nederlands Centrum voor Laser Research (NCLR), P.O. Box 2662
7500 CR Enschede, The Netherlands

Abstract

Based on measurements and calculations, a theory for the pointing stability of the optical beam from a pulsed XeCl excimer laser equipped with a positive branch unstable resonator is introduced.

1 Introduction

The position of the focus field of the beam from a long pulse XeCl excimer laser, equipped with a positive branch unstable resonator, shows some small shot-to-shot variations. This is the result of variations of the direction of the optical axis of the output beam. This effect is called beam pointing variation and a parameter that can be used to describe it is the beam pointing stability parameter. The beam pointing stability is an important design parameter for optical resonators, especially in applications like micromachining and hole drilling. In the literature the pointing variation has been observed, however not explained [1,2]. Based on calculations and measurements, we present a more founded explanation of the beam pointing variation.

2 Experimental configuration

The experiments have been performed with a XeCl laser system having a $2.5 \times 2 \times 60 \text{ cm}^3$ (electrode distance \times discharge width \times discharge length) x-ray preionised high pressure discharge [3]. The gas mix-

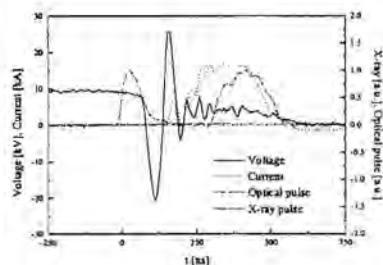


Figure 1: Typical waveforms of the discharge voltage, discharge current, x-ray preionisation pulse and optical output pulse.

ture (1 mbar HCl, 10 mbar Xe and 5 bar Ne) is excited by a spiker-sustainer circuit, which is operated in the resonant overshoot mode [4]. To reach optimal efficiency conditions, as well as to avoid electrode wear the system is operated under matched discharge conditions, i.e. the voltage on the sustainer circuit is twice the steady state voltage of the discharge [3]. Figure 1 shows some typical waveforms of the laser.

The (attenuated) laser beam is focussed by a 10 m concave mirror onto a scintillator. The scintillator image is recorded by a fast image intensified CCD camera equipped with a microscope objective.

The position of the maximum of the focus field is determined for 150 shots. The standard deviation of the maximum of the focus field is taken as a measure for the beam pointing stability (BPS).

3 Theory

According to literature, the number of cavity round trips of the optical field in an unstable resonator before saturation of the gain determines whether the beam becomes single mode or stays multimode [5]. The intracavity field builds up from noise (spontaneous emission). The lowest order mode has in general the lowest losses and will therefore survive in the mode competition process if the modes have sufficient overlap. If there are enough round trips between the start of the gain and its saturation the intracavity field will only consist of the lowest order resonator eigenmode. If the gain saturates earlier, higher order modes will be present as well, resulting in a decreased beam quality. This can not only be seen in the intensity distribution of the beam, but in the phase front as well. A distorted wavefront can result in a variation of the direction of the optical axis of the beam, i.e. a variation of the position of the focus field.

4 Calculations

The evolution of the optical field inside a cavity, starting from noise, can be calculated using Huygens' integral for that resonator [6]. For one pass through the resonator this integral is

$$\tilde{u}_2(x_2) = \sqrt{\frac{j}{B\lambda_0}} \int_{-a}^a \tilde{\rho}(x_0) \tilde{u}_0(x_0) \exp \left[-j \frac{\pi}{B\lambda_0} (Ax_0^2 - 2x_2x_0 + Dx_2^2) \right] dx_0 \quad (1)$$

where A, B and D are elements of the resonator's ABCD matrix. Using fast fourier transform algorithms these calculations can be performed fast and accurately [7].

The calculations have been performed

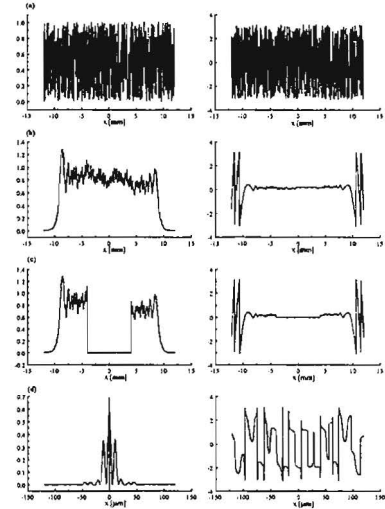


Figure 2: The calculation of the beam pointing variation. On the left the intensity of the optical field and on the right the phase. Phases: (a) start from noise, (b) calculation of intracavity field, (c) passage through the outcoupler and (d) the propagation of the beam to the focus.

in three steps. First, the calculations for a certain number of round trips through the cavity are executed. Subsequently the resulting intracavity field is transported through the outcoupling mirror. The last step is the propagation of the beam to the

focus of a 5 m lens. This calculation procedure is illustrated in figure 2.

Figure 3 shows the dependence of the pointing variation on the number of intracavity round trips. It can be seen that

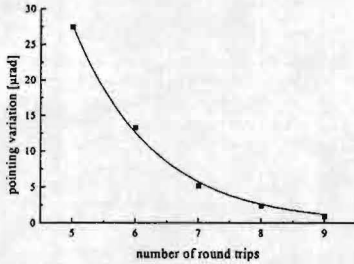


Figure 3: Calculated pointing variation as a function of the number of cavity round trips before saturation of the gain.

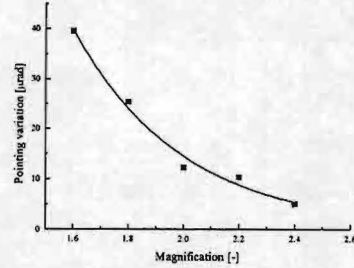


Figure 4: Calculated pointing variation as a function of magnification of the resonator.

pointing variation decreases with increasing number of pre-saturation round trips. This means that the beam pointing stability increases with an increasing number of pre-saturation round trips. As aforementioned, the number of round trips before saturation determines the mode character of the beam. Similarly it determines the pointing stability of the beam.

The number of pre-saturation round trips is determined by the gain medium and the resonator feedback. Thus, if resonators with different magnification but equal feedback are used, a fixed saturation moment is obtained if the gain medium remains unaltered. This can be obtained by changing the outcoupling mirror reflectivity. The beam pointing variation of these resonators is, in this situation, solely determined by the resonator magnification. Figure 4 shows the influence of the magnification on the pointing variation. A larger magnification results in a smaller pointing variation, and thus a higher pointing stability.

5 Results

In table 1 the measured beam pointing variation is given for different hard edge unstable resonators. For the first group of three resonators the resonator magnification M is kept constant while the reflectivity of the outcoupler R is varied. For the second group of three resonators the magnification is reduced. In order to keep the feedback γ equal, the reflectivity of the outcoupler had to be reduced as well.

In table 1 the duration of the optical pulse τ_{opt} (FWHM) and the period that the gain is above threshold τ_{thr} (FWHM) is given. The difference between these two times is the build-up time τ_{bu} .

It can be seen from the measured pointing variation (BPS) that for constant resonator magnification the beam pointing variation decreases with increasing build-up time, as was expected from the calculations (see figure 3). From the second set of measurements it can be seen that for equal build-up time the pointing variation decreases with increasing resonator magnification. Again, this is in agreement with our theoretical expectations (see figure 4).

M [—]	R [%]	γ [%]	τ_{thr} [ns]	τ_{opt} [ns]	τ_{bu} [ns]	BPS [μrad]
2.4	100	17.7	200	139	61	8.0
2.4	72	12.5	190	132	58	8.1
2.4	45	7.8	176	128	52	9.5
2.4	100	17.7	200	139	61	8.0
2.0	72	17.5	200	135	65	17.3
1.6	45	17.5	200	135	65	21.8

Table 1: Measured beam pointing variation for different hard edge unstable resonators.

6 Conclusions

The measurements show a behaviour in accordance with the calculations. Therefore, we believe that the theoretical background for the pointing instability introduced in this article should be a basis for further calculations and experiments. In our view the beam pointing variation originates from the build-up phase of the optical field in the resonator. If the optical field in the resonator gets more build-up time before the gain saturates the beam pointing stability increases. In pulsed laser systems this results in an additional restriction with respect to resonator design.

Acknowledgements

The present work has been supported by the Netherlands Technology Foundation (STW).

References

- [1] T.J. McKee and S. Fendrykowski, *Long-pulse excimer laser with a variable reflectivity mirror resonator*, Applied Optics 32 (3), p. 275-277, 1993.
- [2] S. Bollanti, P. di Lazzaro, F. Flora, T. Letardi, D. Murra, C. Petrucci and O. Uteza, *Study of a compact three-electrode oscillator-amplifier excimer laser system*, Optics Communications 132, p. 565-573, 1996.

- [3] J.C.M. Timmermans, *Double discharge XeCl-laser*, PhD thesis, Twente University, Enschede, the Netherlands, 1995.
- [4] J.W. Gerritsen, A.L. Keet, G.J. Ernst and W.J. Witteman, *High-efficiency operation of a gas discharge XeCl laser using a magnetically induced resonant voltage overshoot circuit*, Journal of Applied Physics 67 (7), p. 3517-3519, 1990.
- [5] T.J. McKee, *Optical cavity design for long pulse excimer lasers*, Applied Optics 30 (6), p. 635-644, 1991.
- [6] A.E. Siegman, *Lasers*, University Science Books, 20 Edgehill Road, Mill Valley, CA 94941, USA, 1986.
- [7] Genesee Optics Software, Inc., Rochester, New York 14623, USA, *Paraxia 2.0.1*.

Application of silicon oxynitride in telecommunication devices

K. Wörhoff, P.V. Lambeck, R.M. de Ridder, and A. Driessen

MESA Research Institute, University of Twente, Lightwave Devices Group

P.O. Box 217, 7500 AE Enschede, The Netherlands

Phone: +31-53-489 3477, Fax: +31-53-489 3343, E-mail: K.Worhoff@tn.utwente.nl

A silicon oxynitride based waveguiding structure has been developed for application in telecommunication, fulfilling demands on tolerance towards technological limitations, losses, polarization dependency and efficient fiber-to-chip coupling. First results are presented with emphasis on technology.

INTRODUCTION

A silicon oxynitride (SiON) based waveguiding structure for application in telecommunication devices, e.g. tunable WDM add-drop wavelength filters [1], operating at @ 1550 nm wavelength has been developed. With respect to some key design parameters, the waveguiding structure has to fulfill the following demands: channel loss $\alpha_{ch} \leq 0.2 \text{ dB/cm}$, fiber-to-chip coupling loss $\alpha_{f-c} \leq 1 \text{ dB/facet}$, bend radius $r_b \leq 2 \text{ mm}$ with bend loss $\alpha_b \leq 0.1 \text{ dB/90}^\circ$, polarization dependency $\Delta n_{eff} = n_{eff, TM} - n_{eff, TE} < 5 \times 10^{-5}$. In the optimization procedure, the influences of a non-ideal waveguiding structure, due to the tolerances in the applied technological fabrication processes, has been taken into account, too.

In this paper, the design of the waveguiding structure will be described and the experimental results with respect to fabrication of this structure will be presented.

DESIGN OF THE WAVEGUIDING STRUCTURE

In order to optimize the design of the waveguiding structure, the parameters of various structures have been determined by simulation, applying different refractive indices of the waveguiding layer ($n_{co} = 1.48 - 2$) and different shapes of the channel structure. The structure that is shown in figure 1, was found to be most promising for application in telecommunication devices. Assuming that all applied materials will be isotropic and loss-less, the calculated

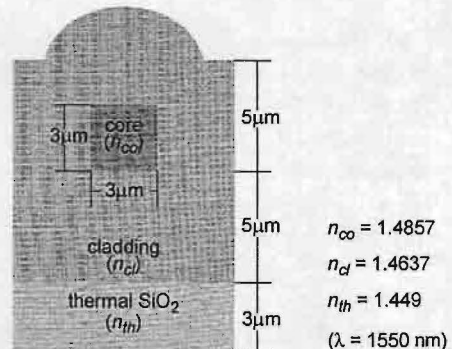


Figure 1 3x3 μm waveguiding structure with PECVD SiON core layer and PECVD SiO₂ cladding layer

parameters of the optimized structure are as follows: effective refractive index of the waveguiding channel $n_{eff} = 1.4707$ for both polarizations, minimum bend radius $r_b = 1.6$ mm with an optical loss of $\alpha_b = 0.1$ dB/90° (Whispering Gallery Mode [2]), polarization dependence of the waveguiding channel $\Delta n_{eff} = 0$ and mode mismatch loss of the fiber-to-chip coupling applying a standard telecommunication fiber of $\alpha_{f-c} = 2.5$ dB/facet. Furthermore, the absorption losses at 1550 nm wavelength are expected to be low, since the concentration of N-H and Si-H bonds, whose overtones cause absorptions close to this wavelength, is small for SiON with a low refractive index [3].

When comparing the properties of the 3×3 μm waveguiding structure with the required parameter values, the mode mismatch loss of the fiber-to-chip coupling is apparently too high. The mismatch can a.o. be reduced by expanding the modal field in the waveguiding channel, e.g. by horizontal tapering resulting in a decrease of the channel width. The reduction of the fiber-to-chip mode mismatch loss by decreasing the width of the channel waveguide is shown in figure 2a. When tapering the channel width to $1 \mu\text{m}$, the mode mismatch loss will be below the demanded value, even at a slight fiber displacement (figure 2b).

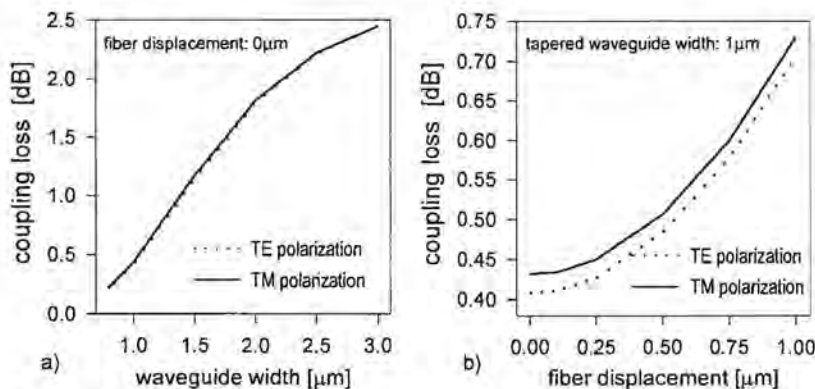


Figure 2 calculated fiber-to-chip overlap coupling loss vs. waveguide width (a) and fiber displacement (b)

Furthermore, the sensitivity of the index contrast, the channel index and the polarization dependency of the 3×3 μm waveguiding structure on the technological tolerances have been calculated. The following technological tolerances have been assumed: core thickness non-uniformity $\delta d = 0.7 - 1$ %, refractive index non-uniformity $\Delta n = 6 \times 10^{-4}$, uncertainty in channel width $\Delta w = 0.1 - 0.5$ μm . Then, for the non-ideal structure, the worst case change is 6×10^{-4} in effective index contrast, $7 - 18 \times 10^{-4}$ in the effective channel index and $0.7 - 3 \times 10^{-5}$ in the polarization dependency.

EXPERIMENTAL RESULTS AND DISCUSSION

The optimized waveguiding structure has been fabricated on thermally oxidized $\langle 100 \rangle$ Si wafers. The cladding and the core layers have been deposited from $2\% \text{SiH}_4/\text{N}_2$ and N_2O , applying an Electrotech 210 PECVD machine with a low frequency mode (187.5 kHz). Both layers have

been grown at a substrate temperature of 300°C, a pressure of 650 mTorr and a plasma power of 60 W. For deposition of the cladding layer, the flowrates of SiH_4/N_2 and N_2O have been 200 sccm and 710 sccm, respectively, while the core layer has been grown from 700 sccm SiH_4/N_2 and 1000 sccm N_2O . The layer properties, shown in table 1, have been measured by ellipsometry and prism coupling. It can be concluded that the optimization of the deposition processes has been successful, since, except for the material birefringence, the measured parameters of the PECVD silicon oxide and oxynitride layers are sufficiently close to the values on which the simulations have been based. The slight birefringence of the PECVD layers is caused by compressive stress [4] and is not expected to be eliminated by further process optimization. Therefore, adaption of the waveguiding structure in order to achieve reliable birefringence compensation, will belong to one of the future research items.

Table 1 measured parameters of the optimized PECVD SiO_2 and SiON layers

measured parameter	cladding layer	core layer
growth rate R [nm/min]	30	46
n_{TE} at $\lambda = 1550$ nm	1.4633	1.4841
n_{TM} at $\lambda = 1550$ nm	1.4642	1.4858
material birefringence $\Delta n = n_{TM} - n_{TE}$	9×10^{-4}	17×10^{-4}
δd over 50x50 mm area [%]	3	0.8
Δn over 50x50 mm area	2×10^{-4}	7×10^{-4}
α at $\lambda = 1550$ nm [dB/cm]	-	0.5 ^{a)}

a) uncladded slab-type waveguide

For fabrication of the waveguiding channels, a 200 nm thick chromium masking layer has been sputtered on top of the SiON core layer. The waveguide pattern was defined in the chromium layer with standard lithography, applying S1805 photoresist, and a wet Cr-etching step. Then, the waveguiding channels have been etched in an SF_6 plasma, applying an Electrotech 240 RIE machine with the following processing parameters: 20 sccm SF_6 flow, 10 mTorr pressure, 75 W plasma power and cooling of the lower electrode to 10°C.

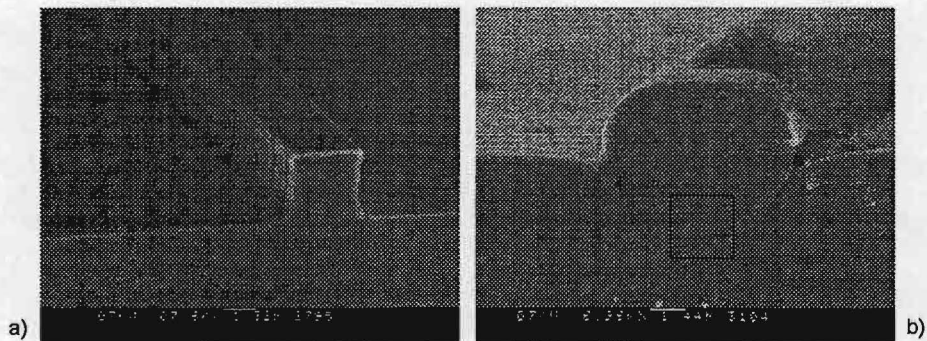


Figure 3 SEM photographs of the waveguiding channel after RIE etching (a) and after deposition of the upper cladding layer (b)

The etch rate of this process is 160 nm/min and the selectivity with regard to the chromium etching is sufficiently high. The non-uniformity in etching depth over the wafer, approximately 1.3%, is excellent. Furthermore, the etching is anisotropic, as it can be seen in the SEM photograph in figure 3a. The slight side-wall roughness of the channels is probably a consequence of the wet etching step of the chromium layer. The roughness is expected to be significantly reduced by replacing the wet etching by a dry etching step, e.g. ion-beam etching.

After removal of the chromium mask by wet etching, the upper cladding layer (PECVD SiO_2) has been deposited. A cross-section of the growth profile of the upper cladding is shown in figure 3b. For orientation, the approximate position of the waveguide channel has been marked in the SEM photograph by a black frame. Although, the step coverage of the cladding deposition turned out to be excellent, a nano-slit remains between the two growth planes. This nano-slit can be annoying for a good contact when introducing electrodes on top of the upper cladding or might cause some problems when applying the devices in a humid environment. Therefore, the growth profile of the upper cladding layer has to be optimized, either by improvement of the deposition process or by re-flowing techniques [5].

CONCLUSION

A silicon oxynitride based waveguiding structure, which is sufficiently insensitive to fabrication tolerances to be well utilized in advanced telecommunication devices, has been designed and realized. For realization of the structure, the technologies to be applied have been thoroughly improved. Future research will be concentrated on compensation for the stress-induced material birefringence, reduction of the side-wall roughness of the waveguiding channels and improvement of the growth profile of the upper cladding layer.

ACKNOWLEDGEMENT

The authors would like to thank Bert Otter from the MESA research laboratory for the SEM measurements.

REFERENCES

- [1] B. Sikken, R.M. de Ridder, K. Wörhoff, R.G. Heideman, and A. Driessen: *Tunable WDM add-drop multiplexer using cascaded Mach-Zehnder wavelength filter*, these proceedings.
- [2] M.K. Smit, E.C.M. Pennings, and H. Blok: *A Normalized Approach to the Design of Low-Loss Optical Waveguide Bends*, J. Lightwave Technol. 11(11), 1737 (1993).
- [3] H. Albers, L.T.H. Hilderink, E. Szilágyi, F. Paszti, P.V. Lambeck, and Th.J.A. Popma: *Reduction of hydrogen induced losses in PECVD SiO_xN_y waveguides in the near infrared*, Proceedings IEEE / LEOS, 8-th Annual Meeting, 88 (1995).
- [4] T.R. Bearda, R.M. de Ridder, K. Wörhoff, P.V. Lambeck, and H. Albers: *Stress and birefringence in PECVD SiO_xN_y waveguides*, Proceedings IEEE / LEOS Symposium Benelux Chapter, 222 (1996).
- [5] Th. Feuchtner: *Active and Passive Optical Waveguides by Plasma Enhanced chemical Vapor Deposition*, Ph.D. Thesis, Technical University of Denmark, 1996.

The spatial structure of a transverse RF excited Ar-He-Xe laser

F.J.Blok, I.V.Kochetov, A.P.Napartovich*, V.N.Ochkin, P.J.M.Peters,
S.A.Starostin, Y.B.Udalov and W.J.Witteman*

*Department of Applied Physics, University of Twente, P.O. Box 217, 7500 AE Enschede,
The Netherlands. Phone (+31)-53-4893965, fax (+31)-53-4891102
e-mail: f.j.blok@tn.utwente.nl*

**TRINITI, 142092, Troitsk, Moscow region, Russia*

Abstract

Measurements of the transverse intensity profile of the output beam of a slab Ar-He-Xe laser with a plane parallel resonator were made for three different laser lines and gas mixtures. The transverse mode profiles for the experimental conditions were calculated. The strong influence of the active medium on the mode structure of laser output has been shown.

1 Introduction

The recent development of the RF-excited Ar-He-Xe laser has resulted in a substantial increase of continuous wave output power from relatively compact devices [1,2] (Watts compared to less than mW laser output for the DC excited systems). This has opened new fields of applications for such a laser. One of the most promising applications seems to be the development of an eye-safe 2 μ m LIDAR based on this system.

In our previous work [3] we already have shown that the small signal gain profile for the RF excited Ar-He-Xe laser is strongly inhomogeneous in the direction transverse to the electrodes and has two maxima in the vicinity of the electrodes. This experimental fact can be explained from the point of view of general RF discharge properties. In an RF discharge a high electric field exists

in the vicinity of the electrodes (see for instance [4]). There high energy electrons are formed. It is well known that one of the necessary conditions for an efficient atomic Xe laser operation is the presence of high energy electrons.

The low electron density in this discharge region is also favorable for the inversion of the laser levels because a high density of low energy electrons (as in the case of the DC-excited Xe laser, or of the RF bulk plasma) leads to the electron collisional mixing of laser levels and subsequently decreases the inversion.

The inhomogeneity of the RF discharge parameters leads thus to the inhomogeneity of the gain profile. The inhomogeneity of the active medium can also affect the spatial structure of the output laser beam, and the laser beam quality is an important parameter for applications.

In this publication we present measurements of the laser intensity profiles from a plan-parallel resonator and analyze the obtained results.

2 Experiment

The discharge geometry of the slab laser will be described first. The aluminum electrodes, 15mm wide and 370mm long, were placed at the distance of 2mm. Al₂O₃ side walls were used as spacers and to confine the discharge plasma. The

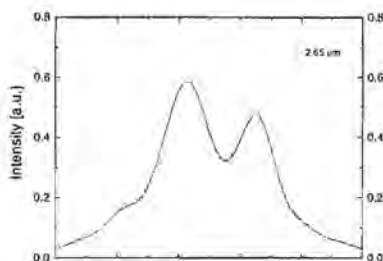


Figure 1 : Near field spatial structure of the laser output intensity in transverse direction for a 150mbar gas mixture of Ar:He:Xe = 59.5:40:0.5

frequency of the RF power supply was 109MHz and the input RF power 350W. The resonator had a length of 390mm and consisted of two flat mirrors: a totally reflecting rear mirror (Au coated Al) and an outcoupling mirror with 40% reflectivity. For the intensity profile registration a SPIRICON array (model LP 128-22-BaF₂) was used. To distinguish the laser lines we made use of narrow band spectral filters. The signal from the SPIRICON array was registered by a digital oscilloscope and stored in a PC.

The measurements were done for two gas mixtures. A previously optimized gas mixture for this laser (Ar:He:Xe=59.5:40:0.5, mixture 1) produced the highest laser output of 1.7W. A helium rich mixture (Ar:He:Xe=9.5:90:0.5, mixture 2) delivered a maximum laser output of

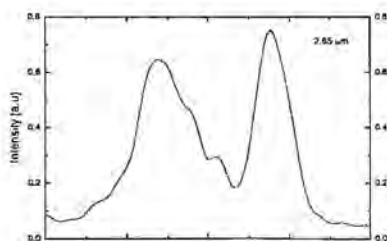


Figure 2 : Transverse spatial gain for a helium-rich mixture.

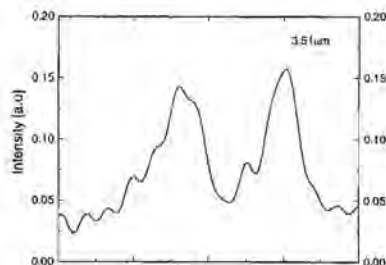


Figure 3 : transverse spatial distribution for a helium-rich mixture

0.3W. In both cases the gas pressure was 150mbar. With mixture 1 the wavelengths 2.03μm and 2.65μm were observed.

The spectral resolution of the band-pass filters was not high enough to distinguish between the 2.63μm and 2.65μm lines, however it is known from our previous experiments [5] that the 2.65μm line dominates. In fig.1 the intensity profiles for these lines are presented. For mixture 2 the 2.03μm, 2.65μm as well as 3.51μm laser lines were observed. The corresponding intensity profiles are presented in figures 2 and 3.

It is noticeable that the observed structure of the output laser beam was quite insensitive to the RF input power even when the laser power changed substantially.

3 Discussion

In order to explain the measured laser intensity profiles the problem of the mode structure in media with an inhomogeneous refractive index and with a strongly inhomogeneous gain profile should be resolved. This problem is even more complicated because the experimental cavity condition corresponds to an intermediate case: the laser cavity can be treated neither as a pure open resonator nor as a waveguide

one. The importance of effects of the transverse inhomogeneity in gas lasers has been shown for both open resonators [6] and for waveguide laser resonators [7]. In our calculations we used the waveguide approximation; a more exact approach will be applied in the future. The field in the waveguide with an inhomogeneous refraction index can be described as (see for instance [8])

$$E_m'' + [k^2 n^2(x) - \beta_m^2] E_m = 0 \quad (1)$$

Here $k (=2\pi/\lambda)$ is the wave number, $n(x)$ is the refractive index, β_m is the propagation constant and m is a mode number. The waveguide loss was assumed to be small compared to the outcoupling and coupling losses and therefore neglected. In this case β has a real value.

The refractive index for an Ar-He-Xe gas mixture can be calculated using the formula:

$$n = 1 + \delta n \quad (2)$$

$$\delta n = \delta n_0 \frac{273}{T} \frac{P(\text{Torr})}{760} \quad (3)$$

and

$$\delta n_0 = 2.84 \cdot 10^{-4} y_{Ar} + 7.02 \cdot 10^{-4} y_{Xe} + 3.5 \cdot 10^{-5} y_{He} \quad (4)$$

where y_i is the gas fraction i , T the gas temperature [K] and P the gas pressure in Torr.

The gas temperature profile was calculated from the thermal conductivity equation:

$$\frac{\partial}{\partial x} (\lambda(T) \frac{\partial T}{\partial x}) + W = 0 \quad (5)$$

where $\lambda(T)$ is the temperature dependent thermal conductivity coefficient of the gas mixture and W is the heat source density. We assumed that the heat source density is homogenous in the discharge gap, which is a reasonable approximation for an RF discharge.

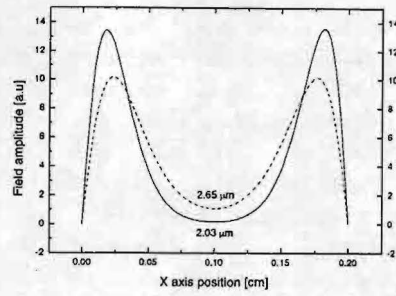


Figure 4 : calculated spatial profile for the fundamental mode in the case of a 150mbar mixture of Ar:He:Xe=59.5:40:0.5

To find the eigenvalue and eigenfunction, equation (1) was solved numerically using a shooting method with Numerov's algorithm of integration.

In fig. 4 the calculated profile for the fundamental mode ($m=1$) is presented for the experimental conditions: $P=150\text{mbar}$, $W=350\text{W}$ and optimized laser gas mixture (Ar:He:Xe=59.5:40:0.5). One can see that the fundamental mode profile differs substantially from the one for a homogeneous refraction index (in the last case the solution of equation (1) is a sine function). The field is "concentrated" near the electrodes in the high gain region. We expect an efficient operation of the laser at the fundamental mode due to the "good" gain - mode profiles overlap.

In fig. 5 the calculated fundamental

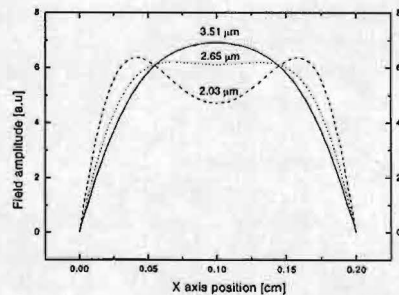


Figure 5 : calculated spatial profile for the fundamental mode in the case of a 150mbar helium-rich mixture

mode profile ($m=1$) for a helium rich mixture (mixture 2) is presented. In this case the mode splitting is less pronounced. It is caused by the lower refractive index and higher thermal conductivity coefficient of the helium rich mixture. However the resulting experimental laser intensity distribution does not correspond to the fundamental mode profile. This shows that the influence of the strong non-uniformity of the gain can not be neglected in the resonator calculations.

4 Conclusion

The transverse intensity profiles from a slab Ar-He-Xe laser were measured for the $2.03\mu\text{m}$, $2.65\mu\text{m}$ and $3.51\mu\text{m}$ transitions. Typically two maxima in each distribution are formed in the near field.

Our calculations show that for an experimentally optimized gas mixture and a typical power deposition the influence of the non-uniform refractive index on the waveguide mode profile is strong. For the low order modes ($m=1,2$) the field amplitude is high in the high gain region that creates favorable conditions for efficient laser generation. Generally the observed structure of the laser intensity can not be explained in terms of single transverse mode operation. An active resonator model which takes into account both the index of refraction and the gain inhomogeneity should be developed.

Aknowledgements

The present work has been supported by the Netherlands Technology Foundation (STW) and by the Foundation for Fundamental Research of Matter (FOM). Both foundations are financially supported by the 'Nederlandse

Organisatie voor Wetenschappelijk Onderzoek (NWO)'

References

- [1] Y.B. Udalov, P.J.M. Peters, M.B. Heeman-Ilieva, F.H.J. Ernst, V.N. Ochkin and W.J. Witteman, "New continuous wave infrared Ar-Xe laser at intermediate gas pressures pumped by a transverse radio frequency discharge", *Appl. Phys. Lett.*, **63**, pp. 721-722, (1993).
- [2] S.N. Tskhai, Y.B. Udalov, P.J.M. Peters, W.J. Witteman, and V.N. Ochkin, "Continuous wave near-infrared atomic Xe laser excited by a radio frequency discharge in a slab geometry", *Appl. Phys. Lett.*, **66**, pp. 801-803, (1995).
- [3] S.N. Tskhai, F.J. Blok, Y.B. Udalov, P.J.M. Peters, W.J. Witteman, and V.N. Ochkin, "Spatial gain profiles of a cw RF pumped atomic Xe laser", *Appl. Phys. Lett.*, **70**, pp. 1921-1922, (1997).
- [4] Y.P. Raizer, M.N. Schneider, and N.A. Yatsenko, 'Radio-frequency capacitive discharges'. 1995, Boca Raton: CRC Publishing Co.
- [5] S.N. Tskhai, Y.B. Udalov, P.J.M. Peters, W.J. Witteman, and V.N. Ochkin, "Spectral investigation of a cw rf-pumped atomic Xe laser with a slab geometry", *Appl. Phys. B*, **62**, pp. 11-14, (1996).
- [6] G.J. Ernst, W.J. Witteman, "Mode structure of active resonators", *IEEE J. Quantum Electron.*, **QE-9**: pp. 911-918, (1973).
- [7] B. Schröder, "Transverse modes of active hollow waveguide resonators", *IEEE J. Quantum Electron.*, **27**, pp. 158-165, (1991).
- [8] L.A. Coldren, S.W. Corzine., *Diode Lasers and Photonic Integrated Circuits*. Wiley series in microwave and optical engineering, ed. K. Chang. 1995, N.Y, Chichester, etc.: John Wiley & Sons, Inc.

An x-ray preionised discharge pumped ArF-laser

L. Feenstra, O.B. Hoekstra, P.J.M. Peters and W.J. Witteman
Twente University, P.O. Box 217, 7500 AE Enschede, The Netherlands

Abstract

An x-ray preionised discharge pumped ArF-laser ($\lambda = 193$ nm) has been realised using a spiker-sustainer excitation technique. We report on preliminary investigations to achieve a long pulse duration and high output power.

Introduction

For a number of years ArF-lasers have been used for various applications, ranging from eye-surgery to photo-lithography. Rather than the short pulses of the lasers systems now available, a long laser pulse with a high optical quality is preferred, to minimise damage to optics and to increase the processing power of the pulse [1]. These laser pulses demand a good discharge quality, i.e. a homogeneous discharge during the pulse. In order to study the feasibility of an ArF-laser having the desired properties, we investigate the use of techniques proven to be successful with the high repetition rate, high output power XeCl-laser built at the Nederlands Centrum voor Laser Research (NCLR) [1].

Experimental setup

The laser head is a rectangular stainless steel vessel which can be pressurised up to 10 bar. The vessel is closed at the ends with laser mirrors or with uncoated MgF_2 windows. The nickel covered aluminium laser cathode is of the uniform field type [2], the aluminium anode is flat, see Fig. 1. The short-pulse x-ray source is mounted against the laser vessel, so that the x-rays enter the discharge volume through the laser anode, which is milled down to 1 mm in the middle to attenuate the x-ray

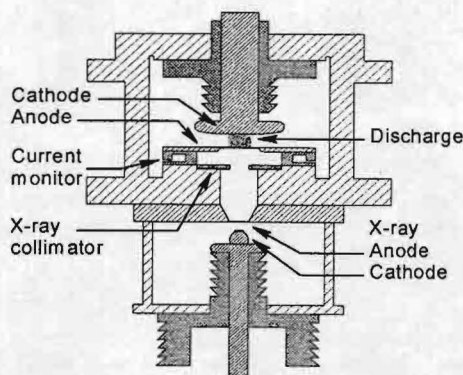


Figure 1: The laser chamber with the carbon-felt cathode x-ray source. The laser gas is preionised by a collimated x-ray beam through the laser anode. The x-ray source and the laser gas are separated by the 1 mm thick aluminium pressure window annex x-ray source anode.

beam as little as possible. The vacuum of the x-ray source is separated from the laser gas mixture by a 1 mm thick aluminium pressure window.

Two different x-ray sources were used during the experiments. The first x-ray source used a cold cathode made of carbon-felt. The anode was a 20 μm thick tantalum foil, fastened to the pressure window between the x-ray source and the laser vessel, see Fig. 1. The power supply of this x-ray source was a six-stage coaxial mini-marx generator, with a capacitance of 10.8 nF per stage. At the maximum charging voltage of 30 kV on the mini-marx generator the x-ray source delivered a dose of 6.5 mRad per shot in 130 ns (FWHM) between the laser electrodes.

The second x-ray source used a corona-

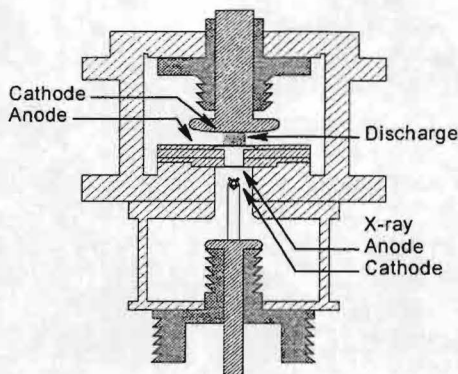


Figure 2: The laser chamber and the corona-plasma cathode x-ray source. The x-ray anode doubles as pressure window.

plasma cathode [3]. The anode was a $20\text{ }\mu\text{m}$ thick tungsten layer, flame-sprayed on the aluminium pressure window. This x-ray source was constructed closer to the laser electrodes to decrease the attenuation of the x-ray dose due to the long distance between the x-ray source and the discharge area, see Fig. 2. A mini-marx generator, with a capacitance of 3.6 nF per stage, was used to drive this x-ray source. The maximum x-ray dose between the laser electrodes was 27 mRad per shot in 50 ns (FWHM).

To increase the specific pumping power in the gas discharge, the discharge was narrowed by blocking part of the x-rays, either with 5 mm stainless steel in the first setup, or with 2 cm aluminium in the second setup. The resulting discharge volume was approximately $60 \times 2 \times 1\text{ cm}^3$ ($l \times w \times h$).

For the excitation of the discharge a prepulse-mainpulse setup, operating in the resonant-overshoot mode [4] is used; a fast high voltage pulse, the prepulse, is used to break down the gas, a long lower voltage pulse, the mainpulse, sustains the discharge. The mainpulse energy is stored on a pulse forming network (PFN), separated from the peaking capacitor by a saturable inductor, made of high-frequency ferrite, see Fig. 3. The slow pulse-charging of the PFN saturates the inductor LS_{AT} , to allow only the current

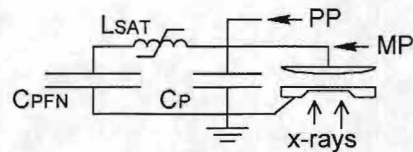


Figure 3: The excitation circuit. $CPFN$: Pulse forming network (324 nF); C_P : Peaking capacitor (2.1 nF); LS_{AT} : Saturable inductor; PP : Prepulse; MP : Mainpulse.

flow into the PFN. The prepulse, of opposite polarity to the mainpulse, is subsequently applied to the peaking capacitor, forcing the ferrite along its hysteresis curve to saturate in the opposite direction. This allows the current to flow from the PFN, thus causing a voltage-overshoot on the peaking capacitor and on the laser cathode. If the laser gas mixture is sufficiently preionised at that time, a homogeneous discharge will start.

Throughout the experiments presented here the gas mixture was kept constant at $4\text{ bar F}_2\text{:Ar:Ne:He}$ in the ratios $0.15:2.50:5.00:92.35$. Typical waveforms are shown in Fig. 4.

During the experiments the laser vessel was closed at one end with an uncoated MgF_2 window, in front of which a 30% transmission outcoupler was positioned, outside the vessel. With the experiments using the carbon-felt cathode x-ray source, the laser was closed at the other end with a flat high reflectivity mirror ($R > 98\%$). When using the second x-ray source, the laser was closed at the other end with an uncoated MgF_2 window. The back mirror in that case was a 10 m concave, $R > 98\%$ mirror, positioned outside the vessel.

The voltage signals were measured with resistive dividers. The discharge current was measured either with a resistive probe mounted in the current return path, or it was measured with an inductive current monitor, mounted underneath the laser anode when the setup with the carbon-felt x-ray source was used [5]. Both probes yielded the same results.

The laser pulse energy was measured us-

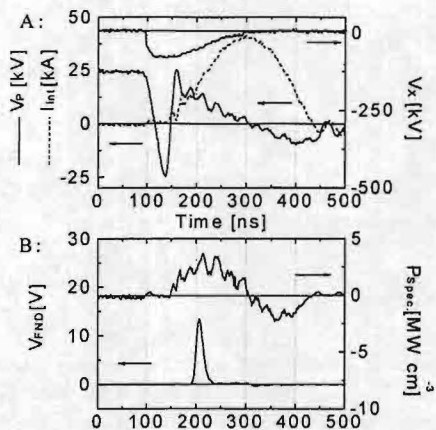


Figure 4: Typical waveforms of an ArF-laser pulse with the carbon-felt cathode x-ray source. Fig. A: V_p : Voltage across discharge; I_{int} : Current through discharge; V_x : X-ray source cathode voltage. Fig. B: V_{FND} : Photodiode signal; P_{spec} : Calculated applied power per cm³ discharge.

ing a calibrated GenTec 500 pyroelectric energy meter. A fast FND 100Q photodiode equipped with a narrow-band 193 nm filter was positioned behind the back reflector of the laser to measure the temporal behaviour of the laser pulse.

After each series of measurements the laser was refilled with a fresh mixture and the experiment was repeated to check the reproducibility.

Results and conclusions

Laser pulses could be generated with a FWHM value of 15 to 20 ns, while the first half of the pumping pulse lasted for approximately 150 ns, see Fig. 4.

The high pumping powers that are needed to generate an ArF-laser pulse (e.g. see ref. [6]) could be reached in our setup only if we applied a very high voltage to the discharge. The input power had to be extra high to overcome the considerable cavity losses due to the resonator design. So far, charging

the sustainer to twice the steady state voltage turned out to be insufficient. Therefore, the main advantages of the prepulse-mainpulse circuit are not yet fully exploited.

The high E/N values reached in the discharge increase the growth rate of instabilities into streamers, which break up the discharge and prohibit further lasing. At this stage in our research no attempt was made to increase the pulse length. However, in the near future we will decrease the self-inductance of the laser head as well as narrow the discharge width to 1 cm. This will increase the pumping power density in the discharge, enabling the sustainer to be charged to lower voltages.

The output energy of the laser pulses was measured at different x-ray charging voltages, V_{XP} , corresponding to different x-ray doses. If the preionisation level of the gas mixture is sufficient to ensure a homogeneous start of the discharge, the output of the laser will reach a steady value [7–10]. This threshold preionisation level depends on the gas mixture and the laser setup, with fluorine containing mixtures needing much more preionisation than HCl-based mixtures [10].

Fig. 5 shows the energy output of the laser as a function of the charging voltage of the x-ray source high-voltage pulsers with both x-ray sources, ranging from the lowest charging voltage at which lasing has been observed, to the maximum charging voltage of 30 kV. It is clear that the setup with the carbon-felt cathode x-ray source does not lead to a steady output energy value, whereas the second setup does. As mentioned above, the output energies of the two setups cannot be compared quantitatively because the resonators were not equivalent.

To determine the threshold preionisation electron density, the laser vessel was used as an ionisation chamber [11]. The laser cathode was charged positively and acted as a collector of the electrons the x-ray pulse produced. Measuring the time-integral of the voltage pulse across the laser electrodes that results from the electron-collection yielded the number of generated free electrons. A $V_{XP}^{7/2}$ -dependent behaviour was expected [11].

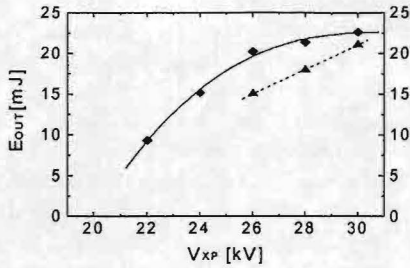


Figure 5: Energy output as a function of the charging voltage of the x-ray source mini-marx generators with the two different x-ray sources. : Corona plasma cathode x-ray source; : Carbon-felt cathode x-ray source. The lines are drawn to guide the eye.

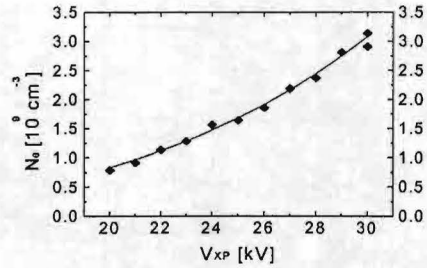


Figure 6: Generated electron density as a function of the charging voltage of the corona-plasma x-ray source mini-marx generator. The drawn line is a $V_{XP}^{7/2}$ -fit [11].

The gas mixture used for the preionisation electron density measurements was the aforementioned laser gas mixture without the fluorine, to prevent electron attachment by fluorine from spoiling the results. The collector voltage was chosen to be 2 kV; at this voltage the effects of the recombination and the multiplication processes in the gas mixture cancelled each other. A $V_{XP}^{7/2}$ -dependency was indeed measured, see Fig. 6.

From comparison of the figures 5 and 6 we can conclude that a minimum preionisation electron density of $2 \cdot 10^9 \text{ cm}^{-3}$ is needed to reach a steady output power in our setup.

Acknowledgements

The authors would like to thank H.M.J. Bastiaens for the stimulating discussions. The present work has been supported by the Netherlands Technology Foundation STW.

References

- [1] F.A. van Goor, W.J. Witteman, J.C.M. Timmermans, J. van Spijker and J. Couperus, In: High-power gas and solid state lasers, M. Bohrer, T. Letardi, D. Schuöcker and H. Weber, eds., Proc. SPIE 2206, 30-40 (1994).
- [2] G.J. Ernst, Opt. Comm. **49** (4), 275-277 (1984).
- [3] S.J. Scott, Appl. Phys. B **56**, 201-208 (1993).
- [4] J.W. Gerritsen, A.L. Keet, G.J. Ernst and W.J. Witteman, J. Appl. Phys. **67** (7), 3517-3519 (1990).
- [5] M. Trentelman, PhD thesis, Twente University, Enschede, The Netherlands (1993).
- [6] V.M. Borisov, I.E. Bragin, A.Yu. Vinokhodov and V.A. Vodchits, Quantum Electron. **25** (6), 507-510 (1995).
- [7] C.R. Tallman and I.J. Bigio, Appl. Phys. Lett. **42** (2), 149-151 (1983).
- [8] K. Midorikawa, M. Obara and T. Fujioka, IEEE J. Quantum Electron. **20** (3), 198-205 (1984).
- [9] R.S. Taylor, Appl. Phys. B **41**, 1-24 (1986).
- [10] M. Steyer and H. Voges, Appl. Phys. B **42**, 155-160 (1987).
- [11] F.A. van Goor, J. Phys. D: Appl. Phys. **26**, 404-409 (1993).

Coherence multiplexing using differential detection

E.J. Kersten, G.H.L.M. Heideman and W. van Etten

University of Twente,
Faculty of Electrical Engineering,
Tele-Informatics and Open Systems group

Abstract:

Coherence multiplexing is a relatively unknown type of Code-Division Multiple Access (CDMA). The method will be explained by comparing it with CDMA. A proper description of the signal-to-noise ratio has not yet been presented. In this paper the calculated characteristics of coherence multiplexing are discussed. The topics covered include single-ended detection, double-ended detection, the influence of different laser spectra and the relation between the number of channels and the signal-to-noise ratio.

1. Introduction

In this paper, results of calculations on coherence multiplexing are presented. After the introduction of a CDMA method and extending to coherence multiplexing, three possible implementations are discussed: single-ended, differential and differential with unequal central frequencies. After this discussion, conclusions based on the results are presented.

2. CDMA and coherence multiplexing

Coherence multiplexing is not a well-known multiplexing method. To explain it, we will look at CDMA. The system in figure 1 illustrates how it's simplest form, direct sequence spread spectrum,

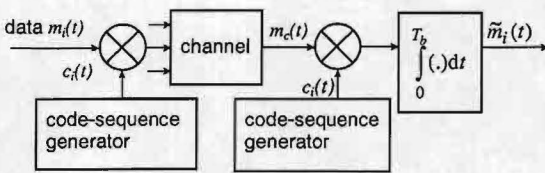


figure 1 : CDMA system

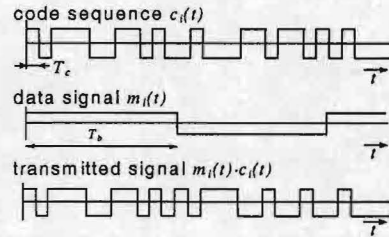


figure 2: Example of CDMA time-diagram

works. The data signal $m_i(t)$ having bit time T_b is multiplied by the code sequence $c_i(t)$ having bit time T_c shown in figure 2, along with a number of different channels. This results in the transmitted signal

$$m_c(t) = \sum_i m_i(t) \cdot c_i(t), \quad (1)$$

shown in figure 2 as well.

After combination with other sequences from different sources and transmission via the channel, all sequences arrive at the receiver. Multiplying the received signal with the same code sequence $c_i(t)$ retrieves the data. Then, the signal is integrated giving $\tilde{m}_i(t)$, an estimate of $m_i(t)$. Effectively, the signal processing in the receiver is equal to taking the inner product of the received signal and the code sequence $c_i(t)$. If the codes are chosen orthogonally, all unwanted sequences result in zero values after integration, leaving only the desired data signal.

$$\tilde{m}_i(t) = \int_0^{T_b} \sum_j m_j(t) \cdot c_j(t) \cdot c_i(t) dt \approx m_i(t) \cdot \int_0^{T_b} c_i(t) \cdot c_i(t) dt \approx m_i(t) \quad (2)$$

Coherence multiplexing works in a similar way as depicted in figure 3. Here, a broadband noise generator is used. This noise generator produces random codes. Since these codes are unknown at the receiver, they must be sent with the messages to be transmitted. This is achieved by delayed sending of the generated signal. The delays and the difference of the delays are chosen so that the autocorrelation function of the generator signal is almost zero for the values T_i and $T_i - T_j$ if $i \neq j$. As drawn in the picture, the following signal is sent:

$$m_c(t) = \sum_i (m_i(t) \cdot c_i(t) + c_i(t - T_i)) \quad (3)$$

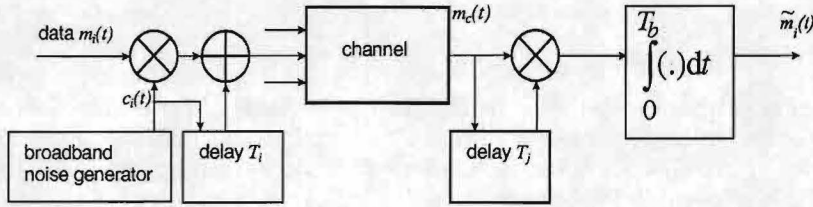


figure 3 : Coherence-multiplexing system, comparable to CDMA

At the receiver side, this is supplied to the receiver both delayed by T_j and undelayed. These two signals are then multiplied and filtered as in CDMA:

$$\tilde{m}_i(t) = \int_0^{T_b} m_c(t) \cdot m_c(t - T_j) dt \approx \int_0^{T_b} c_i(t - T_i) \cdot m_i(t - T_j) \cdot c_i(t - T_j) dt \Big|_{j=i} + \int_0^{T_b} \sum_i (m_i(t) \cdot c_i(t) + c_i(t - T_i)) \cdot \sum_{j \neq i} (m_j(t - T_j) \cdot c_j(t - T_j) + c_j(t - (T_j + T_i))) dt \approx m_i(t - T_i) \quad (4)$$

The double sum is a series of noise components, which result in zero after integration if the codes are orthogonal. So, different channels are constructed by taking different values of delay pairs. Since the random codes are (nearly) orthogonal, the same result is achieved as with CDMA: all unwanted components cancel out after integration.

3. Performance analysis

We have studied the performance of an optical coherence-multiplexing system. We assumed a configuration as drawn in figure 4.

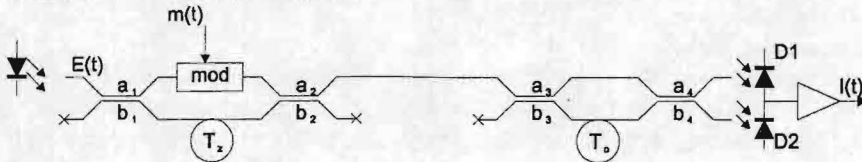


figure 4 : Model of a coherence-multiplexing system

Shown are from left to right the light source, the modulation with $m(t)$ parallel to the delay T_x , the channel, the second delay T_o parallel to a direct line, and then the equivalent of the multiplier of

figure 3. Also, couplers with coupling ratios a and b are shown. Here we assume for both a and b $\frac{1}{2}\sqrt{2}$. In this case, the multiplication occurs when converting the electromagnetic (EM) wave described by $E(t)$ to a current $I(t)$:

$$I(t) = E_{D1}(t) \cdot E_{D1}^*(t) + E_{D2}(t) \cdot E_{D2}^*(t), \text{ with } E(t) = \sqrt{P_0} \cdot e^{j\omega_0 t} \cdot \underline{u}(t) \quad (4)$$

Where E_{D1} and E_{D2} represent the EM wave, with average power P_0 , at the respective diodes and $\underline{u}(t)$ the normalized stochastic process. This system is not the same as in figure 3, but the operational principle is equal. With this system, calculations on current, mean current, autocorrelation of the current and the current spectrum were performed. The assumptions made are:

- $m(t)$ is a no-return-to-zero sequence
 - Gaussian distribution of the source noise $\underline{u}(t)$
 - Delays and difference of delays are large compared to coherence time τ_c of the source
- The system in figure 4 uses differential detection, but first a single ended system is considered.

4. Single-ended detection

Here, we assume that all M sources have exact equal central frequencies, but are otherwise incoherent. A matched receiver has an delay exact equal to the corresponding transmitter's delay. An unmatched receiver has a delay different to the transmitter on study. The mean current equals to:

$$E\{I(t)\} = M \cdot \frac{P_0}{4} + \frac{m(t-T_i)}{2} \cdot \frac{P_0}{4} \quad (5)$$

where the first term represents the unwanted signal power. Therefore, the useful signal power is $\frac{P_0}{4} = P_r$. The noise spectrum at the output of the receiver consists of the following components:

$$\bullet \text{ Beat noise: } S_{bn}(f=0) = M^2 \cdot P_r^2 \cdot \tau_c \quad (6-1)$$

$$\bullet \text{ Shot noise: } S_{sn}(f=0) = k \cdot M \cdot P_r \quad (6-2)$$

$$\bullet \text{ Amplifier noise: } S_{an}(f=0) = S_{am} \quad (6-3)$$

The assumption was made that these noise spectra are flat over the detector bandwidth Δf_e .

The k in eq. 6-1 represents a factor, dependent on, among others, the diode.

It must be noted that the noise of the matched encoder/decoder pair depends on the value of $m(t-T_i)$ and differs a little from an unmatched pair. As far as the beat noise is concerned, this is not taken in account. So, the signal to noise ratio at the output of the receiver is:

$$\left. \frac{S}{N} \right|_{se} = \frac{P_r^2}{(S_{am} + k \cdot M \cdot P_r + M^2 \cdot P_r^2 \cdot \tau_c) \cdot 2 \cdot \Delta f_e} \quad (7)$$

With Δf_e the bandwidth of the detector, and $2 \cdot \Delta f_e \ll \frac{1}{\tau_c}$

5. Differential detection

For a system with differential detection the signal to noise ratio becomes:

$$\left. \frac{S}{N} \right|_{diff} = \frac{4 \cdot P_r^2}{(S_{am} + 2 \cdot k \cdot M \cdot P_r + 2 \cdot M^2 \cdot P_r^2 \cdot \tau_c) \cdot 2 \cdot \Delta f_e} \quad (8)$$

Regarding this equation (8) and comparison with equation 7, the following must be noted:

- Comparing this equation with the $\frac{S}{N}$ of a single ended system, the power of the signal is increased with a factor of 4 because in a differential system the useful signal is doubled, $2 \cdot P_r$, and the average is zero.
- The term representing the shot noise is doubled because the shot noise in each diode behaves like an independent noise source.
- The beat noise in one diode current contains for one half signals that are in phase with the other diode and other signals in anti-phase as compared to the other diode. The in-phase terms cancel out and the anti-phase terms are doubled in amplitude.

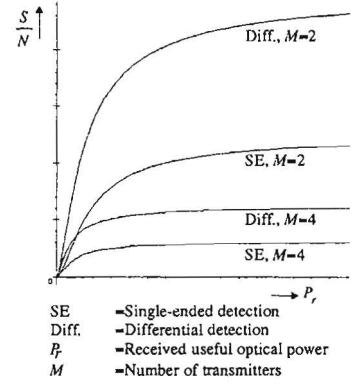


figure 5 :Influence of type of detection and number of sources on performance

For comparison, figure 5 displays the relationship between received useful power and signal-to-noise ratio.

6. Sources with different central frequencies

If the spectra of the light sources of the transmitters have different central frequencies and have only a partial overlap, the beat noise term with quadratic relation to the number of channels changes, depending on the amount of overlap. This is because the inner products of signals from different transmitters are partly orthogonal. Thus, the following signal-to-noise expression results:

$$\left. \frac{S}{N} \right|_{diff, 2} = \frac{4 \cdot P_r^2}{\left(S_{am} + 2 \cdot k \cdot P_r \cdot M + 2 \cdot \alpha_M \cdot M \cdot P_r^2 \cdot \tau_c \right) 2 \cdot \Delta f_e} \quad (8)$$

Where α_M represents the amount of overlap and ranges from 1 to M . $\alpha_M=1$ if there is no overlap and $\alpha_M=M$ when the central frequencies are equal.

7. Conclusions

If we analyze the results of the calculations, it is obvious that differential detection lowers the noise floor by a factor of 2. For small values of P_r , there is a 3dB increase in sensitivity for the differential detection. Another, less obvious result of the calculations is that if the spectra have only a partial overlap, the quadratic relation between the number of channels and the beat noise changes, and if there is no overlap at all it becomes linear. Thus, the signal to noise ratio for large P_r is then proportional to

$$\frac{1}{M \cdot \tau_c \cdot 2 \cdot \Delta f_e} \text{ instead of } \frac{1}{M^2 \cdot \tau_c \cdot 2 \cdot \Delta f_e}$$

References:

- R. H. Wentworth, "Theoretical noise performance of coherence-multiplexed interferometric sensors," *J. Lightwave Technol.*, vol. 7, pp. 941-956, 1989.
- G. J. Pendock and D. D. Sampson, "Increasing the transmission capacity of coherence multiplexed communication by using differential detection," *IEEE Photon. Technol. Lett.*, vol. 7, pp. 1504-1506, 1995.

Estimating Error Probabilities caused by In-Band and Out-Band Crosstalk in Multi-Wavelength All-Optical Networks

A.M.J. Koonen **, D.T. van Veen *

* Lucent Technologies Nederland B.V., P.O. Box 18, 1270 AA Huizen, The Netherlands

** CTIT, Univ. of Twente, P.O. Box 217, 7500 AE Enschede, The Netherlands

Abstract

Upper bounds to the error probability due to in-band and out-band crosstalk in multi-wavelength all-optical networks are derived using Chernoff's method. The impact on system design is compared with results from the common Gaussian approximation.

Introduction

All-optical networks are regarded as the most appropriate infrastructures meeting the future needs for high-speed data transport and easy upgradability. Wavelength Division Multiplexing (WDM) techniques, by which optical paths at different wavelengths can be established simultaneously through the same physical network, are of key importance to realise flexible routing of data streams. Thus the logical network topology can be readily adapted to traffic demands without changing the physical network; also fast path restoration in case of link failures is possible by just rerouting the wavelength channels.

Two WDM building blocks are essential for wavelength routing: a multi-wavelength optical crossconnect node, and a multi-wavelength add-drop node. This paper will address the impact of the crosstalk characteristics of these devices on the system performance. In contrast to the commonly used Gaussian approximation of the crosstalk signal statistics, the Chernoff bound is introduced giving a guaranteed upper bound to the system error probability. Both in-band and out-band crosstalk signals are considered, and an accurate lower bound to the required crosstalk attenuation of the devices is derived.

Wavelength routing building blocks

A multi-wavelength optical crossconnect node (λ -OXC) has N optical input ports, and (usually) N output ports, as shown in Fig. 1. Each input port may carry M wavelength channels. The λ -OXN can route any wavelength channel from any input port to any output port. When wavelength translation inside the λ -OXN is employed, it may even route it to any wavelength channel in any output port.

By denoting by P_{ij}^{in} the signal power at wavelength λ_i in input port j , the input signals can be represented in a matrix

$$\mathbf{P}^{in} = \begin{bmatrix} P_{11}^{in} & \cdot & \cdot & P_{1N}^{in} \\ \cdot & \cdot & \cdot & \cdot \\ \cdot & P_{s,n}^{in} & \cdot & \cdot \\ P_{M,1}^{in} & \cdot & \cdot & P_{M,N}^{in} \end{bmatrix}$$

and the λ -OXN performs a matrix operation transforming \mathbf{P}^{in} into an output signal matrix \mathbf{P}^{out} . For the crosstalk analysis, suppose that $P_{s,n}^{in}$ is transposed without loss to $P_{s,m}^{out}$. Including crosstalk effects inside the λ -OXN, $P_{s,m}^{out}$ is given by

$$P_{s,m}^{out} = P_{s,n}^{in} + \epsilon_{ib} \cdot \sum_{j \neq n} P_{s,j}^{in} + \epsilon_{ob} \cdot \sum_{i \neq s} \sum_j P_{i,j}^{in}$$

where the first term is the desired signal (i.e., the signal at wavelength λ_s from input port n routed to output port m), the second term comprises the $(N-1)$ in-band crosstalk terms leaking at the same wavelength λ_s from the not-selected input ports to output port m , and the third term

contains the $N(M-1)$ out-band crosstalk terms leaking at the not-selected wavelengths from all input ports. For simplicity, the in-band crosstalk leakage factors ε_{ib} and out-band ones ε_{ob} are assumed to be equal across the wavelength channels and input ports. The in-band crosstalk terms are particularly harmful, as they can not be filtered out further on in the network.

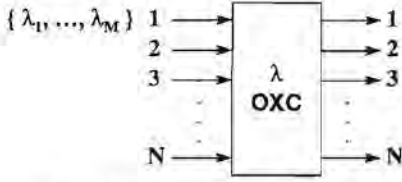


Fig. 1 Multi-wavelength Optical Crossconnect Node

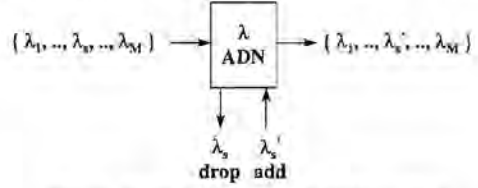


Fig. 2 Multi-wavelength Add-Drop Node

A multi-wavelength add-drop node (λ -ADN) has only one input port and one output port, each carrying M wavelength channels. One or more of the M input channels may be dropped, and may be replaced by signals added at nominally the same wavelength(s). Fig. 2 shows the basic layout of a λ -ADN. The input signal matrix is now a simple vector

$$\mathbf{P}^{in} = [P_{1,1}^{in} \quad \dots \quad P_{s,1}^{in} \quad \dots \quad P_{M,1}^{in}]^T$$

Assuming that the input signal at λ_s needs to be dropped, and replaced by adding a signal P_s^{add} at nominally the same wavelength λ_s' , the output signal P_s^{out} can be written as

$$P_s^{out} = P_s^{add} + \varepsilon_{ib} \cdot P_s^{in} + \varepsilon_{ob} \cdot \sum_{i \neq s} P_i^{in}$$

where the first term denotes the desired signal at λ_s' , the second one the in-band crosstalk term at λ_s leaking from the input port, and the third term the $(M-1)$ out-band crosstalk terms leaking at the not-selected wavelengths from the input port.

Calculating the Bit Error Rate probability due to in-band and out-band crosstalk

As the in-band crosstalk components nominally have the same wavelength as the desired signal, by heterodyne mixing they may yield beat noise products falling into the receiver bandwidth.

Analyzing the crosstalk generated in the λ -OXC, the photocurrent $i(t)$ after detecting $P_{s,m}(t)$ is given by (cf. [1, 2])

$$i(t) = R_d \cdot \left[\frac{1}{2} |E_{s,n}(t)|^2 + \text{Re} \left(E_{s,n}(t) \cdot \sqrt{\varepsilon_{ib}} \cdot \sum_{j \neq n} E_{s,j}^*(t) \exp \left[j(\omega_{s,n} - \omega_{s,j})t + j(\varphi_{s,n} - \varphi_{s,j}) \right] \right) + \frac{1}{2} \sum_{i \neq s} \sum_j \varepsilon_{ob} |E_{i,j}(t)|^2 + n_{th}(t) \right]$$

where R_d is the photodiode responsivity, the first term denotes the desired signal at wavelength $\lambda_s = 2\pi c_0 / \omega_s$ with c_0 the speed of light in vacuum, the second term the in-band crosstalk, the third term the out-band crosstalk, and the fourth term the thermal receiver noise. The electric field amplitudes $|E_{i,j}(t)|$ are related to the signal powers by $P_{i,j}^{in}(t) = \frac{1}{2} |E_{i,j}(t)|^2$.

The theoretical probability density function (pdf) of each in-band crosstalk term deviates considerably from a Gaussian pdf, and is given by

$$p(x) = \frac{1}{\pi A \sqrt{1 - (x/A)^2}} \quad \text{for } |x| < A$$

$$= 0 \quad \text{elsewhere}$$

where A is the amplitude of the (harmonically varying) crosstalk term ($A = \sqrt{\epsilon_{ib} \cdot |E_{s,n}| \cdot |E_{s,j}|}$). Calculating the moment generating function $M_x(s) = E[e^{sx}]$ yields

$$M_x(s) = \int_{-A}^{+A} \frac{e^{sAx} \cdot dx}{\pi A \sqrt{1 - (x/A)^2}} = I_0(sA)$$

where $I_0(\cdot)$ is the modified Bessel function of zeroth order.

Assuming statistical independence of the X in-band crosstalk components and the thermal receiver noise (dominating the signal shot noise), and perfect signal extinction ratio, an upper bound to the bit error rate (BER) can be derived using the Chernoff bound (see [3])

$$BER < I_0^X(sA) \cdot \exp(-sD + \frac{1}{2} s^2 \sigma_{th}^2)$$

where s is optimized such that the right hand side is minimized, and σ_{th}^2 denotes the thermal receiver noise power; D is the threshold level set in the binary decision circuit.

The traditional Gaussian approximation yields

$$BER \approx \frac{1}{2} \operatorname{erfc}\left(D / \sqrt{2\sigma_{th}^2 + X \cdot A^2}\right)$$

where $\operatorname{erfc}(\cdot)$ denotes the complementary error function.

Each out-band crosstalk term may take a value between $+A$ and $-A$ at the input of the AC-coupled decision circuit. Assuming a cosine pulse shape at this input, and uniformly distributed pulse phase at the decision moment t_s , the pdf of each crosstalk term follows the same distribution as the one for each in-band crosstalk term, but with $A = \frac{1}{2} \epsilon_{ob} \cdot |E_{i,j}(t_s)|^2 = \epsilon_{ob} P_{i,j}(t_s)$. Assuming again statistical independence of the X out-band crosstalk terms and the thermal noise, the expression for the Chernoff upper bound to the BER has the same form as the one for the in-band crosstalk.

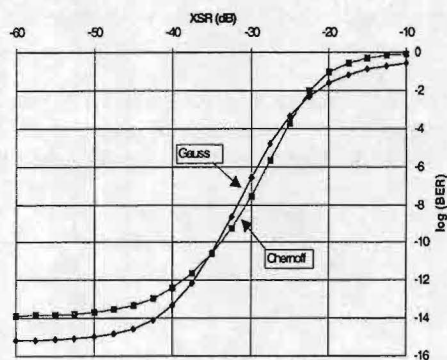


Fig. 3 In-band crosstalk for 4-port 4- λ optical crossconnect

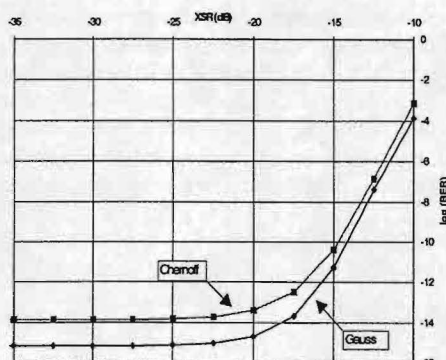


Fig. 4 Out-band crosstalk for 4-port 4- λ optical crossconnect

Calculation results

As an example, the BER performance of a binary $M=4$ wavelengths system has been analysed. The normalised decision threshold level has been set at $D=1$, and the thermal receiver noise at $\sigma_{th} = 1/8$; assuming a perfect signal extinction ratio, this implies a $BER = \frac{1}{2} \operatorname{erfc}(8/\sqrt{2}) \approx 10^{-15}$ when the system is crosstalk-free.

For an $N=4$ ports λ -OXC, there are $X_{ib}=N-1=3$ in-band crosstalk terms, and $X_{ob} = N(M-1) = 12$ out-band crosstalk terms. Fig. 3 shows the BER versus the in-band-crosstalk to signal ratio

$XSR_{ib} = \epsilon_{ib} \cdot P_{s,j}^{in} / P_{s,n}^{in}$; Fig. 4 shows it versus the out-band-crosstalk to signal ratio $XSR_{ob} = \epsilon_{ob} \cdot P_{i,j}^{in} / P_{s,n}^{in}$.

For the λ -ADN, there is $X_{ib}=1$ in-band crosstalk term, and $X_{ob} = (M-1) = 3$ out-band crosstalk terms. Fig. 5 shows the BER versus the in-band-crosstalk to signal ratio $XSR_{ib} = \epsilon_{ib} \cdot P_{s,j}^{in} / P_{s,n}^{in}$; Fig. 6 shows it versus the out-band-crosstalk to signal ratio $XSR_{ob} = \epsilon_{ob} \cdot P_{i,j}^{in} / P_{s,n}^{in}$.

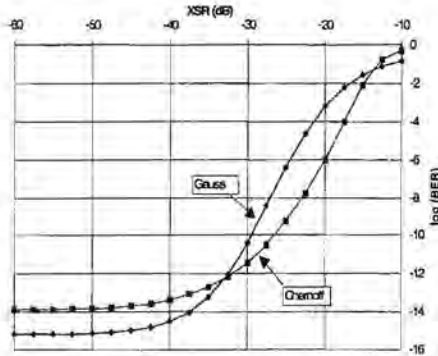


Fig. 5 In-band crosstalk for 4- λ add/drop node

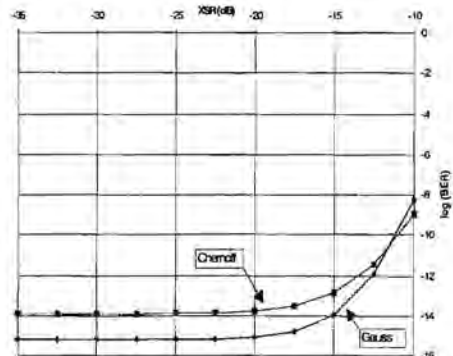


Fig. 6 Out-band crosstalk for 4- λ add/drop node

Conclusions

The Chernoff bound provides an upper limit to the system bit error rate, and as such provides safe design targets for multi-wavelength optical crossconnect nodes and multi-wavelength add-drop nodes. The in-band crosstalk attenuation needed per wavelength channel in order to guarantee a certain BER performance is considerably higher than the out-band one. For a $BER < 10^{-9}$, the Chernoff bound indicates that the in-band crosstalk attenuation needed is lower than the one resulting from the Gaussian approximation; the difference is for the add-drop node larger than for the optical crossconnect (due to a larger deviation of the actual crosstalk statistics from the approximative Gaussian ones).

Acknowledgements

Financial support of the IOP Electro-Optics project IEO 94100 and the ACTS project AC028 TOBASCO is gratefully acknowledged.

References

- [1] H. Takahashi, K. Oda, and H. Toba, "Impact of crosstalk in an arrayed-waveguide multiplexer on $N \times N$ optical interconnection", J. of Lightwave Techn., Vol. 14, No. 6, June 1996, pp. 1097-1105
- [2] E. Tangdiongga, I. Tafur, H. de Waardt, and M.O. van Deventer, "Performance analysis of cross-connects corrupted by in-band crosstalk", in Proc. of Symp. IEEE/LEOS Benelux Chapter, Enschede, The Netherlands, pp. 152-155, Nov. 1996
- [3] D.T. van Veen and A.M.J. Koonen, "Evaluating Crosstalk in Multiwavelength All-Optical Networks using the Chernoff Bound", in Proc. of 5th Symp. IEEE/CVT Benelux Chapter, Enschede, The Netherlands, pp. 143-148, Oct. 1997

Stability analysis and spectral properties of a diode laser with sluggish phase-conjugate feedback

W. A. van der Graaf,^a L. Pesquera,^b and D. Lenstra^a

^a*Department of Physics and Astronomy, Vrije Universiteit, De Boelelaan 1081, 1081 HV Amsterdam, The Netherlands*

^b*Instituto de Física de Cantabria (CSIC-UC), Facultad de Ciencias, E-39005 Santander, Spain*

For a diode laser subjected to feedback from a phase-conjugating mirror we present (a) the first exact stability-analysis and (b) various spectra. The stability properties are intermediate between those of the injection laser and the laser with conventional optical feedback. The role of a finite response time of the mirror is to drastically enhance the steady-state stability. For moderate feedback the frequency noise is suppressed by several orders of magnitude, and the main relaxation frequency of the laser shows a crossover from the relaxation oscillation frequency to a new frequency determined by the amount of feedback.

Optical feedback from a phase-conjugate mirror (PCM) is preferred over conventional feedback (COF) for stabilization purposes, since the laser with COF is very sensitive to mirror distance variations within an optical wavelength. The low-frequency noise is reduced with phase-conjugate feedback (PCF) due to phase locking [1]. For a realistic description of a diode laser with PCF the finite response time, t_m , of the PCM must take into account. We report on the stability and noise properties of a single-mode diode laser with sluggish PCF based on nearly-degenerate four-wave mixing.

An exact linear stability analysis is performed using the principle of the argument [2]. Fig. 1 shows that at low feedback reduced stability occurs whenever the relaxation oscillation (RO), with angular frequency ω_R , matches an external roundtrip resonance. This phenomenon, which shows similarity to the case of COF, was not seen in previous approximate analyses [1]. The role of t_m is to drastically enhance the steady-state stability. The shift with t_m in the location of the peak is due to the mirror delay time, which resembles a larger cavity. For an instantaneous mirror the laser becomes unstable when increasing the feedback rate γ_p , except for a small region of short cavities. When t_m is nonzero, the laser returns to stable operation for moderate feedback for the whole range of τ (Fig. 1). The stability areas for low and moderate feedback turn out to be connected when considering the influence of detuning, δ_0 , of the mirror-pump beam, which has frequency ω_p , with respect to the laser frequency (see Fig. 2). A remarkable similarity with an optically injected laser is found for nonzero t_m , where ω_p plays the role of the injection frequency. Steady states are found only when $|\delta_0| \leq \gamma_p \sqrt{1 + \alpha^2}$, with α the linewidth enhancement factor.

Concerning noise properties, the relative intensity noise and frequency noise spectra (FNS) at low feedback are reduced at low frequencies [1], while the height of the RO peak varies periodically with τ in the same way as the lower stability boundary

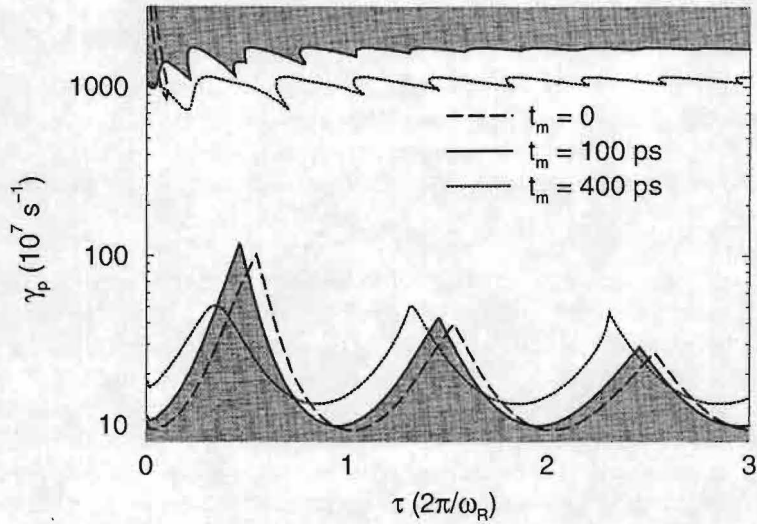


FIG. 1. Stability diagram for a laser pumped 5% above threshold in the feedback versus cavity-roundtrip-time (normalized to the RO period, which in this case is 1.3 ns) plane for different values of the mirror delay time as indicated. For a 100 ps delay time the region of stable operation is hatched.

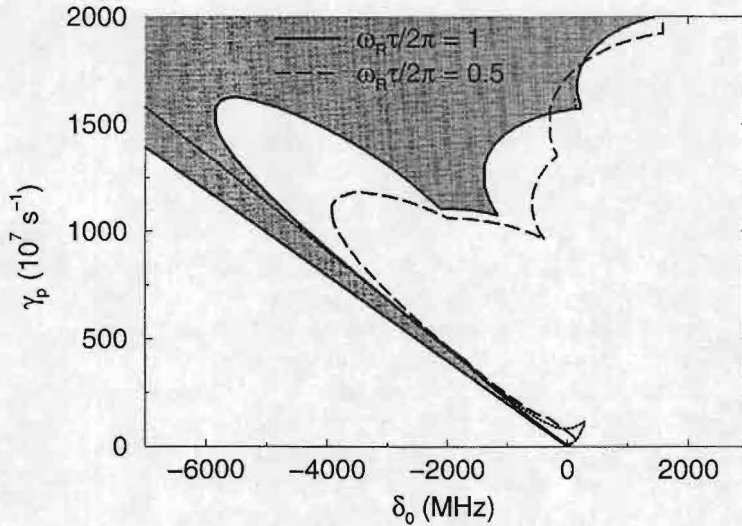


FIG. 2. Stability diagram as a function of the feedback rate and the pump detuning δ_0 . The mirror delay time is 100 ps, except for the dotted curve. The hatched area is the stable region with $\omega_R\tau/2\pi = 1$. The dotted curve corresponds to an instantaneous mirror at $\omega_R\tau/2\pi = 0.5$; in this case a narrow stripe of stable operation is found.

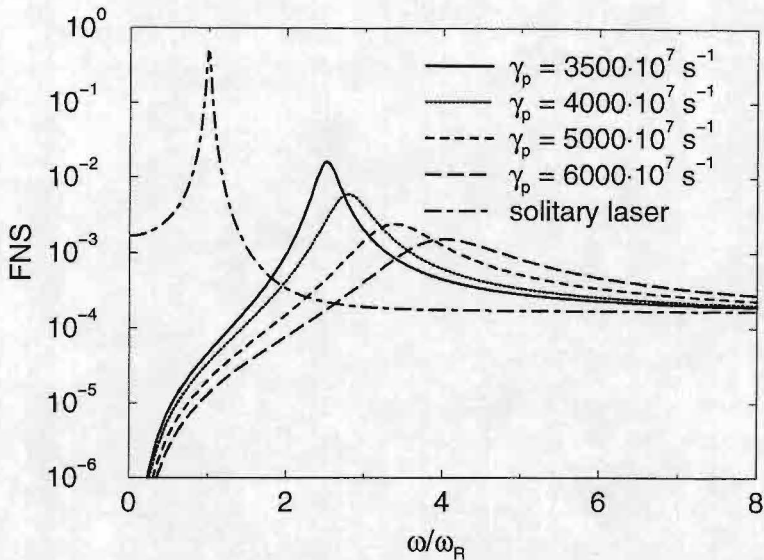


FIG. 3. Frequency noise spectra for several feedback rates as indicated for a laser pumped 50% above threshold, and with moderate PCF (in the upper stability region), mirror delay $t_m = 400$ ps and $\tau = 66.7$ ps. The dash-dotted curve corresponds to the solitary laser. These cases correspond to a solitary laser linewidth $\Delta\nu|_{FWHM} = 10$ MHz.

in Fig. 1. When t_m is increased this resonance is washed out due to mirror-induced spectral filtering. For nonzero mirror delay time the laser is stable at higher PCF and the overall noise level is decreased by several orders of magnitude (Fig. 3). Double roundtrip resonances are obtained for large τ , that are washed out by increasing t_m . Furthermore, comparison with the spectrum of the solitary laser shows that instead of the RO peak a broad resonance appears at a higher frequency. The frequency of this main resonance approaches $\gamma_p \alpha / \sqrt{1 + \alpha^2}$ at high feedback, and thus increases linearly with γ_p (Fig. 3). This explains pulse-frequency scaling with γ_p discovered in numerical simulations [3].

In conclusion, due to the mirror delay the laser becomes stable at higher PCF. At these feedback rates the frequency noise is considerably reduced and the frequency of the main resonance increases with feedback.

-
- [1] G. P. Agrawal and G. R. Gray, Phys. Rev. A **46**, 5890 (1992).
 - [2] J. J. DiStefano, A. R. Stubberud, and I. J. Williams, *Feedback and control systems*, Schaum's Outline Series, McGraw-Hill Book Co. (1967).
 - [3] D. H. DeTienne, G. R. Gray, G. P. Agrawal, and D. Lenstra, IEEE J. Quantum Electron. **33**, 838 (1997).

Quantum Electrodynamical Modeling of Light Emission in Semiconducting Devices ¹

Christa Hooijer ² and Daan Lenstra

*Department of Physics and Astronomy, Vrije Universiteit, De Boelelaan 1081,
1081 HV Amsterdam*

A fully quantized theory for the interaction between light and semiconducting structures is presented. A Green's function technique is used to separate the quantum mechanical problem from the electromagnetic problem. Preliminary results regarding spontaneous emission are shown.

BACKGROUND

Semiconductor lasers, amplifiers and light emitting diodes tend to become continually smaller, now approaching the size of optical wavelengths. These small devices have the possibility to emit non-classical light [1, 2]. An example of non-classical light is squeezed light where uncertainties in the field phase or the field amplitudes are reduced below the quantum-noise level (which then causes larger uncertainties in the field amplitude or field phase respectively). Squeezed light can be used in optical communication, spectroscopy, cryptography and few photon communication.

APPROACH

A theoretical framework lacks where both the electromagnetic field and the electrons as well as the interaction between them is treated fully quantum mechanically in a very general geometry. The standard approach to field quantization is to use a mode decomposition of the EM-field and introduce photon creation and annihilation operators for each mode. The devices of interest here are essentially open structures that leak away their energy. Mode-decomposition-related methods can then be used, but either they do not account for the radiation condition at infinity, or when introducing quasi-modes with complex frequencies, their quantization is by no means trivial. We avoid such problems completely by dealing with the full field operators in combination with the classical Green's tensor which accounts for the full wave-guiding and diffraction aspects of the dielectric device geometry. We are then left with an electromagnetic problem (i.e. the calculation of the Green's tensor) separate from the quantum mechanical problem. This method will allow us to naturally calculate radiation pattern expectation values and photon correlation functions anywhere in space and time, and, as a first application, it enables us to directly calculate spontaneous emission rates without using Fermi's Golden Rule of first-order-perturbation theory, which would require the use of

¹This work is part of the research programme of the 'Stichting voor Fundamenteel Onderzoek der Materie (FOM)', which is financially supported by the 'Nederlandse Organisatie voor Wetenschappelijk Onderzoek (NWO)'.

²email-address: hooijer@nat.vu.nl

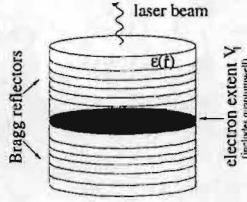


Figure 1: A typical VCSEL structure. The black area is the interaction volume, but one can see that the Bragg reflectors and the losses to the outside world will have influence on the behavior within the interaction volume. Information the structure is contained in the Green's tensor associated with it.

an adequate density of modes. This density of modes is easier to calculate than a full Green's tensor, but the latter has to be calculated only once, and then it can be used in principle to calculate any field property.

In quantum optics with atoms the electrons interacting with the electromagnetic field are well localized within the wavelength. In contrast in our case the carrier states are extended in space, and the dipole moment is no longer well defined. The relevant interaction Hamiltonian now is:

$$H_I \propto \int_{V_I} d^3r \hat{\mathbf{A}}(\mathbf{r}, t) \cdot \hat{\mathbf{J}}(\mathbf{r}, t) = \sum_{n, n', \mathbf{k}, \mathbf{k}'} \int_{V_I} d^3r \hat{\mathbf{A}}(\mathbf{r}, t) \varphi_{n\mathbf{k}}^*(\mathbf{r}) \nabla \varphi_{n'\mathbf{k}'}(\mathbf{r}) \hat{c}_{n\mathbf{k}}^\dagger \hat{c}_{n'\mathbf{k}'}(t), \quad (1)$$

where the hats indicate that these quantities are the quantum mechanical operators. $\hat{\mathbf{A}}(\mathbf{r}, t)$ is the vector-potential operator, $\hat{\mathbf{J}}(\mathbf{r}, t)$ is a current-like operator associated with all transitions of electrons from band n' , wave vector \mathbf{k}' to band n , wave vector \mathbf{k} (represented by the operator $\hat{c}_{n\mathbf{k}}^\dagger \hat{c}_{n'\mathbf{k}'}(t)$), $\varphi_{n\mathbf{k}}^*(\mathbf{r}) \nabla \varphi_{n'\mathbf{k}'}(\mathbf{r})$ represents the coupling strength between the two states and $\varphi_{n'\mathbf{k}'}(\mathbf{r})$ is a electron wave function associated with the bandstructure of the semiconductor. The interaction between field and electrons is confined to the active layer where the actual light is generated. For example in a VCSEL, the active region consists of the quantum well where the light is generated. Thus the integral in (1) only runs over the region to which the interaction is confined.

EQUATIONS OF MOTION

We work in the Heisenberg picture. This picture provides us with an equation of motion for every operator involved, while the electron and field states remain unchanged. Due to the interaction between the field and the electrons the field operators will acquire as time proceeds an electron character as well, and the electron operators will acquire a field character. To fully describe the processes we only have to look at the temporal development of the relevant operators. This gives the following equation of motion for $\hat{\mathbf{A}}(\mathbf{r}, t)$:

$$\left(\frac{\partial^2}{\partial t^2} + \vec{\nabla}^2 \right) \hat{\mathbf{A}}(\mathbf{r}, t) = \hat{\mathbf{J}}(\mathbf{r}, t). \quad (2)$$

Note that this equation has the form of the Helmholtz wave equation and that it can be solved using a Greens tensor technique, thus

$$\hat{\mathbf{A}}(\mathbf{r}, t) = \hat{\mathbf{A}}_{free}(\mathbf{r}, t) + \sum_{n, n', \mathbf{k}, \mathbf{k}'} \int_{V_I} d^3 r' \int dt' G(\mathbf{r}, \mathbf{r}', t, t') \varphi_{n\mathbf{k}}^*(\mathbf{r}') \nabla \varphi_{n'\mathbf{k}'}(\mathbf{r}') \hat{c}_{n\mathbf{k}}^\dagger \hat{c}_{n'\mathbf{k}'}(t'), \quad (3)$$

where $\hat{\mathbf{A}}_{free}(\mathbf{r}, t)$ is the free-field solution to the sourceless Helmholtz wave equation. In (3) we see that for the source-part of $\hat{\mathbf{A}}(\mathbf{r}, t)$ we have separated the quantum mechanical problem from the electromagnetic structure, which is fully contained in the Greens tensor, while the quantum mechanical character of the $\hat{\mathbf{A}}$ -field is contained in $\hat{c}_{n\mathbf{k}}^\dagger \hat{c}_{n'\mathbf{k}'}(t)$.

The equations of motion for the electron operators are:

$$\frac{d}{dt} \hat{c}_{n\mathbf{k}}^\dagger \hat{c}_{n\mathbf{k}}(t) = \frac{1}{i\hbar} \sum_{n', \mathbf{k}'} \int_{V_I} d^3 r \left[\varphi_{n\mathbf{k}}^*(\mathbf{r}) \nabla \varphi_{n'\mathbf{k}'}(\mathbf{r}) \hat{\mathbf{A}}(\mathbf{r}, t) \hat{c}_{n\mathbf{k}}^\dagger \hat{c}_{n'\mathbf{k}'}(t) - \text{h.c.} \right], \quad (4)$$

$$\begin{aligned} \frac{d}{dt} \hat{c}_{n\mathbf{k}}^\dagger \hat{c}_{n'\mathbf{k}'}(t) &= i\omega_{nn'}(\mathbf{k}, \mathbf{k}') \hat{c}_{n\mathbf{k}}^\dagger \hat{c}_{n'\mathbf{k}'} \\ &+ \frac{1}{i\hbar} \int_{V_I} d^3 r \varphi_{n\mathbf{k}}^*(\mathbf{r}) \nabla \varphi_{n'\mathbf{k}'}(\mathbf{r}) \hat{\mathbf{A}}(\mathbf{r}, t) \left(\hat{c}_{n\mathbf{k}}^\dagger \hat{c}_{n\mathbf{k}} - \hat{c}_{n'\mathbf{k}'}^\dagger \hat{c}_{n'\mathbf{k}'} \right). \end{aligned} \quad (5)$$

Here terms like $\hat{c}_{n\mathbf{k}}^\dagger \hat{c}_{n\mathbf{k}}$ count the number of electrons in band n with wavevector \mathbf{k} . $\omega_{nn'}(\mathbf{k}, \mathbf{k}')$ denotes the frequency proportional to the energy difference $E_n(\mathbf{k}) - E_{n'}(\mathbf{k}')$.

SPONTANEOUS EMISSION

As a first application of our theory we calculate from equation (4) spontaneous emission coefficients in three simple cases, which can also be calculated using the Fermi Golden Rule. In this way we are provided with a test of our theory. The model we chose is very simple, we consider a two-band model for the semiconductor, with one electron initially in the conduction band and no electrons in the valence band. The Green's tensor is taken as the free-field Green's tensor in a homogeneous medium with constant refractive index. Within the limits of our approximation the model is exact and the results are obtained analytically. In figure 2 the results are given. All results are consistent with each other.

FUTURE APPLICATIONS

With this theory, we have the full equations of motion of all relevant operators. When we want to calculate some spectra or field correlation functions, we already have all information needed to do so, apart from the Greens tensor of a specific structure. Once we know that Green's tensor, all higher order correlation functions are accessible.

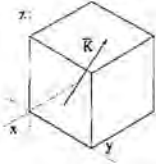
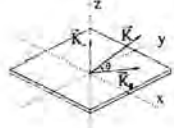
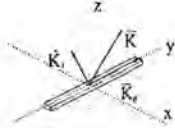
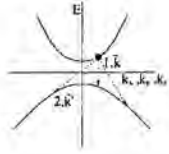
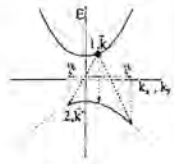
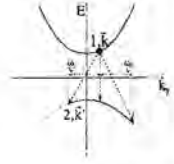
	bulk semiconductor	quantum well	quantum wire
configuration			
bandstructure			
lifetime	$\frac{1}{\tau} = \frac{\mu_0 \hbar e^2 K^2 \omega_0}{3\pi m^2 v}$	$\frac{1}{\tau} = \frac{\mu_0 \hbar e^2 (2K_{\perp}^2 + K_{\parallel}^2) \omega_0}{4\pi m^2 v}$	$\frac{1}{\tau} = \frac{\mu_0 \hbar e^2 K^2 \omega_0}{2\pi m^2 v}$

Figure 2: In this overview, we show our main results concerning spontaneous emission. The results are completely consistent with each other. If for the quantum well we average the spontaneous emission lifetime over all possible orientations of the quantum well, we obtain the spontaneous emission lifetime for the bulk semiconductor, and for the quantum wire the same holds. (Thus for the case of the quantum well, with $K_{\perp} = K * \sin \theta$, and $K_{\parallel} = K * \cos \theta$, integrate $\frac{1}{\tau}$ over θ with θ running from 0 to 2π , normalize, and the result for the bulk semiconductor is found.)

Currently we are working on the problem of resonance fluorescence. A device is pumped with a frequency closely corresponding to the gap energy between the highest valence band and the lowest conduction band. From two level atoms this situation is well studied [3, 4], and we therefore seek similarities in the resonance fluorescence spectrum in both cases, such as photon antibunching, Rabi frequencies and Lamb shifts.

REFERENCES

- [1] Y. Yamamoto, W.H. Richardson, "Squeezed states; a closer look at the amplitude and phase of light," *Opt. & Photon. News*, vol. 6, pp. 24-29, May 1995.
- [2] S. Kakimoto, K. Shigihara, Y. Nagai, "Laser diodes in photon number squeezed state," *IEEE J. Quantum Electron.*, vol. 33, pp. 824-830, 1997
- [3] H.J. Kimble, L. Mandel, "Theory of resonance fluorescence," *Phys. Rev. A*, vol. 13, pp. 2123-2144, 1976.
- [4] L. Mandel, E. Wolf, *Optical Coherence and quantum optics*. Cambridge: Cambridge University Press, 1995.

This paper was withdrawn at the last moment

This paper was withdrawn at the last moment.

This paper was withdrawn at the last moment

This paper was withdrawn at the last moment

Chopped InGaAs/InP quantum well for polarization independent interferometric switching at $1.55\ \mu\text{m}$

B.H.P. Dorren*, A. Yu. Silov, M.R. Leys, J.E.M. Haverkort and J.H. Wolter

COBRA Inter-University Research institute, Eindhoven University of Technology,

P.O. box 513, 5600 MB Eindhoven, Netherlands.

D.H.P. Maat, Y. Zhu, Y.S. Oei and F.H. Groen

Delft University of Technology

Abstract

An InGaAs/InP chopped quantum well layer sequence specially designed for Mach-Zehnder interferometric space switching is presented. Each chopped quantum well consists of three 27\AA InGaAs strained quantum wells separated by 11\AA InP barriers. The structure shows a red shift of the absorption edge as high as 80nm with applied bias of 10V . The heavy hole and light hole subbands cross at tensile strain of approximately 0.7% . Using these chopped quantum wells, we realized Mach-Zehnder interferometric space switches with low propagation loss and a switching voltage of 3.1V for 4mm long phase shifting sections. Finally, we realized full polarization independent switching using 0.85% tensile strained chopped quantum wells.

A first constraint for the design of a Mach-Zehnder interferometric (MZI) space switch at $1.55\mu\text{m}$ is waveguide transparency. When using tuning sections based on the Quantum Confined Stark Effect (QCSE) with InGaAs/InP quantum wells, the QW-thickness is limited to a maximum of 40\AA for preserving waveguide transparency. Such a small QW-thickness is far from optimum for an appreciable QCSE resulting in a small index of refraction change (left graph figure 1) and thus in long switches.

The bandgap change in a quantum well due to the QCSE, increases rapidly with increasing quantum well width [1]. Chopped quantum wells (CQW) allow to tune the position of the bandgap and the total CQW width separately. In the QCSE, the CQW will act as a single quantum well with a width L_{CQW} (figure 2). This is caused by the excellent coupling of the carrier wave functions between the neighboring quantum wells. The bandgap, however, is set by average potential of the individual quantum wells and the barriers. We designed CQW's consisting of three 27\AA InGaAs quantum wells separated by 11\AA InP barriers (figure 2). These CQW's combine a room temperature bandgap at 1390nm , necessary for waveguide transparency at 1550nm , with a total CQW well width of 103\AA required for an optimized QCSE.

Energy level calculations on a CQW structure shows a giant 55nm red-shift for the lowest electron to heavy hole transition at 75kV/cm applied field (right graph figure 1). The first excited

*e-mail b.h.p.dorren@cobra.tue.nl

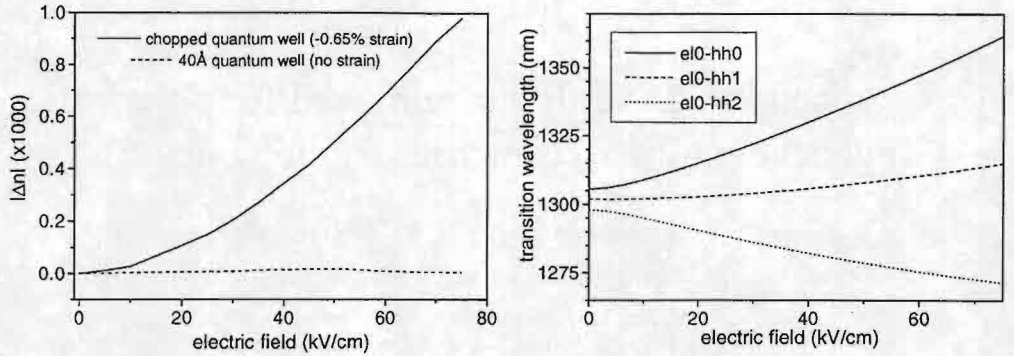


Figure 1: **Left:** calculations of the index of refraction change 100nm below the bandgap due to the QCSE in: 40Å quantum wells and in chopped quantum wells. **Right:** calculations of the shifts of several electron to heavy hole levels in a chopped quantum well.

heavy hole level also shifts red while the second excited state shifts blue. The net effect on the index of refraction change, as obtained by the Kramers-Kronig relations [2], of the red shifting levels is somewhat compensated by the blue shifting level. Nevertheless, a large improvement in the index of refraction change in respect to 40Å InGaAs/InP quantum wells is expected. This is shown in the left graph of figure 1 where the calculated index of refraction change in TE polarization of a 40Å InGaAs/InP quantum well and of a CQW are compared.

We have grown three CQW samples consisting of 20 CQW's embedded into a p-i-n structure. A cross-sectional view of the structures is depicted in figure 2. We applied tensile strain of 0.50%, 0.65% and 0.85% within the wells of the different samples to obtain polarization independent switching [3].

The left graph in figure 3 shows photocurrent measurements for the 0.50% tensile strained sample under an applied electric field at 4K. These measurements show an effective red shift of the lowest confined energy state of 80nm at a reverse bias of 10V. Some structure is visible in the spectra which we explain by the different energy shifts of the levels as shown in the right graph of figure 1.

The right graph in figure 3 shows the effective absorption edges for TE and TM polarization as

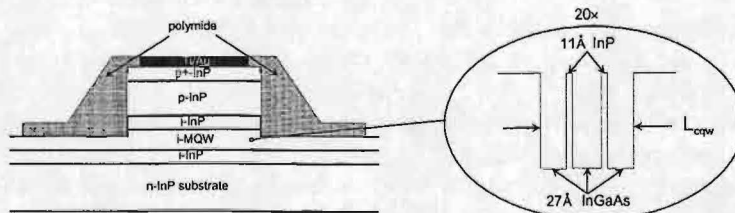


Figure 2: A cross-sectional view of the modulator structure.

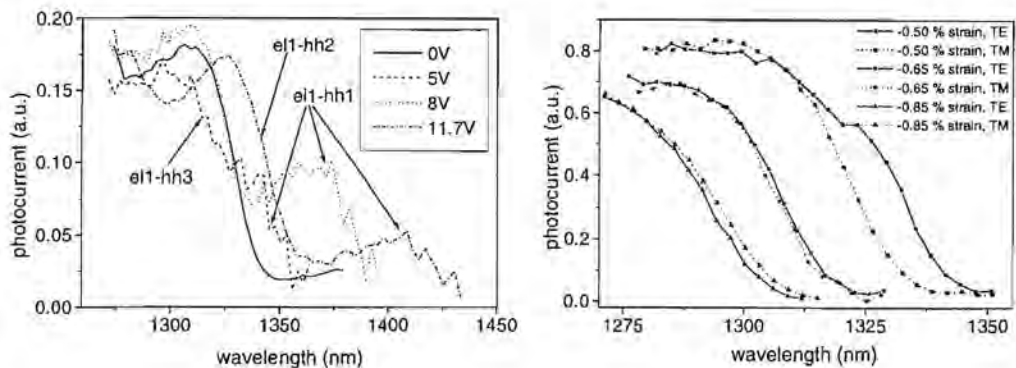


Figure 3: Photocurrent measurements of the chopped quantum well samples. **Left:** photocurrent measurements of the -0.5% strained sample under applied bias. **Right:** cleaved side photocurrent measurements with TE and TM polarized light on samples with 0.5%, 0.65% and 0.85% tensile strain.

obtained by cleaved-side photocurrent measurements at 4K. We observe a strain dependence of the relative positions of the absorption edges for TE and TM polarized light. Below 0.70% tensile strain the TE absorption edge lies at a higher wavelength than the TM absorption edge. This is caused by the lower confinement energy of the heavy hole than the light hole and by the fact that TM polarized light couples only with the electron to light hole transitions [4]. At tensile strain of 0.70% the heavy hole and the light hole levels are degenerated. At even higher strain the absorption edge is light hole dominated. Consequently, we expect polarization independent switching slightly above 0.70% tensile strain.

We have realized MZI-switches employing CQW-material. The switch with 0.65% tensile strained CQW's shows a waveguide propagation loss of 3.8dB/cm and 2.5dB/cm for TE and TM, respectively at 1.55 μ m. This is comparable with the propagation loss of undoped waveguides without CQW's.

In figure 4 switching curves at 1.55 μ m are shown for switches with 4mm long phase shifting sections. A switching voltage of 3.1V and a cross-talk of 16.5dB are observed for the -0.65% strained switch. Operating the switch with a constant bias of 3.1V applied to the phase shifting section reduces the switching voltage to 2.2V, but also increases the crosstalk. This is caused by attenuation in one of the arms of the switch due to electro-absorption.

The right graph of figure 4 shows the polarization independent switching curves of 0.85% tensile strained CQW's showing identical switching voltages within 0.1V. The curves have been vertically scaled for clarity.

Using an InGaAs/InP chopped quantum well we designed an efficient and polarization independent phase shifting section. The chopped quantum well material design combines a bandgap at 1390nm, required for low loss wave-guiding, with 110Å well width needed for an optimal quantum confined Stark effect (QCSE). Measurements of the propagation losses of straight waveguides show indeed acceptable propagation losses. Red shifts as high as 80nm at 10V due to the

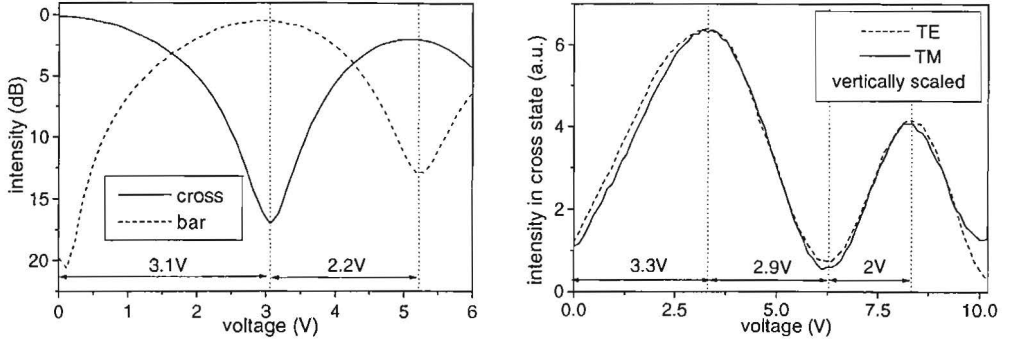


Figure 4: **Left:** switching curves for the -0.65% strained modulator in logarithmic scale. **Right:** vertically scaled switching curves for the -0.85% strained sample in TE and TM polarization.

quantum confined Stark effect are measured. The present design shows switching voltages of 3.1V without applied bias and 2.2V with 3.1V applied bias for 4mm long phase shifting sections. The InGaAs/InP chopped quantum well design shows polarization independent switching voltages within 0.1V for -0.85% applied strain.

References

- [1] H. Temkin, D. Gershoni, and M.B. Panish. InGaAs/InP quantum well modulators grown by gas source molecular beam epitaxy. *Appl. Phys. Lett.*, 50(25):1776–1778, June 1987.
- [2] D.A.B. Miller J.S. Weiner and D.S. Chemla. Quadratic electro-optic effect due to the quantum-confined Stark effect in quantum wells. *Appl. Phys. Lett.*, 50(13):842–844, March 1987.
- [3] T.Y. Wang and G.B. Stringfellow. Strain effects on $\text{Ga}_x\text{In}_{1-x}\text{As}/\text{InP}$ single quantum well grown by organometallic vapor-phase epitaxy with $0 \leq x \leq 1$. *J. Appl. Phys.*, 67(1):344–352, January 1990.
- [4] G. Bastard. *Wavemechanics applied to semiconductor heterostructures*. les éditions de physique, 1988.

Selective Photoluminescence of Self-Assembled Quantum Dots

A.W.E Minnaert, A.Yu. Silov, W. van der Vleuten, J.E.M. Haverkort, J.H. Wolter
Cobra Inter-University Research Institute, Eindhoven University of Technology
P.O. Box 513, 5600 MB Eindhoven, The Netherlands

We observe a continuous transition from an inhomogeneously broadened photoluminescence line into strong phonon-replica dominated PL-lines under selective excitation of Self-Assembled Quantum Dots (SAD's). Excitation above the InAs-wetting layer allows for carrier thermalization inside the wetting layer. The subsequent capture into SAD's of different sizes explains the inhomogeneously broadened line. Direct excitation into the SAD's shows narrow PL bands at one and two LO-phonon energies below the laser line which seems to be in contradiction with energy conservation since the level spacing is generally not equal to the optical phonon energy within a quantum dot. The observed spectrum can only be explained by assuming strong electron phonon coupled processes in dots.

Introduction

Spontaneous 3D-island formation during molecular-beam epitaxy (MBE) of highly strained InAs/GaAs is known as Stranski-Krastanov growth. These self-assembled semiconductor quantum dots show strong zero-dimensional confinement (0D) of carriers in high quality, defect-free material^{1,2}. SAD samples show a very strong photoluminescence, which is in contradiction with the prediction of the (optical) phonon bottleneck³. The phonon bottleneck would strongly restrict luminescence because the interlevel spacing in the dots is generally not equal to the optical phonon energy thus prohibiting relaxation between discrete energy levels by LO-phonon emission. Experimentally however, strong phonon assisted interband transitions have already been observed in several papers⁴⁻⁹. A possible explanation for these strong LO-phonon assisted interband transitions is a strong electron-phonon coupling in quantum dot structures^{5,8}.

In this paper we present the results on the recovery of the broadened PL-peak and discuss the origin of the very strong phonon assisted transitions seen under selective excitation of the dots.

Sample

The self-assembled quantum dots are grown on an exact oriented [001] CrO-doped GaAs substrate. After a buffer layer of GaAs is grown, the temperature is dropped to 555 °C and 2.0 ML's InAs are deposited. At this layer thickness we exceed the critical layer thickness for InAs and so the InAs growth will change from pure two-dimensional growth to 3D growth. The SAD's are then overgrown with a GaAs cap-layer in which we rise the temperature to 760 °C. Within this top layer we insert an AlGaAs window layer to prevent any surface electrical field.

Experiment

For the photoluminescence experiments we used a tunable Ti-Sapphire laser (760-1020 nm) pumped by an Ar^+ laser. With this lasers system we can excite both resonant and non-resonant photoluminescence. For a non-resonant PL-spectrum we tuned the Ti-Sapphire laser above the bandgap of GaAs (1.61 eV). This spectrum is shown in figure 1 (dotted line). As can be seen it is a very broad peak around 1.311 eV with a full width at half maximum of ± 50 meV. This broadening has been observed by many others and is ascribed to inhomogeneous broadening due to the size-distribution of the quantum dots. The spectrum of a single quantum dot yields a very narrow PL line (0.6 meV) as is observed in micro-PL^{10,11}. The broad peak reflects the size distribution of the dots. Since we excite above the bandgap of the wetting layer which is connecting all the dots, carriers can first thermalize inside the wetting layer and can subsequently be captured into the SAD's by LO-phonon emission. In this way, dots of all sizes are populated and contribute to the broad PL-line.

If the Ti-Sapphire laser is tuned within the broad PL-line described above and a so called resonant photoluminescence experiment is performed a completely different spectrum is observed as shown in figure 1 (solid line). We observe two narrow PL-bands at a distance of 34.5 ± 0.5 meV and 68.9 ± 0.5 meV below the laser-line, indicating strong phonon assisted transitions.

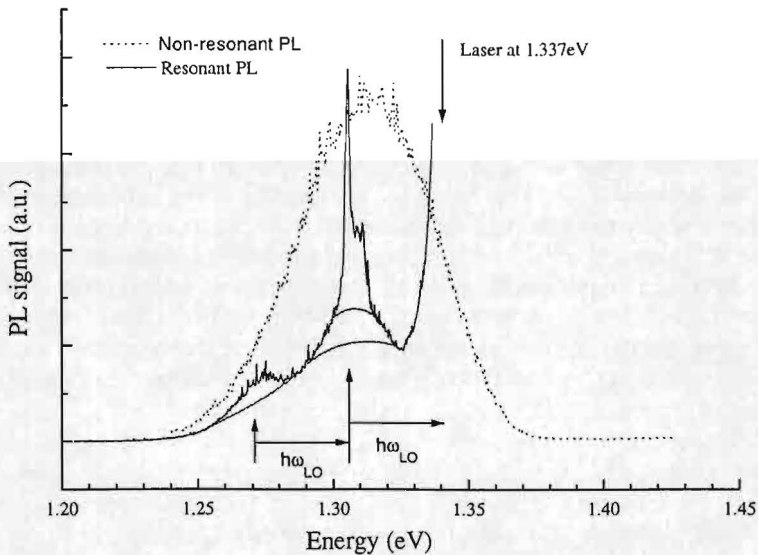


Fig. 1. Non-resonant PL spectrum (dotted line) and a resonant PL-spectrum (solid line) with excitation of the dots at 1.337 eV. For the resonant spectrum two broadened feature at one and two LO-phonon energy below the laser line are observed

This resonant PL-experiment is repeated for different excitation energies across the non-resonant PL-peak as shown in figure 3. We observe that the distance between the two peaks and the laser-line stays the same. In addition, we observe the recovery of the broad photoluminescence line below the two resonant features.

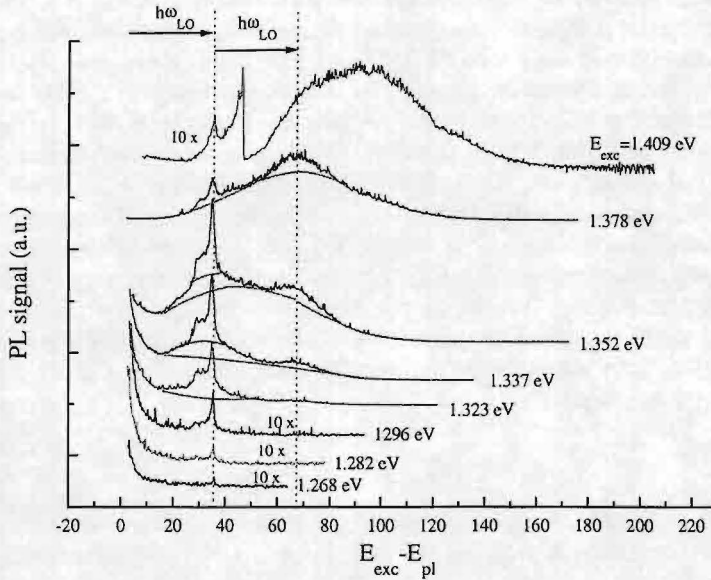


Fig. 2. PL spectra obtained for different excitation energies across the non-resonant PL line.

The recovery of the broad PL-line is due to excitation into the wetting layer. The absorption spectrum of the wetting layer as observed in PLE is quite broad and its low energy tail extends to 1.345 eV. If we excite into the wetting layer, carriers can be captured by a all dots again and the non-resonant photoluminescence will start to come up again. The intensity of this recovery will depend on the fact how high we are exciting into the wetting layer, since the higher we pump the more dots can be populated.

We now turn our attention to the two broadened features at 34.5 ± 0.5 meV and 68.9 ± 0.5 meV below the laser. The height of these resonant bands is proportional to the height of the non-resonant PL-line which means that we are not dealing with Raman-lines. If we look more carefully to the first resonant band we can split it up into three feature, a broad pedestal at 34.5 meV, like the second resonant band at 68.9 meV, with on top a sharp peak at 35.1 meV (GaAs LO-phonon energy) and a broadened shoulder at 31.5 meV (the InAs LO-phonon energy in a dot). The second resonant band is different from the first one since we do not observe any additional feature on top of it. The second band is broadened by 10 meV FWHM, like the first pedestal. It can not be interpreted as a side band of the first one since it disappears if we excite at the low energy tail of the non-resonant PL-line.

Discussion

In the remainder, we will discuss a few possible mechanisms for the non-resonant photoluminescence bands. First, since the heights of the resonant peak are proportional to the height of the non-resonant PL spectrum as mentioned above, we interpret these peaks as "photoluminescence peaks" and not "Raman peaks". Additional evidence that these peaks are not "Raman peaks" is the broadening and the observed pedestal. For similar reasons, these peaks can also not be interpreted as phonon replica's. Secondly it should be stated that it is very unlikely that the optical phonon energy happens to coincide with the intersubband spacing within a SAD for each excitation energy. In other words, the resonant photoluminescence seems to be in contradiction with the existence of a phonon bottleneck as mentioned earlier. A possible explanation is strong electron-phonon coupling inside the SAD's, which consists of two major mechanisms. The first one is Fröhlich, or polar, interaction. If an exciton is brought into a dot it will polarize the surrounding matrix since the electron and hole distribution in a SAD do not overlap. After the exciton recombination, the matrix will depolarize by emitting LO-phonons. The second one is the rippling mechanism^{12,13}. This coupling results from a time varying modulation of the interface. Previously considered only for acoustical phonons, it also has to play a significant role in coupling to the optical modes since this type of exciton-phonon coupling does not vanish in quantum dots due to the mixing of the heavy and light holes as shown in ref. 5.

Conclusions

We observed a clear transition from a inhomogeneously broadened photoluminescence peak from SAD's under non resonant excitation into phonon-replica dominated PL-lines as soon as we excite the dots resonantly. The recovery is due to excitation into the wetting layer. Carriers in the wetting layer can be captured by dots of all different sizes resulting in the non-resonant photoluminescence peak. The resonant bands observed are due to a strong electron-phonon coupling by a combination of two mechanisms; Fröhlich interaction between the polarized exciton and the lattice and the rippling mechanism.

References

- 1 D. Leonard *et.al.*, J. Vac. Sci. Technol. B12, 2516, (1994), D. Leonard *et.al.*, Appl. Phys. Lett. 63, 3203, (1993)
- 2 G. Wang *et.al.*, Appl. Phys. Lett. 64, 2815, (1994)
- 3 H. Benisty *et.al.*, Phys. Rev. B51, 13281, (1995), U. Bockelmann, Phys. Rev. B48, 17637, (1993), U.
- 4 M. Grundmann *et.al.* Supp. And Microstruc. 19, no.2, , 81, (1996)
- 5 A.V. Fedorov *et.al.*, Phys. Rev. B56, no.12, 7491, (1997)
- 6 S. Fafard *et.al.*, Phys. Rev. B52, no.8, 5752, (1995)
- 7 B. R. Bennett *et.al.*, Appl. Phys. Lett. 68, no.7, (1996)
- 8 T. Inoshita *et.al.*, Phys. Rev. B56, no.8, R4355, (1997)
- 9 R. Heitz *et.al.*, Appl. Phys. Lett 68, 361, (1996)
- 10 J.-Y. Marzin *et.al.*, Phys. Rev. Lett. 73, 716, (1994)
- 11 M. Notomi *et.al.*, Phys. Rev. B53, 15743 (1996)
- 12 P.A. Knipp and T.L. Reinecke, Phys. Rev. B52, no.8, 5923, (1995)
- 13 P.A. Knipp and T.L. Reinecke, 22nd I.C.P.S. Vol.3, 1927, (1996)

An improved polarisation independent switch

D.H.P. Maat, Y. Zhu, C.G.M. Vreeburg ², F.H. Groen, H. van Brug,
H.J. Frankena, I. Moerman ³

Research Group for Optics
Department of Applied Physics
Delft University of Technology
P.O.Box 5046, 2600 GA Delft, The Netherlands
Fax: +31 152788105; Phone: +31 152781444
E-mail: maat@optica.tn.tudelft.nl

² Department of Electrical Engineering
Delft University of Technology, Delft, The Netherlands

³ Department of Information Technology (INTEC)
University of Gent-IMEC, Gent, Belgium

An improved polarisation independent switch is presented. Polarisation independence is achieved by balancing the TE/TM electro-optical effects using a switch angle of 28° with respect to the $[1\bar{1}0]$ direction.

I. Introduction

In a wide range of opto-electronic integrated circuits (OEIC's), like switch matrices, reconfigurable add-drop nodes and optical cross-connects, the space switch is a key component. One of the most important requirements for these OEIC's is polarisation independent operation since the fibre network does not maintain the state of polarisation.

For the InP-based electro-optical space switches presented here, polarisation independence has been achieved in different ways. Firstly, by using carrier induced (polarisation independent) electro-optical effects through n-doping of the light guiding layer [1]. In this way most of the polarisation dependence of the switch can be removed [2,3]. Secondly, by placing the phase shifting sections of the switch under an angle. In this case the polarisation dependent electro-optical effects can be balanced resulting in the removal of the remaining part of the polarisation dependence of the switch.

The switches have been successfully integrated with a wavelength demultiplexer in an optical cross-connect [4].

II. Design and production

Our switch is of the Mach-Zehnder interferometer (MZI) type (Fig. 1). It consists of two MMI couplers which act as 3 dB splitting and combining sections and two, 2 mm long, phase shifting sections in between. Switching from the cross state to the bar state is obtained by reverse biasing the pin-diode in one of the phase shifting sections

up to the switching voltage. To have electrical insulation between the two phase shifting sections, the waveguides between the phase shifting sections and the MMI's are etched down to the pn-junction. The proper orientation of the phase shifting sections is introduced by placing the entire structure under an angle, including the MMI's. In this way the symmetry between the branches, as observed in the unrotated switch, is maintained.

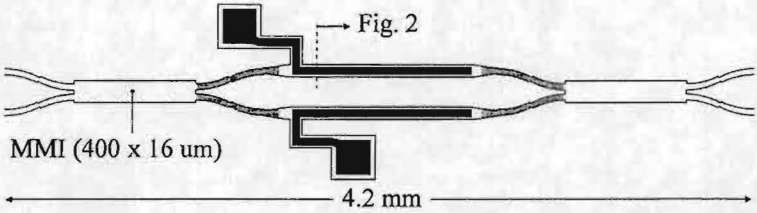


Fig. 1 Schematic layout of the switch. The black areas represent the metal contacts on top of the waveguides, the grey areas represent the lowered ridges for electrical insulation between both phase shifting sections.

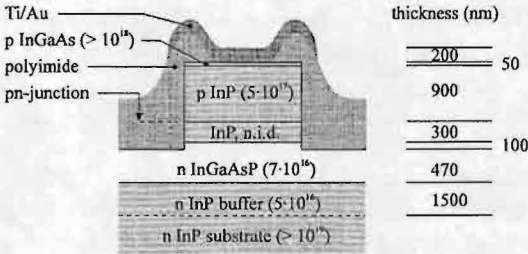


Fig. 2 Cross section of the phase shifting sections (doping levels are given in cm^{-3}).

The InGaAsP/InP/InGaAs layer stack was MOVPE-grown on a (001) oriented n^+ substrate. The thickness and doping level of the various layers can be found in Fig. 2. The waveguiding pattern is defined using contact UV exposure with positive photoresist and is transferred into a 100 nm (PECVD) silicon-nitride layer using a CHF_3 reactive ion etch process. The waveguiding structure is realised employing an optimised $\text{CH}_4\text{-H}_2/\text{O}_2$ RIE/descum process. After removal of the silicon-nitride, metallisation windows are defined in polyimide, that is also used to passivate the pn-junction. The final production step is to place Ti/Au contacts on the phase shifting sections using vacuum evaporation and a lift-off technique.

III. Description of the experiment

As already mentioned, the switch can be made polarisation independent using two methods: *proper doping* of the guiding layer and the *correct orientation* of the phase shifting sections of the switch.

At the *proper* (n) *doping* level, given in Fig. 2, polarisation independent carrier induced electro-optical effects are introduced. This results in a relative reduction of the polarisation dependent electro-optical effects, thus, it makes the switch more polarisation independent [3]. At higher doping levels light absorption increases rapidly, which makes it unfavourable to increase the doping level. Apart from this, the doping of the film has two more advantages. In the first place, higher electro-optical effects will result in a lower switching voltage and/or a shorter switch. Secondly, at the doping level mentioned, the switching voltage is less sensitive to deviations from this doping level, which results in a more stable switch.

Switching voltages of switches having an optimal doping level of the film are 6.5 V for TE and 7.5 V for TM polarisation [2,3]. Total polarisation independence can be obtained by using an additional method: *correct orientation* of the phase shifting sections of the switch [5]. In this method one uses the orientation dependence of the polarisation dependent electro-optical effects to balance them. For the linear electro-optical effect (Pockels effect), which only affects TE polarised light, it is known that the refractive index change for light propagating in the $[1\bar{1}0]$ direction is raised while for light propagating in the $[110]$ direction the refractive index change is lowered. For light propagating in the $[1\bar{1}0]$ direction the electro-optical effect is stronger for TE polarisation than for TM polarisation. For light propagating in the $[110]$ direction it is the other way around. From this the conclusion can be drawn that at a direction between the $[1\bar{1}0]$ and the $[110]$ directions, there is a direction at which TE and TM electro-optical effects are equal. In addition to the Pockels effect more electro-optical effects are responsible for polarisation dependent behaviour of the switch like the quadratic Franz-Keldish effect. Since the behaviour of these effects as a function of the switch angle is unknown, an experiment should be performed to find the proper angle for polarisation independent operation.

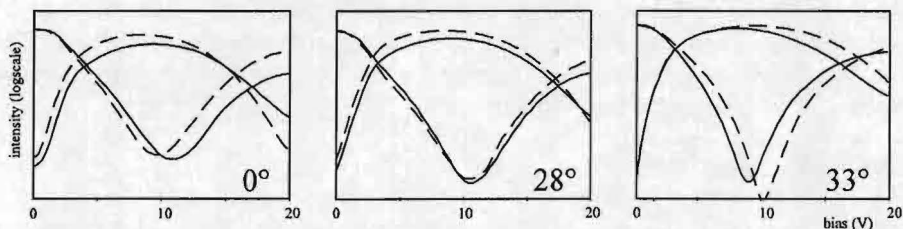


Fig. 3 Switching curves for both TE (dashed) and TM (solid) polarisation of switches under an angle of 0° , 28° and 33° with respect to the $[1\bar{1}0]$ direction.

IV. Measurement results

Switches under a variety of angles have been produced on a single chip. Measurements were performed at a wavelength of $1.55 \mu\text{m}$ using microscope objectives for coupling light into and out of the switch-waveguides. The results of these measurements are given in Fig. 3 and Fig. 4. Both figures show that polarisation independent operation is obtained for a switch under an angle of 28° or -28° with respect to the $[1\bar{1}0]$ direction. Fig. 4 shows two unexpected features. Firstly, the 28° and -28° switches show different switching voltages of resp. 10.4 V and 7.6 V. Secondly, the TM switching voltage shows an angle dependence.

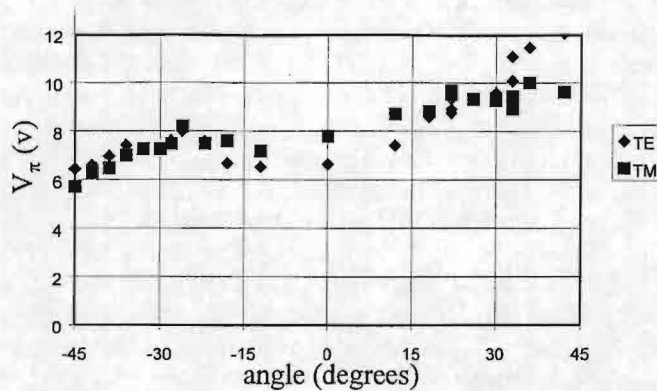


Fig. 4 Switching voltage as function of switch angle (switch angle given with respect to the $[1\bar{1}0]$ direction)

Both could be explained by variations in the layerstack and/or the presence of a series resistance. The crosstalk level of the polarisation independent switch is -14 dB, which is much higher than the crosstalk level of the unrotated switch [2,3] (-20 dB). The higher crosstalk is caused by deviations in the shape of the MMI's due to a bad waveguide lithography.

V. Conclusions

A polarisation independent switch is reported. In this switch polarisation independence is obtained by using both a proper doping level of the film and by placing the switch under an angle of 28° with respect to the $[1\bar{1}0]$ direction. The switch shows low switching voltages of 10.4 V and 7.6 V for switches resp. under 28° and -28° with respect to the $[1\bar{1}0]$ direction.

VI. References

- [1] J.F. Vinchant, J.A. Cavailles, M. Erman, P. Jarry and M. Renaud, 'InP/InGaAsP guided-wave phase modulators based on carrier-induced effects: theory and experiment', *Journ. Lightw. Techn.*, Vol. 10 (1), pp. 63-69, 1992.
- [2] T. Uitterdijk et al., 'Integrable Polarisation Insensitive InGaAsP Mach-Zehnder Switch', *Integrated Photonic Research*, vol. 6, 1996 OSA Technical Digest series, pp 486-489.
- [3] T. Uitterdijk, Integrated Electro-Optical Switches on InP, PhD Thesis, Delft University of Technology, 1997, ISBN 90-9010549-2.
- [4] C.G.P. Herben et al., 'A Compact Integrated Single PHASAR Optical Crossconnect on InP', *Proceedings of 1997 IEEE/LEOS Symposium, Benelux Chapter*, 1997.
- [5] R. Krähenbühl, R. Kyburz, W. Vogt, M. Bachmann, T. Brenner, E. Gini and H. Melchior, 'Low-Loss Polarisation-Insensitive InP-InGaAsP Optical Space Switches for Fiber Optical Communication', *IEEE Phot. Techn. Lett.*, Vol 8 (5), pp 632-34, 1996

Optical information processing in Massively Parallel Processing

E. E. E. Frietman

Dept. of Applied Physics, Delft University of Technology, Lorentzweg 1
2628 CJ, Delft, the Netherlands

Abstract

Communication in Massively Parallel Processing is carried out by distributing the aggregate data, arranged as an optical image, through free space to all the nodes simultaneously. The matching High Performance Processing & Networking subjects of discussion are addressed.

Keywords: free space optical image distributor, fully connect network topology, scalability

Preamble

Massively parallel, distributed-memory oriented, architectures are the primary target machines for *Grand Challenge* applications, like weather forecasting and satellite-collected image analysis. Such machines, incorporating 2^p ($6 \leq p \leq 16$) nodes, must provide for teraflops of computational power in processing trillions of data points and handling terabytes of data. In designing such systems, obstacles are caused by difficulties to come up with solutions that guarantee efficient communication by way of a direct or a switched network - the properties of which are determined by the topology, the complexity, the routing control and its ability to be partitioned - and are not induced by the all the time increasing improvements in speed of future microprocessors. Unfortunately large concentrations of nodes suffer from communication congestion. This phenomenon, known as the von Neumann bottleneck, is caused by a bus contention as busses line up the processed data when distributing data among the nodes.

A contemplative analysis of future to be developed massively parallel processing (MPP) systems was performed. The outcome of this reflection, taken the blue-print of a fully connected multiple-instruction, multiple-data organized system (known as the Delft Parallel Processor: DPP) as a starting-point, rendered an account of the network and its prospects of scalability related to the number of nodes. To forestall the constraints of communication in such an architecture, communication is not carried out by guiding the information through individual channels but by distributing the aggregate data, arranged as an optical image, through free space to all the nodes simultaneously. To accomplish this optics implied parallelism is put into practice in exploring optical interconnects (OIs) at a crate-to-crate, node-to-node, chip-to-chip or gate-to-gate level.

This paper briefly discusses the features of the different building stones of a free space oriented image distributing system, suitable to be implemented in an architecture incorporating a large number of independent performing computing nodes (CNs).

Bottlenecks of a conventional computer system

A characteristic feature of a conventional von Neumann computer is that computing power is delivered by a single computing unit. Although increasing the clock frequency improves the performance of the computer, the switching speed of the semiconductor devices and the finite speed at which electrical signals propagate along the bus set the boundaries.

Architectures containing large numbers of nodes can solve this performance dilemma, providing that there is a suitable network. While structures with complexity $O\{N\}$ - the costs of which increase linearly with the number of nodes - can be found at the low-end, high-end's offer schemes of complexity $O\{N \log(N)\}$.

In considering actual implementations; a classical example of a switched network is the crossbar with $2N$ busses and N^2 switches that allows a parallel transmission of N messages at best. Owing to its high costs the crossbar is applied for low values of N .

Its opposite is a direct network without switches. Separate from problems to realizing such a *fully connect* scheme electrically, it can be altered into any other topology of which one-to-many and many-to-one schemes can be derived. A second aspect is that the bisection bandwidth grows proportionally with the number of nodes N , but at the cost of an increase of the number $\{N \times (N-1)\}$ of links. The numbers become even worse when the width of the computer word P is allowed for, i.e. $\{P \times N \times (N-1)\}$.

Features of a Massively Parallel Processing architecture

The block diagram at the end of this paper shows the various components of a *Fully Connect Parallel Processor System* (FCPPS), that put together an MPP system. While a *fully connect* topology is explored for considerations of manipulating terabytes of data, only a configuration for $N = 9$ and $P = 64$ bits is discussed. A photograph of the 1-to-9 prototyped optical backplane

(known as the Kaleidoscope) is shown in the middle; its future 1-to-32 successor is drawn at the upper right corner. Following these starting-points there are 5,184 (64×9×9) links involved in processing a 24-by-24 (64×9) sized data array. Inseparable to the *fully connect* network is the ubiquitousness of the array of information, the contents of which is put together by the outputs of all the nodes. A photograph of a 7-by-7 array result is shown at the top left. Nine replica's of the original combination of outputs, located at the center, are shown on the outside of the image plane. The lower right corner, reflecting the principle of an electrical-to-optical converter, gives an impression of a future to be developed byte-wide optical buffer. There are eight of these devices required to process a 64 bit computer word. The lower left corner demonstrates the qualities of a Parallel Optical Write, Electrical Read Multi-port, multi-Access cache Memory (POWERMAM) that exploits optics implied parallelism in simultaneously processing the 24-by-24 pixel-array of information. The number of opto electronic logic elements in such a Photonic Integrated Circuit (PIC) scales with the total number of nodes and the width of the computer word. A bipolar as well as a CMOS version of a Random Access and Content Addressable Memory PIC were prototyped. The overall data throughput rate achieved was 0.025 Gb/s/link and 0.5 Gb/s/link respectively. The data throughput rate in case of 5,184 links resulted in 2,592 Gb/s.

Qualities of a fully connect network

To come to the development of a prototype of an *optical backplane*, both transparent and reflective technologies were explored. Faceted optics, in which a single ray of light is divided into multiple beams (this way performing a 1-to- N broadcast) is commercially available because of improvements of diamond fly cutting techniques. Among the facet geometry's are the *pyramid*, the *pentagon* and the *hexagonal polycone* respectively producing a focal spot array of four, five and six spots. Unfortunately, such a solution is not suitable for distributing an array of 24×24 data pixels. Simulations with CODE V, to finally design a prototype of the Kaleidoscope, evaluated the resolving capabilities of the optical system. CODE V is a registered trademark of Optical Research Associates at Pasadena, California.

Multiple imaging is obtained by dividing the collimated beams from a 24-by-24 sized data array object into separate bundles by means of refocussing the information with separate lenses or with a multi-facet mirror or prism. Together with the Optics group of the Institute of Applied Physics at Delft, a prototype was constructed consisting of a standard off-the-shelf Mamiya lens objective, an optical rail system supporting the mechanical construction and a facet mirror with nine facets. The fiber bundle at the center forms the object plane. The other nine bundles distribute a replica of the complete image back to the POWERMAMs on the nine nodes. During experimenting a 50×50 pixel array could not be clearly distinguished by the eye because of the coarse scattering regions on the circular glass screen. The degree of parallelism (the maximum number of spots in the array) that can be achieved with this Kaleidoscopic prototype is limited by the image quality through optical aberrations in the lens system. An increase of the number of facets on the mirror to broadcast to more than nine outputs restricts the optical aperture and lowers the imaging resolution.

Scalability by means of the Kaleidoscope

Scalability is the ability of a computing system to scale from a few to a large number of nodes with only marginal changes in the existing system configuration. In considering the available power budget and yet fully utilizing free space imaging techniques, either a single Kaleidoscope is implemented that provides for a large fanout or multiple (identically designed) small sized Kaleidoscopes are cascaded to compose a data distributing system of same magnitude.

The first possibility appears to be impractical due to the cumbersome manufacturing of a large-scale facet mirror. In other words it would be easier to design a 1-to-32 device than a 1-to-1024 alternative at one piece.

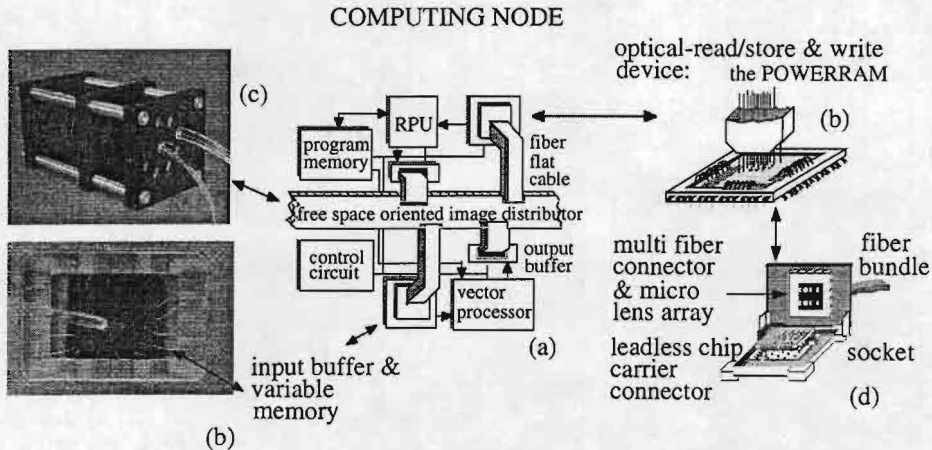
When cascading, this way enabling the distribution of 1024 64-bit words to 1024 nodes, a single 1-to-32 sized Kaleidoscope divides a data array of 256×256 pixels over a second layer containing thirty-two of these identical devices. The bottleneck would still be the net optical gain of the flux budget, the result of which has to produce enough radiant power to change the conditional state of a photonic integrated circuits, such as the POWERMAM. High powered lasers could solve the problem to a certain extent, but introduce the bottleneck of excessive dissipation.

Interaction between the Photonic Integrated Circuit and the Kaleidoscope

This paper only illustrates solutions where each node performs its I/O activities through a low latency designed output port and a massively parallel accessible input port. The final goal is to adapt the node's structure (illustrated but not described in detail) to simultaneously process the information of all the nodes, with a special emphasis on the input device, because it is the only place where optics implied parallelism can be maintained up to the level of electronics within the node.

The figure shows our vision (See reference 3 for more detailed information) of a future to be developed node, here indicated by item (a), in case OIs are implemented in future MPPs. In this design, each node contains one or more processors (only one vector processor is shown), a program memory that stores the programs to be executed, a routing or communication processor unit (RPU) that directs data and program streams from and to the optical image distributor, and an output buffer that delivers the optically transformed results through a 64-channel wide multi-mode fiber ribbon to the free space oriented image distributor, here indicated by item (c).

A second set of multi-mode fiber ribbons leads the 24×24 rays of information from the image distributor to the surface of the PIC.



A distributed multi-port, multi-access cache architecture.

The PIC, here indicated by item (b), consists of a 2-dimensional array of simultaneous accessible opto electronic logic elements [for detailed information, see references 1, 2, 3 & 4]. Only a single (optically) read, (opto-electronically) store and (electrically) write action is required to fetch the information from all the nodes involved and next placing it to the disposal of the various microprocessors within the node. The technology of exploiting the space on top of the PIC also solves the pin limitation problem.

Conclusions

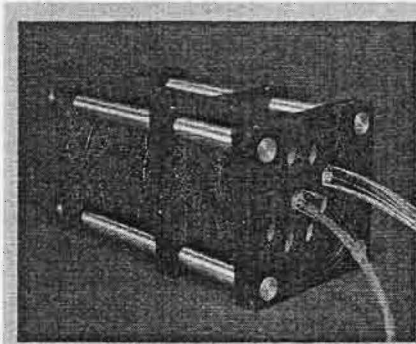
Electronic backplanes will probably fail to meet the necessary interconnect densities for large scale computers, but optical techniques appear to hold promise. So studying interconnect requirements for node-to-node level applications, particularly at the massively parallel processor level, comes down to efficiently exploring and exploiting optics implied parallelism. Notwithstanding the promises, the success of optical interconnects for massively parallel processors depends strongly on the advances of electro-to-optic devices in delivering sufficient power, the choice of the network topology in handling large amounts of data simultaneously and the requirements for the sensitivity of the opto-to-electronic element to performing its conversion at high throughput rates.

References

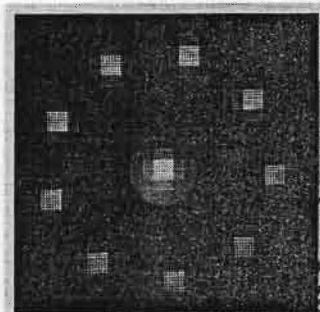
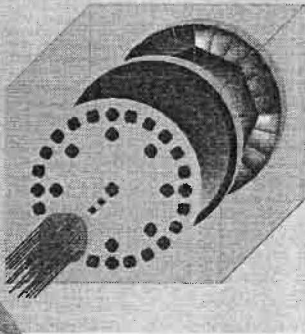
- [1] Frietman, E.E.E., W. van Nifterick; Opto-electronic IC's for High-Speed Parallel Processing; LASER & OPTRONICS, Las Vegas, Nevada, U.S.A., August 1987, pp. 69-72.
- [2] Frietman, E.E.E., W. van Nifterick, L. Dekker, Th.J.M. Jongeling; Parallel Optical Interconnects: implementation of Optoelectronics in Multi-Processor architectures; Applied Optics, Special Issue of Applied Optics on Optical Interconnections, Vol. 29, No. 8, March 1990, pp. 1161-1177.
- [3] Frietman, E.E.E.; *Opto-Electronic Processing & Networking: A Design Study. Perspectives of Optical Interconnects in Massively Parallel Processing*. Research Monograph: ISBN 90-900 8690-0, November 1995, 315 pages.
- [4] Frietman, E.E.E., G.D. Khoe, L. Dekker; Optical-read/store & write devices: alternatives for the pin limitation problem. Proceedings of HPCS'96. The 10th Annual International Symposium on High Performance Computers, Ottawa, Canada, June 5-7, 1996, on CD-ROM ISBN 0-88629-301-4.

Building stones for exploring Optical Interconnects

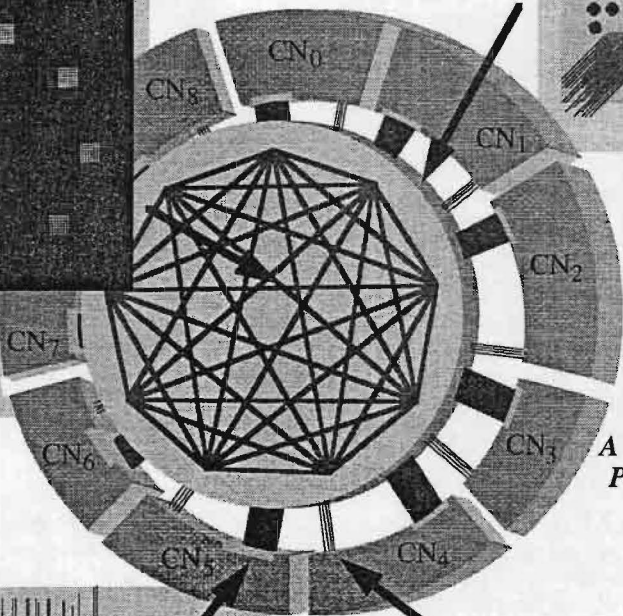
N : number of nodes
P : width of computer word



A 1-to-N nodes image distributor
Reality N \Rightarrow 9
Future N \Rightarrow 32

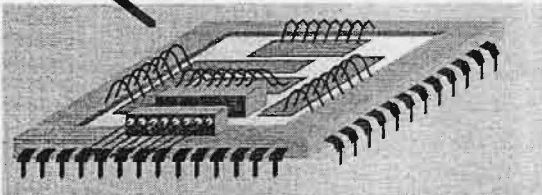
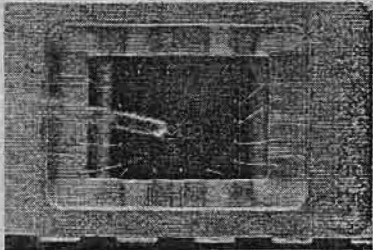
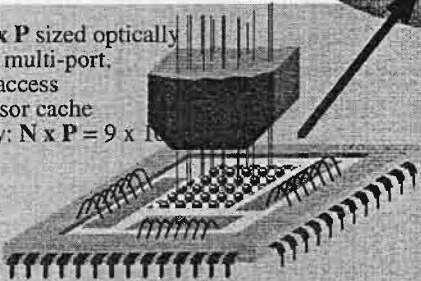


An $N \times P$ sized array of pixels

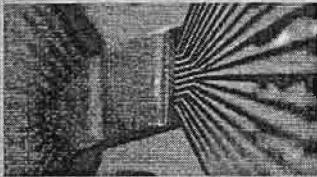


A "Fully Connect" Parallel Processor System

An $N \times P$ sized optically driven multi-port, multi-access processor cache
Reality: $N \times P = 9 \times 16$



A byte-wide Optical buffer (Future)



Integration of Optical Amplifiers and Waveguide Devices on InP

P.J. Harmsma[&], C.G.M. Vreeburg[&], C.A. Verschuren*, M.R. Leys*, H. Vonk* and Y.S. Oei[&]

COBRA Interuniversity Research Institute

[&]Delft University of Technology, Faculty of Electrical Engineering
P.O. Box 5031, 2600 GA Delft, The Netherlands

* Eindhoven University of Technology, Department of Physics

Integration of optical amplifiers and passive waveguide devices on InP-based material is carried out by Selective Area Chemical Beam Epitaxy. On discrete amplifiers which are suitable for integration, a gain of 15 dB was measured.

Introduction

The monolithic integration of Semiconductor Optical Amplifiers (SOAs) and passive waveguide devices (PWDs) offers the opportunity to compensate for device- and coupling losses. Moreover, advanced components such as wavelength converters and multi-wavelength lasers can be realised. The integration requires the deposition of different layer structures on a single chip. This can be achieved by performing an embedded selective area regrowth step. In this case, the SOAs and PWDs can be realised in their own optimised layer stacks. We are currently working on active-passive integration by butt-joint coupling [1], using a Chemical Beam Epitaxy (CBE) regrowth step [2]. In this paper we present recent results on selective area CBE. In addition we describe the fabrication and characterisation of ridge lasers and SOAs which are suitable for integration.

Selective Area Chemical Beam Epitaxy (SA-CBE)

First step of active/passive integration using SA-CBE is the epitaxial growth of the layer structure for the PWDs. On this structure, a SiN_x layer is deposited using Plasma Enhanced Chemical Vapour Deposition (PECVD). The SiN_x layer is removed from the regrowth sections (fig. 1a), and is used as a masking layer for a deep etch through the cladding and film layers. The same SiN_x layer provides the selectivity for the following CBE regrowth step. The etched holes can be refilled with the active layer stack, resulting in butt-joined active and passive regions.

Before applying this technique for active/passive integration, a number of issues were investigated: the selectivity of the regrowth, the quality of the butt-joint coupling and the vertical misalignment of the original and regrown layer stacks. For this purpose a SA-CBE of transparent material was performed. In this way both the original and the regrown layer stack can be characterised at the operating wavelength of 1.55 μm .

SA-CBE of transparent material

In the first epitaxy an InP buffer, a 600 nm transparent InP/InGaAs Multi Quantum Well (MQW) film layer and a 300 nm InP cladding layer were successively grown on an InP substrate. After deposition and patterning of a 100 nm SiN_x layer, 1200 nm deep holes

were etched using Reactive Ion Etching (RIE). The side wall profile was tailored using wet chemical etching. Experiments showed that this is necessary to provide a high quality connection between original and regrown material. In the following regrowth step the etched holes were refilled with a 250 nm InP buffer, a 700 nm transparent InP/InGaAs MQW and a 250 nm InP cladding. The selectivity of the regrowth was optimised by careful adjustment of the growth parameters and the use of a high quality, clean SiN_x surface. Figure 1b shows a SEM picture of the butt-joint between original and regrown material. Note the high quality interface due to the tailored side wall profile. The high selectivity of the regrowth is proven by the absence of material deposition on the SiN_x .

After regrowth and removal of the SiN_x , waveguides were fabricated and characterised using Fabry Perot measurements. The butt-joint coupling loss was deduced from loss measurements of waveguides that pass through the original as well as through the regrown material. A typical coupling loss of 0.25 dB/interface was found, whereas the lowest loss of 0.1 dB/interface has been measured. The variation in measured coupling loss may be due to vertical misalignment of the original and regrown layer stacks, caused by non-uniform RIE-etch rate and CBE-growth rate.

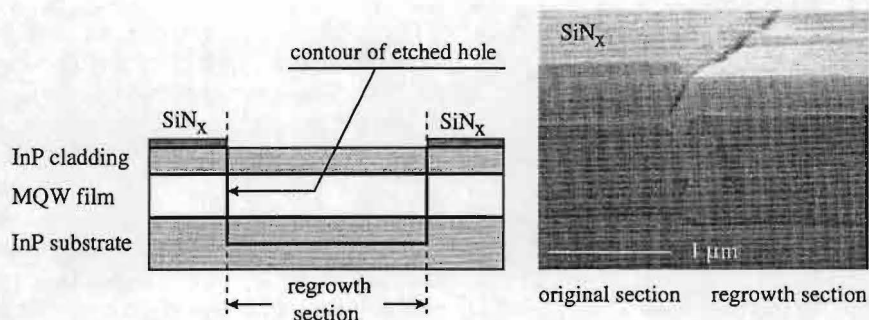


Fig. 1a: Schematic representation of SA-CBE regrowth.

Fig. 1b: SEM picture of SA-CBE regrowth.

SA-CBE on top of the film layer

At the expense of a lower confinement factor of the active layer, the vertical alignment can be facilitated by growing the active layer directly on top of the original film layer [3,4]. We have carried out this experiment on a wafer consisting of an n-InP substrate and buffer layer, a 600 nm undoped Q(1.3) film layer and an 800 nm undoped InP cladding layer. At the regrowth sections, the cladding layer was selectively removed using a wet chemical etch (fig. 2). A layer stack that is suitable for the fabrication of optical amplifiers is deposited at the regrowth sections. It consists of a 90 nm undoped active MQW layer (5 x 10 nm InGaAs well, 4 x 10 nm InP barrier), a 650 nm p-InP cladding layer and a 50 nm p^{++} -InGaAs contact layer. The SEM picture in fig. 2 shows the high quality butt-joint, indicating low reflection and high coupling efficiency. The first devices fabricated in this layer stack are being characterised at the moment of writing.

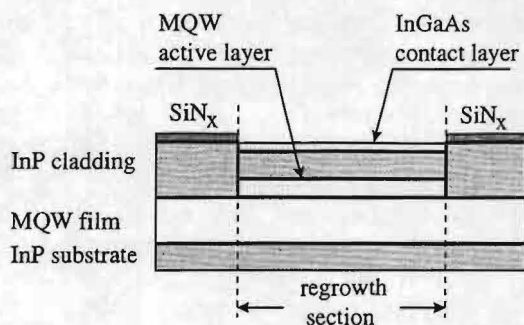
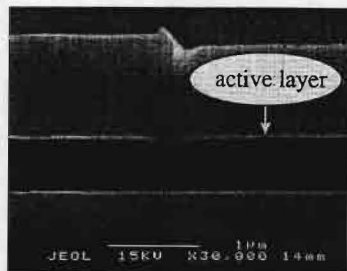


Fig. 2: SA-CBE of an active layer directly on top of the film layer.



original section regrowth section

Fig. 2b: SEM picture of resulting stack

Discrete ridge lasers and SOAs

Fabrication technology and device structure of active and passive components must be compatible for successful integration. We have fabricated discrete ridge lasers and SOAs that are suitable for integration with passive ridge waveguide devices (fig. 3). The MQW active layer consists of 5 InGaAs wells (8 nm), separated by 10 nm Q(1.25) barriers. Ridges were wet chemically etched in the V-groove direction, resulting in angled facets. This facilitates the electrical connection to a contact pad located next to the ridge (fig. 3). A 200 nm SiN_x insulation layer was deposited by PECVD, and opened at the top of the ridge to provide electrical contact to the highly doped InGaAs contact layer. The Ti/Pt/Au metallisation layer was subsequently evaporated on both sides of the wafer. Finally, samples with a typical length of 1 mm were cleaved and indium-soldered on a copper holder. This holder was mounted on a peltier element to provide temperature control.

Uncoated samples showed stable laser operation above a threshold current of 60 mA. The threshold current can be reduced by applying a high-reflection (HR) coating or by using shorter samples. A typical output spectrum is shown in figure 4. Only few longitudinal modes are present. The lasing wavelength is 1.58 μ m, whereas the structure was intended to operate at a wavelength of 1.55 μ m. Obviously the actual wells are wider than designed. At a current of 200 mA an output power of 0.5 mW was measured.

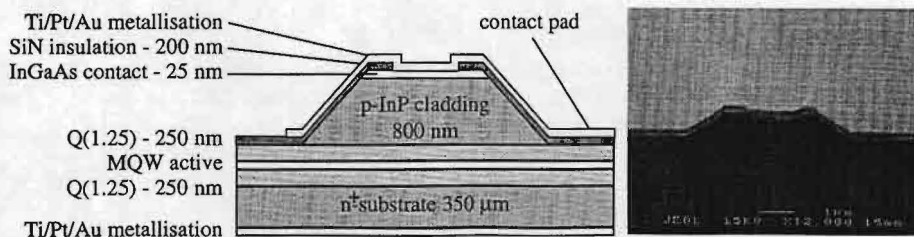


Fig 3: Device structure and SEM picture of ridge lasers and SOAs

SOAs were fabricated by anti-reflection (AR) coating of the cleaved facets. Gain measurements of SOAs were carried out using a 400 μW probe signal of 1.56 μm wavelength. The on-chip gain for various injection currents is shown in figure 5. A maximum on-chip gain of 15 dB was measured at a current of 100 mA. In this experiment the gain of the SOA is limited by two contributions:

- the residual reflection of the AR-coating, estimated to be 3%. Due to this reflection, serious gain ripple occurs at currents higher than 100 mA.
- the difference in wavelength between maximum gain and probe signal. Maximum gain is at a lasing wavelength of 1.58 μm , whereas the probe signal for the SOA characterisation is at 1.56 μm . This is the highest wavelength available in our measurement set-up.

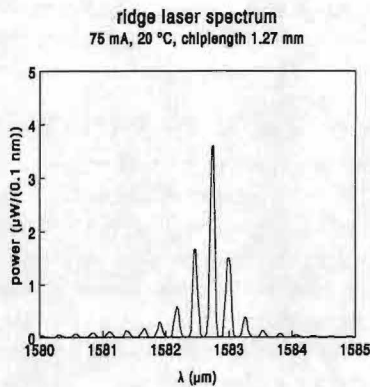


Fig. 4: Fabry-Perot spectrum of ridge laser.

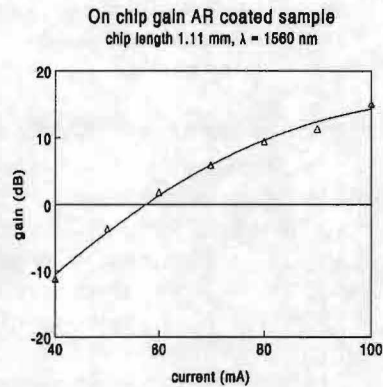


Fig. 5: On chip gain ridge SOA

Conclusions

We have carried out Selective Area Chemical Beam Epitaxy regrowth experiments. High selectivity, good vertical alignment and excellent butt-joint coupling were obtained. A typical butt-joint coupling loss of only 0.25 dB/interface was measured. Furthermore, we have fabricated and characterised ridge lasers and SOAs which are suitable for integration with passive waveguide devices. We will now focus on the fabrication of integrated SOAs and passive waveguide devices using SA-CBE.

References

- [1] A.A. M. Staring, L.H. Spiekman, J.J.M. Binsma, E.J. Jansen, T. van Dongen, P.J.A. Thijs, M.K. Smit, B.H. Verbeek, "A Compact Nine-Channel Multiwavelength Laser", *IEEE Photonics Technology Letters*, vol. 8, pp. 1139 - 1141, 1996.
- [2] C.A. Verschuren, A.S. Bloot, P. Harmsma, C.G.M. Vreeburg, Y.S. Oei, M.R. Leys, H. Vonk, J.H. Wolter, "Photonic Integration by Reactive Ion Etching and selective regrowth using Chemical Beam Epitaxy", *Proc. IEEE/LEOS Benelux Chapter, Enschede*, pp. 120 - 123, 1996.
- [3] M.G. Öberg, B. Broberg, S. Lindgren, "InGaAsP-InP Laser Amplifier with Integrated Passive Waveguides", *IEEE Journal of Quantum Electronics*, vol. 23, pp. 1021 - 1026, 1987.
- [4] G. Glastre, D. Rondi, A. Enard, R. Blondeau, "Polarisation insensitive 1.55 μm semiconductor integrated optical amplifier with access waveguides grown by LP-MOCVD", *Electronics Letters*, vol. 27, pp. 899 - 900, 1991.

Photonic IC for Electronic Radar Beam Control

J.Stulemeijer X.J.M. Leijtens I. Moerman* M.K. Smit

Delft University of Technology, Department of Electrical Engineering, TTT Laboratory, Photonic Integrated Circuits Group, PObox 5031, 2600 GA Delft, The Netherlands,
J.Stulemeijer@ET.TUdelft.nl

*University of Gent-IMEC, Department of Information Technology, Belgium

Photonic ICs offer the potential to make very compact electro-optic circuits for controlling the beam of Phased Array Antennas. Device concept and first experiments for the Photonic IC will be discussed.

Introduction

A Phased Array Antenna consists of an array of microwave antenna elements. By controlling the phase of the individual elements the direction of the antenna beam can be set electronically. In figure 1 this is illustrated for two antennas, the phase difference between antenna A and B causes the outgoing phase front to be tilted. By controlling the signal amplitudes for the different elements the shape of the antenna beam can be adjusted. In this way a fixed array of antennas can produce a very flexible microwave beam.

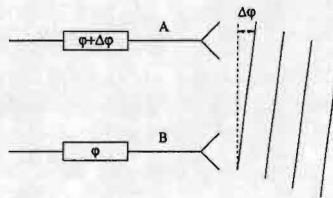


Figure 1: Beam direction using phase difference.

Currently Phased Array Antennas are built with *beam forming networks* using electronic phase and amplitude control. Many experiments have been reported using bulk optics or RF chips to process the radar signal, see for instance [1]. This paper focuses on first experiments on the integration of the beam forming in a single photonic IC, see figure 2. This chip will do the amplitude and the phase control for every antenna element. The miniaturisation will help to bring down the weight and volume of a Phased Array Antenna.

Concept

Optical ICs in our group are based on the InP/InGaAsP system, for use in the long wavelength window for telecommunication. InGaAsP has a higher refractive index than InP. An InGaAsP film with an InP cladding can act as a dielectric slab waveguide. By etching part of the cladding away, such that a ridge is left on top of the InGaAsP film, the light is guided in the horizontal plane as well. Power splitters

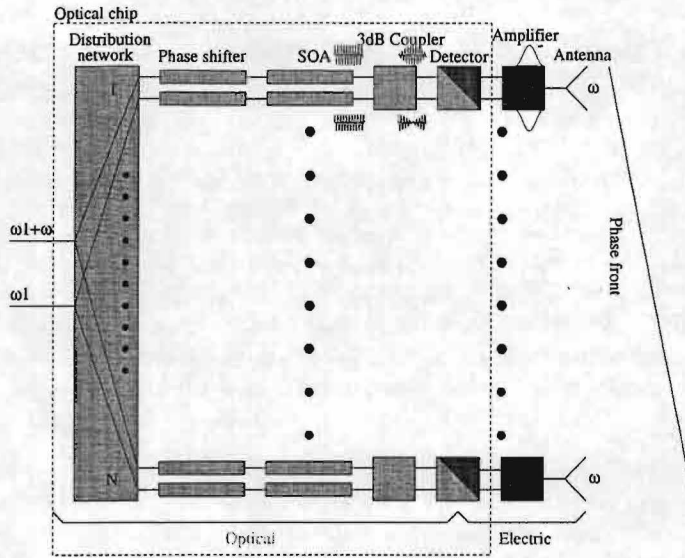


Figure 2: Schematic view of the optical control of a Phased Array Antenna.

and 3 dB couplers can be made by inserting a wide waveguide section. In this section the light will form an interference pattern. By properly choosing the width and the length of the wider section it is possible to form multiple images of the input plane at the output plane. This wide waveguide section is called a Multi Mode Interference or MMI section, for detail see [2]. Phase shifting is done by applying an electrical field over the optical waveguide such that the refractive index of the waveguide is modified. The Amplitude of the guided light can be adjusted with a Semiconductor Optical Amplifier(SOA).

For the transfer of the optical amplitude and phase information to the microwave frequency region we adopted a coherent detection scheme. In our scheme two frequency-locked optical signals with a frequency difference of 10 GHz are combined using a 2x2 optical MMI coupler. Due to the frequency difference the envelope of the combined signals in the output ports will show a periodic fading pattern with a frequency of 10 GHz. The output signals are detected with a balanced detector pair; due to the phase transfer properties of 2x2 couplers the two outputs are in anti-phase, which is convenient for application to a differential (RF) amplifier.

Using a coherent detection scheme the phase and amplitude of the RF signal can be controlled by inserting an amplitude and a phase modulator in one of the optical paths before the 2x2 MMI coupler, as shown in figure 2. An advantage of optical phase and amplitude control is that the controllers are much more compact than their microwave counterparts, so that many of them can be combined on a single chip. In our first experiments we will integrate 16 control sections, each of them consisting of two branches containing an electro-optical phase shifter and an amplitude modulator. The two branches are combined with an MMI-type 2x2 power combiner, and then fed to a balanced detector pair.

In this paper we report on the experimental results of the 2x32 distribution network which is used to distribute the two incoming signals over the 16 control sections.

Distribution network

As a first step the distribution network, with 2 inputs and 32 outputs, was made, see figure 3. The distribution network consists of two 1x16 splitters that are folded together such that the input signals appear in pairs at the output. This folded setup was chosen over two 1x16 MMI splitters, as were demonstrated by [3], because this would lead to over 100 waveguide crossings which would reduce the performance. The structure is built from ridge waveguide. Bends in the waveguides are used to route the light to the proper location. MMIs are used as power splitters. The response of the output waveguides is within -4.7 ± 1.1 dB.

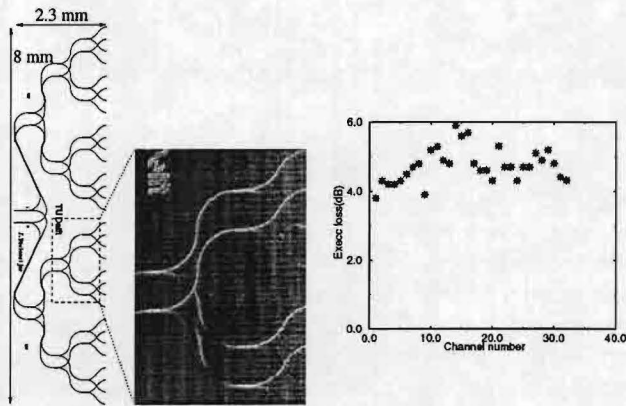


Figure 3: Design, realization and results of the distribution network.

On the chip a number of test structures were included. One test structure, shown in figure 4, consists of a number of power splitters. These power splitters are made by cascading a number of MMIs. The measured power at the outputs in comparison to a straight waveguide is for a 1x4, 1x8 and 1x16 splitter -0.8 ± 0.4 dB, -1.6 ± 0.8 dB and -2.0 ± 0.9 dB respectively.

Other test structures were a set of straight waveguides with $2 \mu\text{m}$ having a loss of 0.9 dB/cm. This waveguide loss is normal for our process. Also a set of waveguide bends (radius $250 \mu\text{m}$) were included. This test structure consisted of five waveguides with respectively 120° , 240° , 360° , 480° and 600° of circular waveguide. Measurements showed a loss of 0.2 dB/ 90° . The bending losses are not very high and mainly due to light scattering at roughnesses on the sidewall of the bend. A number of waveguides with increasing number of crossings at an angle of 90° were used to determine the loss at an intersection of waveguides, this yielded 0.2 dB/crossing. Combining the result from the test structures for the circular waveguide and the crossing test structure results in a loss at the junction of a straight and a curved waveguide of 0.05 dB and at a curved curved waveguide junction of 0.1 dB. From the measurements of the

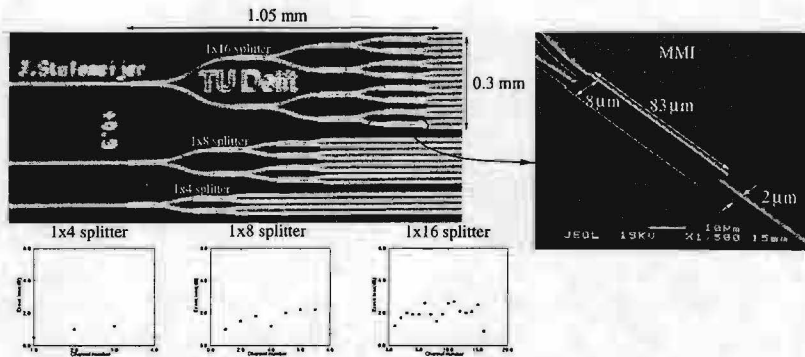


Figure 4: picture plus results of optical splitters with one input and 4, 8, and 16 outputs.

1x4, 1x8 and the 1x16 splitter it can be deduced that the MMIs have an excess loss of 0.3 dB.

Looking at the design of the distribution network there are on average 1.5 crossings per path, 16 curved straight junctions (curved curved junction is counted as two straight curved junctions), 920° of circular waveguide, 4 MMIs and 4 mm of extra straight waveguide. This results in a loss of 4.7 dB. It is hard to bring this number down since smaller bending radii would result in more radiation loss and higher bending radii would result in an enhanced propagation and scatter loss.

As a next step phase shifters will be integrated behind the distribution network. If a high voltage (~ 15 V) is applied to the phase shifters, they become absorbing. We will try to use this effect to realise the amplitude modulators using the same structure.

Conclusion

We have presented a 2x32 distribution network realised on an InP chip. The excess loss of this network is 4.7 ± 1.1 dB. It has been demonstrated that the losses of this network can be expressed as the sum of the losses of the individual components.

References

- [1] A.J. Seeds, "application of Opto-electronic Techniques in Phased Array Antenna Beamforming", in *Proceedings of the Microwave Photonics conference*, 1997, pp. 15-20.
- [2] L.B. Soldano, E.C.M. Pennings, "Optical Multi-Mode Interference Devices Based on Self-Imaging: Principles and Applications", *Journal of Lightwave Technology*, Vol. 13(4), pp. 615-627, 1995.
- [3] L. Spiekman, Y. Oei, E. Metaal, F. Groen, I. Moerman, M. Smit, and B. Verbeek, "Extremely small fabrication tolerant InP-based power-splitting and combining structures by deep etching," in *Proc. 20th Eur. Conf. on Opt. Comm. (ECOC '94)*, pp. 665-668, Firenze, Sep.25-29 1994.

High frequency 8 channel WDM - receiver

A. Siefke¹, C.A.M. Steenbergen², Y.C. Zhu¹, J.W. Pedersen³, M. de Kok¹, I. Moerman⁴,
X.J.M. Leijts¹, M.K. Smit¹

¹ Dept. of Electrical Engineering, Delft University of Technology

P.O. Box 5031, 2600 Delft, The Netherlands

² Lucent Technologies, The Netherlands

³ KPN Research, Leidschendam, The Netherlands

⁴ INTEC-department, University of Gent-IMEC, Belgium

Experiments on high-frequency (HF) integrated WDM receivers and concepts for further improvement of the HF-properties will be reported. The potential for monolithic integration with HEMT-based transimpedance amplifiers will be discussed.

1. Introduction

Wavelength Division Multiplexing (WDM) is an efficient technique for using the high bandwidth offered by optical fibre networks. One of the key components of WDM networks is a multiwavelength receiver.

A compact multiwavelength receiver consisting of a low loss 8 x 10 GHz monolithical polarisation independent phased array demultiplexer with photodetectors was published by Steenbergen et al. [1]. The on-chip losses of the demultiplexer were 3 dB for TE and 5 dB for TM polarization. A negligible TE-TM shift was observed. The frequency response of the detectors was measured to be within 1 dBe for a bandwidth in excess of 10 GHz.

In this paper we present results of a more extensive analysis of the frequency response of the applied photodetectors and we report on the potential of this technology for the integration with 40 Gbit/s MW-receiver frontends.

2. Analysis of the Frequency Response of the Photodetectors

The photodetectors have been characterised up to a frequency of 20 GHz. The measurement system that has been used for the characterisation of the detectors consists of a conventional HP83420A lightwave test set and an external 1.55 μm optical source for the electro-optical conversion. The output of the optical source can be modulated in intensity from 130 MHz to 20 GHz. Via a Cascade Microtech microwave probe the lightwave analyser is connected to the on-wafer photodetector under test. In order to illuminate the device a single mode lensed fibre is used.

The frequency response of the detectors shown in Fig. 2a) is measured at a bias voltage of -5 V. The detectors have a 3-dB bandwidth of more than 20 GHz. Fig. 1a) shows a low frequency (LF) roll-off in the order of 2.5 dB in the region below 2 GHz. This LF roll-off appears to be strongly dependent on the bias voltage of the detector, as shown in Fig. 1b).

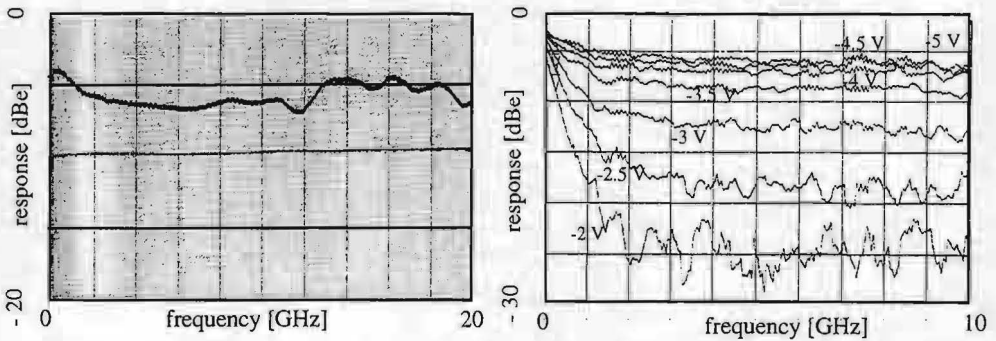


Fig.1 Frequency response of the photodetector a) measured up to 20 GHz at a bias voltage of - 5 V and b) measured at different bias voltages from - 2 V to - 5 V.

Fig. 2 shows the transverse carrier concentration profile of the photodetector at a bias voltage of -2 V and -5 V as calculated with ATLAS BLAZE. The calculation is based on the doping profile of the wafer measured with a CV-profiler.

From the figures it is seen that a voltage much higher than -5 V is required to deplete the absorption layer completely. If the absorption layer is not completely depleted, part of the carriers will be generated in a region without electric field where the rate by which they can be removed is limited by the diffusion speed. This phenomenon, by Williams et al. [3] described as nonlinearities associated with absorption in undepleted semiconductor regions explains the roll-off below 2 GHz.

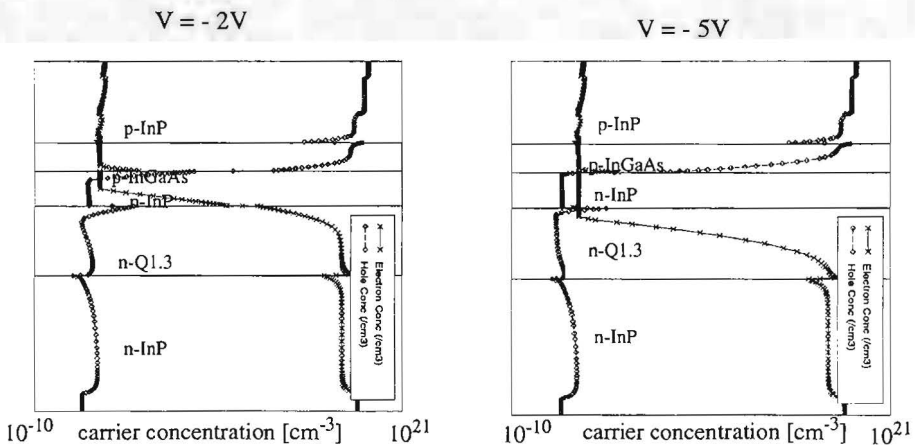


Fig.2 Transverse carrier concentration profile of the photodetector at a bias voltage of -2 V and -5 V.

3. Potential Bandwidth

The problem of the LF roll-off can be solved by reducing the background doping level in the absorption layer. With a doping level below 10^{16} the absorption layer will be fully depleted at a voltage of -2 V.

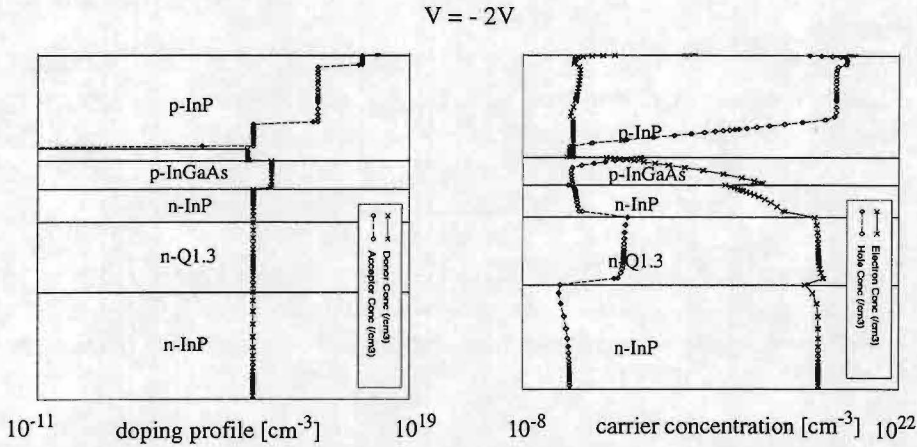


Fig.3 a) A possible doping level in the photodetectors and the transverse carrier concentration profile at a bias voltage of -2 V.

In this case the bandwidth of the receiver is limited by the RC - 3 dB frequency, which has a value of

$$f_{RC} = \frac{1}{2\pi(R_S + 50\Omega)C_d} = \frac{1}{2\pi(6\Omega + 50\Omega)104fF} \sim 27GHz$$

The maximum transit time of electrons of 11 ps yields to a 3 - dB frequency of 31 GHz. Both effects return a bandwidth of ca. 20 GHz. This value can be increased by making the depleted region thinner and the detector area smaller.

We are presently working on the integration of our MW-receiver with HEMT-based transimpedance amplifiers. This is done in cooperation with the Electronic Device Group of Eindhoven University of Technology.

4. Conclusions

From experiments and simulations performed on a high-frequency integrated WDM receiver based on a twinguide detector structure it is concluded that by decreasing the background doping in the absorption layer LF roll-off can be avoided. Further the 3 dB-bandwidth can be reached at a much lower bias voltage.

5. References

- [1] C.A.M. Steenbergen, C. van Dam, A. Looijen, C.G.P. Herben, M. de Kok, M.K. Smit, J. W. Pedersen, I. Moerman, R.G.F. Baets, and B.H. Verbeek, "Compact low loss 8 x 10 GHz polarisation independent WDM receiver", in Proc. 22th. Eur. Conf. on Opt. Comm. (ECOC '96), Oslo, Norway, September 15-19, 1996
- [2] Y. Muramoto, K. Kato, A. Kozen, M. Ueki, K. Noguchi, Y. Akatsu, and O. Najaji ma, "High-efficiency, zero-bias waveguide pin photodiode for low-power-consumption optical hybrid modules", in Electron. Lett. 16th January 1997, Vol. 33, No. 2 pp. 160 - 161
- [3] K. J. Williams, R.D. Esman, M. Dagenais, "Nonlinearities in p-i-n Microwave Photodetectors", Journal of Lightwave Technol. Vol. 14, No. 1, January 1996, pp. 84 - 96

Integrated Indium Phosphide based Photoreceiver

N.G.H. van Melick, F. Karouta, L.M.F. Kaufmann, and A. Siefke*

Eindhoven University of Technology, Electronic Devices Group, P.O.Box 513, 5600MB, Eindhoven, The Netherlands. email: n.g.h.v.melick@ele.tue.nl

**Delft University of Technology, Photonic Integrated Circuits Group.*

Abstract — This paper describes the development of a high electron mobility transistor (HEMT) based on an InP substrate with lattice matched InGaAs/InAlAs layers. The scope of this paper is to provide an overview of the new process developments in our group and the process optimization. The HEMTs will be used to design a transimpedance amplifier. Furthermore the future integration with a PIN photodetector and waveguides into a photoreceiver and additionally the potential for monolithic integration with WDM receivers will be discussed.

Introduction

In the last few years the use of optical fiber systems all over the world has extensively increased. And in the future the demands will even further increase, because of the tremendous growth of popular network services, like email, Internet, and enhanced video. To overcome the bandwidth problem, various systems with higher bandwidth are currently developed extensively. To expand the bandwidth, and therefore yield more capacity, the bit-rate of the transmission systems has to be increased. On the other hand wavelength-division-multiplexing (WDM) can be used, which employs multiple channels at somewhat lower transmission rates, but achieving a larger overall capacity. Both systems, however, require high performance opto-electronic receivers, converting effectively the signal from the optical domain to the electrical domain.

Nowadays, the commercially available systems consist mostly of hybrid circuits. However, to achieve higher bandwidths, monolithically integrated devices are expected to fulfill the future demands, because of the reduced parasitic capacitance caused by the internal bonding of the hybrid systems.

Therefore, monolithically integrated photoreceivers, are widely investigated and developed nowadays. In general four different photoreceiver configurations are used [1]. In fact two different photodetectors are used, i.e. the MSM and the PIN photodetector, these photodiodes act as an input stage for the amplifying stages which consist of either HEMT- or heterojunction bipolar transistors (HBTs)-based transimpedance amplifiers.

Since in our group a GaAs-based photoreceiver had already been developed [2] based on MSM photodetectors and HEMTs, we also used high electron mobility transistors. For this project InP-based HEMTs are used to achieve a higher mobility and as a consequence a higher cut-off frequency, f_T . The photodetector can either be an MSM or a PIN photodiode. Although an MSM photodetector yields a very low capacitance and is in principle more compatible for single crystal growth and therefore monolithically integration [3], the PIN photodiode is more suitable for planar, monolithically integration with waveguide structures.

HEMT Fabrication

The HEMTs, used for the photoreceiver are MBE grown. The lattice matched layer stack consists of a 250nm $\text{In}_{0.52}\text{Al}_{0.48}\text{As}$ buffer layer on an semi-insulating InP substrate, a 20nm $\text{In}_{0.53}\text{Ga}_{0.47}\text{As}$ channel layer, a 5nm $\text{In}_{0.52}\text{Al}_{0.48}\text{As}$ spacer layer, a Si delta-doped layer ($5 \cdot 10^{12} \text{ cm}^{-2}$), a 20nm intrinsic $\text{In}_{0.52}\text{Al}_{0.48}\text{As}$ Schottky contact layer, and a 7nm n-doped ($2 \cdot 10^{18} \text{ cm}^{-3}$) $\text{In}_{0.53}\text{Ga}_{0.47}\text{As}$ ohmic contact cap layer. The spacer layer was taken 5nm to optimize the electron mobility - 2DEG sheet resistivity trade-off [4]. The mesa's were etched 100nm deep. To obtain a low ohmic contact resistance a Ni/Au/Ge/Ni/Au metalization is used, annealed at 280 °C for 60 seconds, resulting in a contact resistance <0.2 mm. The self aligned gate recess is performed in a sussinic acid (SA) etchant. A Ti/Pt/Au gate metalization is used for the Schottky contact.

Results

The devices processed so far show relatively good DC characteristics, see figure 1. The gate length was $2.2\mu\text{m}$ and the gate width $100\mu\text{m}$. There is a low threshold value of 0.7V. As can be seen in figure 1, the HEMT characteristics do not suffer from the kink effect, as no dips in the I_d - V_{ds} curves are visible. Figure 2 shows the I_d and g_m characteristics as a function of gate voltage, V_{gs} , for $V_{ds}=2\text{V}$. From figures 1 and 2 can be seen that the gate leakage current is still rather high for V_{gs} around -1V. Figure 2 also shows that the transconductance yields 120 mS/mm for a gate length of $2.2\mu\text{m}$, which is quite a promising value. However, to decrease the gate leakage current and to improve the overall device performance the HEMT process has to optimized.

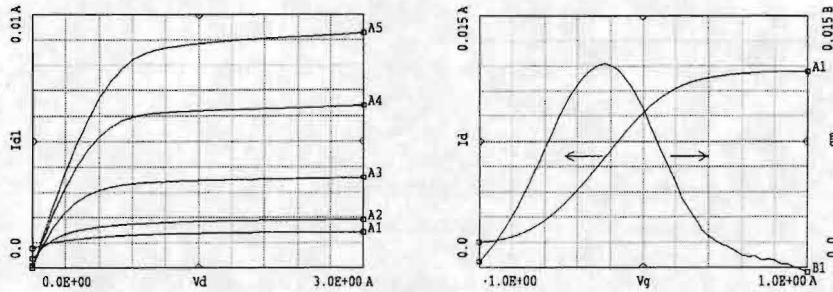


Figure 1: I_D (A)- V_{DS} (V), for $V_{GS}=-1.0, -0.75, -0.5, -0.25, 0.0\text{V}$. Figure 2: I_D (A)- V_{GS} (V) and g_m (S)- V_{GS} (V) for $V_{DS}=2\text{V}$.

Process Optimization

An important parameter for improving the overall transistor performance is the gate length, L_g . Consequently, the gate length has to be decreased. Since at our group only optical lithography can be used the smallest gate length is fixed by the optical limits, i.e. $1\mu\text{m}$ for the smallest mask structures. Nowadays, e-beam lithography is generally used to obtain deep submicron gate lengths [5].

To obtain smaller gates, the gate lithography has been optimized. A thin photoresist is used to diminish the vertical dimensions of the resist layer and consequently improve the horizontal accuracy. Therefore the image reversal resist AZ5206 is used to obtain a



Figure 3: 1 μm opening lift-off profile with the AZ5206, image reversal photoresist.

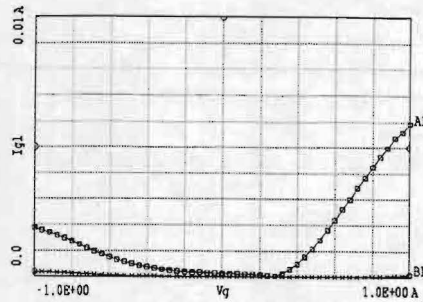


Figure 4: Gate currents I_G (A) for the first (boxed, $L_g=2.2\mu\text{m}$) and optimized (crossed, $L_g=1.0\mu\text{m}$) process.

thin and accurate lift-off profile, see figure 3. Also a different gate metalization is used to increase the Schottky barrier height, ϕ_m , as a result a Pt/Ti/Pt/Au (50/250/250/1500) metalization is applied, since Pt has a higher ϕ_m than Ti and an increased Schottky barrier yields a decreased gate leakage current. Furthermore, the gate recess has been altered from a self aligned etch, where the ohmic contact metalization acts as a mask, into an area restricted etch. Now the etching is performed, also with sussinic acid, after the gate lithography step. Thus, the lateral gate recess can be controlled by means of the time. As a first approximation the gate recess etching time is taken to be 5 minutes, yielding a lateral recess etch of 0.3 μm , since the etch rate is 60 nm/min, which is expected to be a good recess dimension.

The devices processed with these new features show comparable DC characteristics for a gate length of approximately 1 μm . Therefore, the gate lithography is very accurate and sufficiently small. The gate leakage current was significantly smaller as can be seen in figure 4. However, the combination of a thin lift-off photoresist layer and the Pt/Ti/Pt/Au metalization resulted in a very difficult lift-off, with a low transistor yield. Also the DC characteristics and the transconductance were expected to be better.

Future Work and Integration

As described in the previous section the DC characteristics still have to be improved. Therefore the gate lithography has to be optimized, resulting a better lift-off without significant larger gate dimensions, i.e. approximately 1 μm . Also the gate recess etch has to be optimized, because there is a trade-off between cut-off frequency and source- and drain-resistance resulting a better high frequency performance or higher breakdown voltage, respectively. When this is optimized good DC characteristics and good high frequency performance are expected for the high electron mobility transistors. When the HEMT process is developed and the HEMTs can be made reproducibly, the transistors will be modeled. Therefore a semi-empirical, measurement based model is used. The HEMT models are used to develop the TIA circuit. Besides the HEMTs also diodes will be developed, modeled, and used in the TIA circuit. The TIA circuit will be designed as a multi bit receiver. That is, four or eight receiver circuits will be placed side by side to act as amplifier stages for the multi bit WDM receivers designed by the Photonic Integrated Circuit (PIC) group, Delft. Figure 5 illustrates a possible realization of such an opto-electronic integrated circuit. When the transimpedance amplifier circuits are

developed, a mask layout will be designed for the manufacturing of the circuit. Besides the TIA as the amplifying stage the photoreceiver needs a photodetector. Hence a PIN photodiode will be used. This PIN photodiode has already been developed at the PIC group in Delft. Here the PIN structure is integrated with a planar waveguide (WG) structure, see table 1. To design an integrated photoreceiver, the PIN photodetector (MOVPE grown) has to be integrated with the TIA circuits on the same substrate.

Table 1: PIN/WG layer structures.

p ⁺ -InGaAs	50nm	p-contact layer
p-InP	600nm	p-buffer layer
i-InGaAs	250nm	absorption layer
n-InGaAsP	300nm	n-contact layer
i-InP	300nm	waveguide layer
i-InGaAsP	600nm	waveguide layer
i-InP	-	WG layer/substr.

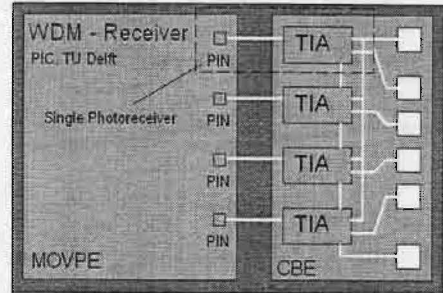


Figure 5: Possible realization of the multi bit WDM receiver (MOVPE grown) integrated with the TIA circuits (possibly CBE grown).

Consequently, a selective regrowth step of the HEMT structures has to be performed to achieve the monolithic integration. First a single PIN photodiode will be integrated with one TIA circuit, as a single photoreceiver, also indicated in figure 5. Hereafter the total multi bit receiver will be developed as indicated in the figure. When the layer stacks are grown on the same substrate, the processing of the total integrated photoreceiver has to be developed, the photoreceiver itself has to be made and finally the characterization of the total circuit will be performed.

Conclusions

The first HEMT process optimization show a decreased gate leakage current, however to improve the HEMT features still some work has to be done on the gate lift-off lithography and gate recess. Hereafter, the HEMTs are used to design a transimpedance amplifier, which has to be integrated with a PIN photodetector. Therefore a selective regrowth step is needed. The PIN photodetector and the TIA will eventually result in a monolithically integrated multi bit photoreceiver which can be used as WDM receiver.

References

- [1] Lunardi, L.M., "InP-based Monolithically Integrated Photoreceivers", *Conf. Proc. IPRM'97*, 11-15 May 1997, Hyannis, MA, USA, p. 471.
- [2] Wellen, J.S., "Modelling, design and fabrication of a GaAs-based integrated photoreceiver for short distance optical communications", *Ph.D. Thesis*, Eindhoven University of Technology, The Netherlands, 1997.
- [3] Fay, P. et al., "18.5-GHz Bandwidth Monolithic MSM/MODFET Photoreceiver for 1.55- μ m Wavelength Communication Systems", *IEEE Photonic Technology Letters*, Vol. 8, no. 5, p. 679, 1996.
- [4] Passenberg, W. et al., "On the potential of δ -doping for AlInAs/GaInAs HEMTs grown by MBE", *Jour. of Crystal Growth*, Vol. 127, p. 716, 1993.
- [5] Nguyen, L.D. et al., "650-A Self-Aligned-Gate Pseudomorphic Al_{0.48}In_{0.52}As/Ga_{0.20}In_{0.80}As High Electron Mobility Transistors", *IEEE Electron Device Letters*, Vol. 13, no. 3, p. 143, 1992.

MICROWAVE-BEHAVIOUR COMPARISON OF BIAS-PROBES FOR ON-WAFER TESTING OF MMICs AND OEICs.

J.J.M. Kwaspen and H.C. Heyker

Eindhoven University of Technology, Faculty of Electrical Engineering,
Telecommunications Technology and Electromagnetics / Electronic Devices Group,
COBRA Interuniversity Research Institute,
PO Box 513, 5600 MB Eindhoven, The Netherlands.

Abstract: Good DC-bias decoupling of MMICs and OEICs during on-wafer testing is essential for their correct functioning when GHz-bandwidths are involved. Decoupling is done by bias-probes or on-chip. The microwave impedances of a few commercially and in-house made DC-bias probes are compared.

1 Introduction

This contribution gives a brief overview of the microwave performance of a few probes in use to supply DC bias and to decouple circuit parts of MMICs or OEICs during on-wafer testing. In particular they are needed to achieve proper functioning of the circuit, when no on-chip decoupling capacitors are included in the chip design. Decoupling theory is summarized for chip level purpose. Two commercially available and two in-house made bias-probes are described, their input impedances have been measured and the results are compared.

2 Decoupling concepts

In text books on theoretical electronic circuit design, most of the circuits and sub-circuits are described by assuming implicitly, that the DC bias supplies have zero impedances for all frequencies involved, which in practical realisations only can be approximated. Fig. 1 shows a fictive chip design with a number of microwave transistors. When the input impedance Z_b of the drain bias supply or the impedance of the return trajectory Z_r are non-zero, unwanted interference between several stages of the circuit will occur. To prevent this, each stage must be decoupled by a capacitor having an impedance much smaller than the impedance Z_b of the bias supply and 'wiring' at that circuit stage. Also Z_r should be kept to a minimum by large area low-inductance and low-resistance ground planes. The decoupling capacitors can be designed on-chip, mostly at the cost of excessive chip area when the bandwidth of the circuit extends to low frequencies. When no on-chip capacitors are included in a MMIC/OEIC design, decoupling should be undertaken in the package of the chip, as closely as possible to the circuit node, to prevent large bond wire impedances. Note that 0.25mm of 18 μ m bond wire already

presents j50 Ω at 40 GHz. When such a decoupling capacitor-less MMIC or OEIC must be tested on-wafer, the probe that supplies the DC bias should include the decoupling function to the level wanted. This means that the probe's input impedance must be low for all frequencies involved. An ideal bias-probe has infinit parallel and zero series resistances at DC and zero impedance for all AC signals at its chip-contact tips. In practice however, the residual lead length up to the 'decoupling capacitor' and the spacing between bias contact and ground contact presents an unavoidable path inductance, so bias-probes mostly show inductive reactances at the high frequency limit.

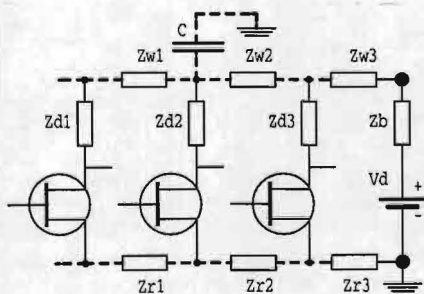


Fig. 1

3 Bias-probe descriptions

Only bias-probes that have a transmission line character will be considered, so we do not describe designs consisting of a single needle for the high level and a single loose return lead of cm-length, because they are totally unsuitable for microwave frequencies.

Probetypes (150 μm contact pitch; P=DC power; G=ground; S=signal) :

- 3-needles bias-probe, GPG-configuration, TUE/EEA design, Fig. 2a.**
This probe was constructed to demonstrate some basic principles of bias-probes. The most important dimensions are shown. The input impedance has been measured for several design modifications.
- Coplanar microwave signal head, WPH305, 50 Ω , GSG-configuration, CASCADE Microtech, Ref. 1.; Fig. 2b.** Actually intended for measurement purposes to 40 GHz.
- Multi-contact bias probe, WPH705, GPGPG-configuration, CASCADE Microtech, Ref. 2; Fig. 2c.** Dual bias supply capability. Bias port terminated into 50 Ω .
- Large-bandwidth bias-probe, GPG-configuration, TUE/EEA prototype, Fig. 2d.**

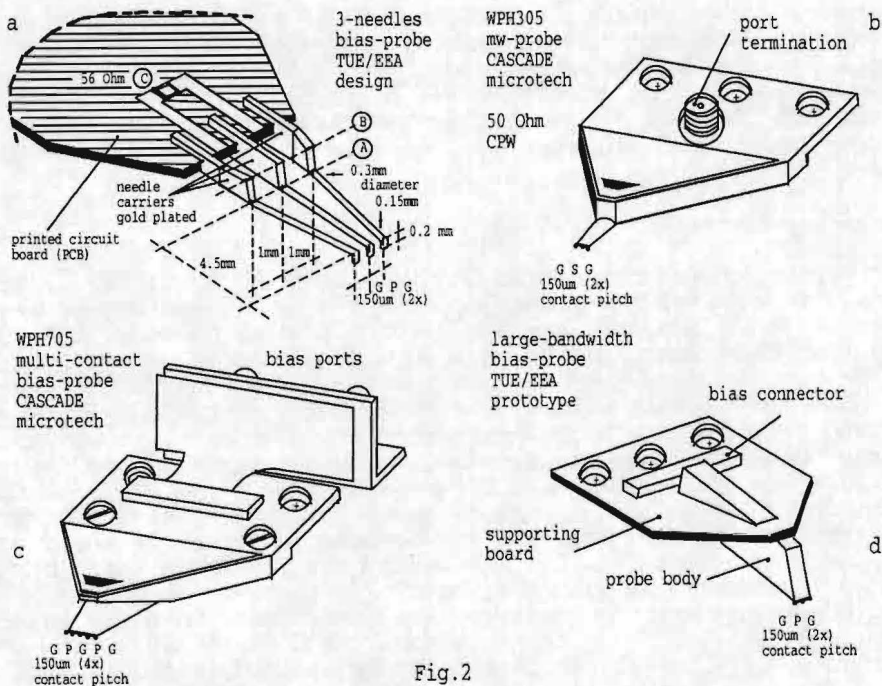


Fig.2

4 Measurement setup

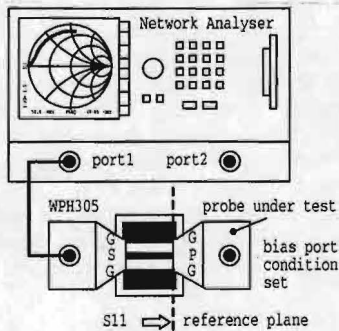


Fig. 3

A WPH305, 50 Ω , DC-40 GHz, ground-signal-ground (GSG) microwave probe is coupled to port 1 of an HP8510B network analyser and this system is calibrated by on-wafer standards at the reference plane (Fig. 3; Ref. 3,4,5). The measurement probe is connected through a short 50 Ω coplanar line (thru-standard on the calibration substrate) to the bias-probe under test and the input reflection coefficient S_{11} is measured and converted to an input impedance Z by $Z=50.(1+S_{11})/(1-S_{11})$. Results of S_{11} , $\text{Re}(Z)$ and $\text{Im}(Z)$ are shown in Fig. 4a-e, under several conditions of the bias port of the probe.

5 MEASUREMENT RESULTS

Fig. 4a

3-needles bias probe
needles short-circuited
by brass bar at position A
in Fig. 2a.

no bias possible

$$L = \text{Im}(Z) / (2 \cdot \pi \cdot \text{FREQ})$$

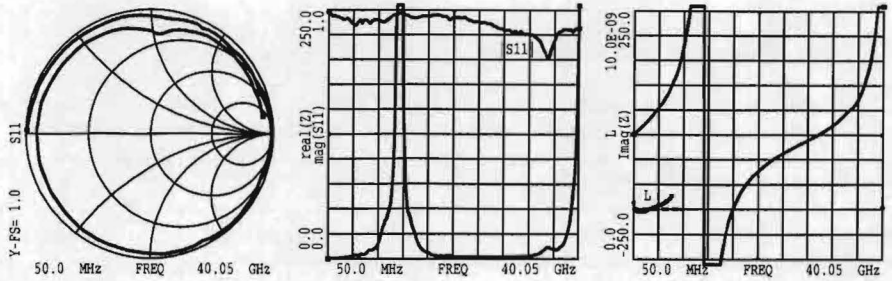


Fig. 4b

3-needles bias probe

development conditions :

a: At position A (Fig.2a)

2x56pF mounted

b: At A 2x56pF and at C

56 Ohm (Fig.2a)

c: At A 2x56pF and at C

56 Ohm (Fig.2a) and

at B 2x1nF

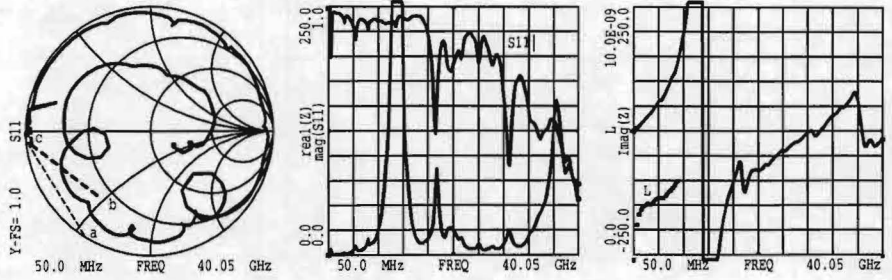


Fig. 4c

WPH305 microwave probe

bias port terminated in 50 Ohm

and bias port short-circuited

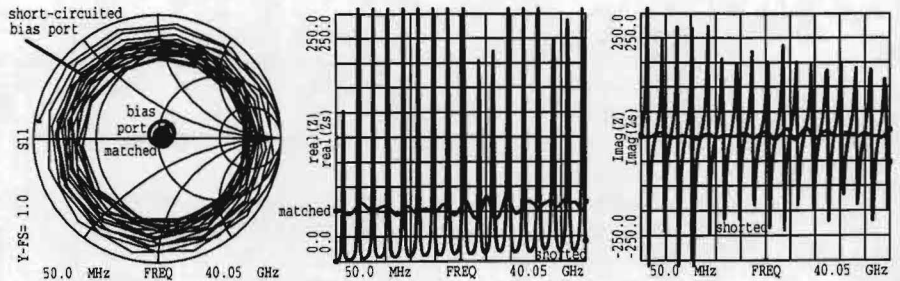


Fig. 4d

WPH705 multicontact bias probe

GPGPG
left right

dual bias supply capability

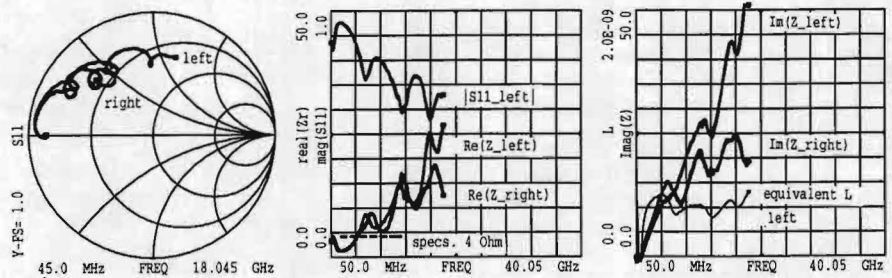
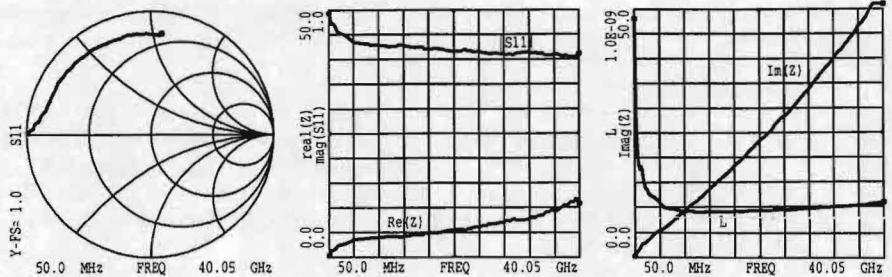


Fig. 4e

Large-bandwidth prototype

open bias port



6 Discussion and conclusions

Whether a bias-probe is useful for a particular purpose and frequency range, will be determined by the circuit impedance relative to the bias-probe impedance. The table below summarizes the measurement results at a number of frequencies of the bias-probes discussed.

Probe	probe input impedance (Ω)			equivalent inductance
	4 GHz	10 GHz	40 GHz	
3-needles	5+j50	220+j540		0-4 GHz : ~ 2.5 nH
WPH305 microwave *)	55+j8	45+j0	60+j15	
WPH705 multi-contact **)	3.5+j10	12+j25		2-18 GHz : ~ 0.4 nH
Large-bandwidth prototype	3.5+j5	4+j12	12+j55	4-40 GHz : ~ 0.2 nH

*) 50 Ω termination **) left GPG

3-needles bias-probe :

the probe is useful in the lower microwave range and in a small frequency band around 30 GHz, dependent on probe element values (length, spacing and diameter of the needles).

Note: the probe can radiate, so interference might occur.

WPH305 microwave probe :

the probe is useful for the higher impedance ranges up to 40 GHz (if terminated into 50 Ω after insertion of a bias-tee). The low frequency limit is determined by the coupling capacitor value. When short- or open-circuited at the bias port, the probe can be applied in small frequency bands, where Z approximates 0 Ω (Fig. 4c).

WPH705 multi-contact probe :

the measured impedance data (Fig. 4d) deviates from the specifications given in Ref. 2, indicating an impedance $Z=4+j\omega L$ Ω . L represents the inductance of the power + ground contacts (0.3+0.1 nH). The bias port was terminated into 50 Ω .

Large-bandwidth prototype :

in the frequency range of 0.05-40 GHz, this bias-probe shows the best performance. Improvements are still possible. A reduction of the inductive reactance by a factor of two, seems feasible.

7 Acknowledgment

The authors would like to thank drs. E. Smalbrugge for technological assistance.

8 References

- 1 CASCADE Microtech WPH305 microwave probe datasheet 305DS-488
- 2 CASCADE Microtech WPH705 multicontact bias-probe datasheet 700S-591
- 3 CASCADE Microtech on-wafer testing instruction manual PROBKT80
- 4 Hewlett-Packard 8510B network analyser manuals
- 5 Hewlett-Packard MDS manuals

Monolithical Integration of GaAs-based Laser-Photodetector

H.A. Langelier, F. Karouta, J.J.W. v. Praagh and W.C. van der Vleuten*

COBRA Inter-University Research Institute on Communication Technology
Eindhoven University of Technology - Department of Electrical Engineering
Telecommunication, Technology and Electromagnetics - Section Electronic devices
P.O.Box 513, NL-5600 MB Eindhoven.

*COBRA - Eindhoven University of Technology - Semiconductor Physics

ABSTRACT - Using an established processing technique of Wet Etched Mirror Lasers we have fabricated a laser-photodetector pair, monolithically integrated in a GaAs-based GRINSCH laser structure having a GaAs bulk active layer. Linear photocurrent versus laser output power is obtained.

Introduction

A versatile processing technique has been developed to realise Wet Etched Mirror Lasers (WEML) in GaAs/AlGaAs structures. WEML were successfully fabricated using a Double Hetero Structure (with bulk GaAs active layer) and Graded Index Separate Confinement Heterostructures (GRINSCH) having quantum well active regions of a SQW GaAs, a SQW $\text{In}_{0.2}\text{Ga}_{0.8}\text{As}$ and 6 QWs of $\text{Al}_{0.2}\text{Ga}_{0.8}\text{As}$ respectively [1].

A set of masks has been designed and realised which allows the fabrication of WEML with various cavity lengths. Another part of the mask is intended to fabricate an integrated laser-photodetector. We present in this paper the experimental results concerning the fabrication and the characterisation of the monolithically integrated laser-photodetector (int-LD).

Experimental

The processing of the int-LD requires five photolithography steps. Each of these steps is accompanied by some processing steps:

- 1- definition of mesa blocks followed by etching the ridge waveguides, deposition of SiO_2 .
- 2- definition of the p-type contact followed by the p-metallisation [Ti/Pt/Au (50/20/200 nm)].
- 3- definition of openings in the SiO_2 layer followed by etching the windows using a buffered HF solution.
- 4- etching of the tilted detector facet. This is done by etching a V-shaped channel where one of the walls will be the detector facet.
- 5- definition of the mirrors stripes for etching the mirrors taking into account the under etch effect which is equal to the etch depth.

Figure 1 shows the schematic drawings of the 5 photolithography steps including the performed processing steps at each lithography step.

The laser & detector section of the masks set defines lasers with a ridge length of 300 μm and ridge widths of 10, 6 and 4 μm . These ridges are aligned with detectors having ridges of 20 μm and lengths of 200, 400, 800 and 1600 μm respectively.

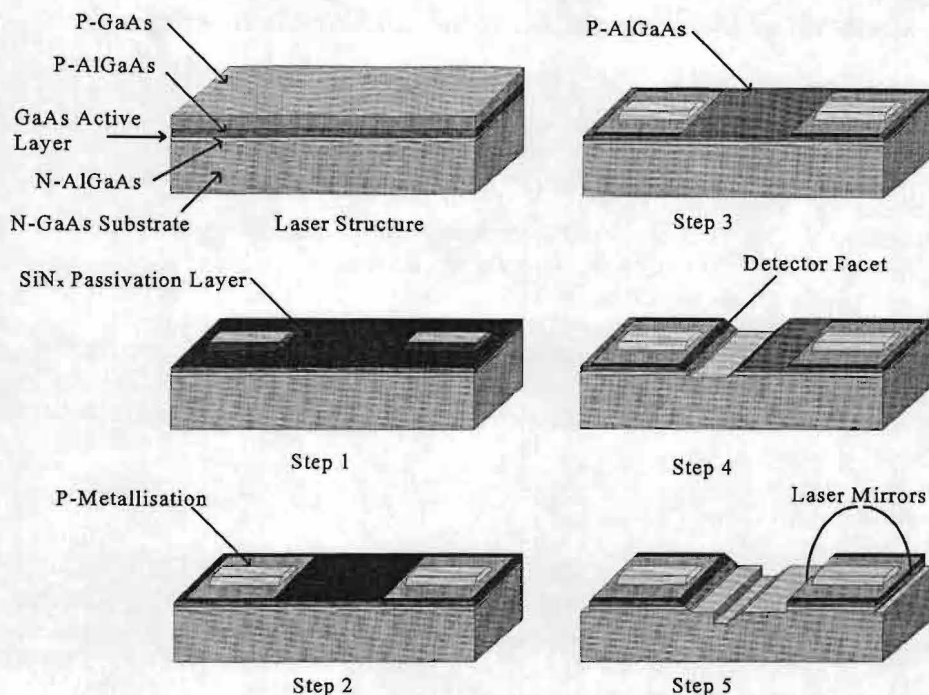


Figure 1 - Schematics of the photolithography and the corresponding processing steps.

The V-shaped channel is etched in a sulfuric acid based solution ($\text{H}_2\text{SO}_4\text{:H}_2\text{O}_2\text{:H}_2\text{O}$ -1:1:10) at 20°C . This etchant has an etch rate of $0.75\text{ }\mu\text{m/min}$ and etches a groove with walls making an angle of about 30° with the vertical. Etching is done during 2 minutes 30 seconds. The channel is placed closer to the detector than to the laser. The nearest tilted sidewall to the detector will be used as a detector facet. Subsequently the laser mirrors are etched in a ($\text{H}_3\text{PO}_4\text{:H}_2\text{O}_2\text{:H}_2\text{O}$ -1:1:1) at room temperature. The centre channel is a result of the two etch processes and should be regarded as an unavoidable side effect. Nevertheless this should not have any negative consequences on the int-LD.

Afterwards the processing is similar to that of cleaved lasers i.e. thinning the substrate by mechanical and chemical polishing down to $\pm 150\text{ }\mu\text{m}$. A metallisation of Ge/Ni/Au (20/15/200 nm) is used as n-type contact on the back side of the sample followed by an annealing step. We have chosen to mount some LD-chips, in order to allow characterisation of these devices in continuous wave mode (CW). Mounting is done using half dual in-line packages (DIL). Each half package can contain two pairs of int-LD. The chips are attached with silver cement (Epo-tek) onto the package. Gold wires connect the devices to the package pins. Only lasers $300\text{ }\mu\text{m}$ long with $10\text{ }\mu\text{m}$ wide ridges, and their inline detectors with cavity lengths of 800 and $1600\text{ }\mu\text{m}$ have been connected and eventually characterised.

DC-characterisation of the LD pairs

We have chosen to characterise the LD pairs in continuous wave mode (CW) to avoid crosstalk problems experienced with pulse mode operation of the laser. The following characteristics have been recorded: $P_L = f(I_L)$ and $I_D = f(P_L)$, in which I_L is the laser current, P_L the laser optical output power and I_D the detector photocurrent.

The laser is connected via an ampere meter to a DC power supply. The detector photocurrent is measured with an ampere meter. No bias is applied to the detector (solar cell mode). The laser output has been measured with an optical power meter. Figure 2 shows the LI-curves of the laser operated in CW mode (solid line) as well as the photocurrent of the integrated detector (dashed line). As it can be seen a photocurrent of 12.5 $\mu\text{A}/\text{mW}$ has been obtained.

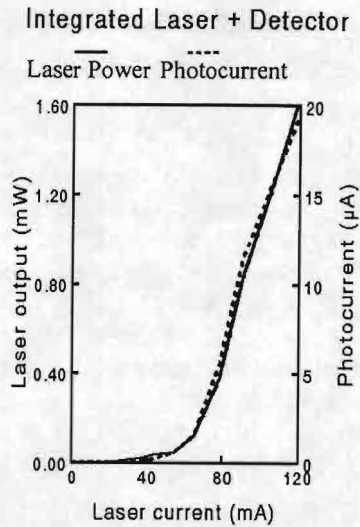


Figure 2 - Laser output power and photocurrent of the integrated photodetector.

Figure 3 shows an almost linear relation of I_D as a function of the output power. However this linearity degrades at higher output power. Also it has been observed that at constant laser output the photocurrent decreases slightly. This is probably due to heating effect in the laser resulting in a slight red shift making the laser light more transparent for the detector.

N. Bouadma, et al. [2] reported about GaAs/AlGaAs LD pairs with ion beam etched facets. The sensitivity of their detectors was about 5 $\mu\text{A}/\text{mW}$.

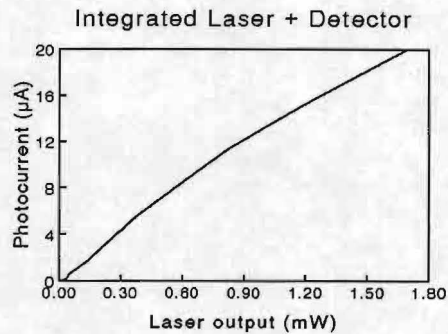


Figure 3 - Photocurrent vs optical power of an integrated pair of a laser and a photodetector.

We have also tried to integrate a three quantumwell laser with a photodetector using the same manufacturing process. The lasers had a lower threshold current than those of the bulk active layer but no reasonable photocurrent could be measured. Since the detector has also three quantumwells in its active layer the amount of generated electron-hole pairs is much less than in a bulk active layer.

Conclusions

We have reported about the fabrication and the DC characterisation of an integrated laser and a photodetector. The photocurrent has been found proportional to the laser output power. The sensitivity of the photodetector was 12.5 $\mu\text{A}/\text{mW}$ which is a good value in comparison to values in literature for similar devices.

Acknowledgements

The authors would like to thank G.A. Acket for fruitful discussions, E. Smalbrugge and B.H. v. Roy for technical assistance.

References

- [1] F. Karouta, H.H.P.M. van den Heuvel, J.G. van Hassel, J.S. Wellen, E. Smalbrugge, J.A.A. Stegeman, L.M.F. Kaufmann and W.C. van der Vleuten, Invited Paper 21st SOTAPOCS - 186 Meeting of The Electrochemical Society, Miami Beach, October 9-14, 1994. Proceedings volume 94-34, SOTAPOCS XXI, Edited by S.N.G. Chu, ISBN 1-56677-093-9, p. 132-39.
- [2] N. Bouadma, P. Correc and F.P. Brillouet, IEEE J. of Quantum Electronics, **QE25**, 1989, p. 2219-2228.

Intermixing in InGaAs/GaAs Structures for Mirror Protection in High Power Lasers.

F. Karouta, J.J.W. v. Praagh, G.A. Acket, T.J. Eijkemans*,
C.M. v. Es* and W.C. van der Vleuten*

COBRA Inter-University Research Institute on Communication Technology
Eindhoven University of Technology - Department of Electrical Engineering
Telecommunication, Technology and Electromagnetics - Section Electronic devices
P.O.Box 513, NL-5600 MB Eindhoven.

*COBRA - Eindhoven University of Technology - Semiconductor Physics

ABSTRACT - We report the results on impurity free interdiffusion in GaAs and InGaAs Quantum Well structures using SiO₂ layers and an annealing step. The intermixing results in a wavelength shift of up to 70 nm in GaAs QW-structures and 45 nm in InGaAs QW-lasers.

Introduction

High power semiconductor lasers are used a.o. in the telecommunication industry as pump lasers for Erbium-Doped Fibre Amplifiers. The maximum optical power, and thus the longevity, of these high power lasers is limited by the Catastrophical Optical Degradation (COD) which occurs at the mirror facets at high power. A way to counter this effect is to change the material properties in the vicinity of the mirrors in a way that the treated area becomes transparent for the laser light.

This can be achieved either by adding complex processing steps involving growth/regrowth or by local interdiffusion.

Interdiffusion techniques are commonly used in semiconductor heterostructures to change the properties of the materials and/or the devices. The interdiffusion creates an intermixing between adjacent layers. Quantum Well (QW) structures are a better choice for this technique than more conventional structures using bulk materials. Intermixing a QW layer with the surrounding layers will lead to a change of the QW shape as well as the composition. For instance, when a GaAs QW layer, embedded between two AlGaAs layers, is intermixed, a migration of Al atoms into the QW will take place. The incorporation of Al atoms in the GaAs alters both the well width and the potential barrier height resulting in general in a blue shift of the QW bandgap.

Two kinds of Interdiffusion techniques can be used: Impurity-induced InterDiffusion (IID) [1-3] and Impurity Free InterDiffusion (IFID) [4-5]. The first technique uses either implantation or diffusion of impurities from the surface into the structure and followed by an annealing step to enhance the intermixing. A drawback of this technique is the introduction of undesired changes to the resistivity and to the trap concentration. The second technique is realised by depositing a dielectric layer like SiO_x which induces Ga-vacancies on the surface and a subsequent annealing step at a very high temperature (~900°C) which enhances the outdiffusion of the Ga-atoms.

In this paper we report the use of silicon oxide layers to intermix GaAs and InGaAs QW structures. Lasers having a Single Quantum Well (SQW) of In_{0.2}Ga_{0.8}As lasers, fabricated using intermixing, showed a wavelength shift of more than 40 nm.

Experimental

We used an IFID technique to disorder the epitaxial structure which leads to a change of the material bandgap. Plasma Enhanced Chemical Vapour Deposition (PECVD) of silicon oxide and silicon nitride were investigated as possible candidates for generating and/or preventing disordering. Silicon nitride has been reported to prevent intermixing [4].

The technique consists of depositing a dielectric layer layer on the sample followed by an annealing step at very high temperature ($\sim 900^\circ\text{C}$). Typically 150 and 300 nm thick SiO_x or SiN_x layers were used for this purpose. Annealing temperature was varied from 870 to 930°C while annealing times of 20 seconds up to 6 minutes were applied. Low temperature Photoluminescence is used to characterise the sample and to determine the position of the photoluminescence peak.

We started our investigations using an MBE-grown structure having four GaAs QWs of 40, 70, 110 and 160 Å embedded in 50 nm $\text{Al}_{0.33}\text{Ga}_{0.67}\text{As}$ barriers. The four QWs are positioned at 67, 121, 178 and 239 nm respectively from the surface. This technique was later extended to an undoped MBE-grown GRINSCH laser structure (GRaded INDEX Separate Confinement Heterostructure) having $\text{Al}_{0.70}\text{Ga}_{0.3}\text{As}$ cladding layers and an 8 nm SQW of $\text{In}_{0.20}\text{Ga}_{0.8}\text{As}$ located at $1.8\text{ }\mu\text{m}$ from the top surface. Ultimately we applied this technique to a similar structure with doping and followed by a full processing of ridge waveguide lasers. The InGaAs QW is located at $2.2\text{ }\mu\text{m}$ from the surface. Laser spectra measurements determine the emission wavelength. Figure 1 shows details of the doped GRINSCH laser structure.

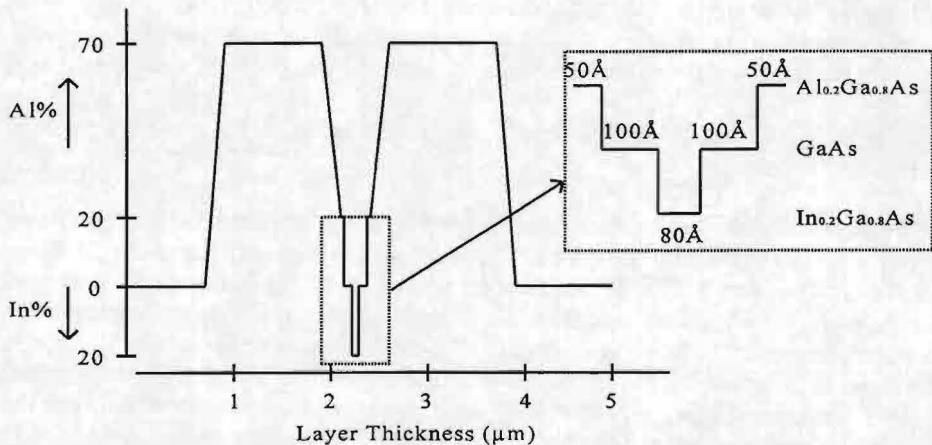


Figure 1- Details of the InGaAs laser structure.

GaAs QW Structure

The effect of annealing temperature and the dielectric thickness form the goal of our first investigations. Few tests were carried out using the GaAs-QWs structure. SiO_x layers of 150 and 300 nm thick and a 300 nm thick SiN_x were used. Furthermore the annealing temperature and time were varied. The RT-PL measurements did not clarify the role of the silicon nitride in the interdiffusion process. The SiO_x layer thickness did not have any influence of the wavelength shift while the annealing temperature had a clear effect as well as the annealing time. The RT-PL measurements of the widest quantum well (160 Å, located at 239 nm from the top) are given in the following table. The results of SiN_x -capped samples clearly show some inconsistency.

Dielectric	thickness (nm)	Annealing Temperature	Annealing Time	Wavelength Shift (nm)
SiO _x	150	900°C	1 min	11.2
SiO _x	150	930°C	1 min	26.2
SiO _x	150	900°C	2 min	19.8
SiO _x	300	900°C	1 min	10.8
SiO _x	300	930°C	1 min	24.1
SiN _x	150	900°C	1 min	8.1
SiN _x	150	930°C	1 min	-11.2
SiN _x	150	900°C	2 min	-16.3

InGaAs SQW Structure

A number of intermixing experiments were performed using a GRINSCH structure having an 8 nm thick SQW of In_{0.2}Ga_{0.8}As. PL measurements reveal that a wavelength shift as high as 90 nm can be obtained when performing an annealing step at 900°C for two minutes. These measurements show that a wavelength shift occurs also even when no SiO_x layer is covering the sample. Although this shift is not as important as the one obtained when using the SiO_x layer, it remains undesirable when eventually this technique would be applied to protect the mirrors of high power lasers. This intermixing is probably due to thermal alloying effect.

As our interest was more towards devices we create an intermixing in a sample using a 110 nm thick SiO_x layer and an annealing step at 900°C for two minutes. Subsequently ridge waveguide lasers were processed from an intermixed sample having a ridge width of 4 µm. In parallel a reference sample was processed into 50 µm wide lasers. Laser spectrum measurements showed that the intermixed laser emits at 932 nm while the reference laser emits at 975 nm. Figure 2 shows laser spectra of the two samples.

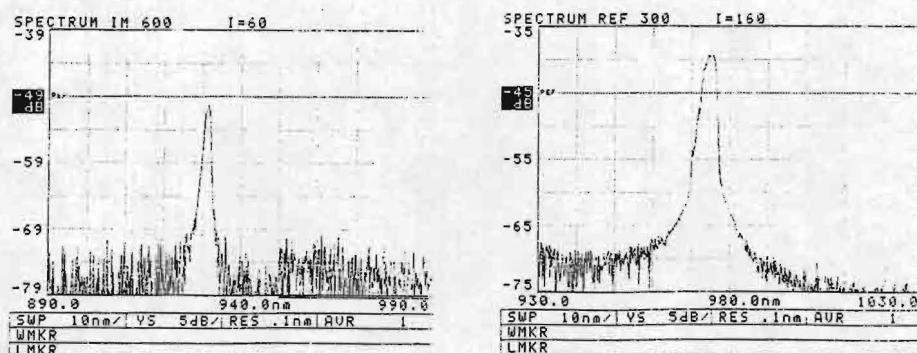


Figure 2- Laser spectra of an intermixed laser (left) and a reference laser (right).

Conclusions

An impurity free interdiffusion technique was successfully applied to GaAs-based structures using a SiO_x layer followed by an annealing step at 900°C . A large wavelength shift was obtained as well with GaAs as with InGaAs quantum well structures. We applied this technique to a laser structure and a wavelength shift of more than 40 nm was achieved.

Acknowledgements

The authors would like to thank M. Buda for useful discussions and E. Smalbrugge and B.H. v. Roy for technical assistance.

References:

- [1] D.G. Deppe and H. Holonyak Jr., J. Appl. Phys. **64**, R93 (1988).
- [2] I. Harrison, H.P. Ho, B. Tuck, M. Henini and O.H. Hughes, Semicond. Sci. Technology, **4**, 841 (1989).
- [3] H.H. Tan, J.S. Williams, C. Jagadish, P.T. Burke and M. Gal, Appl. Phys. Lett. **68**, 2401 (1996).
- [4] M. Kuzuhura, T. Nozaki and T. Kamejima, J. Appl. Phys. **66**, 5833 (1989).
- [5] H. Marsh, Semicond. Sci. Technology, **8**, 1136 (1993).

Polarization memory in vertical-cavity semiconductor lasers

R.F.M. Hendriks, M.P. van Exter and J.P. Woerdman

Leiden University, Huygens Laboratory, P.O. Box 9504, 2300 RA Leiden, The Netherlands

Polarization properties of semiconductor vertical-cavity surface-emitting lasers (VCSELs) have recently attracted a lot of attention. Based on a polarization model developed by San Miguel, Feng and Moloney (SFM) [1] theoretical work has been performed by various groups [2,3]. The SFM model treats the quantum-well gain medium as a discrete-level system. A nonequilibrium population of the magnetic sublevels, as produced by the optical field via saturation, corresponds to a nonlinear anisotropy and thus affects the polarization. Experimentally it has been observed, however, that unintentional linear anisotropies dominate the polarization of currently used VCSELs. For this reason critical experimental tests of the SFM model have not yet been reported.

The important parameter in the SFM model is the normalized spin relaxation rate Γ_s (i.e. normalized with respect to the inversion decay rate), which describes the relaxation of population differences of magnetic sublevels. Γ_s is a phenomenological parameter that models a variety of microscopic relaxation processes for electrons and holes. From the laser-physics point of view [2] the spin relaxation rate determines the degree of spin hole burning and thus the ratio, ξ , of cross- and self-saturation of two circularly polarized laser modes. Knowledge of Γ_s is thus essential to understand the nonlinear aspects of the polarization properties of VCSELs. If Γ_s is close to unity the saturation intensity is strongly polarization dependent, while for $\Gamma_s \gg 1$ the saturation is nearly independent of the polarization of the laser modes [1].

In this paper we report on a direct measurement of the parameters that govern the nonlinear aspects of the polarization properties of VCSELs, including Γ_s .

By using pump light with a definite polarization we create a non-equilibrium population distribution of the carriers. If we use linearly(circularly)-polarized pump light a non-equilibrium momentum (spin) distribution is created. The important point here is that we create these non-equilibrium population distributions by an external force, that is: *not* via the saturation due to the optical field of the VCSEL itself. Therefore the anisotropy due to the non-equilibrium carrier distribution will show up in the linear part of the polarization physics of the VCSEL, which greatly simplifies the interpretation of the data.

The VCSEL wafer, as grown by MOVPE, consists of three 8-nm thick GaAs QWs centered in a $1-\lambda$ cavity of $\text{Al}_{0.18}\text{Ga}_{0.82}\text{As}$, with the top (bottom) DBRs consisting of 20(25.5) pairs of $\text{Al}_{0.18}\text{Ga}_{0.82}\text{As}/\text{AlAs}$ layers. It operated best at a temperature of -5°C . At this temperature the output wavelength was 857 nm and the pump wavelength 762 nm (i.e. we deal with strongly non-resonant pumping). The output power of the VCSEL was 50 μW at a pump power of 45 mW in a pump spot with a radius of 3.0 μm . The threshold pump power was 32 mW.

For linearly polarized pump light the VCSEL emitted in two modes, linearly polarized along the birefringence axes: a strong lasing mode and a weak "nonlasing" mode at slightly higher frequency. The splitting between the modes was $\Delta\nu = 1.6 \pm 0.4$ GHz. In ω -units the birefringence is expressed as $\sigma = \pi \Delta\nu = (5.0 \pm 1) \cdot 10^9 \text{s}^{-1}$. By applying pressure on

the edges of the wafer piece we could vary the birefringence, σ , between $3.1 \cdot 10^9 \text{s}^{-1}$ and $47 \cdot 10^9 \text{s}^{-1}$.

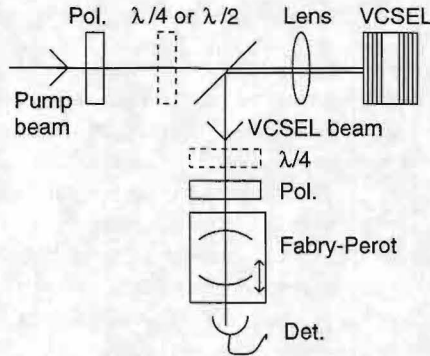


FIG. 1. Experimental setup.

Fig.1 shows the experimental setup. A $\lambda/4$ -plate or $\lambda/2$ -plate is used to set the polarization ellipse of the pump light. The polarization modes of the VCSEL are analyzed by means of a $\lambda/4$ -plate, a polarizer and the Fabry-Perot interferometer. Due to intensity fluctuations of the VCSEL output the accuracy of the ellipticity measurement is limited to 1° .

When using pump light with elliptical polarization both the lasing and the nonlasing VCSEL mode were found to be elliptically polarized. Within our detection accuracy the two modes were orthogonally polarized, i.e. the principal axes of the two ellipses were mutually orthogonal and the handednesses were opposite. The handedness of the lasing mode was equal to the handedness of the reflected pump light.

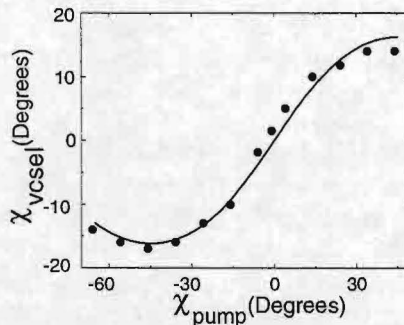


FIG. 2. Dependence of the ellipticity of the VCSEL output (χ_{VCSEL}) on the ellipticity of the pump light (χ_{pump}) for a birefringence $\sigma = 19 \cdot 10^9 \text{s}^{-1}$.

The memory effect for the pump beam ellipticity is illustrated in Fig. 2 for a birefringence of $\sigma = 19 \cdot 10^9 \text{s}^{-1}$. The ellipticity is expressed as $\chi = \arctan(E_y/E_x)$, with E_x and E_y the field amplitudes along the axes of the polarization ellipse. The black dots denote the ellipticity of the high-frequency mode of the VCSEL as a function of the ellipticity of the pump light. The amplitude of the sinusoidal fit is $\chi = 16^\circ \pm 1^\circ$.

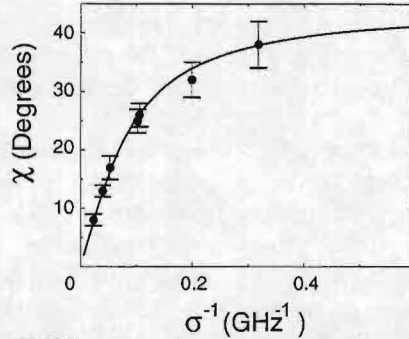


FIG. 3. Ellipticity of the VCSEL output (χ_{VCSEL}) versus linear birefringence for right-handed circularly polarized pump light.

Experiments like those presented in Fig. 2 have been repeated for different values of the birefringence. This birefringence could be adjusted by applying strain to the VCSEL. In Fig. 3 the amplitude of the sinusoidal fit as obtained from Fig. 2 has been plotted as a function of the inverse of the birefringence. We found that the ellipticity decreases when increasing the birefringence.

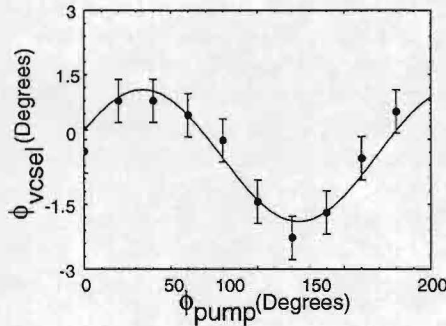


FIG. 4. Orientation of the VCSEL polarization (ϕ_{VCSEL}) versus the orientation of the linearly polarized pump beam (ϕ_{pump}) for a birefringence of 6.6 GHz .

We also measured a memory effect for the orientation of linearly polarized pump light. In Fig. 4 this effect is shown for a birefringence of $\sigma = 6.6 \cdot 10^9 \text{ s}^{-1}$. The horizontal axis displays the orientation of the pump polarization ϕ_{pump} and the vertical axis the orientation of the VCSEL output ϕ_{VCSEL} . The offset of this curve (i.e. the VCSEL polarization averaged over ϕ_{pump}) is determined by the strain-induced birefringence in the VCSEL. This is concluded from the fact that if we rotated the VCSEL wafer over a certain angle around its normal this offset is changed by the same angle. The deviation of the ϕ_{VCSEL} from this average is towards ϕ_{pump} . The magnitude of the deviation, i.e. the amplitude of the sinusoidal fit, was found to be $1.5^\circ \pm 1^\circ$ (Fig. 4). The observed memory effect for the linearly polarized pump light is roughly an order of magnitude smaller than the memory effect for the pump beam ellipticity. This effect cannot be explained within the SFM model.

From the SFM model with circularly polarized pump light we determine the polarization eigenmodes. The solid curve in Fig. 3 is a fit of the theoretical ellipticity to the experimental data, using $\kappa\alpha/\Gamma_s$ as a fit parameter, while assuming $\alpha \gg 1$. This yields $\kappa\alpha/\Gamma_s = 12 \pm 1 \cdot 10^9 \text{s}^{-1}$.

Within the SFM model the quantity that has been determined directly from Fig. 3, $\kappa\alpha/\Gamma_s$, is also the important parameter governing the influence of the polarization dependent saturation, when using unpolarized optical pumping or electrical pumping. This ratio determines directly the stability boundary for two linearly polarized modes [1,3], and also the red-shift of the nonlasing mode [2]. An estimate of Γ_s itself implies a larger error margin due to uncertainties in α (we take $\alpha = 3.5$) and in particular, in κ . The value for the cavity loss rate, κ , can be determined from the estimated mirror reflectivity, $R = 99\%$ yielding $\kappa = 1 \cdot 10^{12} \text{s}^{-1}$. Thus we find $\Gamma_s = 290 \pm 100$. If we take for the population decay rate $\gamma_{\parallel} = 1 \cdot 10^9 \text{s}^{-1}$ this yields for the spin relaxation rate (γ_s [3] or γ_J [4]) a value of $(290 \pm 100) \cdot 10^9 \text{s}^{-1}$. This rate is about an order of magnitude faster than estimated in Refs. [1,3]; it corresponds to a spin flip time of approximately 3 ps.

To conclude, we have observed a memory effect for the polarization of the pump light on the polarization of an optically pumped VCSEL. By using the flexibility allowed by the optical pumping scheme we could compare the strength of the memory effect for the ellipticity of the pump light to predictions from the SFM model. This yields a direct measurement of the most important parameter in the SFM model, $\kappa\alpha/\Gamma_s = (12 \pm 1) \cdot 10^9 \text{s}^{-1}$, and an estimate for the normalized spin flip rate, $\Gamma_s = 290 \pm 100$. We also observed a weaker memory effect for the orientation of linearly polarized pump light, which cannot be explained within the SFM model. Although our measurements have been performed on optically pumped VCSELs the conclusions drawn in this paper are also essential input for understanding polarization properties of electrically pumped devices. Due to the fast thermalization of the carriers in conduction and valence band microscopic details of the pump mechanism (i.e electrical or optical pumping) are not expected to influence the polarization properties. Thus measurements on the parameters that determine the polarization dependent saturation in optically pumped VCSELs are also relevant in electrically pumped devices.

-
- [1] M. San Miguel, Q. Feng and J.V. Moloney, *Phys.Rev.A* **52**, pp. 1728-1739, (1995).
 - [2] M.P. van Exter, R.F.M. Hendriks and J.P. Woerdman, submitted to *Phys.Rev.A*.
 - [3] J. Martin-Regalado, F.Prati, M. San Miguel and N.B. Abraham, *IEEE J. Quantum Electron.*, **33**, pp. 765-783 (1997).
 - [4] A.K. Jansen van Doorn, M.P. van Exter, M. Travagnin and J.P. Woerdman, *Opt. comm.* **133**, pp. 252-258, (1997).

Polarization Excess Quantum Noise

A.M. van der Lee¹, N.J. van Druten, A.L. Mieremet, M.A. van Eijkelenborg, Å.M. Lindberg, M.P. van Exter and J.P. Woerdman

Huygens Laboratory, Leiden University,

¹ email: lee@molphys.LeidenUniv.nl

The quantum noise in a laser-mode is enhanced when the resonator eigenmodes are nonorthogonal. Experimentally we demonstrate a 60-fold enhancement of the quantum-limited laser linewidth for nonorthogonal *polarization* eigenmodes. Theoretically this is described by a simple two-mode model.

The linewidth of a laser is fundamentally limited by spontaneous emission in the laser mode. In a laser above threshold this corresponds to the well-known result of the one extra noise photon in the lasing mode. Surprisingly, a resonator with *nonorthogonal* modes was predicted to have K noise photons in the lasing mode instead of one [1]. This so called excess noise factor or K -factor caused controversy in the beginning as it seemed to contradict the fundamental result of the one noise photon in the mode.

Recently, large excess noise factors have been convincingly demonstrated for the first time in *unstable* resonators [2,3], i.e. a resonator where the usual concave mirrors have been replaced by convex mirrors. In these experiments the origin of the excess noise factor can be directly traced back to the nonorthogonality of the transverse resonator eigenmodes. The physical interpretation is, however, still much less clear. One of the complicating factor seems to be the intrinsically complicated structure of the transverse eigenmodes when large excess noise factors occur. Instead of nonorthogonal *spatial* modes (transverse K , longitudinal K), we study here the case of nonorthogonal *polarization* modes.

It is well known that the polarization dynamics of a laser can be described as a two-mode system. We have found that when the two polarization modes are coupled by a combination of dissipative coupling and conservative coupling, the eigenmodes can become degenerate and consequently very large excess noise factors arise [4]. To verify this prediction

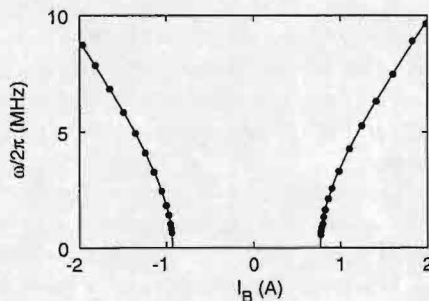


FIG. 1. Fundamental rotation frequency ω of the polarization as function of the current (I_B) generating the axial magnetic field. Circles: measured frequencies. The solid curve: fit to theory, from which all relevant laser parameters can be determined.

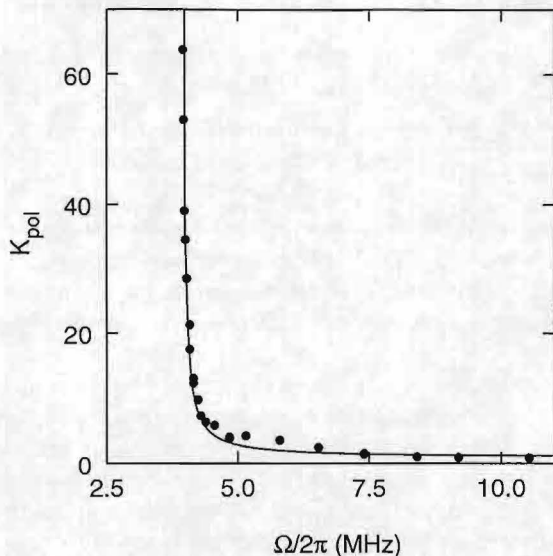


FIG. 2. Measurement of the polarization excess-noise factor, K_{pol} which shows strong enhancement of the quantum noise as a function of the Faraday rotation Ω , which is proportional to the applied magnetic field. The solid curve is the theoretical expectation from mode nonorthogonality theory, it contains no adjustable parameters: all the relevant laser parameters were determined from the fit in Fig. 1.

experimentally, we used a miniature He-Xe gas laser operated on the 3.51- μm laser transition. The polarization modes were dissipatively coupled by introducing a glass plate near Brewster angle in the (stable) cavity, this creates a difference in loss between two orthogonal linear polarizations. The conservative coupling is achieved by applying an axial magnetic field along the resonator. The resulting Faraday rotation of the He-Xe gas caused a difference in refractive index of the right and left-handed circularly polarized modes. By tuning the magnetic field the ratio of conservative and dissipative coupling could be controlled and this determined the nonorthogonality of the polarization modes.

The polarization-anisotropic saturation, that is present in our gas laser, forces the polarization of the laser light to be linear. As a consequence the polarization will rotate above a critical value of the magnetic field. The polarization rotation is measured by routing the laser light through a polarizer. In Fig. 1 the rotation frequency of the polarization as function of the magnetic field is shown.

We determine the quantum linewidth of the laser from the spectral width of the rotation frequency of the polarization. By plotting the quantum noise as function of the magnetic field in Fig. 2 an large increase in the quantum noise can be seen. An maximum enhancement of about factor 60 was achieved. The drawn curve in this figure corresponds to the K-factor predicted from the simple two-mode model. Note the excellent agreement with the experimental data. A more detailed calculation, including the anisotropic gain saturation yields similar agreement [4].

An application of polarization excess noise could be to reduce the coherence of semicon-

ducteur vertical-cavity surface-emitting lasers (VCSELs); coherence is generally an undesirable property of VCSELs in an optical recording/reading system because it increases their sensitivity to optical feedback. The near-degeneracy of polarization eigenmodes could here be obtained, e.g., by using a linear birefringence and a linear dichroism at 45° [5].

In conclusion we have shown that nonorthogonal polarization modes give also rise to large excess noise factors. The polarization variant has the charm of being two-mode system yielding a simple theoretical model, which describes the experimental data excellently.

-
- [1] A. E. Siegman, Phys. Rev. A **39**, 1253, 1264 (1989) and references therein.
 - [2] Y.-J. Cheng, C. G. Fanning, and A. E. Siegman, Phys. Rev. Lett. **77**, 627 (1996).
 - [3] M. A. van Eijkelenborg, Å. M. Lindberg, M. S. Thijssen, and J. P. Woerdman, Phys. Rev. Lett. **77**, 4314 (1996).
 - [4] A. M. van der Lee *et al.*, Phys. Rev. Lett. (tentatively scheduled for 24 November 1997).
 - [5] A. K. Jansen van Doorn, M. P. van Exter, A. M. van der Lee, and J. P. Woerdman, Phys. Rev. A **55**, 1473 (1997).

Non-linear optical properties of dendrimeric structured chromophores

A.W. GERBRANDIJ, A. PUGŽLYS AND C.A.G.O. VARMA
*Leiden Institute of Chemistry
 Leiden University
 Leiden, the Netherlands*

S.J.E. MULDER, A.J. BROUWER AND R.M.J. LISKAMP
*Utrecht Institute for Pharmaceutical Sciences
 Utrecht University
 Utrecht, the Netherlands*

Abstract

The second-order NLO properties of dendrimeric structures functionalized with NLO-chromophores are investigated by using the hyper-Rayleigh scattering technique at two different spectral regions. Second-order hyperpolarizabilities of different generations NLO-dendrimers are presented.

Introduction

There is an increasing interest in applying nonlinear optics (NLO) phenomena in technological fields concerning e.g. fiber-optic data transmission for telecommunications and optical sensors. NLO-devices are based on the nonlinear response of the polarization \mathcal{P} on an incoming electrical (optical) field E :

$$\mathcal{P} = \chi^{(1)}E + \chi^{(2)}EE + \chi^{(3)}EEE + \dots$$

where $\chi^{(i)}$ is the i th order susceptibility. In order to have a useful and efficient material, the NLO-susceptibilities must be large and at the same time absorption of the optical wavelengths at interest should be neglectable. Essential requirements for practical NLO materials are temporal and chemical stability, ease of processing and low cost. Organic materials may meet these demands [1].

Second-order NLO-processes such as second harmonic generation (SHG) and the electro-optic (EO) effect demand NLO-materials possessing a large $\chi^{(2)}$. The constituting molecules of an organic material must have a large second-order hyperpolarizability β and must be closely packed in a non-centrosymmetric fashion. The latter is required since centrosymmetry excludes the second-order NLO effect.

Much progress has been made in the synthesis of organic NLO materials by attaching NLO-chromophores to e.g. linear polymer chains. Instead of the linear chains, here three-dimensional polymeric structures are used to support the NLO-chromophores. These types of structures are referred to in literature as dendrimers and exist in different generations depending on the number of endgroups. Figure 1.a shows how the NLO-chromophores may be closely packed on the dendrimer surface and point in a direction which prevents centrosymmetry. Figure 1.b shows how these NLO-dendrimers may be stacked to obtain a bulk second-order NLO material.

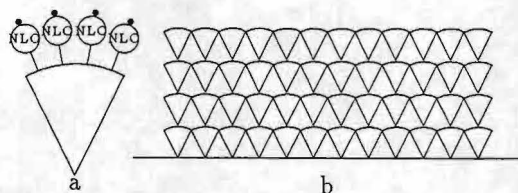


Figure 1: (a) Schematic representation of a NLO-dendrimer. (b) Dendrimers in a layer-structure.

NLO dendrimer	solvent	β (10^{-30} esu)	# of NLO- chromophores	β/β_{pNA}	depolarisation ratio
pNA	DMSO	50	1	1	
1	DMSO	83	2	1.7	0.22
2	DMSO	109	4	2.2	0.23
pNA	CHCl ₃	34	1	1	
3	CHCl ₃	76	2	2.2	0.24
4	CHCl ₃	82	2	2.4	0.28
5	CHCl ₃	121	4	3.5	0.26
6	CHCl ₃		8		0.39

Table 1: First hyperpolarizabilities β for the NLO-dendrimers and their depolarisation ratios.

Hyper Rayleigh scattering

The first hyperpolarizability of a molecule may be derived from the intensity of the hyper-Rayleigh scattering (HRS) from a liquid solution of the molecule. The HRS of solutions is studied by focussing a pulsed laserbeam from either a Nd:YAG ($\lambda = 1064$ nm) or an amplified Ti:Saffire ($\lambda = 810$ nm) laser source into a glass cell containing a sample of dendrimers dissolved in dimethyl sulfoxide (DMSO) or chloroform (CHCl₃). The very weak scattered signal arising from HRS is collected by a lens system and focussed on the entrance slit of a monochromator. A photomultiplier tube is interfaced in a single photon counting system to detect the HRS photons. The resulting signal S can be written as

$$S = GI^2 (N_{NLO} \langle \beta_{NLO}^2 \rangle + N_s \langle \beta_s^2 \rangle)$$

where G is a proportionality factor, I the laser beam intensity, N_{NLO} and N_s the number of NLO-molecules and solvent molecules in the scatter volume respectively and $\langle \beta^2 \rangle$ an orientational average of the squares of the first hyperpolarizability tensor components. If β_s is known, β_{NLO} can be deduced from S at different N_{NLO} .

The depolarisation ratio is the ratio of S polarized perpendicular and parallel to the laserbeam polarisation. A depolarisation ratio close to 0.20 means that only one of 27 β -tensor components is dominant and the molecule can be considered 'linear'.

NLO dendrimers

The compound 3,5-bis(2-*tert*-butyloxycarbonyl aminoethoxy) benzoic acid methyl ester [3, 4] has been used as the building block of our dendrimeric structures. Various generations of

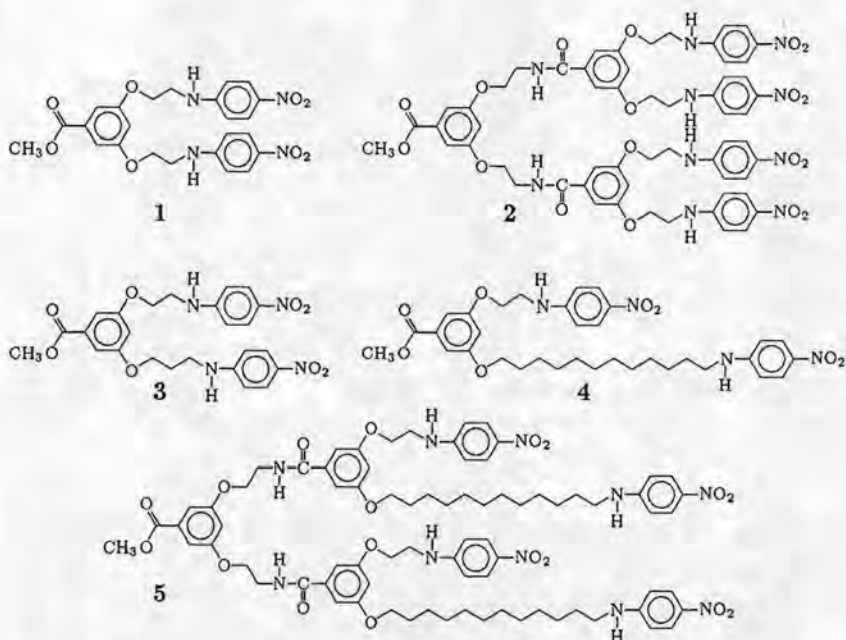


Figure 2: Chemical structures of the first (1) and second (2) generations NLO-dendrimers and the first generations UCL NLO-dendrimers (3 and 4) and the second generation UCL NLO-dendrimer (5).

these dendrimers have been used as the skeleton supporting the NLO-chromophores. The well-studied molecule paranitroaniline (pNA) has been chosen as the NLO-chromophore.

The NLO-dendrimers are shown in figure 2. NLO-dendrimers 1 and 2 cannot be enlarged to higher generations due to their poor solubility. However, by changing the alkyl chain length of one of the NLO-chromophores on the surface building block the solubility of the NLO-dendrimers is enhanced: the unequal chain length (UCL) NLO-dendrimers 4 and 5 can be synthesized up to the third generation with 8 NLO-chromophores (6, not shown).

Table 1 shows the β values of the NLO-dendrimers 1 through 5 obtained from HRS at a fundamental wavelength of 1064 nm. Going to higher generations the first hyperpolarizability increases. The UCL NLO-dendrimers 3, 4 and 5 have, relative to pNA, a larger β compared to 1 and 2. For the first generation UCL NLO-dendrimers 3 and 4 β is even larger than twice the hyperpolarizability of the pNA chromophore. The enhanced β in the UCL-case can be due to better alignment of the NLO-chromophores on the surface building blocks caused by dipole-dipole interaction or an increase of β of the chromophore with the longer alkyl chain. The latter is shown in figure 3 where the first hyperpolarizability relative to pNA of the first generation dendrimers 1, 3 and 4 is shown as a function of the number of carbon atoms in the alkylchain n , as well as a semi-empirical quantum chemically calculated value of β for first generation NLO-dendrimers and N-CH₃(CH₂) _{$n-1$} -4-nitroaniline.

The first hyperpolarizabilities obtained from HRS at 810 nm for 1 and 2 in DMSO are 325 and 361 (10^{-30} esu) respectively. These values are much higher than those at 1064

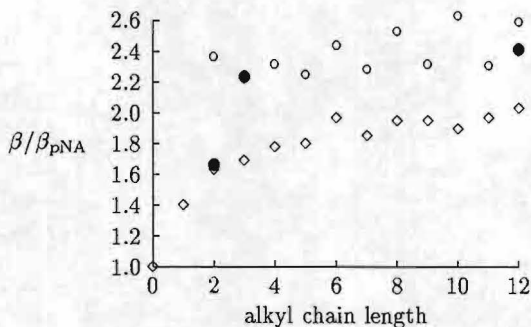


Figure 3: β relative to β_{pNA} as function of the number of $-\text{CH}_2-$ groups in the alkyl chain. (●) Measured for first generation NLO-dendrimers. (○) Calculated for first generation NLO-dendrimers. (◇) Calculated for N-alkyl-4-nitroaniline.

nm which can be attributed to resonance enhancement since the absorption maxima of 1 and 2 dissolved in DMSO are around 395 nm.

The depolarisation ratios indicate that the NLO-dendrimers 1 through 5 approach 'linear' molecules. Note that the third generation UCL NLO-dendrimer with 8 NLO-chromophors (6) has a slightly larger depolarisation ratio, which indicates that these dendrimers deviate substantially from the ideal conical structure showed in figure 1.

Conclusion

Hyper-Rayleigh scattering measurements on new second-order NLO-molecules existing of NLO-chromophores attached on the surface of a conical dendritic backbone reveal that the second-order NLO hyperpolarizability increases with the dendrimer generation. The hyperpolarizability and the solubility can be increased using a different length of the connection of two adjacent NLO-chromophores on the surface building blocks. The total hyperpolarizability of the molecule can even exceed the sum of the polarizabilities of the individual chromophores in the NLO-dendrimer. Going to higher generation obstructs the conical shape and is not advantageous in view of non-centrosymmetry.

References

- [1] P.N. Prasad and D.J. Williams, *Introduction to nonlinear optical effects in molecules and polymers*, John Wiley & Sons, New York (1991)
- [2] K. Clays and A. Persoons, *Hyper-Rayleigh scattering in solution*, Physical Review Letters, **66**, 23, pp. 2980-2983, (1991)
- [3] S.J.E. Mulders, A.W. Brouwer, G.J. van der Meer and R.M.J. Liskamp, *Synthesis of a novel amino acid based dendrimer*, Tetrahedron Letters, **38**, 4, pp. 631-634 (1997)
- [4] S.J.E. Mulders, A.W. Brouwer and R.M.J. Liskamp, *Molecular diversity of novel amino acid based dendrimers*, Tetrahedron Letters, **38**, 17, pp. 3085-3088 (1997)

Germanium Gallium Sulfide glasses as host materials for Pr-doped optical fiber amplifier

R.C. Schimmel^a, A.J. Faber^b

^a Eindhoven University of Technology, Telecommunications Technology and Electromagnetics division, PO Box 513, 5600 MB Eindhoven, The Netherlands.

^b TNO-Institute of Applied Physics, PO Box 595, 5600 AN Eindhoven, The Netherlands.

Ge-Ga-S glasses have been prepared, which are promising host materials for flat gain Pr-doped optical fiber amplifiers at 1.3 micron (quantum-efficiency up to 63%). Thermal properties are evaluated for fiber-drawing. It is predicted that low-loss Ge-Ga-S fibers can be drawn around 500 °C.

1. Introduction.

Chalcogenide glasses are promising low phonon energy host materials for an efficient 1.3 μm Praseodymium Doped Fiber Amplifier (PDFA). When compared with fluoride glasses, the quantum efficiency of the 1.3 μm transition in chalcogenide glasses is much higher. Furthermore, due to the high refractive index ($n > 2$), chalcogenide glasses have a large cross section for stimulated emission.

Gallium lanthanum sulfide (Ga-La-S) and germanium gallium sulfide (Ge-Ga-S) glass systems have been investigated by various groups [1]. Since 1991 the Ge-Ga-S glass system is studied in our laboratories and a procedure for glass formation has been developed.

Simons reported an emission lifetime for $(\text{GeS}_2)_{80}(\text{Ga}_2\text{S}_3)_{20}$ glasses of 360 μs [2], resulting in a quantum efficiency of 63 %. Model calculations on the Pr-doped Ge-Ga-S show a flattened gain spectrum (3 dB gain bandwidth of approx. 50 nm) if the PDFA is operated in the saturated regime, which is an important result for WDM applications [2]. Recently, efficient optical amplification (emission lifetime 300 μs , quantum efficiency 56 %) has been reported by Tawarayama et al. in gallium sodium sulfide (Ga-Na-S) glasses [3].

Germanium gallium sulfide glasses show a high thermal stability which is important for fiber drawing properties. The solubility for Pr-ions in germanium-sulfide based glasses is limited compared to Ga-La-S [4] and Ga-Na-S glasses, but it is enhanced by gallium addition [5].

The objective of this paper is to describe some thermal properties of two selected germanium gallium sulfide (Ge-Ga-S) glass compositions, which are important for optimization of the glass formation and fiber drawing procedures.

2. Experimental procedure

Glasses of composition $(\text{GeS}_{2.5})_{98}(\text{Ga}_2\text{S}_3)_2$ and $(\text{GeS}_3)_{98}(\text{Ga}_2\text{S}_3)_2$ were prepared in small batches (< 10 grams) loaded in silica ampoules. High purity (99.999%) elemental materials, stored in a glovebox under argon atmosphere, were used as starting materials. Both glasses have a sulfur contents above the stoichiometric value (S-excess). After evacuation and sealing, the ampoules were slowly heated to 1000 °C in a rotating

furnace. After 12 hours of melting the ampoules were quenched in air to the annealing temperature, followed by slow cooling to ambient temperature.

3 Thermal characterization

3.1. Viscosity

For fiber drawing the temperature dependence of the viscosity η is an important parameter. At the fiber drawing temperature T_f (defined as the temperature at which $\eta = 10^7$ Pa.s) the viscosity of the glass is sufficiently low to draw the fiber. The viscosity-temperature dependence of a $(\text{GeS}_3)_{98}(\text{Ga}_2\text{S}_3)_2$ sample was measured by Optical Research Centre of the University of Southampton [6] by parallel plate rheometry using a Perkin-Elmer TMA-7 thermo-mechanical analyser.

The viscosity-temperature dependence of a $(\text{GeS}_3)_{98}(\text{Ga}_2\text{S}_3)_2$ glass sample is shown in figure 1. The fiber drawing temperature T_f , derived from this figure, is 465 °C. The predicted glass transition temperature T_g (defined as the temperature at which $\eta = 10^{12.4}$ Pa.s) is 275 °C. The fiber drawing temperature of the $(\text{GeS}_{2.5})_{98}(\text{Ga}_2\text{S}_3)_2$ glass was estimated to be 515 °C.

3.2. Glass transition and crystallization temperatures

The difference between the glass transition temperature and the crystallization temperature is an indication of the stability of the glass.

The glass transition temperature was determined by dilatometry using a Bähr 801 V dilatometer. Samples of an initial length of about 25 mm and a diameter of 8 mm were heated in the measuring chamber of the dilatometer.

At the glass transition temperature the expansion coefficient changes. The glass transition temperature is determined by linear extrapolation of the expansion data (see figure 2). The T_g values are presented in table 1.

For further characterization of the glass stability a Netsch Simultaneous Thermal Analyzer (Type STA409) was used. Combined differential thermal analysis (DTA) and thermogravimetric analysis (TGA) measurements were performed on powdered samples of the glass ($d < 200 \mu\text{m}$). The samples were heated in stainless steel crucibles while the furnace was flushed with argon (flow rate 50 ml/min). The heating rate was 5 °C/min over the temperature interval from 25 - 800 °C. A typical DTA/TGA plot is shown in figure 3.

The resolution of the DTA apparatus was too small to determine a step like change in the DTA-signal at the glass transition temperature.

The first exothermic peak in the DTA-signal is assigned to the crystallization of the material at the crystallization temperature T_x . The T_x values are presented in table 1.

The liquidus temperature of the glass can not be measured accurately due to decomposition of the materials. Comparison of figure 3 to other TGA-data (not presented here) show that decomposition of the material at elevated temperatures is

dependent on the sulfur excess. No mass loss occurs until about 500 °C for sulfur-rich glasses, while the glasses with less sulfur excess are stable up to 550 °C.

The glass transition temperatures and crystallization temperatures of both studied glass compositions are summarized in table 1.

Table 1. Glass transition- and crystallization temperatures

Composition	T_g (°C)	T_x (°C)	ΔT (°C)
$(\text{GeS}_3)_{98}(\text{Ga}_2\text{S}_3)_2$	285	510	225
$(\text{GeS}_{2.5})_{98}(\text{Ga}_2\text{S}_3)_2$	325	550	225

4. Discussion and conclusions

From table 1 it can be seen that for the selected glasses a difference between T_g and T_x of 225 °C is found, which is a favorably large difference for chalcogenide glasses. For gallium lanthanum sulfide glasses the corresponding value is 120 °C [7].

The $(\text{GeS}_3)_{98}(\text{Ga}_2\text{S}_3)_2$ glass, which has the highest sulfur content, has the lower characteristic temperatures. This is in agreement with [8] in which it is shown that barium gallium germanium sulfide glasses have a maximum in glass transition temperature for glasses with a small sulfur excess.

The glass transition temperature of the $(\text{GeS}_3)_{98}(\text{Ga}_2\text{S}_3)_2$ glass measured with dilatometry corresponds well with the value estimated from the viscosity data $T_g = 275$ °C

In the fiber drawing process a preform with a core - cladding (step-index) structure is constructed and heated in a small furnace. For the selected glasses the fiber drawing temperature T_f is approximately 465 - 515 °C, which is about 50 °C below the measured crystallization temperature $T_x = 510 - 550$ °C. It is expected that at the fiber drawing temperature no noticeable formation of crystals in the fiber will occur. In this way low-loss fibers can be produced.

Praseodymium doped germanium gallium sulfide glasses have been prepared successfully with good optical quality. The materials show a high thermal stability, which is important in the fiber drawing process. The fibers can be drawn at temperatures up to 500 °C. Praseodymium doped germanium gallium sulfide glasses are very promising host materials for an efficient PDFA.

- [1] J.S. Wilkinson, M. Hempstead, "Advanced materials for fibre and wave guide amplifiers", *Current opinion in Solid State & Materials Science*, 2 (1997) 194-199.
- [2] D.R. Simons, Germanium Gallium Sulfide Glasses for Pr-doped Fiber Amplifiers at 1.3 μm , Thesis Technische Universiteit Eindhoven, Eindhoven, 1995.
- [3] H. Tawarayama, E. Ishikawa, K. Itoh, H. Aoki, H. Yanagita, K. Okoda, K. Yamanaka, Y. Matsuoka, H. Toratani, "Efficient amplification at 1.3 μm in a Pr^{3+} -doped Ga-Na-S Fiber" in proceedings of conference "Optical amplifiers and their applications", Victoria, July 1997.

- [4] D. Marchese, G. Kakarantzaz, A. Jha, " ^{147}Sm lifetimes, optical and thermal characteristics of Pr-Doped GeS_2 -chalcogenide glasses", J. Non-Cryst Solids 196 (1996) 314-319.
- [5] D. Marchese, A. Jha, "The structural aspects of the solubility of Pr^{3+} ions in GeS_2 -based glasses", J. Non-Cryst Solids 213&214 (1997) 381-387.
- [6] J. Wang, private communication
- [7] J.A. Medeiros Neto, E.R. Taylor, B.N. Samson, J. Wang, D.W. Hewak, R.I. Laming, D.N. Payne, E. Tarbox, P.D. Maton, G.M. Rob, B.E. Kinsman, R. Hanney, "The application of Ga:La:S-based glass for optical amplification at 1.3 μm J. Non-Cryst. Solids 184 (1995) 292-296.
- [8] B.G. Aiken, R.S. Quimby, "Rare-earth-doped multicomponent Ge-based sulphide glasses", J. Non-Cryst Solids 213&214 (1997) 281-287.

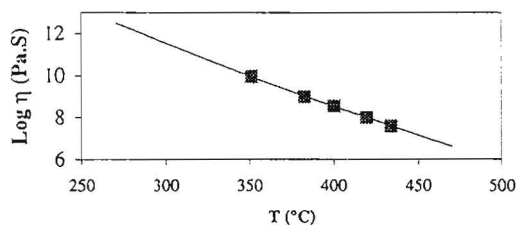


Figure 1: Viscosity vs. Temperature plot for $(\text{GeS}_3)_{98}(\text{Ga}_2\text{S}_3)_2$

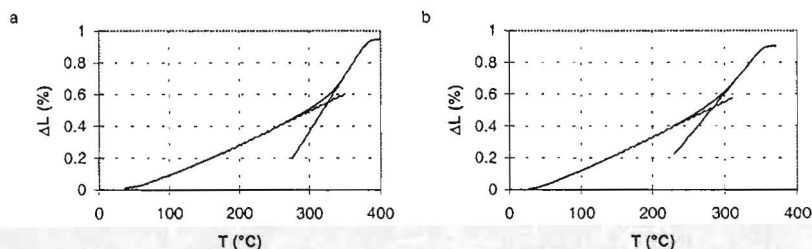


Figure 2: Transition temperature by dilatometry
a) $(\text{GeS}_{2.5})_{98}(\text{Ga}_2\text{S}_3)_2$ b) $(\text{GeS}_3)_{98}(\text{Ga}_2\text{S}_3)_2$

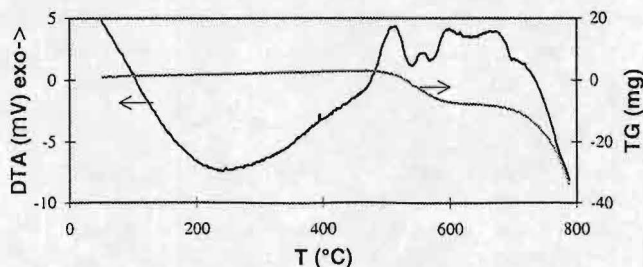


Figure 3: DTA-TGA plot of $(\text{GeS}_3)_{98}(\text{Ga}_2\text{S}_3)_2$ glass

Towards Low PMD Characterisation Techniques for New Generation Optical Fibres

F. Ravet, Y. Choquet, B. Heens, X. Wang, J.-C. Froidure, M. Blondel.

MULTITEL Telecom, Service d'Electromagnétisme et de Télécommunications,

Faculté Polytechnique de Mons, Boulevard Dolez, 31, B-7000 Mons, Belgium.

Tel.: +32 65 37 43 22, Fax.: +32 65 37 41 99, e-mail: ravet@telecom.fpm.ac.be

We implemented the modified interferometer for low PMD optical fibres. We got PMD values from 0.1ps to 0.031ps. We successfully compared this method with measurements we carried out with a broadband wavelength scanning technique.

Since the beginning of the eighties, Polarisation Mode Dispersion (PMD) has appeared as a limiting factor in optical fibre systems. It affects the bit-rate of digital links and contributes to distortions in analogue communications. In order to limit this effect, fibre and cable manufacturers have developed new products with very small PMD, typically lower than $0.1/\text{km}^{1/2}$. This is a most driving factor for cable manufacturers because they should guarantee PMD as low as possible. PMD could also be considered as a quality control parameter. These are the reasons why researches carried out in such a field should be interesting for the standardisation bodies as well as the optical fibre and cable industries. Moreover PMD measurement techniques are currently under discussion in the standardisation committees¹. These last years, efforts have been achieved to improve the PMD interferometric technique and its dual, the Wavelength Scanning Fourier Transform (WSFT) technique, in order to characterise PMD values below $0.1 \text{ ps}^{2,3,4}$. In this paper, we use the modified Michelson interferometer described in reference 3 for the characterisation of single-mode fibres. In fact, the authors of this paper validated the technique by using short Polarisation Maintaining Fibre samples (PMF). We compared our results to measurements we carried out with the WSTF discussed in reference 4.

The Broadband WSFT and the Modified Interferometer Techniques

The first way we propose to follow in this work is the use of the wavelength scanning technique⁴ (figure 1). The basic idea lies in the observation that the wavelength bandwidth of the source is the main limitation in low PMD measurements. The broadband source is composed of coupled $1.3 \mu\text{m}$ and $1.55 \mu\text{m}$ Light Emitting Diodes [LED]. For instance, when measurements are done with a source scanning from 1470 to 1570 nm, the lowest PMD value is about 0.16 ps. Increasing the wavelength window up to 550 nm reduces this limit below 0.03 ps. The measured power density ratio is processed by a Fourier transform analysis. So we got the autocorrelation function. PMD is then completed by computing the second moments of this distribution. The experimental set-up is fully automated. And thus we are able to quickly (less than 3 minutes) measure PMD values below 0.05 ps with a good accuracy due to large spectrum involved in the measurement. Typical results obtained on low PMD fibres are presented in figure 2.

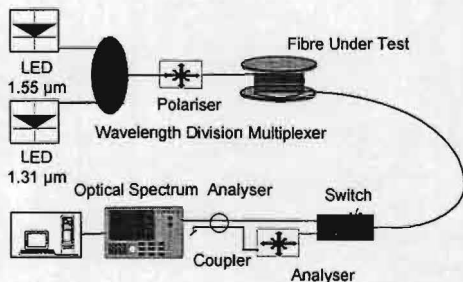


Figure 1. Broadband Wavelength Scanning technique.

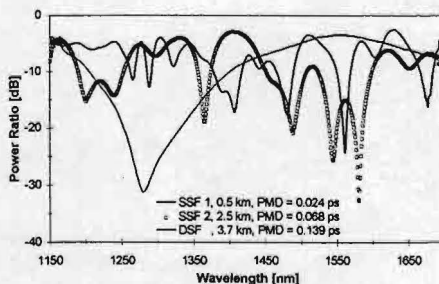


Figure 2. Power density ratio of two SSF's and one DSF.

Another way to proceed³ is to implement the experimental set-up shown in figure 3. Two new elements have been added to the classical interferometer: a polarisation controller and a PMF with $\text{PMD} \gg 0.1$ ps (which is the coherence time of the source). This experimental set-up is based on the following idea: when the PMD of the Fibre Under Test (FUT) is lower than or equal to the coherence time of the source, the FUT behaves as a low mode coupling device. It means that the FUT birefringence and consequently the PMD between the FUT Principal States of Polarisation, also known as the Differential Group Delay (DGD) are constant over the source spectrum. When the fast mode of the FUT PSP is aligned on the fast mode of the PMF PSP, the extension of the typical triplet structure is maximum. On the other hand, when the FUT slow mode is aligned on the PMF slow mode, the triplet structure is minimum. This alignment operation is achieved by using the polarisation controller (composed of three fibre loops). By calculating the difference between maximum and minimum separations, respectively defined as the maximum and minimum distance between the lateral peaks centroid, one gets the FUT PMD four times. The PMD can also be evaluated by calculating the distance between the two left or right peaks. The left part of four interferogrammes is presented in figure 4. These interferogrammes result from four mirror scans of various polarisation controller positions. Practically, one has to measure a large number of interferogrammes in order to be sure of getting the two extrema separation. An alternative way of doing lies in measuring a large number of interferogrammes at various polarisation controller positions. From these datas one has to derive the temporal distance distribution. The PMD is given by the standard deviation of this distribution. An example of such a large sampling is illustrated by figure 5. This figure shows twenty interferogrammes measured for various position of the polarisation controller. The fibre considered in this figure here is a 2500 m SSF measured at $1.55 \mu\text{m}$.

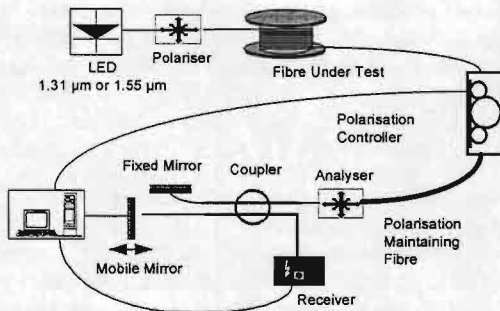


Figure 3. Modified Michelson interferometer.

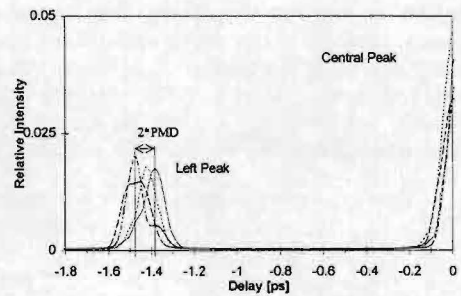


Figure 4. Left part of a set of four interferogrammes; the maximum separation is shown and is twice the PMD.

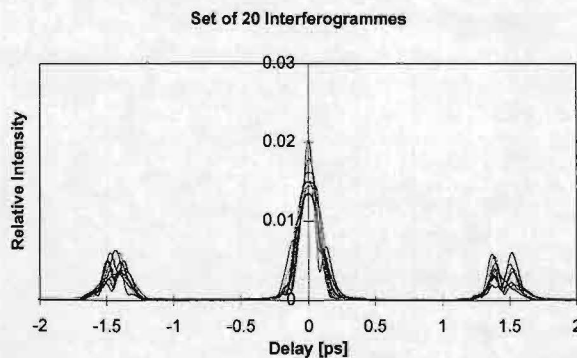


Figure 5. Set of 20 interferogrammes of a 2500 m SSF measured at $1.55 \mu\text{m}$; all these interferogrammes are associated with various positions of the polarisation controller.

Gisin *et al.* have demonstrated that the measurement uncertainty is reduced when the wavelength bandwidth is increased⁵. The relation derived in reference 5 is useful when one has information on the theoretical PMD mean value $\overline{\Delta\tau}$. We have derived an experimentator-oriented relation from this expression. We expressed $\overline{\Delta\tau}$ as a function of $\Delta\tau_{mes}$:

$$\frac{0.2}{\Delta\omega} \left(\sqrt{1 + 5\Delta\tau_{mes}\Delta\omega} - 1 \right)^2 \leq \overline{\Delta\tau} \leq \frac{0.2}{\Delta\omega} \left(\sqrt{1 + 5\Delta\tau_{mes}\Delta\omega} + 1 \right)^2$$

In order to validate this relation, let us consider the following example. When $\Delta\omega = 518 \text{ ps}^{-1}$ (wavelength scanning from 1150 to 1700 nm), $\Delta\tau_{mes} = 0.050 \text{ ps}$ has an uncertainty of about 17 %. When $\Delta\omega = 80 \text{ ps}^{-1}$ (source spectrum extended from 1500 to 1600 nm, typically our 1.55 μm LED), $\Delta\tau_{mes} = 0.050 \text{ ps}$ has an uncertainty of about 41 %. We applied this relation in order to estimate the uncertainty of our PMD measurement results.

Results

We first tested the modified interferometer by implementing the experimental set-up presented in figure 3 at 1.55 μm on a set of optical fibres composed by two Birefringent (PMF) fibres and five Standard Single-Mode Fibres (SSF). All the results are presented in figure 6. Both PMF have PMD coefficient of about 1.6 ps/m. Their respective lengths are 6 cm and 4 cm. The PMD values we got were respectively 0.100 ps and 0.068 ps with a Root Mean Square (RMS) better than 0.011 ps in both cases. These values are very confident with the PMD we could calculate knowing the fibre length. The five SSF's we also characterised are certified to have low PMD by the manufacturer (about 0.05 ps/km^{1/2}). The measured bobbins had lengths comprised between 500 m and 2600 m. We got PMD values from 0.031 to 0.084 ps with a RMS better than 0.006 ps in all the cases. We calculated the PMD mean value uncertainty of each set of measurements by using the relation introduced hereabove. Figure 6 summarises the PMD mean value, the RMS and the calculated uncertainty of the seven fibres. It clearly appears that all the PMD values we measured remain within the calculated uncertainty. The way we followed to estimate the PMD is based on the maximum and minimum separation method (as illustrated by figure 4): in a samples set of at least ten measurements, we extracted the two interferogrammes presenting the largest and the smallest separation. The RMS is calculated here on at least four sets of ten mirror scans.

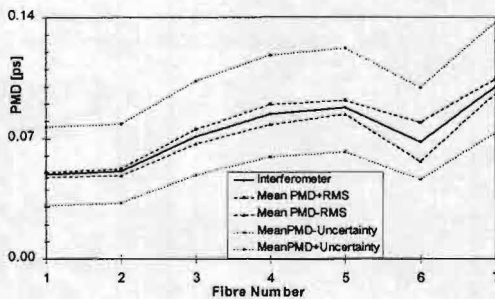


Figure 6. Measurements performed with the modified interferometer; fibres 1 and 2 are two 500 m SSF's; fibres 3 to 5 are three 2 500 m SSF's; fibres 6 and 7 are respectively the 4 and 6 cm PMF's.

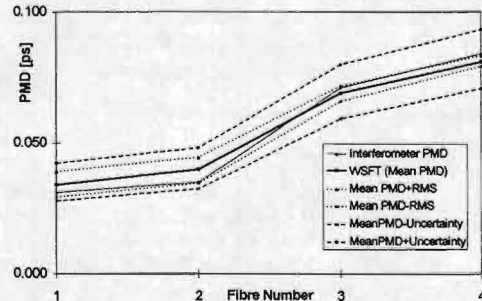


Figure 7. Measurements performed with both techniques; these fibres are the four first fibres presented in figure 5 (two 500 m SSF's and two 2500 m SSF').

Among these fibres, we choose two 500 m SSF and two 2500 SSF and we characterised them by the broadband WSFT. Mean values of PMD from 0.034 to 0.081 ps were achieved with a maximum RMS below 0.005 ps. A worse calculated uncertainty of 21% has been completed. All these results and their comparison with the modified interferometer results are presented in figure 7. In the case of our WFST measurements, we make at least ten scans for each fibre we characterised. It appears in figure 7 that the PMD mean value we got by the interferometric technique remains close to the PMD

mean values derived from WSFT measurements. The RMS is larger in the case of the interferometric measurements (0.011 ps) than for the WFST measurements (0.006 ps). Such a behaviour is reasonable since a larger measurement uncertainty is associated with the narrower spectrum of the interferometer source. This is probably not the only reason. We also observed that the measurement was sensitive to the experimental conditions. If the launched State Of Polarisation is aligned on one of the PSP of the FUT, it will not be possible to measure any PMD. As the PSP of the FUT can be sensitive to external stresses, it will be always difficult to realise an ideal launching. Another cause of difficulties lies in the fact that we used a fibre PC made of three fibre loops. The coupling conditions from the FUT to the birefringent fibre and from the birefringent fibre to the interferometer could be different when stresses are applied on the patchcords and on the polarisation controller loops. As a last remark, it is easy to understand that the modified interferometer is a time consuming experiment compared with the duration of measurements carried out with our broadband WSFT technique (less than three minutes). These are the reasons why the optimisation of the modified interferometer set-up should be done in order to improve the repeatability and to decrease the duration of this technique. Nevertheless, this interferometer is able to measure PMD below the WSFT technique limit.

Conclusions

In this paper, we presented our PMD measurements with the modified interferometer. Due to this technique we were able to characterise fibres with PMD values below the coherence time of the interferometer source. PMD measurements of birefringent and telecommunication fibres have been carried out. The PMD values from 0.1 ps to 0.031 ps have been achieved with a RMS better than 0.011 ps and remaining within the calculated uncertainty. A comparison of this method with the WSFT has been discussed and PMD results have been given similar. Nevertheless, the uncertainty and RMS of the WSFT measurements are better due to the broader source spectrum involved in the measurements. The comparison with the Jones Matrix Eigen Analysis is currently under investigation.

Acknowledgements

MULTITEL Telecom is supported by Région Wallonne and the European Commission (OBJECTIF 1 project) and located at the *Service d'Electromagnétisme et de Télécommunications* of the *Faculté Polytechnique de Mons*. We would like to warmly thank Prof. N. Gisin from University of Geneva for the helpful discussions and MM. Y. Choquet and D. Biagi from MULTITEL for their kind collaboration. The discussions within the frame of the European Commission Action COST 241 were also appreciated.

References

1. ITU-T SG15-WP4, Draft Recommendations, November 1995;
IEC SC 86A/WG1, Draft Recommendations, June 1996;
Fibre Optic Test Procedures (FOTP) 113, 122 and 124, Telecommunications Industry Association.
2. A. J. Barlow, T. Voots and T. G. Arnold, "Measurements of Ultra-low Polarisation Mode Dispersion in Single-Mode Optical Fibers by a Technique of PMD Biasing", *Proceedings OFMC'95*, Liège, September 1995, pp. II.4.
3. Ph. Oberson, K. Julliard, F. Prieto and N. Gisin, "Interferometric Polarization Mode Dispersion Measurements with Femtoseconds Sensitivity", *Proceedings SOFM'96*, Boulder, October 1996, pp. 143-146.
4. F. Ravet, Y. Choquet, B. Heens, X. Wang, L. Meuleman, M. Blondel, "PMD Measurements Below 0.05 ps by the Fixed Analyser Technique", accepted to *NOC'97*, Antwerp, June 97, pp. 161-164.
5. N. Gisin, B. Gisin, J. P. Von der Weid, R. Passy, "How Accurately Can one Measure a Statistical Quantity Like Polarization Mode Dispersion", *IEEE Photon. Technol. Lett.*, Boulder, vol. 3, 1671 (1991).

A New Differential Optical Amplifier Based on Nonlinear DFB/F-P Bragg Gratings

X. Wang, B. Heens, F. Ravet, J-C. Froidure, and M. Blondel

Service d'Electromagnétisme et de Télécommunications-MULTITEL Telecom
Faculté Polytechnique de Mons, Bld Dolez 31, B-7000 Mons, Belgium
Tel: +32-65-37 43 24, Fax: +32-65-37 41 99, E-mail: Wang@telecom.fpms.ac.be

Abstract: In this paper, a new differential optical amplifier is theoretically proposed. This amplifier is constructed by the Kerr-type nonlinear DFB/F-P fiber Bragg grating, which has extremely low switching thresholds. The simulated results of its static and dynamic optical operations are demonstrated.

1. Introduction: Considerable effects have been devoted in recent years to study optical propagation in nonlinear periodic media because of its potential applications for all-optical bistable switching and differential amplification devices. Until now, the main problem to realize these devices with optical fiber gratings is that very high threshold power is required. S. Larochelle *et al*[1] demonstrated that the threshold power of a 3 cm-long photoinduced fiber grating with silica glass is about 1 kW. Therefore, not only are high power sources needed but thermal problems connected with material absorption at such high intensities introduce additional complications. With the consideration of the relatively weak nonlinearities of most optical material, several methods have been proposed to reduce the threshold values, for example, nonlinear phase-shifted periodic structures[2] and optical fiber gratings with active medium[3]. These two methods can provide a 10 times lower threshold value compared with passive uniform fiber gratings. Recently, we proposed a distributed feedback fiber grating combined with a Fabry-Perot fiber cavity (DFB/F-P fiber grating structure)[4], which can provide again more than 1000 times lower threshold value.

In this paper, a new differential optical amplifier, constructed by a nonlinear DFB/F-P fiber grating structure, is introduced. Both differential gain and dynamic frequency spectrum of this differential amplifier are analyzed by solving the corresponding time-dependent coupled-mode equations.

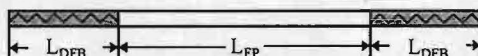


Fig. 1. Schematic diagram of nonlinear DFB fiber grating structure combined with F-P cavity.

2. DFB/F-P Fiber Grating Structure: Consider a DFB/F-P fiber grating structure, as shown in Fig. 1, which is composed of two uniform gratings separated by a short piece of optical fiber (Fabry-Perot cavity). This structure is similar with distributed Bragg reflectors (DBR) semiconductor laser. In the regions of Bragg grating, the refractive index along the optical fiber (z -axis) can be given by

$$n(z) = n_0 + \Delta n \cos(2\beta_B z) \quad (1)$$

where n_0 is the average refractive index, Δn is the grating amplitude, and β_B is the Bragg wave vector, which is given by $\beta_B = 2\pi/\lambda_B$. The Bragg wavelength λ_B is related to the grating period Λ as $\Lambda = \lambda_B/2n_0$. For a fiber grating $n_0 \approx 1.46$, while Δn is at most approximately 0.01 and usually much smaller. Therefore, the standard assumption of small coupling strength ($\Delta n \ll n_0$) are always valid. In this case, the coupled-mode equations can be used to describe the field propagation in fiber gratings quantitatively. In coupled mode theory the electric field inside the grating, $E(x, y, z, t)$, which are assumed to be linearly polarized, is written as

$$E(x, y, z, t) = F(x, y) [A_+(z, t) \exp(i\beta_B z - i\omega_B t) + A_-(z, t) \exp(-i\beta_B z - i\omega_B t)] \quad (2)$$

where transverse variations for the two counter-propagating waves are governed by the same modal distribution $F(x,y)$. The quantity ω_B is the associated (angular) frequency medium at the Bragg resonance. In order to find the evolution equations for the field envelopes $A_{\pm}(z,t)$, we can substitute (2) into Maxwell's equations. Making use of the knowledge that the $A_{\pm}(z,t)$ are slowly varying, it is found that they satisfy the following time-dependent coupled-mode equations

$$\frac{\partial A_+}{\partial z} + \beta_1 \frac{\partial A_+}{\partial t} + \frac{i}{2} \beta_2 \frac{\partial^2 A_+}{\partial t^2} - \frac{\alpha}{2} A_+ = i\gamma(|A_+|^2 + 2|A_-|^2)A_+ + i\delta\beta A_+ + i\kappa A_- \quad (3)$$

$$-\frac{\partial A_-}{\partial z} + \beta_1 \frac{\partial A_-}{\partial t} + \frac{i}{2} \beta_2 \frac{\partial^2 A_-}{\partial t^2} - \frac{\alpha}{2} A_- = i\gamma(|A_-|^2 + 2|A_+|^2)A_- + i\delta\beta A_- + i\kappa A_+ \quad (4)$$

where α is the fiber loss, $\delta\beta (= \beta - \beta_B)$ is a measure of the detuning of incident light from Bragg resonance, κ is the coupling coefficient and γ is the nonlinear Kerr coefficient. $\beta_1 = n_0/c$ with c vacuum light speed and β_2 governs group velocity dispersion. It should be noted that the optical fiber without grating can be regarded as a special case of optical fiber gratings with zero coupling coefficient. As a result, above equations (3) and (4) for the DFB/F-P fiber grating structure can be numerically solved by our time-dependent transfer matrix method[3].

3. Differential Amplification Properties:

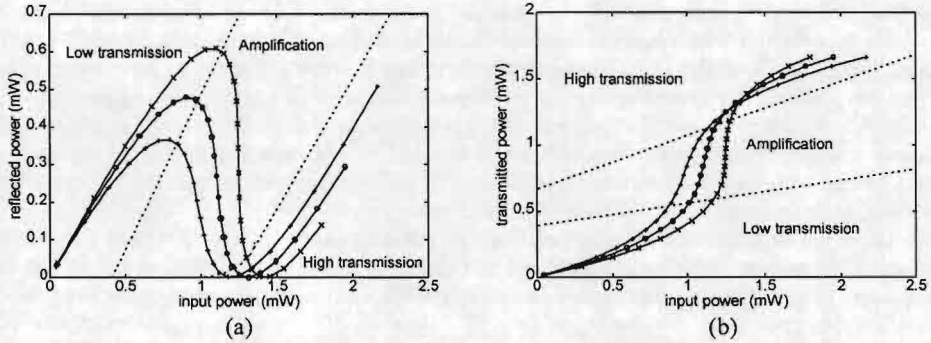


Fig. 2. (a) Reflected power and (b) transmitted power against input power for nonlinear DFB/F-P fiber grating with DFB grating length $L_{DFB}=20$ mm, $\kappa L_{DFB}=4.0$ and detuning parameter $\delta\beta L_{DFB}=0.3$, taking F-P cavity length L_{FP} as a parameter, $L_{FP}=99.784$ mm ('+' curve), $L_{FP}=99.79$ mm ('o' curve), and $L_{FP}=99.796$ mm ('x' curve).

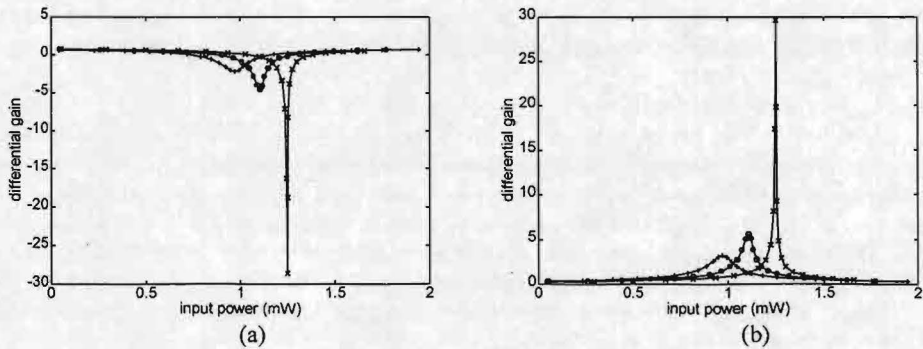


Fig. 3. Differential gains, including (a) reflected differential gain and (b) transmitted differential gain, against the input power, which are calculated by using the results in Fig. 2 (a) and (b), respectively.

The differential amplification operation of nonlinear DFB/F-P Bragg gratings can be analyzed by solving time-dependent coupled-mode equations [Eqs. (3) and (4)]. Fig. 2 and Fig. 3 demonstrate our signification results for the nonlinear DFB/F-P fiber gratings with DFB grating length $L_{DFB}=20$ mm, $\kappa L_{DFB}=4.0$ and detuning parameter $\delta\beta L_{DFB}=0.3$ where the F-P cavity length L_{FP} is taken as a parameter: $L_{FP}=99.784$ mm, 99.79 mm, and 99.796 mm. As shown in Figs. 2 (a) and (b), the transmission characteristics has been divided into three operation states: low transmission, amplification, and high transmission. With the increase of L-P cavity length, the distinguish of low transmission from high transmission becomes more and more obvious, and the dynamic amplification range of input power is moved to higher values. When the L-P cavity length is greater than a certain value (a critical power), bistable behavior of transmission and reflection will be generated.

Figs. 3 (a) and (b) show our calculated results of reflected differential gain and transmitted differential gain with F-P cavity length as a parameter. These results are calculated from the derivative of their corresponding reflection and transmission functions as shown in Figs. 2 (a) and (b), respectively. When the fiber grating parameters are chosen, the differential gains are very sensitive to the change of F-P cavity length and become shaper for a longer F-P cavity. As shown in Figs. 3 (a) and (b), these two differential gains have opposite symbol. In other words, the transmitted differential gain has positive value, i.e., transmitted output power is inphase with input power, whereas the reflected differential gain has negative value, i.e., reflected output power has 180° phase difference with input power. It is also noted that the dynamic amplification range of input power is decreased with the increase of maximum differential gain.

4. Dynamic frequency spectrum: Another important property of differential amplifier is its dynamic frequency response. Figs. 4 (a)-(f) show our calculated amplitude modulation (AM) frequency spectra of both reflection and transmission for a nonlinear DFB/F-P fiber grating with the following parameters: DFB grating length $L_{DFB}=20$ mm, L-P cavity length $L_{FP}=99.79$, $\kappa L_{DFB}=4.0$ and detuning parameter $\delta\beta L_{DFB}=0.3$. Three bias input powers is used to make the differential amplifier into three working states: low transmission, amplification, and high transmission. In the case of amplification state, as shown in Figs. 4 (c) and (d), both reflected and transmitted AM responses have very narrow bandwidths and maximum points of their passbands are located at zero bias modulation frequency. Beyond the passbands, the transmitted AM frequency response trends to zero, but the reflected AM frequency response trends to a nonzero constant, whose value is less than 1 and greater than 0. On the other hand, in the cases of low and high transmission states, much wider bandwidth and two symmetric peaks can be observed from both reflected and transmitted AM frequency responses. At low transmission state, two peaks of reflected AM frequency response are stronger than those of transmitted AM frequency response, as shown in Figs. 4 (a) and (b). However, at high transmission state, opposite situation is observed, as shown in Figs. 4 (e) and (f). Finally, It is noted that even at high transmission state, input power within its passband can be differentially amplified at the reflected output power [Fig. 4 (e)], but not at the transmitted output power [Fig. 4 (f)].

5. Conclusion: Differential amplification in the Kerr-type nonlinear DFB/F-P fiber gratings has been considered. The differential gains and dynamic frequency responses of this structure have been calculated. Three main characteristics of this differential amplifier include its very low threshold value (about 1 mW), very narrow passband (less than 1 MHz), and high differential gain. The reasons of very low threshold operation in this grating structure are the introduction of F-P fiber cavity, which provides two functions: cavity resonance and phase shifting. The cavity resonance enhances the nonlinear effect by the optical field round-trip in the cavity. The phase shifter gives rise to higher intensity distribution along the Fabry-Perot fiber cavity when its value is set to be about $\lambda/4$ (or $\pi/2$). Further researches of this differential amplifier include (1) replacing uniform fiber gratings by chirp fiber gratings in order to increase the amplification bandwidth and (2) using several differential amplifiers in parallel in order to augment the dynamic amplification range of input power.

Acknowledgments: X. Wang, B. Heens, F. Ravet, J-C. Froidure are working in the frame of an R&D contract commonly supported by the *Ministère de la Région Wallonne* and the *European Commission*.

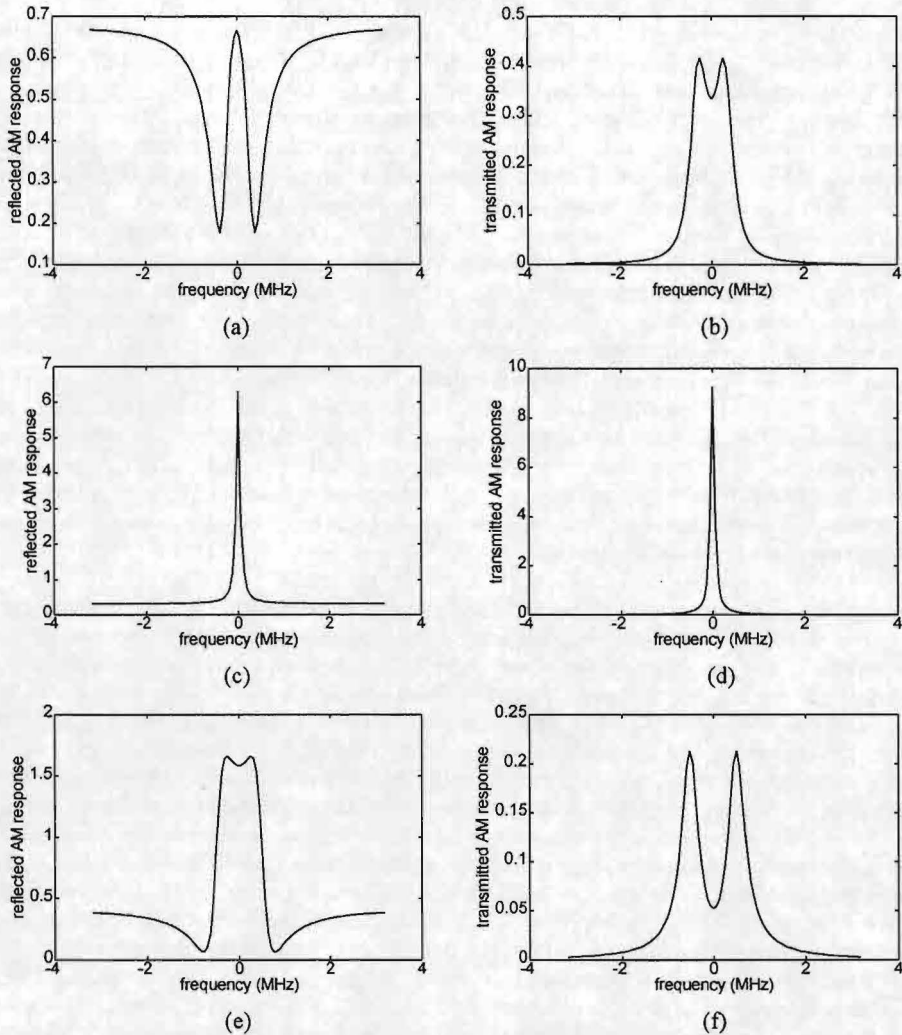


Fig. 4. Dynamic frequency responses for a nonlinear DFB/F-P fiber grating with DFB grating length $L_{\text{DFB}}=20$ mm, F-P cavity length $L_{\text{FP}}=99.79$ mm, $\kappa L_{\text{DFB}}=4.0$ and detuning parameter $\delta\beta L_{\text{DFB}}=0.3$. (a) reflected AM response at low transmission state; (b) transmitted AM response at low transmission state; (c) reflected AM response at amplification state; (d) transmitted AM response at amplification state; (e) reflected AM response at high transmission state; and (f) transmitted AM response at high transmission state.

References:

- [1] S. Laroche, Y. Hibino, V. Mizarhi, and G. I. Stegeman, *Electron. Lett.*, vol. 26, p. 1459 (1990).
- [2] S. Radic, N. George, and G. P. Agrawal, *J. Opt. Soc. Am. B*, Vol. 12, p. 671 (1995).
- [3] X. Wang, L. Meuleman, B. Heens, J-C. Froidure, P. Mégret and M. Blondel, *Proc. IEE Colloquium on Optical Fiber Gratings*, p. 10/1 (London, UK, 1997).
- [4] X. Wang, L. Meuleman, B. Heens, F. Ravet, J-C. Froidure and M. Blondel, *IOOC/ECOC'97*, p. 3/190 (Edinburgh, UK, 1997).

Acket, G.A.	65, 225	Gyselings, T.	89
Al-Remawi, A.	53	Harmsma, P.J.	45, 201
Baets, R.	49, 89, 101, 105, 109, 113, 129	Haverkort, J.E.M.	185, 189
Bakker, A.F.	33	Heens, B.	244, 248
Bakker, A.	145	Heideman, G.H.L.M.	165
Balistreri, M.L.M.	17	Heideman, R.G.	29, 37
Baukens, V.	13, 21, 129	Hendriks, R.F.M.	229
Bertsev, V.V.	133	Hendrix, J.	105
Blok, F.J.	157	Herben, C.G.P.	41
Blom, F.C.	137	Heremans, P.	13, 125
Blondel, M.	244, 248	Hermanne, A.	13, 21
Blondelle, J.	101	Heuvel, J.J.B. van den	73
Bockstaele, R.	113	Heyker, H.C.	217
Boom, H. v.d.	9	Hoekman, M.	145
Borrisé, X.	117	Hoekstra, O.B.	161
Brouwer, A.J.	237	Hoekstra, H.J.W.M.	137
Brug, H. van	193	Hofstra, R.M.	69, 149
Buczynski, R.	13	Hooijer, C.	177
Buda, M.	65	Hove, A. van	113
Bureiko, S.F.	133	Hovenier, J.N.	61
Caeekebeke, K.	49	Hulst, N.F. van	17
Caenegem, B. van	93, 97	Jacob, D.	5
Choquet, Y.	244	Jacobs, B.	97
Coosemans, T.	113	Jacobs, K.	105
Coppée, D.	13, 25	Janssen, A.W.L.	5
Daele, P. van	49, 101, 105, 113, 117	Jennen, J.G.L.	1
Danckaert, J.	121	Joppe, J.L.	33
Demeester, P.	41, 97	Karouta, F.	213, 221, 225
Demeester, P.	93, 101, 105	Kaufmann, L.M.F.	213
Depreter, B.	101	Kelderman, H.	137
Dhoedt, B.	49, 105, 113, 129	Keller, A.A.	133
Diemeer, M.B.J.	33, 117	Kersten, E.J.	165
Diet, G.	109	Khoe, G.	9
Dobbelaere, P.M. de	117	Kirk, A.	125
Dorren, B.H.P.	185	Klaassen, T.P.	61
Dorren, H.J.S.	73, 77	Kochetov, I.V.	157
Driessen, A.	33, 37, 137, 145, 153	Koczyk, P.	125
Druten, N.J. van	233	Koike, Y.	9
Dubbeldam, J.L.A.	57	Kok, M. de	209
Eijkelenborg, M.A. van	233	Koonen, A.M.J.	33, 169
Eijkemans, T.J.	225	Kortenk, J.P.	17
Es, C.M. van	225	Krijnen, G.J.M.	33, 37, 145
Etten, W. van	165	Kufner, M.	13, 21, 129
Exter, M.P. van	53, 229, 233	Kufner, S.	13, 21, 129
Faber, A.J.	241	Kuijk, M.	25, 125
Farrell, T.	109	Kwaspen, J.J.M.	217
Feenstra, L.	161	Lagendijk, A.	3
Flamand, G.	105	Lambeck, P.V.	29, 141, 153
Frankena, H.J.	193	Langelier, H.A.	221
Frietman, E.E.E.	197	Lee, A.M. van der	233
Froidure, J.-C.	244, 248	Leijtens, X.J.M.	41, 205, 209
Genoe, J.	13	Lenstra, D.	57, 173, 177
Gerbrandij, A.W.	237	Leys, M.R.	45, 185, 201
Gilde, M.J.	33	Li, W.	9
Goeman, S.	49	Lindberg, A.M.	233
Goor, F.A. van	69, 149	Linden, J.E. van der	117
Goulet, A.	125	Liskamp, R.M.J.	237
Graaf, W.A. van der	173	Maat, D.H.P.	41, 193
Groen, F.H.	41, 193	Melick, N.G.H. van	213

Mieremet, A.L.	233	Verschuren, C.A.	45, 201
Minnaert, A.W.E.	189	Verstuyft, S.	49
Moerman, I.	101, 105, 193, 205, 209	Visser, T.D.	181
Morthier, G.	109	Vleuten, W.C. van der	65, 189, 221, 225
Morthier, G.	89	Vonk, H.	45, 201
Mulders, S.J.E.	237	Vounckx, R.	13, 25, 49, 125
Muys, P.	5	Vreeburg, C.G.M.	41, 193, 201
Napartovich, A.P.	157	Vynck, P.	13, 21, 129
Nieuborg, N.	49, 125	Waardt, H. de	1, 9, 77
Ochkin, V.N.	157	Wang, X.	244, 248
Oei, Y.S.	41, 45, 201	Wang, H.	85
Ottevaere, H.	21, 129	Wauters, N.	11
Pan, W.	25	Wenckebach, W.Th.	61
Panajotov, K.	121	Willems, F.W.	5
Parys, W. van	93	Willems, F.	13
Pastor, A.A.	133	Witterman, W.J.	69, 149, 157, 161
Pedersen, J.W.	209	Woerdman, J.P.	53, 229, 233
Peeters, M.	121	Wolter, H.H.	185
Pesquera, L.	173	Wolter, J.H.	45, 189
Peters, P.J.M.	157, 161	Wörhoff, K.	37, 153
Plaats, J.C. van der	5	Yabre, G.	81
Popma, Th.J.A.	137	Yamazaki, S.	9
Praag, J.J.W. van	221, 225	Zhu, Y.C.	193, 209
Prassas, M.	5	Zwegers, M.J.	69, 149
Pugžys, A.	237		
Ranson, W.	125		
Ravet, F.	244, 248		
Ridder, R.M. de	33, 37, 145, 153		
Rijkers, E.	33, 145		
Roer, T.G. van de	65		
Ryvkin, B.	121		
Sarlet, G.	109		
Schimmel, R.C.	241		
Serdobintsev, P.Yu	133		
Siefke, A.	209, 213		
Siffels, J.	77		
Sikken, B.H.	37		
Silov, A.Yu.	185, 189		
Sitens, J.	49		
Smalbrugge, E.	65		
Smets, R.C.J.	1		
Smit, M.K.	33, 41, 205, 209		
Starostin,	157		
Steenbergen, C.A.M.	5, 209		
Stiens, J.	25		
Stulemeijer, J.	205		
Tafur Monroy, I.	77		
Tandt, C. de	125		
Thienpont, H.	13, 21, 49, 121, 125, 129		
Tol, J.J.G.M. van der	41		
Tuteleers, P.	13, 21, 129		
Udalov, Y.B.	157		
Vandenbergh, B.	93		
Varma, C.A.G.O.	237		
Veen, D.T. van	33, 169		
Veldhuis, G.J.	141		
Veretennicoff, I.	13, 21, 121, 125, 129		
Verhoeve, P.	109		
Verschaffelt, G.	13, 21, 129		

Bibliotheek

Technische Universiteit Eindhoven

Postbus 90159

5600 RM

Eindhoven

Telefoon (040) 24 72224



9716750



ISBN: 90-73461-13-8

STW-1997 11 10-01

<http://www.stw.nl/commtech>